Exploring the Hardness of Nitride Ceramics: Electronic Properties and Band Gap Studied using Soft X-ray Spectroscopy

A Thesis Submitted to the

College of Graduate Studies and Research

in Partial Fulfillment of the Requirements

for the degree of Doctor of Philosophy

in the Department of Physics and Engineering Physics

University of Saskatchewan

Saskatoon

By

Teak D. Boyko

Permission to Use

In presenting this thesis in partial fulfilment of the requirements for a Postgraduate degree from the University of Saskatchewan, I agree that the Libraries of this University may make it freely available for inspection. I further agree that permission for copying of this thesis in any manner, in whole or in part, for scholarly purposes may be granted by the professor or professors who supervised my thesis work or, in their absence, by the Head of the Department or the Dean of the College in which my thesis work was done. It is understood that any copying or publication or use of this thesis or parts thereof for financial gain shall not be allowed without my written permission. It is also understood that due recognition shall be given to me and to the University of Saskatchewan in any scholarly use which may be made of any material in my thesis.

Requests for permission to copy or to make other use of material in this thesis in whole or part should be addressed to:

Head of the Physics and Engineering Physics
163 Physics Building
116 Science Place
University of Saskatchewan
Saskatoon, Saskatchewan
Canada
S7N 5E2

Abstract

Research into determining what intrinsic characteristics cause materials to be hard is imperative if one would like to design future materials with a hardness exceeding that of diamond. Measuring the hardness of materials in order to obtain a fundamental quantity independent of extrinsic factors is difficult, if not impossible. However, many theories have been proposed pertaining to the quantification of hardness as a fundamental property. While it is clear that the hardness of a material will strongly depend on its crystal structure, another fundamental quantity, the electronic band gap, has also been linked to the intrinsic hardness of materials. The electronic band gap is a seemingly simple quantity, but is difficult to determine for novel or complicated materials. Core-level spectroscopy techniques that probe the occupied and unoccupied density of states separately allow for an indirect determination of the electronic band gap. These methods have several advantages over conventional techniques in that they do not strongly depend on the extrinsic material properties such as defects and impurities. The electronic band gap has been determined in this way for several novel materials. These include group 14 nitrides with spinel structure that were recently studied over the last decade. The electronic band gap of three synthesized binary spinel nitrides γ-Si_3N_4, γ-Ge_3N_4 and γ-Sn_3N_4 are determined using core-level spectroscopy to be 4.8 ± 0.2 eV, 3.5 ± 0.2 and 1.6 ± 0.2 eV, respectively. These measurements agree with the calculated values of 4.97, 3.59 and 1.61 eV for γ-Si_3N_4, γ-Ge_3N_4 and γ-Sn_3N_4, respectively. We have also extended these measurements and calculations to include the solid solutions γ-$(Ge_xSi_{1-x})_3N_4$ and γ-$(Sn_xGe_{1-x})_3N_4$ showing these spinel-structured nitrides form a multi-functional class of semiconductors. This band gap measurement technique has also been applied successfully to the phosphor converting light emitting diode material $Ba_3Si_6O_{12}N_2$ and the novel semiconductor MnNCN. This shows that using core-level spectroscopy is a very effective method to determine the electronic band gap where there are no other feasible techniques. Aside from the electronic band gap, core-level spectroscopy is also a complementary technique to determine the crystal structure, which is also an important parameter with regard to hardness. The crystal structure, particularly aspects such as anion ordering and vacancy ordering, have been determined for the spinel-structured oxonitride Ga_3O_3N and a novel phase of calcium

nitride Ca_3N_2. These results show that core-level spectroscopy is a powerful technique to determine the anion ordering in oxonitrides and was further applied to the material class β-sialons, allowing for the determination of the electronic band gap as well as ascertaining both the anion and cation ordering. Combining all of these aspects we show that the electronic band gap is not only useful for predicting the hardness of materials, but in some cases can be used to predict the existence of certain materials. We use theoretical methods, combined with experimental measurements, to calculate the hardness and electronic band gap of all possible binary and ternary group 14 spinel-structured nitrides. Through the correlation of the hardness and electronic band gap we show that only the three already synthesized binary group 14 spinel-structured nitrides are stable along with their solid solutions and that the elusive spinel-structured carbon nitride γ-C_3N_4 will be never synthesized.

Acknowledgements

I would like to thank my supervisor, Professor Alexander Moewes, for all of his support in completing this thesis. Prof. Moewes acquired me as a student in my last year of undergraduate studies and it has been a very successful relationship ever since. With his guidance I have been awarded both the NSERC masters and doctoral scholarships during my graduate studies and managed to publish more than 10 papers. Without his significant contributions, the completion of this thesis and associated published papers would not be possible. I would also like to thank all of my collaborators, as none of this research would also be possible without their dedication to material synthesis. Additionally, I would also like to thank all the members of the Beamteam, past and present, for their insightful discussions and support.

The X-ray absorption measurements included in this thesis and the papers were performed at the Canadian Light Source, which is funded by the Canada Foundation for Innovation, the Natural Sciences and Engineering Research Council of Canada, the National Research Council Canada, the Canadian Institutes of Health Research, the Government of Saskatchewan, Western Economic Diversification Canada, and the University of Saskatchewan. The included X-ray emission measurements were performed the Advanced Light Source, which is supported by the Director, Office of Science, Office of Basic Energy Sciences, of the U.S. Department of Energy under Contract No. DE-AC02-05CH11231. The theoretical calculations have been enabled by the use of computing resources provided by WestGrid and Compute/Calcul Canada.

To my loving wife Jamie, whose support throughout my graduate studies has been invaluable.

Contents

Permission to Use i

Abstract ii

Acknowledgements iv

Contents vi

List of Tables viii

List of Figures viii

List of Abbreviations ix

1 Introduction 1
- 1.1 Ultra-hard Materials . . . 1
- 1.2 Mechanical Hardness . . . 4
  - 1.2.1 Microhardness . . . 5
  - 1.2.2 Nanohardness . . . 8
  - 1.2.3 Bulk and Shear Moduli . . . 9
  - 1.2.4 Alternatives to Hardness Measurements . . . 13
- 1.3 Intrinsic hardness . . . 14
  - 1.3.1 Empirical models . . . 14
  - 1.3.2 Semi-*empirical* models . . . 16
  - 1.3.3 *ab initio* models . . . 18
  - 1.3.4 Intrinsic Hardness Results . . . 20

2 Electronic Structure 22
- 2.1 Electronic Band Gap . . . 22
  - 2.1.1 Conventional Measurements . . . 23
  - 2.1.2 Indirect Measurements . . . 24
- 2.2 Core-level Spectroscopy Measurements . . . 25
  - 2.2.1 X-ray Absorption Spectroscopy . . . 27
  - 2.2.2 X-ray Emission Spectroscopy . . . 31
- 2.3 Electronic Structure Calculations . . . 32
  - 2.3.1 Exchange-correlation Functionals . . . 34
  - 2.3.2 WIEN2k . . . 35
- 2.4 Core-level Spectroscopy Electronic Band Gap Measurements . . . 36
  - 2.4.1 Broadening . . . 37
  - 2.4.2 Core Hole Effects, Nonequivalent Site Splitting and Spin-orbit Splitting 41
  - 2.4.3 Calibration . . . 43

2.5 Publications 44

3 Crystal Structure **89**
3.1 Conventional Techniques 89
3.2 Electronic Structure 90
3.3 Publications 90

4 Predicting the Structure of Materials **120**
4.1 Hardness Predictions and Structure 120
4.2 Publication 120

5 Conclusions **127**

References **130**

A Author Publications **135**

B Copyright Agreements **137**
B.1 APS 137
B.2 ACS 137
B.3 Wiley 138

List of Tables

1.1 Measured Vickers microhardness, shear modulus and bulk modulus values for an array of materials. 13
1.2 A comparison of measured and calculated hardness values for an array of materials. 21
1.3 The calculated hardness of spinel structured nitrides using intrinsic hardness models. 21

List of Figures

1.1 Visualization of the two most common microhardness indenter profiles. . . . 6
1.2 The load profiles of microhardness and nanohardness measurements. 7
1.3 Visualization of the two most common nanohardness indenter profiles. 10
1.4 The visualization of bulk compression and shear strain. 11

2.1 A diagram of band gap transitions 23
2.2 An example of a UV-Vis absorption spectrum. 24
2.3 Examples of other methods to determine the electronic band gap. 38
2.4 The electronic band gap determination of silicon. 44

List of Abbreviations

CB	Conduction Band
DFT	Density Functional Theory
DOS	Density of States
ECF	Exchange-correlation Functional
EXAFS	Extended X-ray Absorption Fine Structure
GGA	Generalized Gradient Approximation
H	Mechanical Hardness
H_v	Vickers Microhardness
HOMO	Highest Occupied Molecular Orbital
IPFY	Inverse Partial Fluorescence Yield
LDA	Local Density Approximation
LO	Local Orbital
LPDOS	Local Partial Density of States
LUMO	Lowest Unoccupied Molecular Orbital
ND	Neutron Diffraction
pc-LED	Phosphor Converting Light Emitting Diode
PFY	Partial Fluorescence Yield
PL	Photo-luminescence
RIXS	Resonant Inelastic X-ray Scattering
SIAM	Single Impurity Anderson Model
TEY	Total Electron Yield
TFY	Total Fluorescence Yield
UV-Vis	Ultraviolet-Visible
VB	Valence Band
XAS	X-ray Absorption Spectroscopy
XANES	X-ray Absorption Near Edge Structure
XES	X-ray Emission Spectroscopy
XRD	X-ray Diffraction

Chapter 1

Introduction

1.1 Ultra-hard Materials

Materials with outstanding chemical and mechanical properties are entrenched in our everyday lives. Hard materials find the vast majority of their uses in mechanical applications, whether it be coatings for cutting blades or bearings for automotive engines. Mechanical blades and cutting tools take advantage of the extreme wear resistance that is present in hard materials, which are often coated with titanium nitride (c-TiN) or zirconium nitride (c-ZrN) increasing their lifespan significantly. The Vickers microhardness (H_v) of these materials is comparable to that of the commonly used silicon carbide ($H_v[c\text{-TiN}] = 20 \pm 2$ GPa, $H_v[c\text{-ZrN}] = 27 \pm 2$ GPa, $H_v[\beta\text{-SiC}] = 26 \pm 2$ GPa [1]). Aside from cutting tools, hard materials are commonly used for surfaces in mechanical engines that experience excessive wear. Bearings or turbines are coated with silicon nitride (β-Si_3N_4) whose hardness is larger still ($H_v[\beta\text{-}Si_3N_4] = 30 \pm 2$ GPa [1]) improving the longevity and performance of these machines. These materials have a significant advantage over conventional steels in both wear resistance and thermal stability making them ideal for industrial cutting applications and an array of mechanical coatings. So far the applications discussed are devices that society commonly encounters, but likely the most demanding hard material application is industrial abrasives that are used for polishing. A large improvement in this field occurred with the discovery of cubic boron nitride (c-BN), which is the second hardest material today ($H_v[c\text{-BN}] = 63 \pm 5$ GPa [1]) and has the distinct advantage over diamond in that it does not react with steel. One can infer, increasing the array of hard materials that can be deposited as thin films could provide a means to eliminate most service requirements from our everyday mechanical devices and improve the performance of these devices. Additionally, discovering materials

with a hardness larger than c-BN could once again revolutionize the abrasive industry.

Ultra-hard materials are classified as any material with a mechanical hardness (H) larger than 40 GPa. This criterion restricts the pool of ultra-hard materials to include only diamond (c-C), cubic boron nitride (c-BN), wurtzite boron nitride (w-BN), boron carbide (B_4C), and the recently discovered spinel silicon nitride (γ-Si_3N_4) [1, 2]. The prediction that the bulk modulus of hexagonal carbon nitride (β-C_3N_4) would be comparable to diamond [3] drew interest to group 14 nitrides and soon thereafter at the turn of the millennium a new phase of group 14 nitrides was discovered, the γ phase [4]. This phase has spinel structure ($MgAl_2O_4$), but in the binary nitride case it would be γ-AD_2N_4, where the A and D sites are tetrahedral and octahedral coordinated cations, respectively. The clear advantage here over the previous group 14 binary nitrides phases (α and β, which have tetrahedral and trigonal planar bonding polyhedra) are the tetrahedral and octahedral bonding polyhedra. As a result, the measured hardness of γ-Si_3N_4 is over 40% larger than β-Si_3N_4 [1, 2]. With this in mind, one would expect that the spinel phase of carbon nitride (γ-C_3N_4) would have a hardness comparable to diamond. However, the only group 14 spinel nitrides that have been synthesized are γ-Si_3N_4 [4–8], γ-Ge_3N_4 [9–12] and γ-Sn_3N_4 [13] making the successful synthesis of the coveted γ-C_3N_4 still unreported. Similarly, the successful synthesis of γ-Pb_3N_4 also remains unreported, but it will likely be much too soft to find use in any hard material applications discussed here and is also likely conducting making its uses rather limited. In the proceeding articles, we have developed a model to correlate the theoretical hardness and electronic band gap that shows the elusive γ-C_3N_4 will never be synthesized. Therefore, understanding the origin of the mechanical properties of the already synthesized spinel nitrides may lead to the discovery of further ultra-hard materials.

While the majority of applications for ultra-hard materials reside in mechanical applications, there is quite an array of electronic devices that would benefit from a thermally stable material provided it possesses the appropriate electronic properties. Devices that use these materials can include: high speed switches, high-temperature sensors and high-power lighting applications. These devices require materials that are thermally stable, semiconducting and in the case of lighting applications, have a direct electronic band gap with a sufficiently large exciton binding energy. Conveniently, many novel hard materials are synthesized un-

der extreme pressures and temperatures making their decomposition temperature quite large providing a host of thermally stable materials. Additionally, most hard materials are also semiconducting making them an ideal candidate for the ascribed electronic applications. In some cases, these desirable properties are inherent to the material itself, while others are obtained with specific preparation methods.

One of the primary directions for improving mechanical devices is the discovery of new materials with improved mechanical, chemical and even electronic properties. This direction of research requires meticulous characterization of new materials to ascertain whether further research into more efficient synthesis methods is warranted. Predicting the hardness of recently discovered and yet to be discovered materials is a very important challenge. It has been the goal of many scientists to be able to understand what causes materials to be hard and subsequently predict the hardness of novel or unknown materials. There are several competing theories [14–17], but the electronic band gap and crystal structure are material parameters that are commonly present in all theories [18, 19]. It is therefore the goal of this thesis to characterize and discuss the electronic and mechanical properties of novel materials in an effort to improve our understanding of the intrinsic mechanical, chemical and electronic properties.

In the proceeding chapters/sections the methods currently used to measure mechanical hardness and how these measurements correlate to fundamental material properties is discussed. The current theoretical models for calculating the intrinsic hardness is outlined, comparing the advantages and short-comings of competing theories. This will show that the electronic band gap, a fundamental material quantity, is useful when to comes to studying the intrinsic hardness of materials. In a later chapter the techniques used in this thesis to determine the intrinsic electronic band gap are discussed in detail. From there, another important parameter for studying hardness, the crystal structure, is discussed and a method to determine the anion ordering in materials using electronic structure measurements is outlined. Combining both of these aspects, we suggest a novel method to evaluate the likelihood of synthesizing a semiconducting material and show the hardness and the electronic band gap are largely intertwined. The included published, submitted and prepared manuscripts showcase both the results of applying the electronic band gap and crystal structure deter-

mination techniques, as well as the correlation between the intrinsic hardness and electronic band gap.

1.2 Mechanical Hardness

Quantifying material hardness has been developed for the better part of a century. The first hardness measurements were completed nearly 100 years ago using a spherical indenter, which is now better known as a Brinell indenter and is still being carried out today. Conventional hardness testing can be broken down into two main groups: scratch resistance and indentation resistance, which measure the resistance a material has to scratching from a harder material and the resistance a material has to plastic deformation, respectively.

Scratch resistance, most commonly used by mineralogists, is not an exact measurement of the hardness, but is more or less a relative measurement that compares a material to known minerals rating the hardness on a scale of 1 – 10. These measurements use a sclerometer with interchangeable tips (of different minerals) and grade materials on what is called the Mohs scale. Strictly speaking this scale is somewhat arbitrary and is not linear with the most commonly used reference materials in ascending order from 1 – 10 being: Talc, Gypsum, Calcite, Fluorite, Apatite, Feldspar, Quartz, Topaz, Corundum, and Diamond. The value of hardness for the preceding materials on a linear scale are: 1, 3, 9, 21, 48, 72, 100, 200, 400, 1600, respectively. This technique is a very good method to estimate whether a material is harder than a reference material, but it requires large pieces (minerals) since it is macroscopic in nature. Conversely, scientists more commonly use indention resistance tests and aim to grade the hardness of materials on an absolute scale in effort to study materials hardness more fundamentally. The indentation test is carried out in the following way: an indenter (Brinell, Vickers, Knoop, etc.) with a load of 1 – 120 kg (typically 50 kg) is applied to the material for approximately 15 – 20 seconds. The hardness H is then calculated using Eq. 1.1, where F is the applied load force and A_s is the resultant indentation surface area. Here, we calculate the hardness standardized to the gravity of earth meaning the load will be in force rather than mass, this is contrary to the historically quoted values which neglect the acceleration due to gravity producing a value in the units kg/mm^2 rather than pressure

(Pa). Conventional hardness testing is macroscopic, requires large amounts of high quality material similar to scratch testing and is also static since this hardness testing technique the material is allowed to relax fully minimizing rebound of the deformation. Hardness tests require permanent deformations known as plastic deformations, rather than elastic deformations, which rebound when the load is removed. The size limitation of conventional hardness testing and the typically small available amount of novel high-pressure materials means that more specialized hardness testing is required.

$$H = \frac{F}{A_s} \tag{1.1}$$

1.2.1 Microhardness

Microhardness indentation testing is a specialized method for measuring the hardness of materials and is ideal when there are very small quantities of materials available, as is the case for many novel high-pressure materials. This method of measuring hardness differs from the conventional macroscopic method described above in that both the indenter and optical devices are on the micro scale with indentations being μm^2 instead of typically mm^2. Specifically, microhardness indentation loads are restricted to 1 – 1000 g, but for most measurements the loads are 100 – 500 g as opposed to 1 – 120 kg in conventional testing. There are many indenter shapes available, but the Knoop and Vickers types are the two most common. Fig. 1.1 shows the geometry and indentation profiles for these two indenter types.

The microhardness H_n^{micro} of type n (v = Vickers and k = Knoop) is calculated from the general form of indentation hardness as in Eq. 1.1. However, the strict form needs to be modified to suit the indenter profile that is used and Eq. 1.2 and 1.3 show the calculations for Knoop and Vickers indentions, respectively. These calculations are very similar with the difference manifesting from the specific geometry of the indenter. Knoop hardness is measured using an elongated pyramidal indenter, where the only measurement taken after indentation is the length L in Eq. 1.2 and Fig. 1.1. This arises from the very narrow profile of the indentation where the width of an ideal indentation is 30 times smaller than the length. The Vickers hardness however, is measured using a square pyramidal indenter and also requires only one measurement, the width of the symmetric indentation along the diagonal D in Eq. 1.3 and

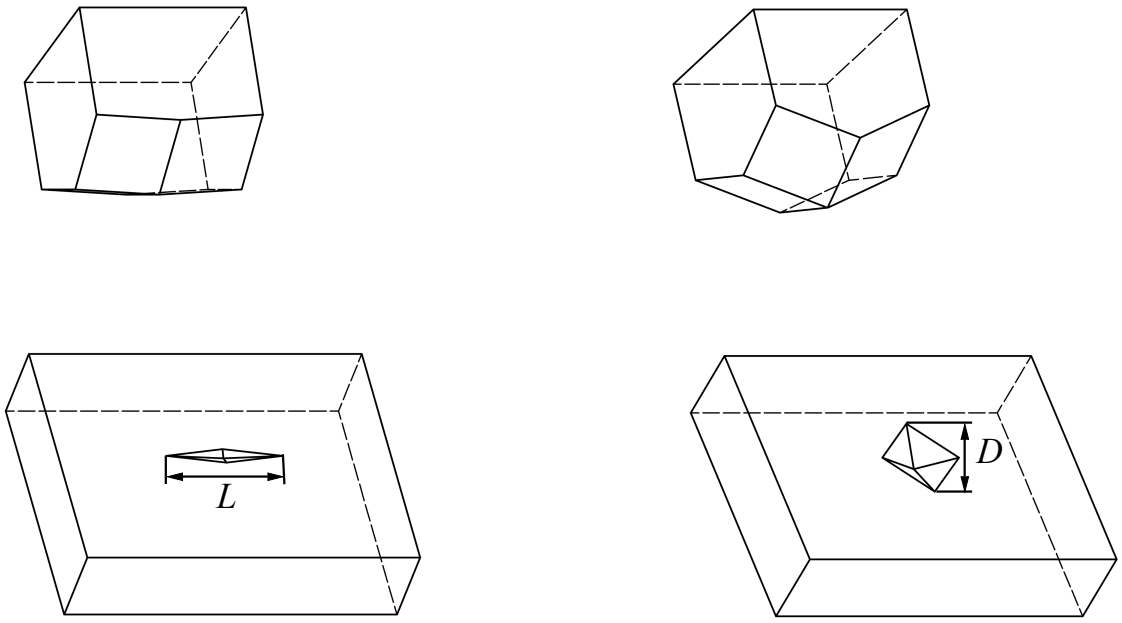

Figure 1.1: Visualization of the two most common microhardness indenter profiles: Knoop indenter (left) and Vickers indenter (right). The measured quantities correspond to those in Eqs. 1.2 and 1.3.

Fig. 1.1. Eq. 1.3 applies to any square pyramidal indenter, but here we restrict ourselves to a 68° angle between the faces, which is the most common. Both of these indenter profiles are commonly used to measured the hardness of novel materials, with Knoop being more widely used in the United States and Vickers more widely used in Europe. However, the Knoop indenter is believed to be more accurate due to the elongated indentation thereby making length measurements more accurate. The indenter is made of diamond in all cases, and although both methods seemingly measure the same quantity, there are distinct differences between the results of Knoop and Vickers hardness measurements.

$$H_k^{micro} = \frac{F}{L^2 C_k}, \quad C_k \approx 0.070279 \tag{1.2}$$

$$H_v^{micro} = \frac{2F}{D^2 \sin(68^\circ)} \tag{1.3}$$

Comparing the results of Knoop and Vickers hardness tests is difficult and one needs to

account for all possible inconsistencies, the first being the load dependence of the indentation. Typically, the indentation load is adjusted such that the size of the indentation is sufficient to be measured. For this reason, the load is always given with the hardness value. Fig. 1.2 shows the dependence of the measured hardness on the indentation load revealing certain issues in consistency for small loads. The values of both hardness tests can be compared provided the loads for the Knoop and Vickers indenter are kept above 500 g and 100 g, respectively [20]. The reason for these load dependent behaviours is ascribed to the elastic recovery of the indentation for a Knoop indenter and the inaccuracy in the width measurement of the indentation for a Vickers indenter. The minimum load masses are quite general since the reason behind the discrepancy is dependent on the hardness of the material being tested. While these load dependent behaviours are problematic for ascertaining the hardness of materials as a fundamental quantity, there are many other effects that can skew the results of indentation hardness measurements.

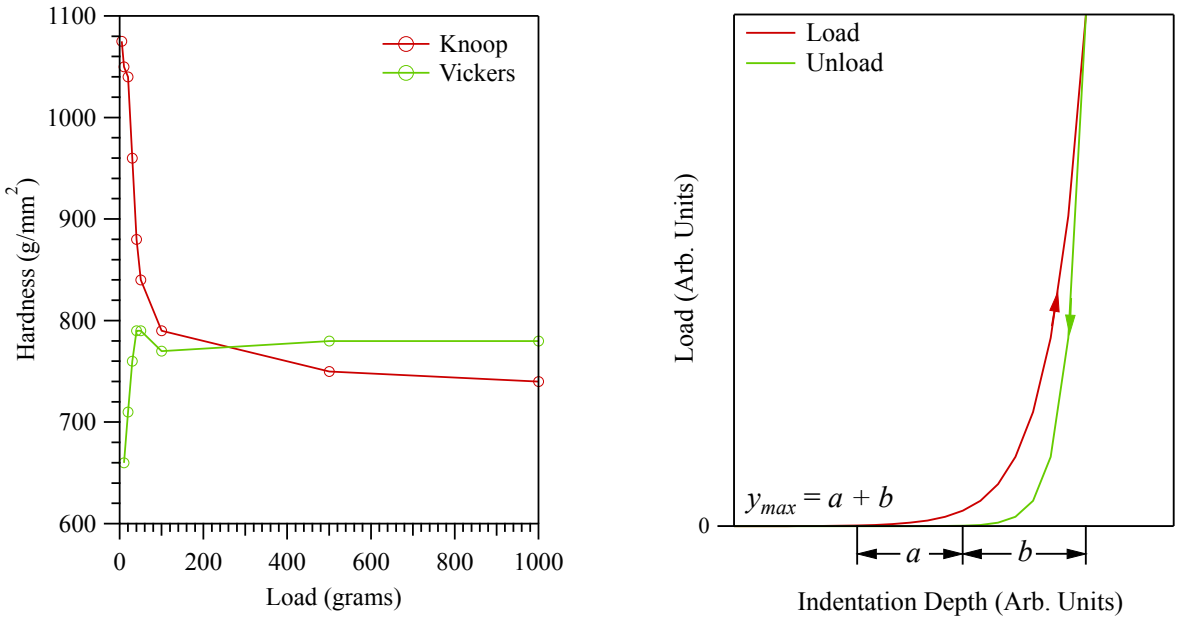

Figure 1.2: The load profile of Vickers and Knoop microhardness measurements (left) comparing the hardness dependence on the load for both measurements. The typical hardness load curve that is generated from nanohardness measurements (right) with the max displacement being $a + b$, the residual depth being a and the elastic recovery being b. These data have been taken from Ref. 20.

There are many material attributes that can affect the results of indentation hardness measurements. The material itself, must be an isotropic single crystal free of defects, otherwise there will be a directional component of the measured hardness. This means that conducting an indentation hardness test on different sides or in different locations of the same crystal could produce different values. This type of anisotropic behaviour would also apply to different crystal cuts. Furthermore, if a material is polycrystalline, not a single crystal, there may be breaking between the grains themselves rather than plastic shearing of the crystal and would likely reduce the measured hardness. This shortcoming of indentation hardness measurements is very important since most novel high-pressure materials are polycrystalline. There are also two other possible indentation issues that can drastically affect the measured hardness, which include plastic flow and cracking around the indentation site. The plastic flow arises from the large pressures of the indentation generating excess heat melting the material itself. Since this plastic flow of the material will affect the size of the indentation, and is dependent on the melting temperature of the material, examining the indentation for signs of this behaviour is very important. The cracking around indentation is also problematic since the measured hardness, similar to grain separation will be smaller than expected as a tremendous amount of energy is released during the cracking making the indentation much larger than expected. These short-comings of microhardness measurements aside, indentation hardness still remains the staple hardness measurement technique to study the hardness of novel high-pressure materials.

1.2.2 Nanohardness

Nanohardness measurements differ strongly from the other hardness testing methods discussed in that they are no longer static but dynamic, allowing hardness measurements to exhibit more fundamental qualities. The measurements involve similar indenter profiles, typically Vickers or Berkovich. Fig. 1.3 shows the indenter profiles, which are very symmetric, but a Berkovich indenter is preferred since it is easy to fabricate with a very sharp tip. The indentations are typically sub-micron in size and atomic force microscopy or scanning tunnelling microscopy are used to measure the indentations. Eq. 1.4 is used to calculate nanohardness, where F^{max} is the maximum applied load force and A_p^{max} is the maximum

projected area of the indentation. However, for nanoindentation the actual indentation size is not measured since it is much too small, but rather the indentation depth is recorded and plotted against the applied load. Eqs. 1.5 and 1.6 are used to determine the nanohardness for a Vickers and Berkovich indenter, respectively, where y_{max} is the maximum indentation depth. The nanohardness profile in Fig. 1.2 is produced by measuring y, where a is the residual indentation and b is the elastic recovery of the indent. This type of testing, although difficult to carry out, mitigates some of the short-comings of conventional and microhardness testing methods (load dependence, etc.), while making the hardness profile that is more characteristic of the material itself.

$$H^{nano} = \frac{F^{max}}{A_p^{max}} \tag{1.4}$$

$$H_v^{nano} = \frac{F^{max}}{4y_{max}^2 \tan^2(68^\circ)} \tag{1.5}$$

$$H_b^{nano} = \frac{F^{max}}{24.5y_{max}^2} \tag{1.6}$$

1.2.3 Bulk and Shear Moduli

Since hardness is difficult to measure in terms of a fundamental quantity, much research has been carried out correlating other more easily measured and calculated quantities to mechanical hardness, such as the bulk modulus and shear modulus. The bulk modulus of a material is defined as its resistance to volume changes under applied pressure, see Fig. 1.4. Experimentally, the bulk modulus is determined using Eq. 1.7, where V is the initial volume and P is the applied pressure which can be easily extracted from a pressure-volume curve. Although seemingly easy to measure, one should note that by definition the bulk modulus is measured under isotropic compression. However, since predicting the bulk modulus is just as important as measuring the bulk modulus, it can be calculated quite easily with *ab initio* calculations using isotropic compression. This can be done either using an equation of state plot for the calculated equilibrium energy, where one plots the total energy against the volume and fits an equation of state model, for example Birch-Murnaghan [21]. The bulk modulus can also be calculated from Eqs. 1.8 – 1.10 using the calculated elastic stiffness constants C_{ij}

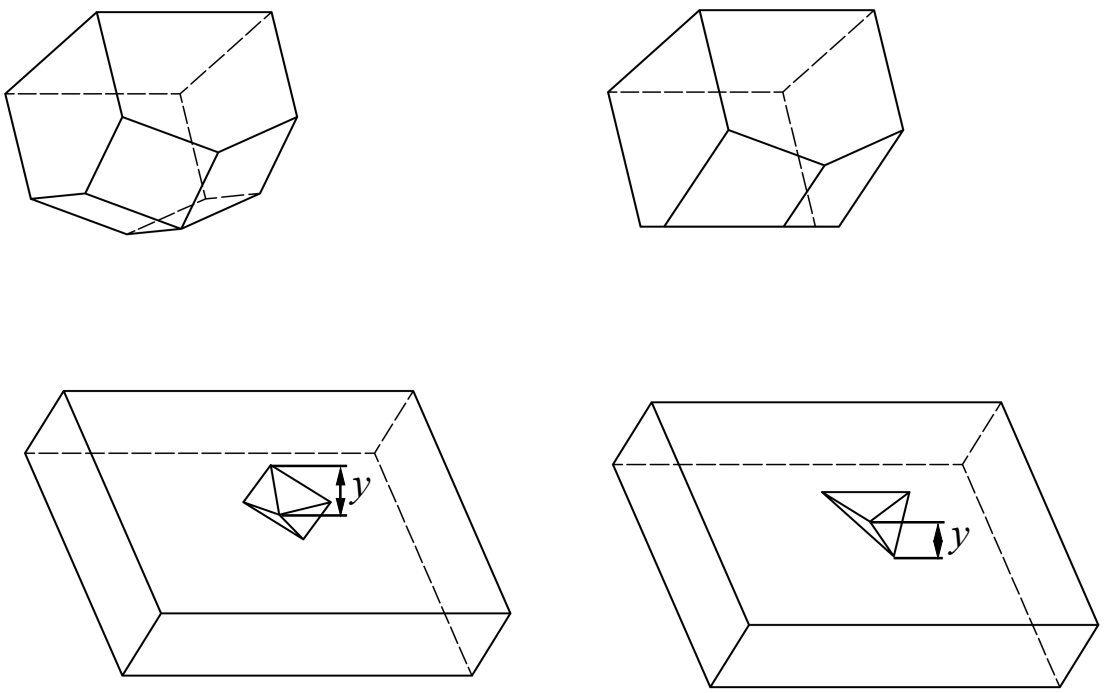

Figure 1.3: Visualization of the two most common microhardness indenter profiles: Vickers indenter (left) and Berkovich (right). The measured quantities correspond to Eqs. 1.5 and 1.6.

and elastic compliance constants S_{ij} that are extracted from *ab intio* calculations. There are two methods to calculate the bulk modulus, proposed by Voigt [22] K_V and by Reuss [23] K_R. With the tendency for K_V to overestimate and K_R to underestimate the bulk modulus, it was found that using Eq. 1.8 and averaging the two values produces a single accurate value of the bulk modulus K [24] that agrees best with measured values. The bulk modulus is in principle simple to calculate and measure, whether it can be related to hardness directly remains a topic of debate [18, 19, 25].

Similar to the bulk modulus, the shear modulus can also be measured and calculated with as much ease. The shear modulus is a measure of how resistant a material is to shear strain. The shear modulus is measured using Eq. 1.11, where F is the applied force to an area A with initial length l and the displacement Δx. Measuring the shear modulus must be done

carefully as one only wants to strain the material. Fig. 1.4 illustrates the distortions caused by shear strain and how the shear modulus is quantified.

$$K = -V\frac{dP}{dV} \tag{1.7}$$

$$K = \frac{1}{2}\left(K_V + K_R\right) \tag{1.8}$$

$$K_V = \frac{1}{9}\left(C_{11} + C_{22} + C_{33}\right) + \frac{2}{9}\left(C_{12} + C_{13} + C_{23}\right) \tag{1.9}$$

$$K_R = \frac{1}{\left(S_{11} + S_{22} + S_{33}\right) + 2\left(S_{12} + S_{13} + S_{23}\right)} \tag{1.10}$$

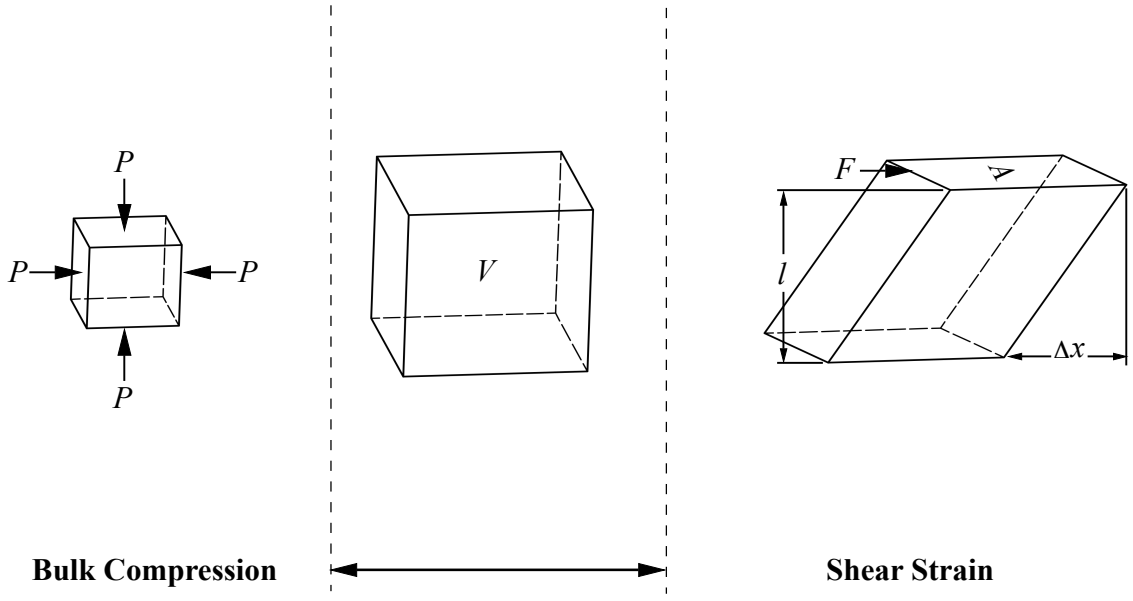

Figure 1.4: The visualization of the bulk compression (left) and shear straing (right) of a cube (centre). The applied pressure P and force F along with volume V, area A, initial length l, and displacement Δx correspond to Eqs. 1.7 and 1.11.

Contrary to the bulk modulus, which is an isotropic quantity, the shear modulus depends on surface where the shear force is applied. Therefore, there is only one method to calculate the shear modulus, that is using elastic stiffness constants C_{ij} and elastic compliance constants S_{ij} that are extracted from *ab intio* calculations. Eqs. 1.12 – 1.14 are similar to those used for the bulk modulus, and again an accurate value is obtained by averaging the values G_V and G_R from the methods of Ref. [22] and Ref. [23] as proposed by Ref. [24] using

Eq. 1.12. The shear modulus is quite similar to the mechanical indentation hardness in that we want to measure a materials resistance to plastic deformations, which would be correlated to shear strain. Therefore, it is well accepted that the shear modulus is a good measure of a material's hardness [18, 19, 25], but there still remains no direct correlation to hardness.

$$G = \frac{Fl}{A\Delta x} \tag{1.11}$$

$$G = \frac{1}{2}\left(G_V + G_R\right) \tag{1.12}$$

$$G_V = \frac{1}{15}\left(C_{11} + C_{22} + C_{33} - C_{12} - C_{13} - C_{23}\right) + \frac{1}{5}\left(C_{44} + C_{55} + C_{66}\right) \tag{1.13}$$

$$G_R = \frac{15}{4\left(S_{11} + S_{22} + S_{33}\right) - 4\left(S_{12} + S_{13} + S_{23}\right) + 3\left(S_{44} + S_{55} + S_{66}\right)} \tag{1.14}$$

The bulk modulus and shear modulus are fundamental material properties that can be calculated using *ab initio* methods. As a result, there has been much effort to relate these quantities to the not so fundamental mechanical hardness. Table 1.1 shows Vickers microhardness, bulk modulus and shear modulus measurements for an array of hard materials. It is clear that for a material to have a large hardness it must have a large bulk modulus and shear modulus, however, having a large bulk and shear modulus does not necessarily mean the material will be hard. Therefore, a material having a large bulk modulus and shear modulus is a necessary but not sufficient condition for a material having a large hardness. These arguments are very apparent if one observes the trend of the bulk and shear moduli in Table 1.1. Particularly, the shear modulus and bulk modulus generally increase as the hardness increases. However, for tungsten carbide (WC) the shear modulus and bulk modulus are comparable to *c*-BN, but its measured hardness is nearly 75% lower. That said, if one compares the bulk modulus to the hardness of similar classes of materials there appears to be an approximately linear correlation [18, 19]. This is not to be confused with the quantity bond modulus proposed by Gilman [16]. Conversely, the correlation between shear modulus and hardness appears to be much more direct exhibiting a nearly linear correlation with hardness for a large array of materials [18]. Although there is a definite correlation between mechanical hardness, shear modulus and bulk modulus, the relationship is not well defined.

Table 1.1: Measured hardness values for an array of materials. The data has been reproduced from Ref. [1] and references therein.

Material	Vickers Microhardness H_v [GPa]	Bulk Modulus K [GPa]	Shear Modulus G [GPa]
c-C	96 ± 5	443	535
c-BN	63 ± 5	400	409
B_4C	40 ± 2	247	171
B_6O	35 ± 5	228	204
TiB_2	33 ± 2	244	263
TiC	30 ± 2	288	198
β-Si_3N_4	30 ± 2	236	122
ZrN	27 ± 2	267	160
SiC	26 ± 2	240	188
TiN	20 ± 2	292	160
Al_2O_3	20 ± 2	250	160
WC	17 ± 2	410	300

1.2.4 Alternatives to Hardness Measurements

The measured mechanical hardness, though incredibly useful for classifying materials, is not a good fundamental material quantity. The more fundamental elastic properties such as shear and bulk modulus are intrinsic, but are not easily related to hardness. In an effort to bring mechanical hardness into the realm of other material attributes, there has been much research put into the calculation of intrinsic hardness. There are many theories that use empirical [16], semi-empirical [14, 17] and strictly *ab initio* [15] methods. The focus of these models/methods is to verify the hardness of well-studied materials and thereby provide a means to predict the hardness of recently discovered and even undiscovered materials. While these methods are seemingly different, they are all correlated to a few fundamental properties, namely the crystal structure and the electronic band gap.

1.3 Intrinsic hardness

Measuring the hardness of materials, previously discussed in Section 1.2, is not without its short-comings. Even though hardness measurements have been carried out for over a century, it is not until recently that a few theories have emerged which are able to predict the hardness of many different materials. While there are many methods to probe various aspects of the hardness of materials – scratch resistance, microhardness, nanohardness – obtaining a singular scalar value that fundamentally quantifies the hardness of a material still remains somewhat elusive. This is especially true when it comes to complicated materials with many different bonding polyhedrons present, or if there is any bond anisotropy present which may be the case in non-tetragonal or non-cubic systems. Since we desire hardness to be a single fundamental quantity that does not necessarily equal the measured hardness, we will henceforth restrict ourselves to calculating the intrinsic hardness as an isotropic quantity that defines the resistance of a material to bond breaking.

1.3.1 Empirical models

The notion of intrinsic hardness as an alternative to hardness measurements first appeared in 1975 [26,27], which was further discussed in 1993 [28]. In this, Gilman an author of several articles discussing mechanical hardness attempts to quantify hardness in covalent crystals. Crystalline silicon is used as an example for which all aspects of the model are tested since it is very well studied and can be synthesized with extremely good quality. Dislocations are used to describe the type of plastic deformations that are typically experienced during hardness measurements. In this regard, it is shown that the activation energy for a dislocation is linearly correlated to the electronic band gap [28]. This is conceptualized in that dislocations behave as kinks meaning the material, although locally distorted, must shear all at one time with many bonds being broken and reformed. The energy required allowing dislocations to proceed is related to the electronic band gap. However, this is restricted to semiconductors and for a dislocation to occur an electron must be promoted to the conduction band during the bond breaking and move back to the valence band during the reformation. Clearly, the energy required for dislocation is not equal to the electronic band gap energy, but is proportional

to the measured electronic band gap, a very fundamental quantity and an excellent foothold from which to study hardness.

Gilman

So far, it should be realized that hardness, although a very attractive material quality to study, is not a fundamental property and difficult to model accurately. Bond dislocations seemingly describe the plastic deformation a material undergoes during an indentation hardness measurement. This activation energy is linearly related to the electronic band gap, which is a very fundamental material property. The hardness of materials is suggestively related to the electronic band gap in the initial 1993 publication [28], but it is was not until many years later that a simple model was introduced that relates the hardness to the structure and the electronic band gap [16]. The measured hardness of materials, as in Eq. 1.15, is proportional to what Gilman coins as the bond modulus B_m. The bond modulus is calculated using Eq. 1.17, where E_g is the electronic band gap and V_m is the molecular volume of the crystal.

$$H \propto B_m \tag{1.15}$$

$$H = AB_m + C \tag{1.16}$$

$$B_m = \frac{E_g}{V_m} \tag{1.17}$$

This linear relationship was shown to be valid for a wide array of materials including group 14 elements and group 13 - 15 binary compounds [16]. However, there are restrictions: the materials must be of the same structural type, specifically isostructural and must also be semiconductors. The two constants A and C in Eq. 1.16 will be specific to a specific material class and need to be ascertained through experimental values. However, this model does have predictive power as we will show later, and if one knows the hardness of at least two materials in a particular material class, then the two unknown constants A and C can be determined easily through linear regression. With the constants known, they can be used to estimate the hardness of materials provided one knows the electronic band gap. While this model was so far used only to verify that semiconducting materials behave according to Eq. 1.15, it may be useful to predict the hardness and maybe possible to apply this relationship to predict

the existence of hypothetical materials.

1.3.2 Semi-*empirical* models

The model proposed by Gilman shows how to relate the electronic band gap to mechanical hardness, but it cannot predict the hardness of materials where the electronic band gap nor the fit constants A and C in Eq. 1.16 are not known. Expanding the theory further to rely on more fundamental parameters – for example structure and electron density – that can be predicted for hypothetical materials may circumvent this problem. There are currently two semi-empirical models proposed recently that rely on knowing the crystal structure and the ionicty [14] or the Pauling electronegativity [17], which are determined using well established approaches [29, 30]. These two models are discussed in detail below.

Gao *et al.*

The first hardness model was proposed by Gao *et al.* [14], which is somewhat an extension of the model proposed by Gilman. The model starts from the idea that the measured hardness of a material will be proportional to the dislocation energy gap and bond density. This bond density N_a in Eq. 1.18 is similar to the contribution from the molecular volume V_m in Eq. 1.17 as both will give a measure of the electron density in the material. From here, the bond density is calculated using Eq. 1.20, where n_i is the number of bonds or bonding coordination and Z_i is the number of valence electrons of atom i, which is then normalized by the unit cell volume V. However, this is further simplified by using the valence electronic density N_e. Next, the bond anisotropy is accounted for by using Eq. 1.21 which determines the effective bond weakening. There may be bonds of different strengths in the system, but these weaker bonds do not directly weaken the system since bonds are not broken individually. The ionicity f_i, which is zero when only one bond is present, can be determined from previous analytical methods using Eq. 1.22, where E_h^* is the homopolar energy gap and E_g^* is hetropolar energy gap. The homopolar energy gap is determined using Eq. 1.22, where d is the bond length. Since the ionicity is known, the total hardness is simplified to Eq. 1.19, where the only required parameters are the ionicity, bond length and valence electron density. The empirical constants 350 and 1.191 are fit to the experimental data where the ionicity is zero

(c-C, c-Si) and very large (Y_2O_3 and Al_2O_3), respectively.

$$H \propto N_a E_g^* \tag{1.18}$$

$$H = 350 \frac{N_e^{2/3} e^{-1.191 f_i}}{d^{5/2}} \tag{1.19}$$

$$N_a = \left(\sum_i \frac{n_i Z_i}{2V} \right) = \left(\frac{N_e}{2} \right)^{\frac{2}{3}} \tag{1.20}$$

$$f_i = 1 - \frac{E_h^*}{E_g^*} \tag{1.21}$$

$$E_h = \frac{39.74}{d^{5/2}} \tag{1.22}$$

Li *et al.*

Another model has been proposed by Li *et al.* [17], which is not all that different from the model proposed by Gao *et al.*. The hardness in this model is calculated from a similar general form, Eq. 1.23, where N_v is the bond density and X_{ab} is the bond electronegativity between atoms a and b. The bond electronegativity is determined using Eq. 1.27, where χ_a and χ_b are the electronegativities, and n_a and n_b are the coordination numbers of atoms a and b. The individual electronegativities are computed using Eq. 1.26, which is a rescaling of the electronegativies according to Pauling [30] taking the electronegativity of carbon to be 2.50 exactly, where Z_j is the number of valence electrons and r_j is atomic covalent radius of atom j. Similar to Gao *et al.*, the difference in bond electronegativities f_g is taken into account using Eq. 1.28. The two constants are determined to be 423.8 and -3.4 for optimal fit to experimental data similar to the model of Gao *et al.*. In Ref. 17 they do not explicitly tabulate the calculated test hardness values, however, they do show that this model is reasonably successful for predicting the hardness for many well known materials.

$$H \propto N_v X_{ab} \tag{1.23}$$

$$H = 423.8 N_v X_{ab} e^{-2.7 f_g} - 3.4 \tag{1.24}$$

$$N_v = \frac{N}{V} \tag{1.25}$$

$$\chi_j = \frac{0.481 Z_j}{r_j} \tag{1.26}$$

$$X_{ab} = \sqrt{\frac{\chi_a}{n_a}\frac{\chi_b}{n_b}} \tag{1.27}$$

$$f_g = \frac{\frac{1}{2}|\chi_a - \chi_b|}{2\sqrt{\chi_a \chi_b}} \tag{1.28}$$

1.3.3 *ab initio* models

So far we have seen both empirical and semi-empirical models that are both very successful in predicting the hardness of materials. However, it is always desirable to eliminate experimental data from a model and eventually calculate the hardness, in this case, from first principles or *ab initio*. While, the model discussed below is *ab initio*, it still arises using similar methodology to the above models, but all values used are determined with *ab initio* calculations requiring only the crystal structure to be known.

Šimůnek *et al.*

A method to calculate hardness from first principles was proposed by Šimůnek *et al.* [15]. The only criteria required for these hardness calculations are that one performs a density functional theory (DFT) calculation using the known, or in some cases, hypothetical crystal structure. The general hardness equation, Eq. 1.29, for this model again looks quite similar to the model of Li *et al.* if one only replaces the bond electronegativity with the bond strength S_{ij} between two atoms i and j. Here, the bond strength is calculated using Eq. 1.33, where e_i and e_j are the average valence electron densities, d_{ij} is the bond length, and n_i and n_j are the coordination numbers of atoms i and j. The average electron density e_i is calculated using Eq. 1.34, where Z_i is the number of valence electrons and R_i is the radius required to enclose Z_i valence electrons. The radius R_i is determined from integrating the electron

charge density that results from DFT calculations. The bond anisotropy is implemented using Eq. 1.32 similar to previous models. The constants in Eq. 1.30, 1550 and 4, are determined similar to the two previously discussed models using established hardness values.

$$H \propto N_v S_{ij} \tag{1.29}$$

$$H = 1550 N_v S_{ij} e^{-4 f_e} \tag{1.30}$$

$$N_v = \frac{N}{V} \tag{1.31}$$

$$f_e = 1 - \left[\frac{2\sqrt{e_i e_j}}{e_i + e_j} \right]^{\frac{1}{2}} \tag{1.32}$$

$$S_{ij} = \frac{\sqrt{e_i e_j}}{d_{ij} n_i n_j} \tag{1.33}$$

$$e_i = \frac{Z_i}{R_i} \tag{1.34}$$

Lastly, if one wants to compute the hardness of a multicomponent system with k inequivalent bonds, Eq. 1.35, is used to calculate the geometric average of all bonds present. This arises from the fact that again, single bonds cannot be easily broken and many bonds will be broken simultaneously meaning the overall hardness is not determined by the weakest bond. Calculating the hardness of a multi-component system, although seemingly simple is quite complicated. In all of the hardness models the bond density is used, but there appears to be a key oversimplification. In the models discussed above, the bond density is determined by dividing the unit cell volume by the number of bonding atoms present. This is correct provided there is only bonding coordination present, which is the case for many of the binary materials presented in Ref. [14, 15, 17]. However, the equations for calculating the hardness should be rewritten to include not general bond density, but specific bond density with V_i being the volume of the bonding polyhedron. This would greatly affect the results for multi-component systems; however, ascertaining the effective bonding volume of the polyhedrons can be very difficult.

$$H = \left[\prod^{k} \left(H^k \right)^{n^k} \right]^{\frac{1}{\sum n^k}} \tag{1.35}$$

1.3.4 Intrinsic Hardness Results

The success of the three hardness models discussed above seems to vary with the materials studied. All models measure their success on very well studied materials and Table 1.2 shows both measured and calculated hardness values for an array of well known materials. Although the similarities between the models were thoroughly pointed to, there was major distinction proposed by Šimůnek *et al.* in that they restrict their hardness calculations to materials with a tetrahedral coordination or higher. If a material has less than tetrahedral coordination the bonds will be able to twist resulting in deformation that is not a result of bond breaking. This bond distortion is apparent when one examines the calculated hardness of quartz (α-SiO_2) in which the hardness calculated by Gao *et al.* is much too large. Therefore intrinsic hardness calculations should be restricted to materials with tetrahedral coordination or higher.

The motivation behind hardness calculations, mentioned in section 1.1, started with the discovery of spinel structured nitrides and was further fuelled by the theoretical suggestion that γ-C_3N_4 may have a hardness comparable to diamond. Table 1.3 shows the calculated hardness for all three considered spinel nitrides using all three models. One can see that all three models were developed to successfully predict the hardness of diamond and silicon, which are arguably the two most studied materials in existence, but there is a significant discrepancy between the values for all three studied spinel nitrides. This is likely due to the difficulty in determining the effective bonding volume of the polyhedrons arising from geometric averaging of multi-component systems. That aside, after examining all available hardness models, there a few common factors between all of the models. These commonalities include the crystal structure, electronic structure and the electronic band gap. The two most fundamental properties of materials, the electronic band gap and the crystal structure, will be the focus of the proceeding chapters.

Table 1.2: The calculated hardness values that resulted from the models of Gao *et al.* and Šimůnek *et al.* are compared to measured Vickers microhardness measurements for an array of materials. The experimental data have been reproduced from Refs. 1, 16 and references therein.

Material	Vickers Microhardness	Calculated Hardness	
		Gao *et al.*	Šimůnek *et al.*
	H_v [GPa]	H [GPa]	H [GPa]
c-C	96 ± 5	93.6	95.4
c-BN	63 ± 5	64.5	63.2
t-SiO_2	33 ± 2	30.4	—
BP	33 ± 2	31.2	26.0
TiC	30 ± 2	—	18.8
β-Si_3N_4	30 ± 2	30.3	—
VC	29 ± 2	—	27.2
SiC	26 ± 2	30.3	31.1
TiN	20 ± 2	—	18.7
Al_2O_3	20 ± 2	20.6	—
WC	17 ± 2	26.4	18.3
α-SiO_2	10 ± 1	30.6	—
c-Si	12 ± 2	13.6	11.3

Table 1.3: The calculated hardness values for the three most widely studied spinel structured nitrides that resulted from the intrinsic hardness models of Li *et al.*, Gao *et al.* and Šimůnek *et al.*.

Material	Li *et al.*	Gao *et al.*	Šimůnek *et al.*
	[GPa]	[GPa]	[GPa]
γ-C_3N_4	71.1	56.7	61.7
γ-Si_3N_4	29.1	30.9	27.4
γ-Ge_3N_4	22.2	24.3	19.1

Chapter 2

Electronic Structure

2.1 Electronic Band Gap

The electronic band gap is arguably one of the most important material parameters pertaining to the study of semiconductors. This energy gap is defined as the minimum separation between the unoccupied states or conduction band (CB) minimum and the occupied states or valence band (VB) maximum. However, in the case of molecules this is often referred to as the LUMO-HOMO gap, which is the separation between the lowest unoccupied molecular orbital (LUMO) and the highest occupied molecular orbital (HOMO). This energy gap should not be mistaken for the optical gap or electric gap, which are the minimum photon energy and electrical energy, respectively, to promote an electron from the VB to the CB. The electronic band gap herein, the intrinsic electronic band gap is defined as the energy separation between the VB maximum and CB minimum with the material in the ground state meaning the VB is completely filled and CB is completely unfilled. The optical and electric band gap may vary from the intrinsic electronic band gap since there will be some exciton interaction, which could possibly reduce the measured band gap.

The importance of knowing the electronic band gap cannot be overstated, however, there is more to the electronic band gap than a single scalar value. In periodic materials, such as crystals, the electrons exist as bands that are delocalized over the crystal momentum (in reciprocal lattice space). Fig. 2.1 shows an example of a band structure plot for a simple periodic solid, where there is a single valence band and two conduction bands. There are two band gap transitions possible, both requiring the same energy. The two transitions, direct and indirect, require no momentum transfer and some momentum transfer, respectively. This momentum input is usually provided by random crystal phonons making the indirect band

gap transition much less probable than the direct band gap transition. Direct electronic band gaps, for this reason, are strongly desired for optical applications.

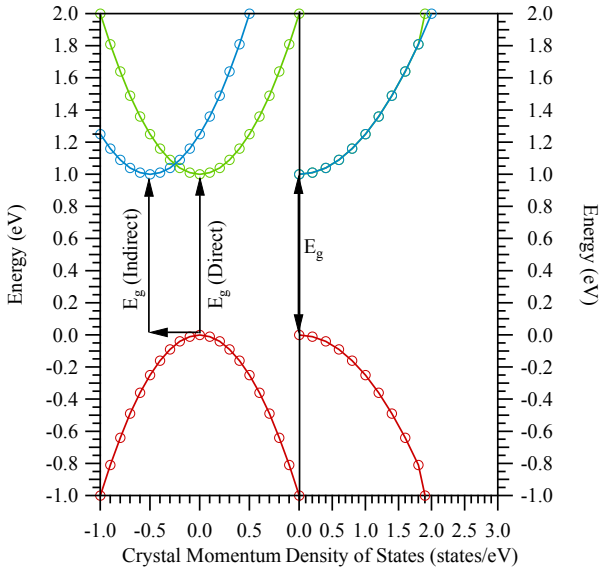

Figure 2.1: A diagram that shows the distinction between a direct and an indirect band transition (left). Further, the integrated density of states (right) shows an alternative to measuring the electronic band gap. The occupied states are red, while the unoccupied states are blue and green.

2.1.1 Conventional Measurements

There are many ways to measure the optical band gap, the most widely used being UV-Visible spectroscopy (UV-Vis). UV-Vis spectroscopy can be measured in both reflectance and transmission providing a method to directly promote electrons from the VB to the CB and monitor the rate that at which these transitions occur. Fig. 2.2 shows an example of a UV-Vis spectrum for manganese carbodiimide [31]. These measurements proceed using a source that typically produces light with a wavelength of 200 – 1000 nm, incident on a material. The photon is absorbed by a valence electron, which is then promoted to an unoccupied state in the CB. This process will reduce the intensity of the photons being reflected or transmitted. In both these cases, the material must be homogeneous and thin or very smooth, which makes their transmission or reflectance efficiency large and uniform

in intensity. This means that films or single crystals are ideal for this type of measurement because either the surface can be very smooth providing an ideal reflection measurement or can be deposited on quartz (α-SiO_2) whose band gap is very large allowing for transmission measurements. However, due to the polycrystalline nature and small quantity of novel ultra-hard materials, this technique is not usually feasible for electronic band gap measurements and an alternative method needs to be developed for these types of materials.

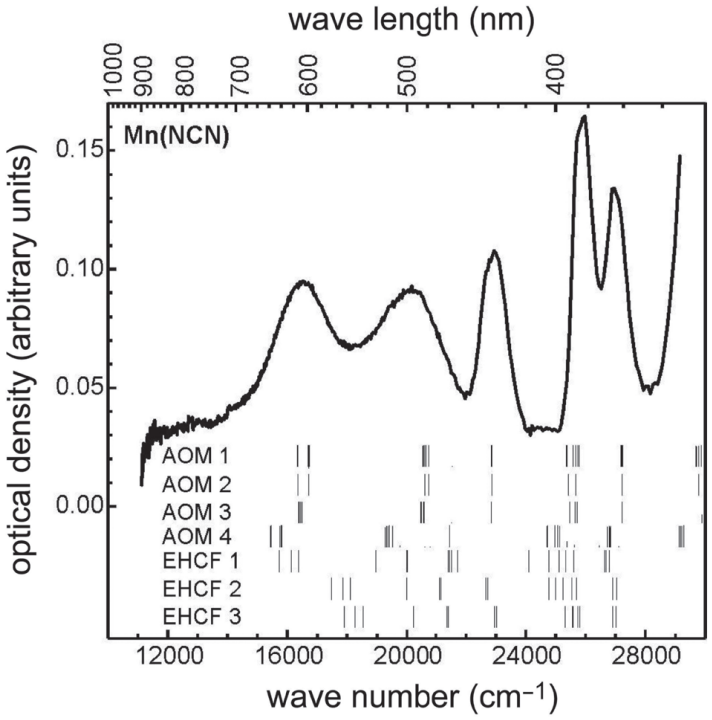

Figure 2.2: An example of a UV-Vis absorption spectrum that is commonly used to determine the optical band gap. Here, the material measured is manganese carbodiimide [31] and contains $d - d$ transitions with the band gap transition.

2.1.2 Indirect Measurements

The electronic band gap measurements using UV-Vis spectroscopy discussed above, while restricted to certain material forms, are not without other short-comings. Direct electronic band gap transitions in an ideal picture probe the electronic band gap very well, but these transitions are not the only ones possible. Other transitions can include VB to inter-band

states and multiplet transitions such as $d - d$ or $f - f$ transitions when defects or impurities and transition metal or rare-earth elements are present, respectively. Fig. 2.2 shows an example where the $d - d$ transtions that are present make determining a value for the optical band gap ambiguous. Furthermore, direct band gap measurements are functional measurements and do not necessarily probe the intrinsic electronic band gap. The value of the intrinsic electronic band gap is a fundamental material property that is desired for hardness research. Instead, the electronic band gap should be measured indirectly, probing the VB and CB separately and taking the energy separation as the electronic band gap. This is illustrated in Fig. 2.1, where the band structure is integrated along momentum space and the occupied and unoccupied density of states (DOS) are plotted on the same energy scale, which is then used to determine the electronic band gap. This has the distinct advantage that it eliminates any type of exciton interaction and inter-band transitions that are associated with optical band gap transitions. The most effective method to probe the VB and CB separately is through X-ray induced core-level spectroscopy.

2.2 Core-level Spectroscopy Measurements

Core-level spectroscopy arises from using high energy X-rays (> 50 eV) to promote bound core electrons into the CB or continuum. The techniques used here are X-ray absorption spectroscopy (XAS) and X-ray emission spectroscopy (XES), which directly probe the CB and VB, respectively. In an XAS measurement, a core electron is promoted to a CB state and the system then relaxes to its ground state emitting photons or electrons, which are then integrated and plotted with respect to excitation energy. During an XES measurement, a core electron is excited into the continuum and then the system also allowed to relax, still photons and electrons are emitted, but only the photons are counted, which are then plotted with respect to emission energy. The discussion below and derivation of the attenuation coefficient is a brief account following Ref. 32. These transitions follow from Fermi's Golden Rule, Eq. 2.1, for a transition from an initial state ψ_i to a final state ψ_f via the harmonic time-dependent perturbation $V(t)$ ($\underline{\mathrm{V}}$ is the time independent transition matrix) with photon energy of $h\nu_{in}$ required for the transition. Eq. 2.2 defines the time-dependent Hamiltonian

and Eq. 2.3 the harmonic time-dependent perturbation.

The absorption cross-section for a core electron excitation follows from Fermi's Golden Rule in Eq. 2.1. The total absorption cross-section, σ is summed over all possible initial and final states and calculated using Eq. 2.4, provided the photon energy is sufficient to promote a core electron from an initial state $|\psi_i\rangle$ to an unoccupied final state $|\psi_f\rangle$. From here, the vector potential for a plane wave in Eq. 2.5 is used to simplify the perturbation operator from Eq. 2.6, where $\vec{p}$ is the linear momentum operator and $\vec{e}$ is the unit vector. Further simplifications can be made if we restrict ourselves to soft X-rays (< 2 keV) in that the plane wave expansion can be truncated after the first term which results in the final form of the absorption cross-section in Eq. 2.4.

$$P_{ij} \propto |\langle\psi_f|\underline{\mathrm{V}}|\psi_i\rangle|^2 \tag{2.1}$$

$$H(t) = H_0 + V(t) \tag{2.2}$$

$$V(t) = \underline{\mathrm{V}}e^{-i\omega t} \tag{2.3}$$

$$\sigma(h\nu) \propto \sum_{i,f} |\langle\psi_f|\underline{\mathrm{V}}|\psi_i\rangle|^2 \delta(E_i - E_f - h\nu) \tag{2.4}$$

$$\vec{A} \propto \vec{e}\left(e^{i(\vec{k}\cdot\vec{x}-\omega t)} - e^{-i(\vec{k}\cdot\vec{x}-\omega t)}\right) \tag{2.5}$$

$$V(t) \propto \vec{A}\cdot\vec{p} \tag{2.6}$$

$$\vec{k}\cdot\vec{x} \ll 1 \Longrightarrow e^{i\vec{k}\cdot\vec{x}} \approx 1 \tag{2.7}$$

$$\sigma(h\nu_{in}) \propto \sum_{i,f} |\langle\psi_f|\vec{e}\cdot\vec{p}|\psi_i\rangle|^2 \delta(E_i - E_f - h\nu_{in}) \tag{2.8}$$

This approximation comes from the fact that momentum for soft X-rays is very small, meaning that for excitations of core electrons in this energy range will be limited to dipole transitions where there angular quantum number l is restricted to $\Delta l \pm 1$. While the restriction in the allowed transitions is $\Delta l \pm 1$, core-level spectroscopy directly probes the VB and CB provided that transition probability is smooth the absorption cross-section and the radial core electron state is effectively a delta function in energy. If the core electron is delocalized in energy, the transition will be severely broadened in energy. Moreover, the DOS probed with core-level spectroscopy is commonly referred to as the local partial DOS (LPDOS) because of the restriction that spatially localized core wave functions must overlap with the VB and

CB wave functions as well as the angular momentum restriction limiting the measurements to probing the DOS around the excited atom through dipole transitions.

The occupied and unoccupied states of any material can be measured through the absorption of X-rays via core electron excitations, which means the band gap is implicitly determined by placing both the XES and XAS spectra on the same energy scale. The energy separation between the two spectra is in principle the electronic band gap. However, in order to accurately use this method one needs to calibrate the two energy axes (emission and excitation) and correct for core hole shifting, spin-orbit splitting and nonequivalent site splitting. Additionally, these spectra are subject to lifetime broadening making the determination of the CB and VB difficult, but when done correctly, core-level spectroscopy techniques are useful tools to determine the intrinsic electronic band gap.

2.2.1 X-ray Absorption Spectroscopy

Measuring XAS spectra, although based on the derivation above, is not as simple to measure as one would expect and measuring a spectral intensity that is proportional to $\sigma(h\nu_{in})$ is not without difficulty. XAS measurements, in the general sense pertain to measuring the absorption coefficient $\mu(E_{in})$ of a material depending on the incident X-ray energy E_{in}. An XAS spectrum is generally distinguished into two regions. The near-edge region, which is restricted to the first 50 eV of the XAS spectrum, henceforth will be referred to the X-ray absorption near edge structure (XANES). The portion of the XAS spectrum larger in energy than 50 eV is referred to the extended X-ray absorption fine structure (EXAFS), which will not be discussed any further. In order to probe the CB, one needs to measure the absorption cross-section; XAS probes the absorption coefficient, which is conveniently proportional to the absorption cross-section for a homogeneous material.

The XANES, as mentioned above, when restricted to soft X-rays can be measured by detecting either photons using total fluorescence yield (TFY) or electrons using total electron yield (TEY). The TEY is typically measured by electrically isolating the material that is being measured and attaching an ammeter to measure the electrons that have been ejected during the X-ray excitation. This method, although extremely simple to do, is sensitive to the charge characteristic of the material. This can be extremely detrimental when studying

semiconductors because the large band gap inhibits the movement of charge causing the material to develop an overall positive charge. This phenomena is known as charging and manifests in the XANES spectrum by reducing the overall intensity as the scan proceeds. TFY measurements are typically measured using a non-energy dispersive detector such as a channel electron multiplier (CEM) or several CEMs in the form of a micro channel plate. These devices measure X-rays in the following manner: An X-ray incident on the detector plate causes secondary emission of electrons initiating a cascade process that is facilitated by a very large bias voltage on a photomultiplier tube. It is important to note that an electron with sufficient energy is also capable of initiating the avalanche process, but usually a negatively biased mesh is placed in front of the CEM to repel electrons. The partial fluorescence yield (PFY) is discussed in detail below and is also measured with an X-ray detector, but the detector is required to have energy-resolving capability. This measurement is not widely carried out because of the low efficiency of these detectors in the soft X-ray range, but recently silicon drift detectors (SDDs) have been implemented resulting in significant improvements of the measurement technique discussed below. Many of the details regarding these devices are omitted because they have little impact on the scientific results.

The equations that describe both TEY and TFY measurement techniques, Eqs. 2.9 and 2.10, are simplified from the rigorous form for an infinitely thick material and incident photon angles larger than 10° from the surface plane. This is appropriate for any soft X-ray experiment since the penetration is at most several microns. The TEY spectra are summed over all core electron absorption edges g, similar to TFY which also needs be to summed over all possible fluorescence lines that occur.

$$I_g^{TEY}(E_{in}) \propto \sum_g \frac{\eta_g \mu_g(E_{in})}{\mu(E_{in}) + \frac{1}{L_g}} \tag{2.9}$$

$$I_g^{TFY}(E_{in}) \propto \sum_g \frac{\varrho_g \mu_g(E_{in})}{\mu(E_{in}) + \frac{1}{D_g}} \tag{2.10}$$

The goal of any XAS measurements is to obtain a spectrum of intensity $I_g(E_{in})$ that is proportional the absorption coefficient $\mu_g(E_{in})$, where E_{in} is the incident photon energy. First, we consider TEY in Eq. 2.9, where η is the electron yield (the efficiency at which

photoelectrons or auger electrons are generated) and L is the escape depth of the photoelectrons and auger electrons. It is apparent that the TEY will be directly proportional to the absorption coefficient since the total X-ray attenuation length will be 100 nm to 2 μm and the electron escape depth will be less than 10 nm, which makes the denominator in Eq. 2.9 approximately constant. Even though the small escape depth of the electrons is a definite advantage for TEY measurements, it is also the main short-coming of this technique. Since the electrons will mostly originate from the surface, this means the absorption coefficient measured will only be representative of the surface. TEY spectral measurements, although extremely easy to carry out and being directly proportional to the absorption coefficient, are subject to charging and very sensitive to the surface of the material.

The short-comings and advantages associated with TEY measurements are completely absent in TFY measurements making these techniques in some ways opposite, but related XANES techniques. The TFY spectra are measured by integrating all of the emitted photons and plotted with respect to the excitation energy. The TFY, in Eq. 2.10, is quantified similar to TEY, where ϱ is the fluorescence yield and D_g is the escape depth of the fluorescence photons. As stated earlier, the goal of such measurements is to probe the absorption coefficient, but in order for this to occur, the other non-resonant fluorescence lines present that are not a result of the core electron excitation of interest should be very small in comparison to what is called the resonant fluorescence line. This simplifies Eq. 2.10 to Eq. 2.11, where G is the assumed constant background fluorescence from the non-resonant excitations.

$$I_g^{TFY}(E_{in}) \propto \frac{\varrho_g \mu_g(E_{in})}{\mu(E_{in}) + \frac{1}{D_g}} + G \tag{2.11}$$

The escape depth D_g of a fluorescence photon of edge g with emission energy E_g^F is defined by Eq. 2.12 and plays a major role in whether the measured spectrum is directly proportional to the absorption coefficient. Strictly speaking a TFY spectrum is not directly proportional to the absorption coefficient and high intensity absorption features are strongly reduced in intensity or saturated. The escape depth is dependent on the geometry of the measurement, where α and β are the angles between the incident photon and fluorescence photon with the material surface, respectively. In order to minimize saturation one should set $\alpha = 90°$ and minimize β as much as possible. This is the only improvement that can be made through

the experimental procedure to reduce saturation.

$$D_g = \frac{1}{\mu(E_g^F)} \frac{sin\beta}{sin\alpha} \tag{2.12}$$

The composition of the material being studied can be a larger contributing factor with regard to saturation. The absorption coefficient can be decomposed into a sum of all absorption edges as in Eq. 2.13. For practical purposes, the excitation energy must exceed the binding energy of edge g, meaning the sum can be truncated for all absorption edges with higher energy. Additionally, the background attention coefficient μ_0 is a combination of contributions from the VB and substrate with no energy dependence. As a result, the measured TFY spectrum does not have very good linear correlation to the attenuation coefficient of materials where the element being probed is very concentrated. Contrarily, when the element being probed is very dilute, the measured TFY spectrum is a very good probe of the attenuation coefficient. This arises from Eq. 2.13, where in the concentrated case $\mu(E_{in}) \approx \mu_g(E_{in})$ and in the dilute case $\mu(E_{in}) \approx \mu_0 + \sum_{j \neq l} \mu_j(E) \approx$ constant. This does not strictly pertain to dilute materials, but also effectively dilute materials such as thin films. For a thin film, where the thickness is less than 50 nm, the fluorescence photon escape depth will be fixed at the film thickness. This is similar to TEY measurements that are free of saturation due to the small escape depth of the electrons. This argument assumes that $1/D_g \approx$ constant for all fluorescence lines. The same is also true for TEY measurements, but since $1/L_g \gg \mu(E_{in})$ in virtually every case, it can be discounted.

$$\mu(E_{in}) = \mu_0 + \sum_{j \leq g} \mu_j(E_{in}) \tag{2.13}$$

Lastly, so far we have only been concerned with TFY and TEY XANES measurements, but TFY measurements are a sum of individual fluorescence lines. These fluorescence lines, when measured separately, are used to measure the PFY as in Eq. 2.14. Normally, PFY measurements are taken with the detector only integrating photons with the emission energy of the resonant core electron excitation. One should note here that any core electron with binding energy less than the excitation energy E_{in} will be excited and produce a fluorescence line, but since these transitions are not into unoccupied states they do not follow from

Eq. 2.1 and thus their intensities do not depend on the attenuation coefficient. Using PFY to measure an XANES spectrum has the distinct advantage in that it will more directly probe the attenuation coefficient because the other fluorescence lines do not need to be assumed constant since they are now discounted.

A recent development in XANES measurement techniques occurred with the discovery of inverse partial fluorescence yield (IPFY) [33], which is bulk sensitive and free of saturation embodying the advantages of the TEY, TFY and PFY with none of the short-comings. This technique exploits the short-coming of TFY measurements by taking advantage of varying non-resonant fluorescence lines. Going back to the TFY equation (Eq. 2.10) and considering a non-resonant fluorescence line j one observes that the spectrum measured will be Eq. 2.15. The fluorescence yield ϱ_j, attenuation coefficient μ_j and escape depth D_j are all constant over the energy range of the resonant absorption edge. These evaluations simplify Eq. 2.15 to Eq. 2.16, where C is a constant. However, in order to measure a spectrum that is proportional to the attenuation coefficient, Eq. 2.16 is inverted resulting in the IPFY equation, Eq. 2.17. This result revolutionizes the way absorption spectra are taken, in that there is now a method to measure the bulk sensitive fluorescence yield that probes the attenuation coefficient without saturation. Of course, this is not always possible since this requires the material to have a lower energy fluorescence line of sufficient intensity and for the fluorescence line to result from an element that is part of the homogeneous material.

$$I_g^{PFY}(E_{in}) \propto \frac{\varrho_g \mu_g(E_{in})}{\mu(E_{in}) + \frac{1}{D_g}} \tag{2.14}$$

$$I_{j\neq g}^{PFY}(E_{in}) \propto \frac{\varrho_j \mu_j(E_{in})}{\mu(E_{in}) + \frac{1}{D_j}} \tag{2.15}$$

$$I_{j\neq g}^{PFY}(E_{in}) \propto \frac{1}{\mu(E_{in}) + C} \tag{2.16}$$

$$I_{j\neq g}^{IPFY}(E_{in}) \propto \mu(E_{in}) + C \tag{2.17}$$

2.2.2 X-ray Emission Spectroscopy

So far, only the probability of the absorption of X-rays, which are used to probe the CB have been discussed. If one now uses a high-resolution energy dispersive detector to measure

fluorescence lines, the VB can be probed very effectively. The probability of a photon transition from the VB to refill the core level follows similarly from Fermi's Golden Rule. The distribution of emitted photons $h\nu_{out}$ is determined using Eq. 2.18, where $\vec{p}$ is the linear momentum operator, $\vec{e}$ is the unit vector, and ψ_i and ψ_f are initial and final states with energy E_i and E_f, respectively. Since in the case of XES, we are less concerned with efficiency of the excitation and more concerned with the relative distribution of emitted photons, it directly probes the VB restricted to dipole transitions. The measurements and calculations of the studies presented here are confined to single electron transitions and the emission that results from resonant excitations causing emission through intermediate states is not discussed.

$$\sigma(h\nu_{out}) \propto \sum_{i,f} |\langle\psi_f|\vec{e}\cdot\vec{p}|\psi_i\rangle|^2 \delta(E_i - E_f - h\nu_{out}) \tag{2.18}$$

2.3 Electronic Structure Calculations

Core-level spectroscopy is a very effective technique for probing the occupied and unoccupied LPDOS. More insight into the electronic structure measurements discussed above can be obtained if one can simulate the measured spectra. The primary method here for simulating the measured LPDOS is density functional theory (DFT), which is a very reliable *ab initio* calculation method to simulate XES and XANES. The following sections regarding DFT calculations follow from the content in Ref. 34.

The exact Hamiltonian for a collection of charged particles, including N nuclei and Z electrons per nucleus in a many body problem is defined by Eq. 2.19, where M_i is the mass of a nucleus at position $\vec{R}_i$ and m_e is the mass of an electron at position $\vec{r}_i$. The terms in Eq. 2.19 are broken down into several parts. The first and second terms are the kinetic energy for the nuclei and electrons, respectively. The last three terms describe the Coulomb interaction between the nuclei and electrons, electrons and electrons, and nuclei and nuclei, in proceeding order. This Hamiltonian, although exact, is very difficult to solve and there are a few approximations that are required to make solving this many body problem feasible.

$$\begin{aligned}\hat{H} = &- \frac{\hbar^2}{2}\sum_i \frac{\nabla^2_{\vec{R}_i}}{M_i} - \frac{\hbar^2}{2}\sum_i \frac{\nabla^2_{\vec{r}_i}}{m_e} - \frac{1}{4\pi\epsilon_0}\sum_{i,j}\frac{e^2 Z_i}{|\vec{R}_i - \vec{r}_j|} \\ &+ \frac{1}{8\pi\epsilon_0}\sum_{i\neq j}\frac{e^2}{|\vec{r}_i - \vec{r}_j|} + \frac{1}{8\pi\epsilon_0}\sum_{i\neq j}\frac{e^2 Z_i Z_j}{|\vec{R}_i - \vec{R}_j|}\end{aligned} \tag{2.19}$$

The are three approximations that are required in order to make solving the above Hamiltonian feasible. The first is the Born-Oppenheimer approximation, which assumes the massive nuclei are frozen in position reducing the Hamiltonian to three terms. The frozen nuclei force the kinetic energy and Coulomb interaction terms for the nuclei to be zero reducing the Hamiltonian to Eq. 2.20, where $\hat{T}$, $\hat{V}$ and $\hat{V}_{ext}$ are the kinetic energy, electron-electron potential energy, and the external potential energy of the system, respectively. This hugely simplifies the problem because the terms $\hat{T}$ and $\hat{V}$ are independent of the system and only $\hat{V}_{ext}$ needs to be determined.

$$\hat{H} = \hat{T} + \hat{V} + \hat{V}_{ext} \tag{2.20}$$

The second approximation that needs to be made is that of Hohenberg and Kohn [35], which makes this seemingly difficult problem very solvable. Firstly, this theory supposes that there is one-to-one correspondence between the ground state electron density $\rho(\vec{r})$ and any observable as in Eq. 2.21. Secondly, if the observable is the energy eigenvalues H, then the resultant total energy will just be the energy of the external potential E_{ext} as in Eq. 2.22, where ψ is the ground state wave function. This is the cornerstone of DFT, in that a given electron density uniquely defines any system.

$$H(\rho) = \langle\psi|\hat{H}|\psi\rangle \tag{2.21}$$

$$E_{ext} = \langle\psi|\hat{T} + \hat{V}|\psi\rangle + \langle\psi|\hat{V}_{ext}|\psi\rangle \tag{2.22}$$

This approximation is further extended to produce what are called the Kohn-Sham equations [36]. These equations are a practical way to solve the DFT problem for a large array of external potentials. Eq. 2.23 is the Kohn-Sham Hamiltonian $\hat{H}_{KS}$ for a many body problem, where operators are $\hat{T}_0$ for the kinetic energy of a non-interacting electron gas, $\hat{V}_H$ for the

Hartree potential energy, $\hat{V}_{xc}$ for the exchange correlation potential energy , and $\hat{V}_{ext}$ for the external potential energy. Eq. 2.24 shows a more explicit form of Eq. 2.23, where the $\hat{V}_{xc}$ is defined by Eq. 2.25. From here, the Kohn-Sham equations are finalized in their most compact form and Eqs. 2.26 and 2.27 are used to iteratively solve the ground state electron density, where $\phi_i(\vec{r})$ is the single particle wave functions and ε_i is the energy of the wave functions. The series of Eq. 2.26 is truncated to contain N lowest energy solutions. While it seems all is solved, we should point out that since $\hat{V}_H$ and $\hat{V}_{xc}$ both depend on $\rho(\vec{r})$, the problem needs to be solve self-consistently and the exact form of $\hat{V}_{xc}$ is still not known.

$$\hat{H}_{KS} = \hat{T}_0 + \hat{V}_H + \hat{V}_{xc} + \hat{V}_{ext} \tag{2.23}$$

$$\hat{H}_{KS} = -\frac{\hbar^2}{2m_e}\vec{\nabla}_i^2 + \frac{e^2}{4\pi\epsilon_0}\int \frac{\rho(\vec{r}')}{|\vec{r} - \vec{r}'|}d\vec{r}' + \hat{V}_{xc} + \hat{V}_{ext} \tag{2.24}$$

$$\hat{V}_{xc} = \frac{\partial V_{xc}[\rho]}{\partial \rho} \tag{2.25}$$

$$\rho(\vec{r}) = \sum_{i=1}^{N} \phi_i(\vec{r})^* \phi_i(\vec{r}) \tag{2.26}$$

$$\hat{H}_{KS}\phi_i = \varepsilon_i \phi_i \tag{2.27}$$

2.3.1 Exchange-correlation Functionals

There is a large array of available exchange-correlation functionals (ECFs) including the local density approximation (LDA) and generalized gradient approximation (GGA). The only true *ab initio* ECF is LDA, and there are many forms of the GGA functional available with different levels of approximation. The LDA functional arises from dividing the entire charge volume into infinitesimal volumes of charge with constant energy; the total exchange energy is defined by Eq. 2.28, where ε_{xc} is the energy of each volume of charge and $\rho = \rho_\downarrow + \rho_\uparrow$ is the charge decomposed by their spin. This ECF performs very well for a system where the charge density is slowly changing. However, if this is not the case then a more effective ECF, GGA is used for these systems. The most widely used GGA functional is that of Perdew-Burke-Ernzerhof or GGA-PBE [37]. Eq. 2.29 shows the general form of a GGA functional,

where f is some function that evaluates the energy and now takes into account the gradient of the charge density, contrary to LDA which assumes it is constant over the infinitesimal volume. There are short-comings of both approximations and making the choice of the appropriate functional depends on the system being studied. However, there is one common short-coming that resides in both functionals; they both severely underestimate the band gap. This band gap underestimation arises from the constant exchange that is applied to all electron orbitals leading to an underestimation of the electron-electron interaction. There has been some success in modifying these functionals to more accurately reproduce the electronic band gap [38] using a modified from of the Becke-Johnson potential in conjunction with the LDA ECF. While this ECF is successful in reproducing many known electronic band gaps, it still underestimates those with partially filled d or f shells.

$$E_{xc}^{LDA}[\rho_{\downarrow}(\vec{r}),\rho_{\uparrow}(\vec{r})] = \int \rho(\vec{r})\varepsilon(\rho_{\downarrow}(\vec{r}),\rho_{\uparrow}(\vec{r}))d\vec{r} \tag{2.28}$$

$$E_{xc}^{GGA}[\rho_{\downarrow}(\vec{r}),\rho_{\uparrow}(\vec{r})] = \int \rho(\vec{r})f(\rho_{\downarrow}(\vec{r}),\rho_{\uparrow}(\vec{r}),\bigtriangledown\rho_{\downarrow}(\vec{r}),\bigtriangledown\rho_{\uparrow}(\vec{r}))d\vec{r} \tag{2.29}$$

2.3.2 WIEN2k

The last approximation that needs to be applied to the many-body electron problem is to map the electron wave functions to a specific basis. There are many different bases to choose from including pseudopotentials, augmented plane waves and linearized augmented plane waves (LAPW). Here, all the DFT calculations presented use the commercially available WIEN2k software [39], which uses LAPW as the main electron basis. The wave functions in Eq. 2.27 still needs to be solved in some basis as in Eq. 2.30, where c_m^i are coefficients for the basis functions ϕ_m^b.

$$\phi_i = \sum_{m=1}^{M} c_m^i \phi_m^b \tag{2.30}$$

The electron wave functions are modelled within WIEN2k in two distinct regions as depicted in Eq. 2.31. The interstitial region I, containing valence electrons, is modelled with plane waves of momentum $\vec{p} = \vec{K} + \vec{k}$. Inside the so-called muffin tin potential S

or sphere in this case, that contain the core electrons, the wave functions are modelled by spherical harmonics with the coefficients A and B for the radial part u chosen such that at the boundary both the value and derivative of the spherical wave functions match the plane waves. However, there is also an additional electron wave function that is not encompassed by the core electrons or valence electrons, namely local orbitals LO. These localized electron orbitals are not easily contained in a sphere of reasonable size and are too localized to be modelled with plane waves. The LOs are modelled using Eq. 2.32, where coefficients A, B and C no longer depend on the plane wave momentum since they do not need to be continuous at the boundary.

$$\phi_{\vec{K}}^{\vec{k}}(\vec{r}) = \begin{cases} \frac{1}{\sqrt{V}} e^{i(\vec{k}+\vec{K})\cdot\vec{r}} & \vec{r} \in I \\ \sum_{l,m} \left(A_{lm}^{\alpha,\vec{k}+\vec{K}} u_l^\alpha + B_{lm}^{\alpha,\vec{k}+\vec{K}} \dot{u}_l^\alpha \right) Y_l^m(\hat{r}') & \vec{r} \in S_\alpha \end{cases} \tag{2.31}$$

$$\phi_{\alpha,LO}^{lm}(\vec{r}) = \begin{cases} 0 & \vec{r} \notin S_\alpha \\ \left(A_{lm}^{\alpha,LO} u_l^\alpha + B_{lm}^{\alpha,LO} \dot{u}_l^\alpha + C_{lm}^{\alpha,LO} u_l^\alpha \right) Y_l^m(\hat{r}') & \vec{r} \in S_\alpha \end{cases} \tag{2.32}$$

Now with an appropriate basis and a method to solve the Hamiltonian of a many body electron system, the electron wave functions are constructed quite easily. In most cases, DFT is labelled *ab initio* as it only requires the crystal structure as the input and can produce the correct ground state electron density with no user bias. However, as discussed above, the choice of the ECF can drastically change the charge density. While these ECFs drastically underestimate the electronic band gap, the DOS that is extracted and the XES or XANES that is calculated using Eqs. 2.8 and 2.18 reproduces experimental measurements quite well.

2.4 Core-level Spectroscopy Electronic Band Gap Measurements

The electronic band gap, although seemingly simple to measure with core-level spectroscopy, has a few effects that need to be taken into account and corrected for before one can arrive at the intrinsic electronic band gap. These effects include lifetime and instrumental energy

broadening, energy shifting of the XANES spectra as a result of the core hole interaction, energy splitting of the spectra resulting from nonequivalent crystal sites or degenerate core electron energy levels, and properly calibrating the energy scale of the XES and XANES spectra that are often measured using two different detectors and in some cases two different synchrotron beamlines.

2.4.1 Broadening

The lifetime and instrumental broadening that is associated with XES and XANES can drastically reduce the detail of the spectra, but more importantly for our case they obscure the VB and CB edge. In order to accurately and reliably determine the edge of the VB and CB using XES and XANES, respectively, a method that unambiguously and precisely determines these locations is needed. Historically, there have been many methods to achieve this including drawing tangent lines that intersect with the energy axis or even using the peaks near the VB and CB edges as the location of the band edges. Fig. 2.3 shows two examples from Refs. 40 and 41. The left panel of Fig. 2.3 shows the band gap determination of zinc sulfide (ZnS) and cadmium sulfide (CdS) using XES and XANES spectra. The intensity of the spectra has been squared to make the measured LPDOS linear assuming that the LPDOS have a square-root dependence on energy. This technique neglects the effects of instrument and lifetime broadening, which would change the energy dependence of the LPDOS. The right panel shows similar measurements on organic LED candidates, NPB and BCP. The edges of the XES and XANES spectra were fit with Lorentz profiles and the peak locations were taken as the HOMO and LUMO locations, assuming that the materials exists purely as a molecule. However, recently it was discovered that taking the second derivation of the XES and XANES spectra with respect to energy is an unambiguous method to determine the VB and CB edges [42]. The first peak in the second derivative that has an appreciable intensity above the noise floor is selected in the XES and XANES as the VB and CB edges, respectively.

The instrumental broadening in XES and XANES spectra results from the energy distribution of synchrotron-based X-rays that are selected and detected by the monochromator and spectrometer, respectively. This type of broadening is modelled well using a Gaussian

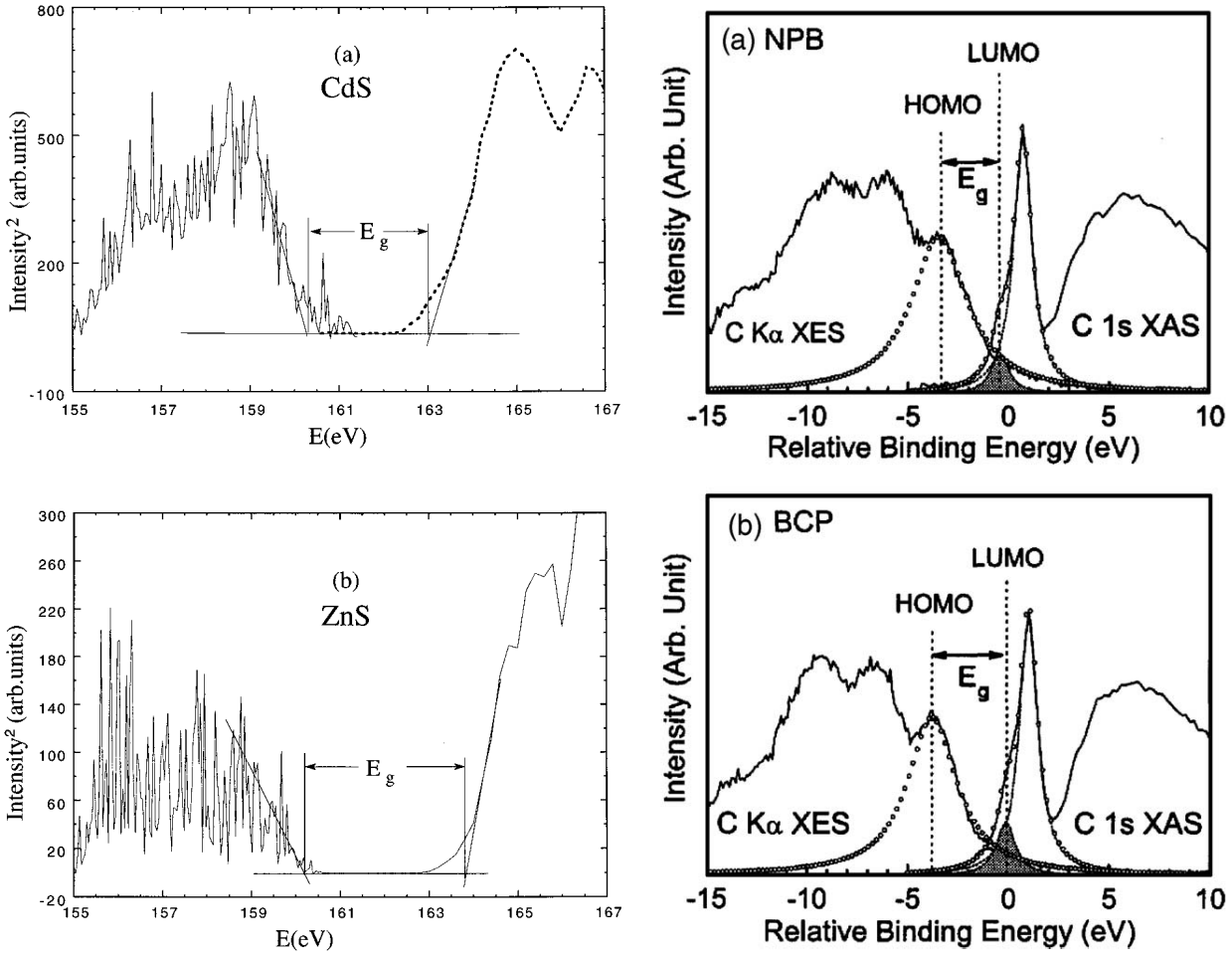

Figure 2.3: Two examples of other methods to determine the electronic band gap include using the energy separation between tangent lines extended to the energy axis (left) [40] and using the energy separation of the lowest and highest energy peaks in the conduction band and valence band, respectively (right) [41].

function and Eqs. 2.34 and 2.35 show how the broadening matrix $\underline{\mathrm{G}}$ with elements G_{ij} is applied to a spectrum vector $\vec{S}$ for XES and XANES measurements, respectively. The Gaussian broadening matrix is defined by Eq. 2.33, where E_j is the energy distribution centered at E_i and the energy width is related to c. The energy width or c is usually known for the beamline being used or can be measured and is inserted directly into Eq. 2.33.

$$G_{ij} = \frac{1}{c\sqrt{2\pi}} e^{-\frac{1}{2}\left(\frac{E_j - E_i}{c}\right)^2} \tag{2.33}$$

The two different summing methods are very important for applying the broadening properly because in XES an emitted photon with a certain energy E is broadened creating

a distribution of energy centred at energy E. Contrarily, during XANES a photon with an energy distribution centred at energy E excites the material and the spectral intensity is assigned to energy E.

$$S_i^{XES'} = \sum_j G_{ji} S_j^{XES} \tag{2.34}$$

$$S_i^{XANES'} = \sum_j G_{ij} S_j^{XANES} \tag{2.35}$$

The lifetime broadening arises from the fact that the electron transitions discussed follow the final-state rule [43]. This rule requires that the photons that are emitted during a transition are indicative of only the final state of the system, regardless of initial transitions that have occurred. In short, XES and XANES are considered a one-step process. However, since the system is in an excited state in both XES and XANES, with the VB missing an electron and with a missing core electron and an additional CB electron, respectively, the system rapidly collapses toward the ground state. The lifetime of the final state τ_{XANES} for an XANES measurement and τ_{XES} for an XES measurement depends on two things: the lifetime of the core hole τ_{CH} and the lifetime of the electron in the CB τ_{CB} or hole in the VB τ_{VB} for XANES and XES, respectively, as in Eq. 2.36 and 2.37. The lifetime of the core hole in both cases is finite and relatively constant. Some lifetimes of core holes have been measured in Ref. [44] where they take advantage of the very long lived CB electrons during XANES measurements that manifest as resonances. During an XANES measurement if a resonance is excited where the lifetime $\tau_{CB} \gg \tau_{CH}$ then $\tau_{XANES} \approx \tau_{CB}$. The lifetimes of the CB and VB states are a little more complicated than the core hole lifetime, which is just the average time for a higher lying electron from filled orbitals higher in energy or electrons in the VB to fill the core hole. The lifetime of the CB electron depends on how easily the CB electron can move to electron states adjacent in energy. The lifetime of the CB electron is severely shortened as it is excited higher in energy in the CB.

The lifetime of the VB hole is a result of an electron filling the core hole during a XES measurement and is again very short. The lifetime is reduced when the hole is created deeper in the VB increasing the chances it will be filled by a higher energy electron. Clearly, there is an important energy dependence of the final state lifetimes associated with the VB hole and

CB electron. While not an exact solution, the lifetimes of these states are often modelled with an energy squared dependence [45] as in Eq. 2.39, where ΔE is the emission or excitation energy width associated with the lifetime of the state. The lifetimes are not additive, but the corresponding energy widths are linked according to Heisenberg's Uncertainty Principle as in Eq. 2.38. Eqs. 2.40 and 2.41 are used to model the energy width associated with lifetime broadening in XES (ΔE_{XES}) and XANES (ΔE_{XANES}), respectively, where W is an arbitrary scaling factor, ΔE_{CH} is the core hole broadening width and E_{CB} is the energy of the CB.

$$\frac{1}{\tau_{XANES}} = \frac{1}{\tau_{CH}} + \frac{1}{\tau_{CB}} \tag{2.36}$$

$$\frac{1}{\tau_{XES}} = \frac{1}{\tau_{CH}} + \frac{1}{\tau_{VB}} \tag{2.37}$$

$$\Delta E \propto \frac{1}{\tau} \tag{2.38}$$

$$\Delta E \propto E^2 \tag{2.39}$$

$$\Delta E_{XES} = W\left(E_{out} - E_{CB}\right)^2 + \Delta E_{CH} \tag{2.40}$$

$$\Delta E_{XANES} = W\left(E_{in} - E_{CB}\right)^2 + \Delta E_{CH} \tag{2.41}$$

Lastly, how the lifetime broadening is applied needs to be addressed. The lineshape of the lifetime broadening is well establish to have a Lorentz profile $\underline{\mathrm{L}}$ as in Eq. 2.42 and is applied similar to the instrumental broadening. Here the broadening width is γ. The lifetime broadening in XES is again a result of a decay and the total spectrum will be a sum of Lorentz functions, while the lifetime broadening in XANES is an excitation and it will be the integrated overlap of a Lorentz function with the unbroadened spectrum as in Eqs. 2.43 and 2.44.

$$L_{ij} = \frac{1}{\pi}\left(\frac{\gamma}{(E_j - E_i)^2 + \gamma^2}\right) \tag{2.42}$$

$$S_i^{XES'} = \sum_j L_{ij} S_j^{XES} \tag{2.43}$$

$$S_i^{XANES'} = \sum_j L_{ji} S_j^{XANES} \tag{2.44}$$

Now that we have discussed both instrument and lifetime broadening individually, they need to be applied to an unbroadened spectrum. Contrary to what is somewhat accepted,

the broadening should be applied in a step-wise process since the emitted or absorbed photon could not possibly know the resolution of the monochromator or spectrometer. The application of XES and XANES broadening proceeds with the lifetime broadening applied first and then the instrument broadening. The procedure results in a double sum, as in Eqs. 2.45 and Eqs. 2.46.

$$S_k^{XES'} = \sum_i G_{ik} \sum_j L_{ji} S_j^{XES} \tag{2.45}$$

$$S_k^{XANES'} = \sum_i G_{ki} \sum_j L_{ij} S_j^{XANES} \tag{2.46}$$

Although the calculation of XES and XANES spectra were treated above, we reiterate the simulation of XES and XANES now that we have discussed the final state of the system during these measurements. The final state of the system during an XES measurement includes a hole in the VB. However, since with DFT calculations the VB is not localized making a local hole the VB is not possible. As a result, an XES measurement is best simulated using the ground PDOS. However, this is not the case for an XANES measurement. For an XANES measurement, the final state of the system includes a missing core electron and an additional electron in the CB. The CB, similar to the VB, is delocalized and local electron cannot be added. But, the missing core electron can easily be added (or the electron can be removed more precisely) and is essential for an accurate simulation of an XANES spectrum. Since during an XANES measurement the likelihood of exciting two core electrons on the same time scale of the decay is quite small, the core hole needs to isolated as much as possible. This is achieved through the use of a supercell, which is a superstructure created by replicating the crystal unit cell along the axes directions. The size of the supercell is dictated by the computational resources available, but in principle larger is better.

2.4.2 Core Hole Effects, Nonequivalent Site Splitting and Spin-orbit Splitting

Broadening that occurs for XES and XANES makes it difficult to determine the VB and CB edges, but there are more effects that affect the measured band gap. These effects all

act to reduce the measured band gap from its intrinsic value and include core hole shifting, nonequivalent site splitting and spin-orbit splitting. The core hole shifting ΔE_{CS}, which occurs only for XANES spectra, acts to shift the measured unoccupied states to lower energy compared to their ground state energy. This effect in our case is modelled using DFT calculations by comparing the location of the ground state to the excited state (with a core hole) unoccupied states, where the energy difference between them is taken as the core hole shift.

Nonequivalent site splitting ΔE_{SS} occurs when there is more than one nonequivalent crystal site present for a single element. This shift arises from there being more than one core electron binding energy value present for the same core electron type. Therefore, when the XES and XANES spectra are measured, the resultant spectra will be a sum the LPDOS from nonequivalent sites of the same element shifted by the differences in the excited core electron binding energy. The spin-orbit splitting ΔE_{SO} results in a similar effect as the nonequivalent site splitting. Spin-orbit splitting occurs for all elements with the same angular momentum l and is known as $L-S$ coupling for elements with $Z < 30$ and $J-J$ coupling for elements with $Z \geq 30$. The splitting arises from how the total angular momentum is defined in Eqs. 2.47 and 2.48 for $L-S$ and $J-J$ coupling for total orbital, total spin and total angular momentum L, S and J and orbital, spin and angular momentum l_i, s_i and j_i, respectively. The energy levels are split into electrons with the same total angular momentum, which changes the relative occupation of different energy levels.

$$J = L + S, \quad L = \sum_i l_i, \quad S = \sum_i s_i \tag{2.47}$$

$$J = \sum_i j_i = \sum_i (l_i + s_i) \tag{2.48}$$

Finally, to determine the electronic band gap, all of the aforementioned effects are combined to determine the intrinsic electronic band gap using core-level spectroscopy. Eq. 2.49 shows the general equation to determine the electronic band gap using XES and XANES to determine the VB E_{VB} and CB E_{CB} edges.

$$E_g = E_{CB} - E_{VB} + \Delta E_{CS} + \Delta E_{SS} + \Delta E_{SO} \tag{2.49}$$

Fig. 2.1 shows an example, crystalline silicon (c-Si), illustrating how an electronic band gap is obtained with core-level spectroscopy. In this case the Si $L_{2,3}$ XES and Si $2p$ XANES, which probe the Si s/d-states, are used to determine the band gap. Spin-orbit splitting of the Si $2p$ levels means there will be an apparent band gap reduction that needs to be corrected. The second derivative is used to determine the VB and CB edges, and in this case the XES spectrum is of such great quality that the two spin-orbit split VB edges are resolved in the second derivative. The final band gap E_g^{Si}, using Eq. 2.49, will be 1.1 ± 0.2 eV and is detailed in Eq. 2.50. The error stated here is associated with precision of calibration (0.1 eV for both XES and XANES) as well as the measured data (0.1 eV for both XES and XANES) giving a total error of 0.2 eV. The core hole shift ($\Delta E_{CS} = 0.1$ eV), not shown explicitly, was previously determined from DFT calculations.

$$E_g^{Si} = 99.6 - 99.3 + 0.1 + 0.0 + 0.7 = 1.1 \tag{2.50}$$

2.4.3 Calibration

A viable method to determine the intrinsic electronic band gap has been outlined in brevity above, but it has so far been assumed that both the XES and XANES spectra can be plotted on the same energy scale. However, in order to do this accurately, special care must be taken to assure that the relative energy separation between the XES and XANES spectra is correct. The calibration of XES and XANES spectra proceeds similarly to any calibration procedure: measure reference spectra where the energy location of features are known, shifting the energy scale from the initial values and then apply the same shift to the spectra of unknown energy position. Of course, this implies that one knows the energy position of reference spectra. The procedure for obtaining calibrated reference spectra is as follows: (1) measure the XANES spectrum of the reference material and shift its position to a reasonable energy value (the actual energy value is not terribly important since we are dealing with XANES making the non-linear energy dependence of grating monochromators insignificant), (2) measure a non-resonant XES spectrum, (3) measure several elastic scattering features without moving the spectrometer, and (4) adjust the spectrometer calibration such that the elastic scattering features appear at the same energy as the excitation energy. These steps

will provide very accurate relative calibration between XES and XANES spectra that can then be used to calibrate future measurements. Fig. 2.1 shows all of the spectra discussed and is appropriately labelled. This method does restrict the reference material, it must exhibit elastic scattering. Furthermore, one must have a reference material for each different element core-level excitation in order for each set of spectra to be calibrated.

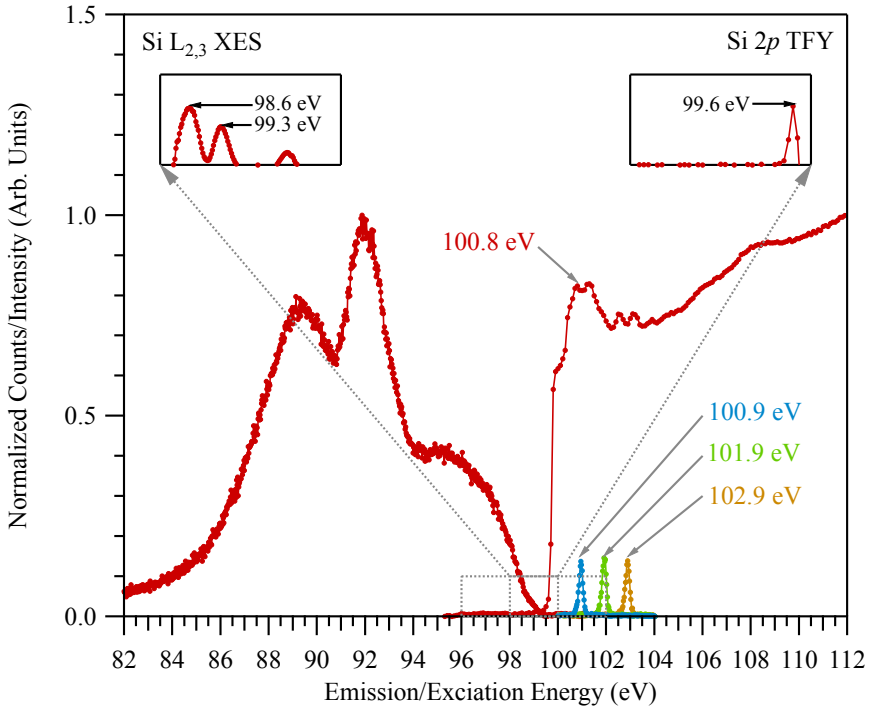

Figure 2.4: Crystalline silicon is used as an example illustrating how to calibrate XES and XANES spectra as well as how to use core-level spectroscopy to determine the intrinsic electronic band gap. The measured Si $L_{2,3}$ XES and Si $2p$ TFY are displayed in red scatter, with the corresponding second derivatives displayed in the inset plots. The peaks of the second derivatives are labelled, as well as the region of interest with grey dashed lines. The measured elastic scattering peaks are displayed with the colour corresponding to their energy position.

2.5 Publications

The following publications are the result of developing and applying the methods described above to determine the electronic band gap. The interest in the electronic band gap in each

paper, although in some cases not directly linked to hardness, stemmed from the desire to study the electronic properties of the materials for practical applications. These studies were instrumental in developing a reliable, accurate and robust method to both calculate and measure the intrinsic electronic band gap, which is one of the major goals as outlined in sections 1.2 and 1.3. The respective authors completed all of the writing pertaining to the specified contributed work of authors listed.

Material Properties and Structural Characterization of $M_3Si_6O_{12}N_2$:Eu^{2+} (M = Ba, Sr) – A Comprehensive Study on a Promising Green Phosphor for pc-LEDs

Authors: *C Braun, M Seibald, S L Böerger, O Oeckler, T D Boyko, A Moewes, G Miehe, A Tüecks, and W Schnick*

Summary and Author Contributions:

In this study [46], the crystal structure, electronic structure and luminescence properties of barium oxonitridosilicate ($Ba_3Si_6O_{12}N_2$) is examined using XRD measurements, DFT calculations, XES, XANES measurements, and UV excited photo-luminescence (PL) measurements. This material shows excellent phosphor-converting light emitting diode (pc-LEDs) behaviour and in order to understand why this materials exhibits such efficient conversion of UV light is important for synthesizing further pc-LEDs with even better efficiency. The sample synthesis, XRD measurements, structural determination and luminescence measurements were carried out by the collaborators, C Braun, M Seibald, S L Böerger, O Oeckler, G Miehe, A Tüecks, and W Schnick. The solved crystal structure, detailed in the attached paper, was used in the DFT calculations to simulate the measured XES and XANES spectra. The goal, in terms of the electronic structure measurements and calculations, which were carried out by T D Boyko under the supervision of A Moewes, was to determine the electronic band gap in an effort to ascertain if it contributed to the efficient pc-LED behaviour of the material. The thought was that the band gap must be very large so that is does not interfere with UV stimulated emission. Through careful measurements and calculations we were not only able to determine the electronic band gap to be 7.05 ± 0.25 eV, but both the calculated electronic band gap of 6.93 eV and simulated XES and XANES spectra agreed very well with the ex-

perimental measurements. The $Ba_3Si_6O_{12}N_2$:Eu^{2+} sample had a couple of impurities, a-SiO_2 and α-Si_3N_4, which would have presented a problem if the electronic band gap was measured using conventional methods. Furthermore, the rare-earth doping of Eu also would have prohibited conventional band gap measurements because the d - d or f - f transitions, which are needed to exhibit pc-LED behaviour would have hindered such measurements. Measuring the electronic band gap of this material was inherently difficult and we used resonant XES measurements, which are used to preferentially excite specific material phases and nonequivalent crystal sites. Combining these measurements with DFT calculations we were able to selectively measure the electronic band gap of the host material alone. This allowed us to show that the efficient pc-LED behaviour was in part due to the large electronic band gap. In summary, the determination of the electronic band gap of $Ba_3Si_6O_{12}N_2$:Eu^{2+} showcases the wide usefulness of core-level spectroscopy and its necessity to determine the electronic band gap rather than using conventional methods.

Electronic Band Gap Reduction in Manganese Carbodiimide: MnNCN

Authors: *T D Boyko, R J Green, R Dronskowski, and A Moewes*

Summary and Author Contributions:

In this study [47], the electronic structure and electronic band gap of manganese carbodiimide (MnNCN) were examined using XES, XANES, resonant inelastic X-ray scattering (RIXS), DFT calculations and Single Impurity Anderson model (SIAM) calculations to study not only the effects of substituting an NCN molecule for an O atom, but to ascertain the electronic band gap. The collaborator – R Dronskowski – provided the material that was studied in the paper. The XES measurements, XANES measurements and simulations using DFT calculations were carried out by T D Boyko, while the measurements and simulations of RIXS spectra using SIAM calculations were carried out by R J Green, both under the supervision of A Moewes. MnNCN is a relatively new material [48] whose measured magnetic properties are similar to manganese oxide (MnO) in that they are both anti-ferromagnetic, but the electronic band gap still was unknown. The difficulty here was similar to Ref. [46] in that the d - d transitions in the optical absorption spectrum [31] make the band gap determination

through conventional means ambiguous. The electronic band gap is determined using the methods described above, but in this case the DFT calculations had to be expanded to include electron correlations through a DFT+U approach. Furthermore, a simplified version of the measured magnetic structure was implemented since preliminary DFT calculations showed there was a negligible difference the calculated PDOS when compared to the PDOS calculated with the full magnetic arrangement. The electronic band gap measured using XES and XANES is 3.40 ± 0.20 eV, which agreed with the calculated electronic band gap of 3.36 eV from DFT+U calculations. The electronic band gap value that resulted from DFT calculations using the MBJLDA functional was smaller at 2.89 eV, but is expected considering previous results [38]. Additionally, an electronic band gap value is also obtained from the SIAM calculations, which is 3.20 eV agreeing well with the measured band gap value. This method also performed equally well for MnO producing a value of 3.8 eV very close to the accepted value [49]. In summary, another successful example of determining the electronic band gap of a novel material using core-level spectroscopy.

Class of Tunable Wide Band Gap Semiconductors γ-$(Ge_xSi_{1x})_3N_4$

Authors: *T D Boyko, E Bailey, A Moewes, and P F McMillan*

Summary and Author Contributions:

In this study [50], the electronic band gap of a new class of possibly ultra-hard materials was determined. The materials studied were solid solutions of the newly discovered γ-Si_3N_4 [4] and γ-Ge_3N_4 [9] to form γ-$(Ge_xSi_{1-x})_3N_4$ [12]. The solid solution materials were provided by the collaborators, E Bailey and P F McMillan. The synthesis and structural details of these materials were previous published [12], but electronic band gap still remained to be measured. The electronic band gap was of particular interest as the previous theoretical studies suggested the band gap value of γ-Si_3N_4 was in the UV range [51], with the band gap value of γ-Ge_3N_4 much smaller. It was expected that these materials could represent a class of materials with tunable band gaps in the visible range. The XES and XANES measurements as well as the DFT calculations used to simulate the XES and XANES spectra were carried out by T D Boyko under the supervision of A Moewes. While the crystal structure was

known, the specific locations of the cations (Si and Ge) were not. However, these materials were known to be homogenous, so it was assumed the cations retained their faced-centred cubic arrangement. This significantly simplified the problem regarding the construction of the crystal structures that were used for the DFT calculations. The simulated XES and XANES spectra actually agreed quite well with corresponding measured spectra affirming the preceding assumptions. The XES and XANES measurements showed that the electronic band gap values γ-$(Ge_xSi_{1x})_3N_4$ were all in the UV range at $3.50 - 5.00 \pm 0.20$ eV making their uses in optical applications limited, but still showing these materials allow the band gap to be tuned to a desired value within this range. More interestingly, using the correlation between the electronic band gap and hardness [16], it was shown that for small amounts of Ge substituted for Si the hardness remained comparable to γ-Si_3N_4. This publication showcased the tunable nature of the solid solutions of group 14 spinel-type nitrides as well as using the electronic band gap to predict hardness of materials within the same structural class.

Electronic structure of Spinel-Type Nitride Compounds Si_3N_4, Ge_3N_4, and Sn_3N_4 with Tunable Band Gaps: Application to Light Emitting Diodes

Authors: *T D Boyko, A Hunt, A Zerr, and A Moewes*

Summary and Author Contributions:

This study [52] is a follow up to Ref. 50 in that we have extended the spinel nitride solid solutions family to include those formed using γ-Ge_3N_4 and γ-Sn_3N_4. Additionally, all three known binary spinel nitrides γ-Si_3N_4, γ-Ge_3N_4 and γ-Sn_3N_4 are studied in greater detail. The materials, γ-Si_3N_4, γ-Ge_3N_4 and γ-Sn_3N_4 were provided by our collaborator A Zerr. The measurements and simulations of the XES and XANES spectra as well using DFT calculations to predict the exciton binding energy of solid solutions γ-$(Ge_xSi_{1x})_3N_4$ and γ-$(Sn_xGe_{1x})_3N_4$ were carried out by T D Boyko under the supervision of A Moewes. A Hunt provided support in both writing and scientific input. Using the measured XES and XANES spectra combined with DFT calculations we have determined the electronic band gap values of γ-Si_3N_4, γ-Ge_3N_4 and γ-Sn_3N_4 to be 4.8 ± 0.2 eV, 3.5 ± 0.2 eV and 1.6 ± 0.2 eV, respectively. The large band gap reduction of nearly 2 eV observed in γ-Sn_3N_4 suggested that the solid solutions

γ-$(Sn_xGe_{1x})_3N_4$ might be very advantageous for optical applications. With these materials not yet synthesised, the band gap values were only calculated. The same assumptions using in Ref. 50 were applied here to successfully create structures for the entire solid solutions series γ-$(Sn_xGe_{1x})_3N_4$. The MBJLDA functional [38] was used to calculate the electronic band gap of γ-Si_3N_4, γ-Ge_3N_4 and γ-Sn_3N_4 and were found to be 4.97 eV, 3.59 eV and 1.61 eV, respectively. With these calculated values agreeing with the experimental measurements, the same approach was applied to the solid solutions showing the band gap values were indeed tunable. However, not only must the band gap be the correct value for optical applications, it must also be direct and the exciton binding energy must also be sufficient to ensure an adequate rate of electron hole recombination. The electron band structures that were calculated using the DFT calculations were used to show that not only are most of the electronic band gaps direct, but all have a very large exciton binding energy. This makes the solid solutions, γ-$(Sn_xGe_{1x})_3N_4$, highly desirable for optical applications and we are confident there will be additional research into synthesizing these materials. In summary, we have studied in detail the electronic properties of the entire spinel nitride material class showing these robust materials have ideal electronic properties that make them suitable for optical and UV applications. This research not only highlights using core-level spectroscopy to determine the electronic band gap of hard materials, but also the successfully calculation of the electronic band gap that may prove useful for studying hypothetical ultra-hard materials.

CHEMISTRY
A EUROPEAN JOURNAL

DOI: 10.1002/chem.201000660

Material Properties and Structural Characterization of $M_3Si_6O_{12}N_2:Eu^{2+}$ (M = Ba, Sr)—A Comprehensive Study on a Promising Green Phosphor for pc-LEDs

Cordula Braun,[a] Markus Seibald,[a] Saskia L. Börger,[a] Oliver Oeckler,[a] Teak D. Boyko,[b] Alexander Moewes,[b] Gerhard Miehe,[c] Andreas Tücks,[d] and Wolfgang Schnick*[a]

Abstract: The efficient green phosphor $Ba_3Si_6O_{12}N_2:Eu^{2+}$ and its solid-solution series $Ba_{3-x}Sr_xSi_6O_{12}N_2$ (with $x \approx 0.4$ and 1) were synthesized in a radio-frequency furnace under nitrogen atmosphere at temperatures up to 1425 °C. The crystal structure ($Ba_3Si_6O_{12}N_2$, space group $P\bar{3}$ (no. 147), $a = 7.5218(1)$, $c = 6.4684(1)$ Å, $wR2 = 0.048$, $Z = 1$) has been solved and refined on the basis of both single-crystal and powder X-ray diffraction data. $Ba_3Si_6O_{12}N_2:Eu^{2+}$ is a layer-like oxonitridosilicate and consists of vertex-sharing SiO_3N-tetrahedra forming 6er- and 4er-rings as fundamental building units (FBU). The nitrogen atoms are connected to three silicon atoms ($N^{[3]}$), while the oxygen atoms are either terminally bound ($O^{[1]}$) or bridge two silicon atoms ($O^{[2]}$) (numbers in superscripted square brackets after atoms indicate the coordination number of the atom in question). Two crystallographically independent Ba^{2+} sites are situated between the silicate layers. Luminescence investigations have shown that $Ba_3Si_6O_{12}N_2:Eu^{2+}$ exhibits excellent luminescence properties (emission maximum at ≈527 nm, full width at half maximum (FWHM) of ≈65 nm, low thermal quenching), which provides potential for industrial application in phosphor-converted light-emitting diodes (pc-LEDs). In-situ high-pressure and high-temperature investigations with synchrotron X-ray diffraction indicate decomposition of $Ba_3Si_6O_{12}N_2$ under these conditions. The band gap of $Ba_3Si_6O_{12}N_2:Eu^{2+}$ was measured to be 7.05 ± 0.25 eV by means of X-ray emission spectroscopy (XES) and X-ray absorption near edge spectroscopy (XANES). This agrees well with calculated band gap of 6.93 eV using the mBJ-GGA potential. Bonding to the Ba atoms is highly ionic with only the $4p_{3/2}$ orbitals participating in covalent bonds. The valence band consists primarily of N and O p states and the conduction band contains primarily Ba d and f states with a small contribution from the N and O p states.

Keywords: density functional calculations · high-pressure chemistry · luminescence · oxonitridosilicates · X-ray absorption spectroscopy

[a] C. Braun, M. Seibald, S. L. Börger, Dr. O. Oeckler, Prof. Dr. W. Schnick
Department Chemie
Lehrstuhl für Anorganische Festkörperchemie
Ludwig-Maximilians-Universität München
Butenandtstrasse 5–13 (D), 81377 München (Germany)
Fax: (+49) 89-2180-77440
E-mail: wolfgang.schnick@uni-muenchen.de

[b] T. D. Boyko, Prof. Dr. A. Moewes
Department of Physics and Engineering
University of Saskatchewan, 116 Science Place
Saskatoon, Saskatchewan, S7N 5E2 (Canada)

[c] Dr. G. Miehe
Technische Universität Darmstadt
Fachbereich Material- und Geowissenschaften
Fachgebiet Disperse Feststoffe
Petersenstr. 23, 64827 Darmstadt (Germany)

[d] Dr. A. Tücks
Philips Technologie GmbH, Forschungslaboratorien
Solid State Lighting, Weisshausstr. 2, 52066 Aachen (Germany)

Supporting information for this article is available on the WWW under http://dx.doi.org/10.1002/chem.201000660.

Introduction

Nitrido- and oxonitridosilicates as well as binary silicon nitride (e.g., Si_3N_4,[1–3] SiAlONs,[4] $Sr_2Si_5N_8:Eu^{2+}$,[5–7] $Eu_2Si_5N_8$[8,9]) are known to exhibit interesting physical[10,11] and luminescence properties.[12–16] During the last ten years, Eu^{2+}-doped nitrido- and oxonitridosilicates emerged as promising materials applicable for phosphor-converted light-emitting diodes (pc-LEDs) owing to their high chemical and physical stability, their extraordinary quantum efficiency of the luminescence process (up to ≈95%), and their very low thermal quenching. Namely $M_2Si_5N_8:Eu^{2+}$[6,7,12,17–19] and $MSi_2O_2N_2:Eu^{2+}$ (M = alkaline earth metal)[20–24] are excellent examples for highly effective red-orange (2-5-8) and yellow-green (1-2-2-2) phosphors, respectively.[25] Thereby, the first warm white all-nitride pc-LED has been realized, exhibiting unprecedented color quality and stability with temperature and drive.[12] Another important red phosphor is the nitridoaluminosilicate $CaAlSiN_3:Eu^{2+}$[26,27] and its derivatives. As the quest for higher energy efficiency represents one of the most fundamental and exigent challenges to be solved by modern science and technology, it becomes apparent that the search for novel and ecologically acceptable energy sources is indispensable. Addressing this challenge, LEDs become more and more important due to their ongoing improved efficiency, their remarkable durability as well as their environmentally friendly production process and waste disposal. Nowadays AlGaInP-based LEDs are accessible emitting in the red to yellow range of the spectrum. It was not before the pioneering work of Nakamura in the 1990s that the technological access to efficient blue LEDs was provided.[28,29] Further band-gap engineering has made AlGaInN-based LEDs accessible emitting in the UV to green range of the spectrum. The concept of down conversion of blue light from InGaN LEDs by suitable color converters (i.e., phosphors) is appropriate for efficient lighting[30] and provides monochrome light of high color purity, especially in the wavelength range in which direct emitting LEDs are relatively inefficient ("yellow gap"). The spectral position of the emission of these down-conversion phosphors doped with rare-earth ions (e.g. Ce^{3+} or Eu^{2+}) depends very much on the ligand field of the rare-earth ions in the host lattice, with stronger covalent interactions driving the emission into the red region of the spectrum (nephelauxetic effect).

The new green-emitting phosphor $Ba_3Si_6O_{12}N_2:Eu^{2+}$ has been discovered recently,[31,32] and its luminescence properties emerged to be promising[31,32] due to a small Stokes shift and a narrow emission band. However, no detailed crystallographic description based on single-crystal structure determination has been reported for $Ba_3Si_6O_{12}N_2:Eu^{2+}$ nor for the related solid solutions with Sr as yet.

As phosphor materials may show phase transitions at elevated temperatures and/or pressures, in-situ investigations of these solids can decisively contribute to a better understanding and optimization of their manufacturing process. In addition, from a more fundamental point of view, new modifications with different luminescence properties (e.g., due to higher symmetry or a lower number of cation sites) may be revealed by applying non-ambient reaction conditions. These aspects are addressed in this work by a systematic investigation of the high-pressure and high-temperature behavior of $Ba_3Si_6O_{12}N_2:Eu^{2+}$.

Furthermore, important material properties (e.g., conductivity, optical absorption, chemical bonding, energy gap) are determined by the electronic structure. For example, the band gap of efficient phosphors must be large enough to avoid the lowest Eu d states being too close to the conduction band, which can result in thermal ionization of the photoexcited 5d-electron of Eu^{2+}. Therefore, the local partial density of states (LPDOS) of $Ba_3Si_6O_{12}N_2:Eu^{2+}$ has been probed by soft X-ray spectroscopy (SXS) utilizing synchrotron radiation, namely by X-ray absorption near edge spectroscopy (XANES) and X-ray emission spectroscopy (XES), and is compared to our theoretical calculations within the density functional theory (DFT) framework.

Results and Discussion

Synthesis: Two different methods for sample synthesis were applied:

1) Mixtures of MCO_3 (M = Ba,Sr), SiO_2 and an excess of α-Si_3N_4 were heated in a radio-frequency (RF) furnace[33] at maximum temperatures of 1425 °C under nitrogen atmosphere according to the reaction below [Eq. (1)].

$$3\,(Ba,Sr)CO_3 + 4.5\,SiO_2 + 1.5\,\alpha\text{-}Si_3N_4 \xrightarrow[EuF_3]{1425\,^\circ C,\ N_2} (Ba,Sr)_3Si_6O_{12}N_2 : Eu^{2+} + 3\,CO_2 + \alpha\text{-}Si_3N_4 \quad (1)$$

During synthesis EuF_3 was used as a dopant. The reaction product was inhomogeneous, but contained single-crystals of $(Ba,Sr)_3Si_6O_{12}N_2:Eu^{2+}$, suitable for X-ray structure analysis

2) A more homogeneous bulk product of highly crystalline material (in this case without europium) was obtained from $BaSi_2O_2N_2$[23] (synthesis with small impurities of different Ba oxosilicates and α-Si_3N_4 according to reference [23]) by high-pressure/high-temperature (HP/HT) synthesis employing the multianvil press technique[34–36] at a pressure of 14 GPa and 1200 °C according to the reaction below [Eq. (2)].

$$BaSi_2O_2N_2 : Eu^{2+} + 2\,BaO + 4\,SiO_2 + \alpha\text{-}Si_3N_4 \rightarrow Ba_3Si_6O_{12}N_2 : Eu^{2+} + \alpha\text{-}Si_3N_4 \quad (2)$$

The atomic ratio M:Si:O:N = 3:6:12:2 of $Ba_3Si_6O_{12}N_2$ was confirmed by EDX measurements (see Experimental Section). However, samples obtained by high-pressure synthesis did not contain single-crystals suitable for X-ray diffraction analysis.

Table 1. Crystallographic data for $Ba_3Si_6O_{12}N_2$, $Ba_{2.56}Sr_{0.44}Si_6O_{12}N_2$ and $Ba_2SrSi_6O_{12}N_2$.[a]

Formula	$Ba_3Si_6O_{12}N_2$	$Ba_{2.56}Sr_{0.44}Si_6O_{12}N_2$	$Ba_2SrSi_6O_{12}N_2$
M_r [g mol^{-1}]	800.58	778.70	750.86
crystal system	trigonal	trigonal	trigonal
space group	$P\bar{3}$ (no. 147)	$P\bar{3}$ (no. 147)	$P\bar{3}$ (no. 147)
a [Å]	7.5218(1)	7.4830(6)	7.4624(2)
c [Å]	6.4684(1)	6.4513(5)	6.4234(2)
V [Å^3]	316.935(8)	312.84(4)	309.78(9)
Z	1	1	1
ρ_{calcd} [g cm^{-3}]	4.195	4.133	4.025
μ [mm^{-1}]	9.857	10.474	11.230
F(000)	362	355	344
crystal size [mm^3]	$0.07\times0.05\times0.03$	$0.01\times0.01\times0.02$	0.04x 0.04×0.02
T [K]	293(2)	293(2)	293(2)
2θ range [°]	6.28–60.78	6.28–54.80	6.30–67.52
total reflns	3294	1423	4591
independent reflns	625	479	838
observed reflns	482	338	757
parameters	36	38	38
GOF	0.921	0.919	1.072
R values [$I>2\sigma(I)$]	$R1=0.0256$	$R1=0.0389$	$R1=0.0165$
	$wR2=0.0479$	$wR2=0.0609$	$wR2=0.0327$
R values (all data)	$R1=0.0406$	$R1=0.0764$	$R1=0.0210$
	$wR2=0.0506$	$wR2=0.0718$	$wR2=0.0340$
max/min residual electron density [e Å^{-3}]	1.660/−1.146	1.422/−1.138	0.678/−0.558

[a] Lattice parameters for $Ba_3Si_6O_{12}N_2$ were taken from the Rietveld refinement based on powder diffraction data. The refined compositions for the solid solution series are: $Ba_{2.56(2)}Sr_{0.44(2)}Si_6O_{12}N_2$ and $Ba_{2.01(2)}Sr_{0.99(2)}Si_6O_{12}N_2$.

Structure determination: The crystal structure of $Ba_3Si_6O_{12}N_2$:Eu^{2+} and its solid-solution series $Ba_{3-x}Sr_xSi_6O_{12}N_2$ (with $x\approx0.4$ and 1) was solved by direct methods[37] and refined[38] in space group $P\bar{3}$ (no. 147) by using anisotropic displacement parameters for all atoms. The atomic parameters for Ba and Sr occupying the same site in the solid solution were constrained to be equal. However, the site occupancies were refined and the presence of Eu^{2+} in the structure (2 mol %) was neglected in these refinements. The details of the single-crystal structure refinement are listed in Table 1. Occupied Wyckoff sites and refined atomic coordinates from the single-crystal diffraction data are shown in the Supporting Information (Table S1). The interatomic distances and angles are within the typical range, selected data are given in Table 2.

Table 2. Selected bond lengths [in Å] and angles [in °] of $Ba_3Si_6O_{12}N_2$, $Ba_{2.56}Sr_{0.44}Si_6O_{12}N_2$ and $Ba_2SrSi_6O_{12}N_2$ derived from single-crystal data (standard deviations in parentheses).

	$Ba_3Si_6O_{12}N_2$	$Ba_{2.56}Sr_{0.44}Si_6O_{12}N_2$	$Ba_2SrSi_6O_{12}N_2$
Ba1−O2 (6×)	2.744(3)	2.687(5)	2.660(2)
Ba2−O2 (3×)	2.819(3)	2.815(5)	2.819(2)
Ba2−O2 (3×)	2.902(3)	2.902(6)	2.884(2)
Ba2−N1 (2×)	2.997(6)/3.471(6)	3.02(2)/3.44 (2)	3.017(3)/3.407(3)
Si1−O2 (1×)	1.587(3)	1.582(6)	1.586(2)
Si1−O1 (2×)	1.649(3)/1.650(4)	1.635(5)/1.651(6)	1.644(2)/1.647(2)
Si1−N1 (1×)	1.735(2)	1.737(3)	1.7311(6)
O2-O1-O1	134.6(5)	133.9(3)	133.2(8)
O2-N1-O2	86.3(4)	87.0(2)	87.7(5)
O1-N1-O1	160.1(5)	158.8(2)	158.0(5)

The refined crystal structure of $Ba_3Si_6O_{12}N_2$ solved by single-crystal diffraction was confirmed by X-ray powder diffraction on a sample obtained from HP/HT synthesis. Crystallographic data and details of the Rietveld refinement[39] are listed in Table 3 and in the Experimental Section. The observed and calculated X-ray powder diffraction patterns as well as their difference curve after Rietveld refinement are shown in Figure 1.

Structure description: A detailed insight into the crystal structure of $Ba_3Si_6O_{12}N_2$ is required to understand its luminescent properties. Here a comprehensive crystallographic structure description is presented, which is based on the structure refinements described above. The structural parameters given by Mikami et al. are basically correct.[31,32]

The structure of $Ba_3Si_6O_{12}N_2$ consists of layers of vertex-sharing SiO_3N tetrahedra of Q^3-type, building 6er- and 4er-rings as fundamental building units (FBU),[40] which leads to a degree of condensation of $\kappa=n(Si):n(O,N)=0.43$ for the $[Si_6O_{12}N_2]^{6-}$ substructure.

According to Pauling's rule[41] and $\{uB,3,1_{\infty2}\}[(Si_6^{[4]}O_6^{[1]}O_6^{[2]}N_{4/2}^{[3]})^{6-}]$[42,43] the O atoms bridge two Si atoms ($O^{[2]}$) or are terminally bound ($O^{[1]}$), respectively, whereas the N atoms connect three silicon tetrahedral centers ($N^{[3]}$; see Figure 2) (numbers in superscripted square brackets beside atoms indicate the coordination number of the atom in question). According to lattice energy calculations (Madelung part of lattice energy, MAPLE)[44–46] there

Table 3. Crystallographic data of $Ba_3Si_6O_{12}N_2$ derived from Rietveld refinement.

formula	$Ba_3Si_6O_{12}N_2$
M_r [g mol^{-1}]	780.54
crystal system	trigonal
space group	$P\bar{3}$ (no.147)
a [Å]	7.5218(1)
c [Å]	6.4684(1)
V [Å^3]	316.935(8)
Z	1
T [K]	293
data range, step width	$5\le2\theta\le60°$, 0.01°
background treatment	18 fixed background points
profile function	pseudo-Voigt (no. 7)
R_{Bragg}	1.56
GoF	1.6
reduced χ^2	2.66

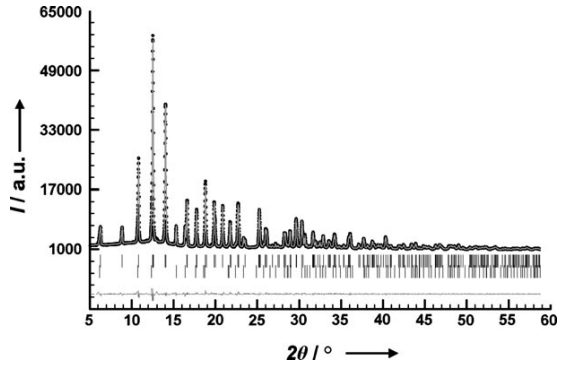

Figure 1. Observed (circles) and calculated (line) X-ray powder diffraction pattern together with their difference curve after Rietveld refinement ($\lambda = 0.709026$ Å). The upper row of reflection marks corresponds to $Ba_3Si_6O_{12}N_2$ and the lower one to β-Si_3N_4 (25% w/w).

is a clear assignment of N/O.[41,32] As expected the MAPLE of $Ba_3Si_6O_{12}N_2$ is almost identical with the sum of the respective MAPLE values of the constituting binary components BaO, SiO_2 and α-Si_3N_4 (see Table 4). The two crystal-

Table 4. Madelung part of lattice energy (MAPLE) values for $Ba_3Si_6O_{12}N_2$ (values given in kJ mol^{-1}).[a]

	$Ba_3Si_6O_{12}N_2$	BaO	SiO_2	α-Si_3N_4		
MAPLE	105684.75	3527.40	15347.60	53017.53		
atom[a]	$Ba1^{2+}$	$Ba2^{2+}$	Si^{4+}	$(O1^{[2]})^{2-}$	$(O2^{[1]})^{2-}$	$(N^{[3]})^{3-}$
MAPLE	1916.15	1890.63	9254.26	2987.00	2303.67	6358.86
total MAPLE ($Ba_3Si_6O_{12}N_2$) exptl						105684.75
total MAPLE ($3\,BaO + 4.5\,SiO_2 + 0.5\,\alpha$-$Si_3N_4$)						106155.17
difference Δ/%						0.44

[a] Typical partial MAPLE values [kJ mol^{-1}]: Ba^{2+}: 1500–2000, Sr^{2+}: 1500–2000, Si^{4+}: 9000–10200, $(O^{[2]})^{2-}$: 2400–2900, $(O^{[1]})^{2-}$: 2050–2800, $N^{[3]3-}$: 5200–6300.[72]

lographically independent Ba^{2+} ions occupy the Wyckoff sites 1*a* and 2*d*. They are situated between the silicate layers and are six- or sevenfold coordinated by (O,N) atoms, respectively (see Figure 3). The crystal structure of $Ba_3Si_6O_{12}N_2$, which is isotypic with recently discovered $Sr_3P_6O_6N_8$,[47] can be derived from the structure of β-Si_3N_4.[48] The isosteric Si_6N_{14} layers in β-Si_3N_4 are linked in the third dimension through SiN_4 tetrahedra. A formal derivation of the structure of $Ba_3Si_6O_{12}N_2/Sr_3P_6O_6N_8$ from β-Si_3N_4 can be achieved by a separation of the Si_6N_{14} layers in β-Si_3N_4 and intercalating Ba^{2+} ions (see Figure 2). Similar layered arrangements of Si/O/N tetrahedra with different degrees of condensation can be found in other Ba oxonitridosilicates as well, namely $Ba_3Si_6O_9N_4$[49] and $BaSi_2O_2N_2$.[23]

While in $BaSi_2O_2N_2$ only 3er-rings can be found, $Ba_3Si_6O_9N_4$[49] exhibits a structure related to $Ba_3Si_6O_{12}N_2$, which however contains different 6er-rings and additional 3er-rings.[50]

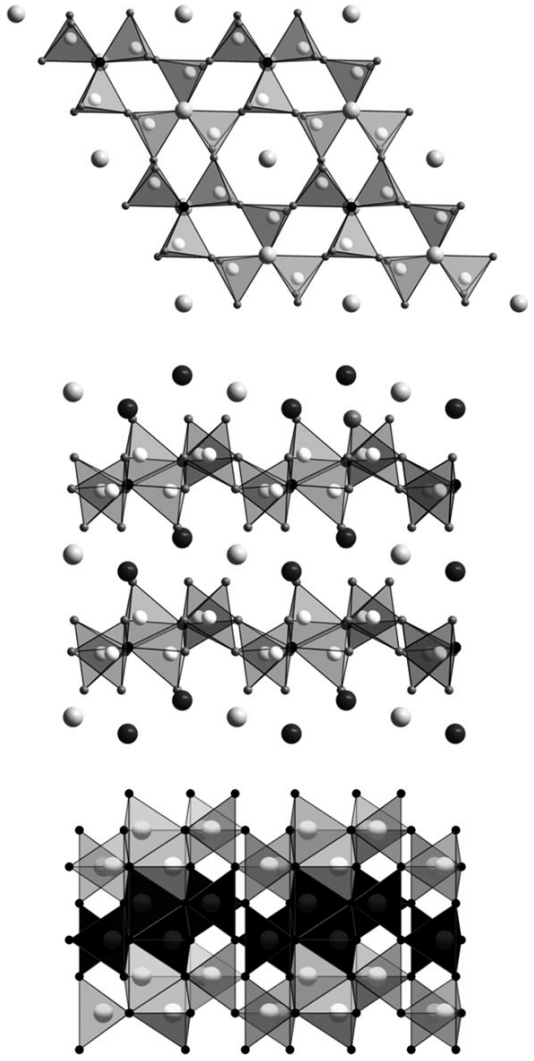

Figure 2. Comparison of $Ba_3Si_6O_{12}N_2$ and β-Si_3N_4: $Ba_3Si_6O_{12}N_2$ view along [001] (top), view along [010] (middle), and β-Si_3N_4 for comparison (bottom, view along [010]), removing every second Si-atom layer (black) and substituting the emerging terminal N-atoms by O-atoms results in layers, topologically similar to those in $Ba_3Si_6O_{12}N_2$ (Si atoms white, N black, Ba1 light gray, Ba2 dark gray and O gray).

The bond lengths Si–O/N in $Ba_3Si_6O_{12}N_2$ are in the typical range with 1.59–1.73 Å ($Ba_3Si_6O_9N_4$: Si–O/N = 1.60–1.75 Å,[49] $BaSi_2O_2N_2$: Si–O/N = 1.66–1.73 Å).[23] The distances Si–$O^{[1]}$ and Si–$O^{[2]}$ range between 1.59 Å for $O^{[1]}$ and 1.61–1.71 Å for $O^{[2]}$ and are therefore comparable with related Ba oxonitridosilicates (e.g. $Ba_3Si_6O_9N_4$: Si–$O^{[1]}$: 1.60 Å, Si–$O^{[2]}$: 1.65 Å,[49] $BaSi_2O_2N_2$: Si–$O^{[1]}$: 1.66 Å).[23] Within the tetrahedra, the Si–$N^{[3]}$ distance is, as expected, the longest one with 1.73 Å ($Ba_3Si_6O_9N_4$: Si–$N^{[3]}$ = 1.73–1.75 Å,[49] $BaSi_2O_2N_2$: Si–$N^{[3]}$ 1.72–1.73 Å).[23] The (O,N)-Si-(O,N) angles range from 103–116° and correspond well with other Ba oxonitridosilicates ($Ba_3Si_6O_9N_4$: 103–114°,[49] $BaSi_2O_2N_2$: 99–118°).[23] Compared to other Ba oxonitridosilicates the

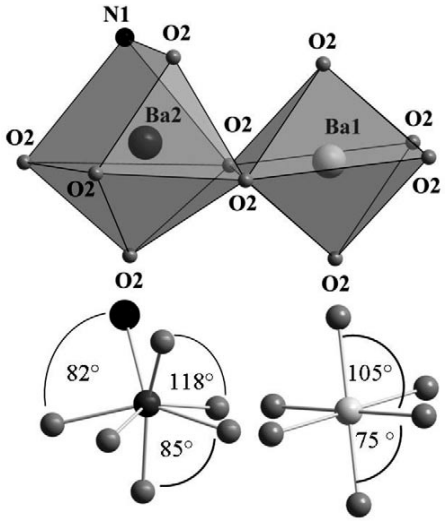

Figure 3. Coordination polyhedra and the corresponding angles of the two different Ba sites in $Ba_3Si_6O_{12}N_2$ (N atoms black, Ba1 light gray, Ba2 dark gray and O gray).

Si-N[3]-Si angle in $Ba_3Si_6O_{12}N_2$ (118°) is in the same range as in $Ba_3Si_6O_9N_4$ (118–120°)[49] and $BaSi_2O_2N_2$ (116–121°).[23] Cation coordination polyhedra in $Ba_3Si_6O_9N_4$ and $Ba_3Si_6O_{12}N_2$ are very similar as well.

In $Ba_3Si_6O_{12}N_2$ the oxygen atoms in the coordination sphere of Ba1 form a trigonal antiprism, which can be described as well as a distorted octahedron with six equal distances (Ba1[6]–O = 2.74 Å), but some angles (see Figure 3) deviating from 90° ($Ba_3Si_6O_9N_4$: Ba1[6]–O = 2.69–2.82 Å).[49] The coordination polyhedron around Ba2 can be described for $Ba_3Si_6O_{12}N_2$ as well as for $Ba_3Si_6O_9N_4$ as a capped distorted octahedron ($Ba_3Si_6O_{12}N_2$: Ba2[7]–O/N = 2.82–3.00 Å, $Ba_3Si_6O_9N_4$: Ba2[7]–O/N = 2.70–3.16 Å).[49]

In contrast to $Ba_3Si_6O_9N_4$, $Ba_3Si_6O_{12}N_2$ features excellent luminescence properties. Mikami[32] has suggested that this may be due to the longer Ba–N distances and a lower energy host absorption band of $Ba_3Si_6O_9N_4$ in comparison to $Ba_3Si_6O_{12}N_2$.

Solid-solution series of $Ba_{3-x}Sr_xSi_6O_{12}N_2:Eu^{2+}$: The influence of the Ba^{2+} substitution by Sr^{2+} in the solid-solution series $Ba_{3-x}Sr_xSi_6O_{12}N_2:Eu^{2+}$ (with $x \approx 0.4$ and 1) has been studied. In $Ba_{3-x}Sr_xSi_6O_{12}N_2:Eu^{2+}$ a substitution of Ba^{2+} by smaller Sr^{2+} mainly affects the Ba1 site (see Figure 3), which might be due to the smaller coordination number of this site. The substitution of Ba^{2+} by Sr^{2+} significantly influences the bond length Ba1/Sr1-O2, which decreases with increasing amount of Sr^{2+} ($Ba_3Si_6O_{12}N_2$: 2.74 Å, $Ba_2SrSi_6O_{12}N_2$: 2.66 Å) as the silicate layers approach along [001] upon substitution. Thereby, the curvature of the corrugated layers increases as well, especially around the Ba1/Sr1 sites. Table 2 shows the interatomic distances of selected atoms for $Ba_3Si_6O_{12}N_2$, $Ba_{2.56}Sr_{0.44}Si_6O_{12}N_2$ and $Ba_2SrSi_6O_{12}N_2$, respectively.

High-pressure and high-temperature behavior: In-situ high-pressure and high-temperature studies of luminescent materials were shown to be useful in optimizing the manufacturing process of several (oxo-)nitridosilicate phosphors. Therefore, ex-situ and in-situ investigations of $Ba_3Si_6O_{12}N_2$ were performed from 0.15 to 18 GPa and temperatures ranging from 100 to 1500 °C in order to evaluate the stability. This should be representative for the Ba/Sr solid-solution series as well. Ex-situ investigations at ambient conditions on HP/HT treated samples in the range from 9 to 18 GPa and at temperatures from 800 to 1200 °C using a Walker-type multi-anvil press were carried out. Formation of small amounts of β-Si_3N_4 besides $Ba_3Si_6O_{12}N_2$ indicate that $Ba_3Si_6O_{12}N_2$ might not be stable above 14 GPa. In-situ high-pressure X-ray diffraction investigations at the synchrotron (MAX80, Beamline F2.1 Desy/Hasylab Hamburg) confirmed the instability of $Ba_3Si_6O_{12}N_2$ and elucidated the underlying mechanism. Above 0.15 GPa decomposition into the related Ba oxonitridosilicate $BaSi_4O_6N_2$[51] was identified already at room temperature. This suggests that the formation of at least one amorphous phase is likely, since no other crystalline phase could be observed, particularly no Si_3N_4. The quantity of crystalline $BaSi_4O_6N_2$ increased in comparison to the remaining $Ba_3Si_6O_{12}N_2$ as the pressure was increased. At 9 GPa the sample showed distinct signs of amorphization, which was reversible after pressure release. Again at ambient pressure the powder pattern indicates mainly $Ba_3Si_6O_{12}N_2$; however, slight traces of $BaSi_4O_6N_2$ still could be detected. Therefore, the pressure-induced transformation from $Ba_3Si_6O_{12}N_2$ into $BaSi_4O_6N_2$ is mostly reversible. The same transformation is also observed at elevated temperatures (≈0.15 GPa) and the relative amount of $BaSi_4O_6N_2$ increases from 100 to 1500 °C successively. Furthermore, above 1200 °C two other decomposition products emerge: $BaSi_2O_2N_2$[23] and β-Si_3N_4.[48]

The temperature- and pressure-induced transformations of $Ba_3Si_6O_{12}N_2$, as observed under in-situ conditions, mainly agree with the final products detected ex-situ after HP/HT treatment. The formation of β-Si_3N_4 results from excursion to high temperatures above about 1200 °C (or at high pressures already at lower temperatures), either as a result of the instability of $Ba_3Si_6O_{12}N_2$ or from crystallization of initially amorphous and therefore in XRD not detectable Si_3N_4.

Luminescence: Samples of $Ba_3Si_6O_{12}N_2$ were doped with 2 mol% Eu^{2+} in order to study photoluminescence. $Ba_3Si_6O_{12}N_2:Eu^{2+}$ exhibits an intense green body color due to $4f^7(^8S_{7/2}) \rightarrow 4f^65d$ absorption of Eu^{2+} in the blue to green spectral range. Under near-UV to blue light irradiation a saturated green emission band with a peak wavelength of ≈527 nm is observed (full width at half maximum (FWHM) ≈65 nm). The broad excitation band enables efficient excitation at wavelengths below 450 nm.

The excitation (PLE) and emission (PE) spectra of several samples of $Ba_{3-x}Sr_xSi_6O_{12}N_2:Eu^{2+}$ are shown in Figures 4 and 5. For $x = 0$ the broad emission band almost matches the

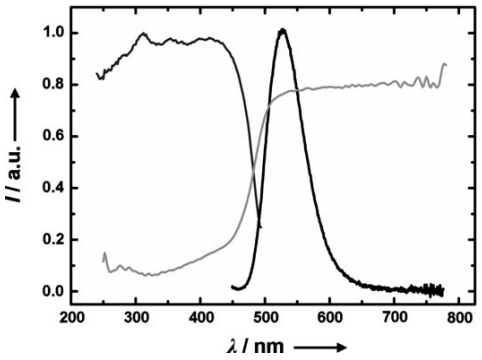

Figure 4. Excitation (gray), reflectance (light gray) and emission (black) spectra of $Ba_3Si_6O_{12}N_2$: Eu^{2+} (2 mol% Eu^{2+}).

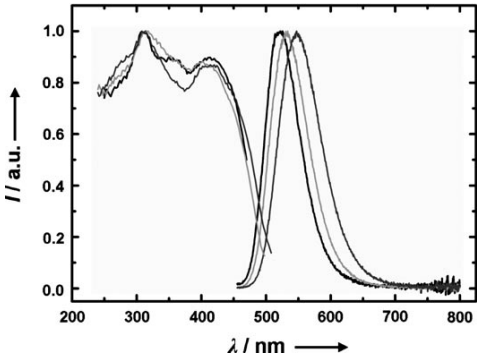

Figure 5. Excitation (PLE) and emission (PE) spectra of $Ba_{3-x}Sr_xSi_6O_{12}N_2$:$Eu^{2+}$ (several samples) with varying Sr contents. Excitation and emission spectra with 0% Sr are depicted in black, with 11% Sr in light gray, with 34% Sr in dark gray.

spectrum of Eu^{2+}-activated $BaSrSiO_4$:Eu^{2+} phosphors[52] and resembles typical Eu^{2+} spectra observed for other oxonitridosilicate compounds (e.g., $MSi_2O_2N_2$:Eu^{2+}).[53] For 11% Sr the emission spectrum nearly coincides with that of $SrSi_2O_2N_2$:Eu^{2+}. The spectral half-width of 2310 cm^{-1} (0% Sr) lies between the values observed for $BaSi_2O_2N_2$:Eu^{2+} (1340 cm^{-1}) and $SrSi_2O_2N_2$:Eu^{2+} (2423 cm^{-1}).[53] The former exhibits an exceptionally small FWHM value that corresponds to direct emitting cyan-green LEDs and can be attributed to the presence of only one very symmetrical crystallographic M^{2+} site as well as a small Stokes shift.

$Ba_3Si_6O_{12}N_2$:Eu^{2+} has a Stokes shift of $\approx$2600 cm^{-1} which is higher than the values for $BaSi_2O_2N_2$:Eu^{2+} (1030 cm^{-1}), but significantly lower than the Stokes shift of $SrSi_2O_2N_2$:Eu^{2+} (4740 cm^{-1}).[53] Partial substitution of Ba by Sr causes a noticeable red-shift and broadening of the emission band (see Table 5). As expected, the unit cell contracts with increasing amounts of Sr^{2+} (see crystallographic data, Table 1). Typically, such a unit-cell contraction involves decreasing interatomic distances between Eu^{2+} and its ligands and thus results in a larger crystal field strength at the activator site, leading to a red-shift of the emission band. Another factor that may affect the spectral shift and half-width

Table 5. Peak emission wavelength and spectral half-width of $Ba_{3-x}Sr_xSi_6O_{12}N_2$, depending on the partial substitution of Ba by Sr (Eu^{2+} content 2%).

Sr concentration [%]	λ_{max} [nm]	FWHM [cm^{-1}]
0	523	2310
11	532	2360
34	549	2510

is the presence of two different crystallographic sites, Ba1 and Ba2, which exhibit slightly different coordination (see Figure 3) and interatomic distances (see Table 2).

Due to their smaller but very similar ionic radii, Sr^{2+} as well as Eu^{2+} (compared to Ba^{2+}) should both preferentially occupy the distorted octahedral Ba1 site. Unless more than 1/3 of Ba is substituted by Sr and Eu, Eu^{2+} can always compete with the larger Ba^{2+} for the smaller Ba1 site. The spectral shift in the Ba/Sr-mixed compound is mainly caused by a unit-cell contraction. The increase in spectral width at higher Sr concentration can be attributed to an increasing Stokes shift. However, Mikami et al. suggested emission from Eu^{2+} primarily occupying the Ba2 site.[32]

Band structure and density of states: The band structure calculations (Figure 6) indicate that the material has an indirect band gap of 4.80 eV (using GGA), which is in good agree-

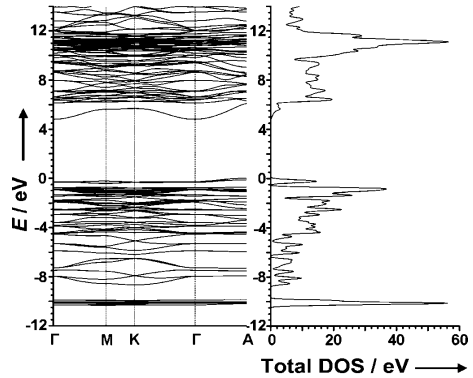

Figure 6. The total density of states (right, measured in states/eV-unit cell) and the band structure (left) of $Ba_3Si_6O_{12}N_2$:Eu^{2+} show the calculated direct (5.08 eV) and indirect (4.80 eV, A–Γ) band-gap values. The density of states (DOS) is broadened by a Gaussian function with a FWHM of 0.1 eV to aid in visual analysis.

ment with the previously reported value of 4.63 eV[32] using GGA. The band gap calculated using a modified Becke-Johnson potential with GGA (mBJ-GGA)[54] is 6.93 eV and accounts for the typical underestimation of the band gap. The modified potential is a semi-local exchange potential that allows for the correct calculation of the band gap in insulators and semiconductors. This potential is ab initio and requires no further input during the calculation. The total density of states (DOS) and partial DOS is derived from integrating momentum space and is shown for all atomic sites

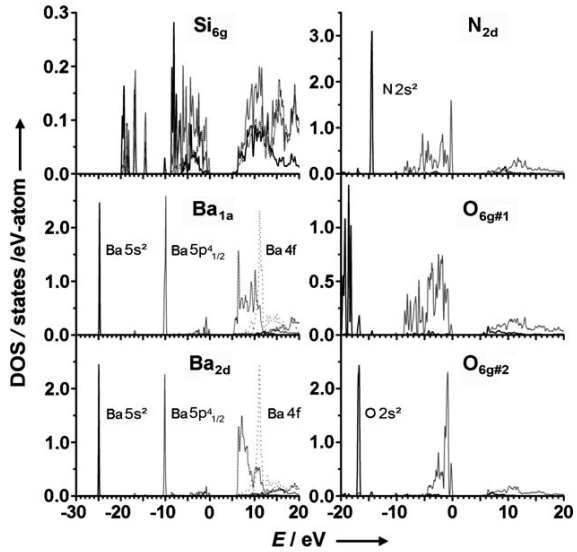

Figure 7. The density of states (DOS) is split into atomic site and electron symmetry contributions. The panels are labelled according to their Wyckoff site, furthermore the $O_{6g\#1}$ site refers to the site that forms bridging bonds to silicon. The s states are displayed black (solid), p states gray (solid), d states black (dotted) and f states gray (dotted). The DOS were broadened with a constant Gaussian of 0.1 eV FWHM and displayed in energy scale such that 0 eV corresponds to top of the valence band (i.e., the filled states). The large intensity peaks were scaled; the Ba_{1a} 5s states (reduced by 80%), $5p_{1/2}$ states (reduced by 80%), 4f states (reduced by 80%), and the Ba_{2d} 5s states (reduced by 85%), $5p_{1/2}$ states (reduced by 88%), 4f states (reduced by 80%).

in Figure 6 and 7, respectively. The DOS shows that $Ba_3Si_6O_{12}N_2$ exhibits a mixture of ionic bonding and weak covalent contributions. The Ba 5s electrons are highly localized and exhibit orbital-like behavior with no bonding. There is no indication of any Ba 6s states, thus the respective electrons of Ba are fully transferred to the N and O anion sites. The Ba 5p states are split by total angular momentum; the *j=1/2* are highly localized and non-bonding, while the *j=3/2* participate largely in the valence band (VB) covalent bonds with a small degree of participation in the conduction band (CB). The Ba 4f states play a key role in the formation of the CB, exhibiting a large peak (localized concentration of states) buried 5 eV into the CB. The CB states that are situated below 10 eV are primarily unfilled Ba 5d states. The Si s,p,d states show a large degree of hybridization with the O and N sites in conjunction with a large amount of charge transfer to the anion sites. The N and O sites suggest weak covalent bonds to the Si atoms; the N_{2d} and $O_{6g\#2}$ 2s states are highly localized with little or no bonding, but the N and O p states have a large degree of hybridization. The $O_{6g\#1}$ 2s states, however, show an affinity to form covalent bonds with Si, extending further to the $O_{6g\#1}$ 2p band as well. The N and O 2p states make up the majority of the VB with modest contribution to the CB.

Band-gap determination using soft X-ray spectra: The participation of the N and O p states in both the VB and CB makes studying the K-edge spectra of these elements an excellent probe for the electronic structure properties in general and the band gap in particular. We will first focus on the oxygen spectra.

Figure 8 shows the O K-edge soft X-ray spectroscopy measurements; this includes the O Kα X-ray emission spectra (XES) and O 1s X-ray absorption near edge spectra (XANES). There are three distinct features labelled d–g (see Figure 8) in the $Ba_3Si_6O_{12}N_2:Eu^{2+}$ O 1s XANES spectrum. The calculated O 1s XANES spectrum reproduces all the marked features and the general shape of the experimental spectrum very well. The true XANES spectrum consists of a summation of two spectra from the two non-equivalent O sites. These O 1s binding energies differ by 1.92 eV, owing to the different local symmetry (bridging bonds and tetrahedral bonds), which was determined with density functional theory (DFT) calculations. However, the energy separation seen in the measured XANES spectra is 1.76 eV, owing to the effect of an O 1s core hole. There is a small disagreement between the calculated and measured spectrum, mainly feature f (see Figure 8) is more intense in the measured spectrum than in the calculated spectrum. The added intensity is due to a third contributing spectrum, which is most likely from SiO_2 contamination. One of the

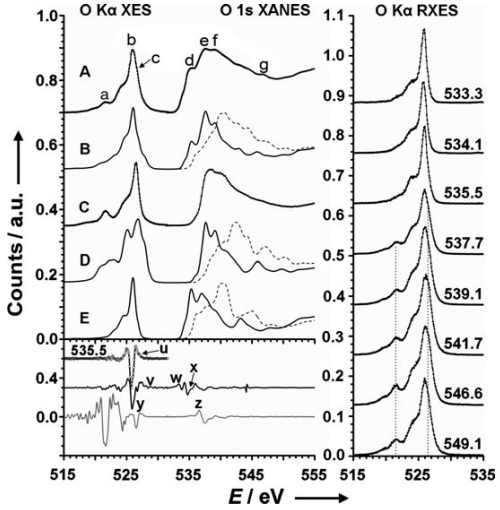

Figure 8. Non-resonant O Kα XES and O 1s XANES (left), and resonant O Kα XES (right) of A) measured $Ba_3Si_6O_{12}N_2:Eu^{2+}$, B) total calculated $Ba_3Si_6O_{12}N_2:Eu^{2+}$, C) measured SiO_2, D) calculated $O_{6g\#1}$ site, and E) calculated $O_{6g\#2}$ site are shown. The main features in the O Kα XES and O 1s XANES spectra for $Ba_3Si_6O_{12}N_2:Eu^{2+}$ are marked a–g. The right panel shows the resonant excitation energy of O Kα XES with the excitation energy indicated above each spectrum. The dashed lines indicate the contribution from SiO_2. The effect of the core hole is demonstrated with the simulated XANES spectra without the inclusion of the core hole, this is displayed as the dashed line plot in the left panel. The second derivatives of the experimental spectra are displayed in the lower left panel. The valence band (E_v) and conduction band (E_c) edges are indicated on the scatter line (the resonant XES spectra with the excitation energy indicated above, $u=O_{6g\#2}:E_v$), the solid black line (the experimental $Ba_3Si_6O_{12}N_2:Eu^{2+}$ spectra, $v=O_{6g\#1}:E_v$, $w=O_{6g\#1}:E_c$, $x=O_{6g\#1}:E_c$) and the gray line plots (the experiment SiO_2 spectra, $y=SiO_2:E_v$, $z=SiO_2:E_c$).

starting materials for synthesis of $Ba_3Si_6O_{12}N_2:Eu^{2+}$ is α-Si_3N_4, and there are significant amounts left after synthesis. Also, this material forms a surface SiO_2 layer under atmosphere readily, which will provide a spectral contribution to the O 1s XANES spectrum. This contamination and the two non-equivalent O sites were explored further with resonant XES. In the O Kα XES spectrum of $Ba_3Si_6O_{12}N_2:Eu^{2+}$ three spectral features can be found. Feature c (see Figure 8) is very subtle and is a high-energy shoulder that has been increased in intensity due to SiO_2 contamination. The low-energy peak a (see Figure 8) not seen in the simulated spectrum is also due to SiO_2. The two non-equivalent O sites are shifted by the difference in the 1s binding energy mentioned above (and not corrected for core hole effect since it is not present in the XES final state). In these spectra the excitation energy is tuned to resonant features of the XANES spectra. This allows the excitation of specific atomic sites within the lattice. Feature a in the O Kα resonant XES increases in intensity with excitation energies of 555.1 to 541.7 eV. The 541.7 eV excitation corresponds to the maximum absorption cross section in SiO_2, which is why the SiO_2 feature is the most intense. Feature c (see Figure 8) also increases in intensity, which is due to SiO_2 and confirms that SiO_2 is present on the surface. Tuning the excitation to even lower energy reduces the contributions of these peaks.

At an excitation energy of 535.5 eV, the emission spectrum changes drastically showing no signs of the $O_{6g\#1}$ site or the features of the SiO_2 contamination. The emission stems now purely from the $O_{6g\#2}$ p states and matches the calculated spectrum perfectly.

The lower energy resonant XES spectra are the same except that there are contributions from the other O atoms in the material; these are more apparent since the absorption cross sections of all the O atom sites are very low. These results suggest that the calculated spectrum for XES and XANES are correct if we properly consider the SiO_2 contamination.

The use of XES and XANES spectra to determine the top of the valence and bottom of the conduction band is not trivial due to the inherent experimental broadening mechanisms, difficulties in energy calibration, and the effect of the core hole on the absorption spectra. The energy positions of the conduction and valence band edges are determined by taking the second derivative of the experimental spectra (see Figure 8) and the first peak (above the level of noise) in the second derivative is used as the edge location.[55] The comparison of the SiO_2 second derivative to the non-resonant $Ba_3Si_6O_{12}N_2:Eu^{2+}$ shows that the SiO_2 valence band edge is located somewhere between the two edges of the oxygen non-equivalent sites. The conduction band edge of SiO_2 is much higher in energy than $Ba_3Si_6O_{12}N_2:Eu^{2+}$ (this is due to the very large band gap) and should present no problem for determining the bottom of the conduction band of $Ba_3Si_6O_{12}N_2:Eu^{2+}$ with O 1s XANES. The top of the valence band, however, can be more accurately determined by using resonant XES. Since the valence band edge of the $O_{6g\#1}$ site is very close to SiO_2, we determined the edge of the $O_{6g\#2}$ site. The O Kα XES spectrum with excitation energy of 535.5 eV is used to determine the $O_{6g\#2}$ site valence band edge; this was shown earlier to resemble the calculated spectrum best for that site. The edge locations of the $O_{6g\#1}$ are determined from the site splitting that is calculated, which makes the band gaps identical. The determined band gap for this site is 7.10 ± 0.20 eV and the corresponding VB and CB edge values are listed in Table 6. The details of the band-gap determination are further discussed in the experimental section.

Table 6. Band-gap determination using data from XES and XANES spectra in conjunction with DFT results. The sites are labelled according to their Wyckoff sites. The measured valence band and conduction edge locations are presented. The core hole effect has been rounded to the nearest 0.05 eV, and the final value of the band gap is average of the two independent determined values of the O K-edge and N K-edge. The measured band gap is compared the values obtained using GGA-PBE and mBJ-GGA.

	N_{2d}	$O_{6g\#1}$	$O_{6g\#2}$
valence band edge [eV]	394.45 ± 0.15	528.45 ± 0.15	526.55 ± 0.15
conduction band edge [eV]	401.20 ± 0.15	535.10 ± 0.15	533.35 ± 0.15
core hole shift [eV]	0.25	0.45	0.30
site band gap [eV]	7.00 ± 0.20	7.10 ± 0.20	7.10 ± 0.20
average measured band gap [eV]		7.05 ± 0.25	
calculated band gap (GGA-PBE) [eV]		4.80	
calculated band gap (mBJ-GGA) [eV]		6.93	

We now turn to the discussion of the nitrogen spectra. The N 1s XANES spectrum of $Ba_3Si_6O_{12}N_2:Eu^{2+}$ exhibits three features k–m (see Figure 9), which are reproduced well in the calculated $Ba_3Si_6O_{12}N_2$: Eu^{2+} N 1s XANES spectrum. The position of feature l is slightly distorted, because of the presence of α-Si_3N_4 (as discussed previously). The addition of this spectrum increases the spacing between the features k and l in the experiment with comparison to the calculated N 1s XANES spectrum. Feature m remains relatively unchanged because the α-Si_3N_4 N 1s XANES spectrum is very smooth in this region. The effect of this impurity is readily seen in the N Kα XES spectra. The non-resonant N Kα XES spectrum displays the features h–j, which are reproduced in the calculated spectrum as well (see Figure 9). There remains still moderate agreement between features i and j in experiment; however feature h is overestimated in the calculated spectrum. This can be explained with the consideration of α-Si_3N_4 contribution to the measured spectrum. Feature h is present in the calculated spectrum and appears not to be present in the measured spectrum. However, this feature is present and has been removed due to the summation of $Ba_3Si_6O_{12}N_2:Eu^{2+}$ and β-Si_3N_4. Furthermore, it is enhanced with selective excitation as seen in the resonant XES spectra. Many of the resonant N Kα XES spectra look very similar except for the two excited at 404.4 and 407.3 eV. In these spectra features h and i are enhanced and provide better agreement with the calculated spectrum. These spectra are the result of exciting on the two resonant features k and l in the N 1s XANES spec-

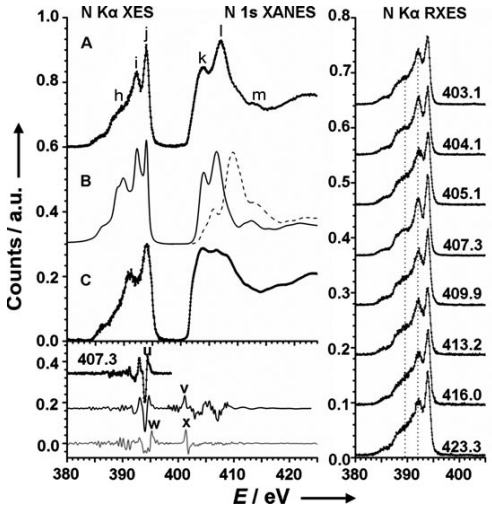

Figure 9. Non-resonant N Kα XES and N 1s XANES (left), and resonant N Kα XES (right) of A) measured $Ba_3Si_6O_{12}N_2$:Eu^{2+}, B) total calculated $Ba_3Si_6O_{12}N_2$:Eu^{2+}, and C) measured α-Si_3N_4 are shown. The main features in the N Kα XES and N 1s XANES spectra for $Ba_3Si_6O_{12}N_2$:Eu^{2+} are denoted h–m. The panel on the right hand side shows the resonant N Kα XES with the excitation energy indicated above each spectrum. The dashed lines indicate the peaks that result from the remaining α-Si_3N_4. The effect of the core hole is demonstrated with the simulated XANES spectra without the inclusion of the core hole, this is displayed as the dashed line plot. The second derivatives of the experimental spectra are displayed in the lower left panel. The valence band (E_v) and conduction band (E_c) edges are indicated on the scattered line (the resonant XES spectra with the excitation energy indicated above, u = N_{2d}:E_v), the solid black line (the experimental $Ba_3Si_6O_{12}N_2$:Eu^{2+} spectra, v = N_{2d}:E_c) and the grey line plots (the experiment α-Si_3N_4 spectra, w = Si_3N_4:E_v, x = Si_3N_4:E_c).

trum, which are attributed to $Ba_3Si_6O_{12}N_2$:Eu^{2+}. This shows that the calculated spectrum is a very reasonable representation of the material with the consideration of α-Si_3N_4 that is present in the sample. The band gap has also been determined using the N sites. The DOS results show that 1) both the N and O electron states contribute to the band gap and 2) that the band gaps determined from the N and O site should be identical. The same method used for the oxygen sites and explained above is applied to the nitrogen sites; resonant XES again is used to preferentially excite the nitrogen atoms that are part of the $Ba_3Si_6O_{12}N_2$:Eu^{2+} matrix. The second derivative of α-Si_3N_4 has a valence band edge that is higher in energy than $Ba_3Si_6O_{12}N_2$:Eu^{2+} and the conduction band edge is higher in energy as well. The band gaps of these materials are predicted to be very similar[32,56] and the offset in the spectra is due to the differences in the nitrogen-bonding environment (the N 1s binding energy is slightly different). The α-Si_3N_4 contribution to the N Kα XES spectrum is removed as much as possible through resonant XES to obtain the best determination of the N valence band edge.

The excitation energy of 407.3 eV of the resonant XES spectrum was used to determine the valence band edge. The band gap obtained is identical to the one obtained for the O K-edge 7.00 ± 0.2 eV and the corresponding VB and CB edge values are summarized in Table 6. To summarize, the average band gap obtained from both oxygen and nitrogen sites is 7.05 ± 0.25 eVThese agree with each other within the experimental precision (± 0.25 eV), and are determined from the experimental spectra with a small correction derived in our calculations to account for the presence of the core hole and non-equivalent sites.

Conclusion

The high color purity, the small thermal quenching[57] at elevated temperatures, and the intense green color with a broadband emission spectrum peaking at ≈527 nm and a FWHM of ≈65 nm renders $Ba_3Si_6O_{12}N_2$:Eu^{2+} a promising phosphor for pc-LED based general illumination and display applications.[12,31,32,52,58,59]

Especially important for the luminescence properties is the band gap being large enough to avoid the lowest Eu d states being too close to the conduction band and the thermal ionization of the photoexcited 5d electrons of Eu^{2+}.[32] In the case of $Ba_3Si_6O_9N_4$:Eu^{2+} this effect becomes very apparent; the narrower band gap and a smaller crystal field splitting provide quite different optical properties compared to $Ba_3Si_6O_{12}N_2$:Eu^{2+}. Although the crystal structure and chemical formula of $Ba_3Si_6O_9N_4$[49] appear rather similar to the one of $Ba_3Si_6O_{12}N_2$, its luminescence properties render it inapplicable for use in pc-LEDs.

Structural studies at high-pressure and high-temperature reveal a decomposition of $Ba_3Si_6O_{12}N_2$, mainly into $BaSi_4O_6N_2$, and can explain the sintering behavior of this material.

The band gap is an important parameter for the luminescent properties. Synchrotron-based soft X-ray emission and absorption spectra were measured and compared to the respective density functional theory calculations. The calculated band gap from these calculations is 4.80 eV (indirect) using GGA-PBE; however, this method strongly underestimates the band gap. The XES and XANES spectra were calculated and show excellent agreement with the experimental ones when the presence of the core hole is taken into account. The calculations were also used to discuss and determine energy shifts due to the presence of the core hole and site splitting in the two non-equivalent oxygen sites. These considerations allow a reliable experimental determination of the band gap of $Ba_3Si_6O_{12}N_2$:Eu^{2+}, which is found to be 7.05 ± 0.25 eV for both the N and O K-edge measurements. This value agrees with the calculated band gap of 6.93 eV (mBJ-GGA) within experimental error. Furthermore, the valence band is shown to be primarily made up of N and O p states and the conduction band of primarily Ba d and f states, with a small contribution from the N and O p states. The bonding of the Ba atoms is highly ionic with only the $4p_{3/2}$ participating in covalent bonds, which makes this material ideal for cation substitution.

As a consequence of this, our future research will focus on in-situ investigations of material properties to intentionally access new compounds with respect to the specific requirements for efficient phosphors.

Experimental Section

High-pressure synthesis of $Ba_3Si_6O_{12}N_2$ and ex-situ high-pressure investigations: The high-pressure synthesis of $Ba_3Si_6O_{12}N_2$ was carried out by using the multianvil technique[34–36] with a hydraulic press (Voggenreiter, Mainleus). Cr_2O_3-doped MgO-octahedra (Ceramic Substrates & Components, Isle of Wight) with an edge length of 10 mm were used. Eight truncated tungsten carbide cubes separated by pyrophyllite gaskets served as anvils for the compression of the octahedra. The truncation edge length was 5 mm. Powder of ambient-pressure $BaSi_2O_2N_2$[23] was loaded into a cylindrical capsule of hexagonal boron nitride (Henze, Kempten) with a capacity of 4 mm^3 and sealed with a BN cap. The capsule was centered within two nested graphite tubes, which acted as an electrical resistance furnace. The remaining volume at both ends of the sample capsule was filled out with two cylindrical pieces of magnesium oxide. The arrangement was placed into a zirconia tube and then transferred into a pierced MgO octahedron. Two plates of molybdenum provided electrical contact for the graphite tubes. The assembly was compressed up to 14 GPa at room temperature within 2.5 h and then heated up to 1000 °C within 12 min. Under these conditions, the sample was held for 12 min and cooled down to 600 °C within 30 min. The sample was then quenched to room temperature, followed by decompression over 9.6 h. By this procedure about 5 mg of $Ba_3Si_6O_{12}N_2$ were obtained as a dark gray substance. The temperature was calculated from the electrical power applied to the furnace which was determined on the basis of calibration curves from measurements with $W_{97}Re_3W_{75}Re_{25}$ thermocouples, as described in ref.[60] Ex-situ high-pressure measurements were performed at 9, 12, 14, 16, and 18 GPa, respectively.

Single-crystal synthesis: To synthesize single crystals of $Ba_3Si_6O_{12}N_2$, $BaCO_3$ (0.49 mmol, powder, Alfa Aesar, 98%), SiO_2 (0.75 mmol, Aerosil® A380 nano-powder, Degussa, ≥ 99.8%), crystalline α-Si_3N_4 (0.25 mmol, excess, powder, UBE Industries, 98%), and EuF_3 (0.01 mmol, powder, Aldrich Chemical, 99.99%) were mixed together, ground in an agate mortar, and placed into a tungsten crucible inside a glovebox under Ar atmosphere (Unilab, Fa. Braun, Garching, O_2 < 1 ppm, H_2O < 1 ppm). The crucible was then heated inductively in the water cooled quartz reactor of a radio-frequency furnace (typ TIG 10/100, frequency: 100 kHz, max. electrical output: 10 kV, Huettinger, Freiburg) under N_2 atmosphere (purified by passing columns of silica gel (Merck), KOH (Merck, ≥85%), molecular sieve (Merck, 4 Å) and P_4O_{10} (Roth, Granulopent®) to 1150 °C with a rate of about 23 °C min^{-1}. The temperature was then increased to 1350 °C over a period of 9 h, kept at this temperature for 1 h, and was then again increased to 1400 °C over a period of 20 h. After another temperature enhancement to 1425 °C over a period of 1 h, the sample was cooled down to 650 °C with a rate of about 0.33 °C min^{-1} to offer best conditions for good crystallinity. $Ba_3Si_6O_{12}N_2$ showing green luminescence when excited with UV-light was obtained in the shape of a hard and flat ingot coated with a transparent Matrix of glassy like α-Si_3N_4 which has to be removed to achieve single crystals. To get samples of the solid-solution series $SrCO_3$ (powder, Alfa Aeser, 98%) was used beside the other reactants.

Single-crystal X-ray diffraction: Mechanically isolated green luminescent ($Ba_3Si_6O_{12}N_2$:Eu^{2+}) and yellow greenish (($Ba,Sr)_3Si_6O_{12}N_2$:Eu^{2+}) single-crystals obtainend by RF-furnace synthesis were mounted on glass fibres and checked for quality by Laue photographs on a Buerger precession camera. Intensity data were collected on a STOE IPDS-I diffractometer with imaging plate detector and graphite monochromator ($Ba_3Si_6O_{12}N_2$) or on a Nonius Kappa-CCD diffractometer with graded multilayer X-ray optics ($Ba_{2.56}Sr_{0.44}Si_6O_{12}N_2$ and $Ba_2SrSi_6O_{12}N_2$), both using $Mo_{K\alpha}$ radiation ($\lambda = 0.71073$ Å). Semiempirical absorption corrections based on equivalent reflections were applied[61] before the structures were solved by direct methods in space group $P\bar{3}$ (no. 147).[37] Full-matrix least-squares refinements of models developed from the initial solutions were executed with SHELXL[38] with anisotropic displacement parameters for all atoms. Further details of the crystal structure investigations may be obtained from Fachinformationszentrum Karlsruhe, 76344 Eggenstein-Leopoldshafen, Germany (fax: (+49)7247-808-666; e-mail, crysdata@fiz-karlsruhe.de, http://www.fiz-karlsruhe.de/request_for_deposited_data.html) on quoting the depository numbers CSD-421322 ($Ba_3Si_6O_{12}N_2$), CSD-421323 ($Ba_2SrSi_6O_{12}N_2$), and CSD-421324 ($Ba_{2.56}Sr_{0.44}Si_6O_{12}N_2$).

Powder X-ray diffraction: X-ray diffraction experiments on powder samples of $Ba_3Si_6O_{12}N_2$ were performed on a STOE STADI P powder diffractometer in Debye–Scherrer geometry with Ge(111)-monochromatized $Mo_{K\alpha1}$ radiation ($\lambda = 0.709026$ Å). The sample was enclosed in a glass capillary with 0.1 mm diameter. A Rietveld refinement was carried out using the program package Fullprof.[39] Estimated standard deviations were calculated in agreement with reference [62]. The atomic parameters agreed with the single crystal data within the standard deviations (2σ). β-Si_3N_4[48] was included as a second phase (24.5% w/w) (see Figure 1).

In-situ high-pressure and high-temperature measurements: In-situ high-pressure measurements were performed with the multianvil high-pressure apparatus MAX80 (NRD Tsukuba, Japan), which is located at the Hamburger Synchrotronstrahlungslabor (HASYLAB, Beamline F.2.1) for in-situ high-pressure and high-temperature X-ray diffraction investigations. Energy-dispersive diffraction patterns were recorded by using white X-rays from the storage ring DORIS III. The pressure was measured by using the high-pressure equation of state for admixed NaCl by Decker.[63] The beamline was equipped with a Ge solid-state detector, situated at the press frame and tracking the adjustment of the whole apparatus in relation to the X-ray beam.

The multianvil apparatus was equipped with six tungsten carbide anvils that were driven by a 2.500 N uniaxial hydraulic ram. The top and bottom anvil were driven directly, the lateral anvils by two load frames and four reaction bolsters. The maximum pressure for the 8 mm cube setup was approximately 9 GPa with temperatures up to 1600 °C, which were produced by an internal graphite heater. The high-pressure cell consisted of a cube made of boron epoxy resin and the gaskets between the anvils are formed from the boron epoxy cube's material during the runs. The high-pressure cell was filled with the ground sample, the graphite heater, the pressure standard (NaCl) and the thermocouple, which was insulated by boron nitride. The sample was surrounded by rings made from pyrophyllite for electrical insulation and as a quasi-hydrostatic pressure transmitting medium. Copper rings contacted the heater at the top and bottom anvils.

Luminescence: Photoluminescence measurements were carried out with a spectrofluorimeter, equipped with a 150 W Xe lamp, two 500 mm Czerny–Turner monochromators, 1800 1 mm lattices and 250/500 nm lamps, providing a spectral range from 230–820 nm.

EDX measurements: The carbon coated sample was examined with a scanning electron microscope (SEM) JSM-6500F (Joel, Japan, maximum acceleration voltage 30 kV). Qualitative and semi-quantitative elemental analyses were carried out using an energy dispersive spectrometer (Model 7418, Oxford Instruments, United Kingdom).

Soft X-ray spectroscopy: The XANES measurements were performed at the SGM[64] beamline of the Canadian Light Source, Saskatoon, Saskatchewan (Canada). The XANES measurements were taken in total fluorescence yield mode with an experimental resolving power $E/\Delta E$ of approximately 5000. The XES measurements were performed with the soft X-ray fluorescence spectrometer at Beamline 8.0.1[65] of the Advanced Light Source, Berkeley, California (USA). The resolving power in the emission experiments was approximately 700. All measurements were taken with the sample orientated 30° from normal with respect to the incoming beam. A powder sample was pressed into freshly scraped indium foil in order to minimize background contributions from oxygen during the measurements. The measured spectra were calibrated with reference spectra from well-characterized samples. The N K-edge spectra were calibrated using hexagonal BN, using the peaks near the band gap with assigned values 392.6 eV for XES and 394.4 eV for XANES, respectively. The O K-edge spectra were calibrated with BGO ($Bi_4Ge_3O_{12}$) with peak

values near to the band gap assigned as 526.4 eV and 532.7 eV for XES and XANES spectra, respectively. The ab initio density functional theory (DFT) calculations employed the commercially available WIEN2k DFT software.[66] This code uses Kohn–Sham methodology with spherical wave functions to model core orbitals, linearized augmented plane waves (LAPW), semi-core, and valence states.[67,68] The exchange interactions used were the generalized gradient approximation (GGA) of Perdew–Burke–Ernzerhof[69] and the modified Becke–Johnson potential within GGA (mBJ-GGA).[54] We note that this approximation is known to strongly underestimate the band gap, but can provide good agreement with the shape of the valence and conduction bands and therefore the measured soft X-ray spectra. The proper simulation of the XES and XANES measurements requires that one considers the final state of the system during the measurement. The final state of the XES measurement can be approximated as the ground state of the system; all of the core electrons are present. The simulation of this measurement requires no modification of the system. The final state after a XANES measurement included a missing core electron. The effects from this core hole were modelled in the current work by including a single core hole inside of a supercell. This supercell was a larger cell made by replicating the unit cell along its common axes approximating the core hole density that is seen in experimental measurements.

The only input to the calculation was the crystal structure as determined by X-ray diffraction. The ground-state calculations were carried out on the unit cell with a 1000 k-point mesh. The sphere sizes used to define the core electrons were 2.400, 1.800, 1.4810, and 1.1590 Bohr for Ba, Si, N, and O, respectively, and the energy cut off was set to −6.0 Ryd. The size of the supercell used was $2\times1\times1$ of the unit cell (46 atoms) with a 100 k-point mesh. Normally a larger supercell would be used, but due the large interstitial space between the Ba ations and the N or O anions extensive memory resources ($\approx$ 6 GB memory per k-point) was required for the plane wave expansion, and so the size of the supercell had to be limited in order to achieve convergence in a reasonable time frame without limiting the plane wave basis size.

The simulated spectra were broadened to facilitate comparison with the experiments. A combination of Lorentzian and Gaussian functions was used to emulate the core-hole lifetime broadening[70] ($\Delta E=0.10$ eV for oxygen and $\Delta E=0.09$ eV for nitrogen), final-state lifetime broadening[71] (this is variable broadening and scales with the energy squared from the central point being the conduction band edge) with a scaling factor of 0.30 for N and 0.20 for O, instrumental broadening with a scaling factor of 0.30 for N and 0.20 for O, and instrumental broadening (this is resolution of the beamline and spectrometer) with a FWHM of 0.40 at 400 eV and 0.40 at 520 eV for the spectrometer, respectively, and 0.80 at 400 eV and 0.80 at 520 eV for the monochromator, respectively.

The band-gap determination used a combination of experimentally measured and calculated results. There were three key considerations this study used when determining the band gap. 1) The VB and CB edge locations were determined by using the second derivative, which has been previously successful.[55] 2) The site splitting, which occurs because of non-equivalent core electron binding energy in non-equivalent sites was determined from DFT results. 3) The XANES measurements were strongly affected by the core hole present in the final state; again DFT calculations provide an estimate in the shift of the CB that is caused by the core hole. These three effects were added numerically to the initially determined band gap and provide a reliable estimate of the actual band gap.

Acknowledgements

The authors gratefully acknowledge financial support from the Fonds der Chemischen Industrie and the Deutsche Forschungsgemeinschaft (priority program SPP 1236, project SCHN 377/13), Germany. We further would like to thank Anke Großer (LMU München) for experimental help, Christian Lathe (Geoforschungszentrum Potsdam) for his help at the Beamline F2.1 of the Hamburger Synchrotronstrahlungslabor at the Deutsches Elektronen Synchrotron (DESY) and for the provided beamtime, Christian Minke (LMU München) for the EDX measurements and Thomas Miller and Dr. Peter Mayer (LMU München) for X-ray single-crystal data collection. Furthermore, we gratefully acknowledge the Natural Sciences and Engineering Research Council of Canada (NSERC) and the Canada Research Chair program for their support in this research. We also thank the Advanced Light Source and Canadian Light Source along with their staff and support for helping us conduct this research.

[1] H. Lange, G. Wötting, G. Winter, *Angew. Chem.* **1991**, *103*, 1606–1625; *Angew. Chem. Int. Ed. Engl.* **1991**, *30*, 1579–1597.
[2] A. Zerr, G. Miehe, G. Serghiou, M. Schwarz, E. Kroke, R. Riedel, H. Fueß, P. Kroll, R. Boehler, *Nature* **1999**, *400*, 340–342.
[3] M. Schwarz, G. Miehe, A. Zerr, E. Kroke, B. T. Poe, H. Fuess, R. Riedel, *Adv. Mater.* **2000**, *12*, 883–887.
[4] W. Schnick, *Int. J. Inorg. Mater.* **2001**, *3*, 1267–1272.
[5] R.-J. Xie, N. Hirosaki, T. Suehiro, F.-F. Xu, M. Mitomo, *Chem. Mater.* **2006**, *18*, 5578—5583.
[6] M. Zeuner, P. J. Schmidt, W. Schnick, *Chem. Mater.* **2009**, *21*, 2467–2473.
[7] M. Zeuner, F. Hintze, W. Schnick, *Chem. Mater.* **2009**, *21*, 336–342.
[8] H. Huppertz, W. Schnick, *Acta Crystallogr. Sect. C* **1997**, *53*, 1751–1753.
[9] H. A. Höppe, H. Trill, B. D. Mosel, H. Eckert, G. Kotzyba, R. Pöttgen, W. Schnick, *J. Phys. Chem. Solids* **2002**, *63*, 853–859.
[10] S. Hampshire in *Materials Science and Technology, Vol. 11* (Eds.: R. W. Cahn, P. Haasen, E. J. Kramer), Wiley-VCH, Weinheim, **1994**.
[11] L.-O. Nordberg, M. Nygren, P.-O. Käll, Z. Shen, *J. Am. Ceram. Soc.* **1998**, *81*, 1461–1470.
[12] R. Mueller-Mach, G. Mueller, M. R. Krames, H. A. Höppe, F. Stadler, W. Schnick, T. Juestel, P. Schmidt, *Phys. Status Solidi A* **2005**, *202*, 1727–1732.
[13] T. Jüstel, H. Nikol, C. Ronda, *Angew. Chem.* **1999**, *111*, 3250–3271; *Angew. Chem. Int. Ed.* **1998**, *37*, 3084–3103.
[14] C. Ronda, *Luminescence: From Theory to Applications*, Wiley-VCH, Weinheim, **2008**.
[15] W. Schnick, *Phys. Status Solidi RRL* **2009**, *3*, A113–A114.
[16] R. Mueller-Mach, G. O. Mueller, M. R. Krames, O. B. Shchekin, P. J. Schmidt, H. Bechtel, C.-H. Chen, and O. Steigelmann, *Phys. Status Solidi RRL* **2009**, *3*, 215–217.
[17] T. Schlieper, W. Schnick, *Z. Anorg. Allg. Chem.* **1995**, *621*, 1037–1041.
[18] T. Schlieper, W. Milius, W. Schnick, *Z. Anorg. Allg. Chem.* **1995**, *621*, 1380–1384.
[19] H. A. Höppe, H. Lutz, P. Morys, W. Schnick, A. Seilmeier, *J. Phys. Chem. Solids* **2000**, *61*, 2001–2006.
[20] H. A. Höppe, F. Stadler, O. Oeckler, W. Schnick, *Angew. Chem.* **2004**, *116*, 5656–5659; *Angew. Chem. Int. Ed.* **2004**, *43*, 5540–5542.
[21] O. Oeckler, F. Stadler, T. Rosenthal, W. Schnick, *Solid State Sci.* **2007**, *9*, 205–212.
[22] F. Stadler, O. Oeckler, H. A. Höppe, M. H. Möller, R. Pöttgen, B. D. Mosel, P. Schmidt, V. Duppel, A. Simon, W. Schnick, *Chem. Eur. J.* **2006**, *12*, 6984–6990.
[23] J. A. Kechele, O. Oeckler, F. Stadler, W. Schnick, *Solid State Sci.* **2009**, *11*, 537–543.
[24] V. Bachmann, C. Ronda, O. Oeckler, W. Schnick, A. Meijerink, *Chem. Mater.* **2009**, *21*, 316–325.
[25] a) C.-C. Yang, C.-M. Lin, Y.-J. Chen, Y.-T. Wu, S.-R. Chuang, R.-S. Liu, S.-F. Hu, *Appl. Phys. Lett.* **2007**, *90*, 123503–1–3; b) R.-S. Liu, Y.-H. Liu, N. C. Bagkar, S.-F. Hu, *Appl. Phys. Lett.* **2007**, *91*, 061119/1–3; c) Y. Q. Li, A. C. A. Delsing, G. de With, H. T. Hintzen, *Chem. Mater.* **2005**, *17*, 3242–3248; d) Y. Q. Li, G. de With, H. T. Hintzen, *J. Mater. Chem.* **2005**, *15*, 4492–4496; e) B.-G. Yun, Y. Miyamoto, H. Yamamoto, *J. Electrochem. Soc.* **2007**, *154*, J320–J325; f) D. Becker, T. Fiedler, W. Hempel, F. Jermann (Patra Patent Treuhand), PCT Int. Appl., WO2007096333A1, **2007**; g) B.-G. Yun, K. Machida, H. Yamamoto, *J. Ceram. Soc. Jpn.* **2007**, *115*, 619–622; h) V. Bach-

mann, T. Juestel, A. Meijerink, C. Ronda, P. J. Schmidt, *J. Lumin.* **2006**, *121*, 441–449; i) A. C. A. Delsing, H. T. Hintzen, Y.-Q. Li (Osram Opto Semiconductors GmbH), PCT Int. Appl., WO2004030109A1, **2004**; j) T. Fiedler, F. Jermann (Patra Patent Treuhand), Ger. Offen., DE 102004051395A1, **2006**; k) H. Brunner, T. Fiedler, F. Jermann, J. Strauss, M. Zachau (Patra Patent Treuhand, Osram Opto Semiconductors GmbH), PCT Int. Appl., WO2005031797A2, **2005**; l) T. Fiedler, F. Jermann (Patra Patent Treuhand), PCT. Int. Appl., WO2005030905A1, **2005**; m) H. Brunner, T. Fiedler, F. Jermann, M. Zachau, B. Braune (Osram Opto Semiconductors GmbH, Patra Patent Treuhand), PCT Int. Appl., WO2005030904A1, **2005**; n) H. Brunner, T. Fiedler, F. Jermann, M. Zachau (Patra Patent Treuhand, Osram Opto Semiconductors GmbH), PCT Int. Appl., WO 2005030903A1, **2005**.

[26] X.-H. He, N. Lian, J.-H. Sun, M.-Y. Guan, *J. Mater. Sci.* **2009**, *44*, 4763–4775.

[27] M. Mikami, H. Watanabe, K. Uheda, S. Shimooka, Y. Shimomura, T. Kurushima, N. Kijima, *IOP Conf. Ser.: Mater. Sci. Eng.* **2009**, *1*, 012002–012012.

[28] S. Nakamura, T. Mukai, M. Senoh, *Appl. Phys. Lett.* **1994**, *64*, 1687–1689.

[29] T. Mukai, S. Nagahama, N. Iwasa, M. Senoh, T. Yamada, *J. Phys. Condens. Matter* **2001**, *13*, 7089–7098.

[30] H. A. Höppe, *Angew. Chem.* **2009**, *121*, 3626–3636; *Angew. Chem. Int. Ed.* **2009**, *48*, 3572–3582.

[31] S. Shimooka, K. Uheda, M. Mikami, N. Kijima, H. Imura, K. Horibe, PCT Int. Appl., WO088966A1, **2007**.

[32] M. Mikami, S. Shimooka, K. Uheda, H. Imura, N. Kijima, *Key Eng. Mater.* **2009**, *403*, 11–14.

[33] W. Schnick, H. Huppertz, R. Lauterbach, *J. Mater. Chem.* **1999**, *9*, 289–296.

[34] H. Huppertz, *Z. Kristallogr.* **2004**, *219*, 330–338.

[35] D. Walker, M. A. Carpenter, C. M. Hitch, *Am. Mineral.* **1990**, *75*, 1020–1028.

[36] D. Walker, *Am. Mineral.* **1991**, *76*, 1092–1100.

[37] M. C. Burla, M. Camalli, B. Carrozzini, G. L. Cascarano, C. Giacovazzo, G. Polidori, R. Spagna, *J. Appl. Crystallogr.* **2003**, *36*, 1103–1103.

[38] G. M. Sheldrick, *Acta Crystallogr. Sect. A* **2008**, *64*, 112–122.

[39] Fullprof. 2k-version 4.40, J. Rodriguez-Carvajal, **2008**.

[40] L. B. McCusker, F. Liebau, G. Engelhardt, *Pure Appl. Chem.* **2001**, *73*, 381–394.

[41] P. E. D. Morgan, *J. Mater. Sci.* **1986**, *21*, 4305–4309.

[42] F. Liebau, *Structural Chemistry of Silicates*, Springer, Berlin, **1985**.

[43] H.-J. Klein, F. Liebau, *J. Solid State Chem.* **2008**, *181*, 2412–2417.

[44] R. Hoppe, *Angew. Chem.* **1970**, *82*, 7–16; *Angew. Chem. Int. Ed. Engl.* **1970**, *9*, 25–34.

[45] a) R. Hoppe, *Angew. Chem.* **1966**, *78*, 52–63; *Angew. Chem. Int. Ed. Engl.* **1966**, *5*, 95–106; b) R. Hoppe, *Z. Naturforsch. A* **1995**, *50*, 555–567; c) C. Weiß, R. Hoppe, *Z. Anorg. Allg. Chem.* **1996**, *622*, 1019–1026.

[46] MAPLE, Madlung Part of Lattice Energy (Program), Version 4, R. Hübenthal, University of Gießen (Germany), **1993**.

[47] S. J. Sedlmaier, J. Schmedt auf der Günne, W. Schnick, *Dalton Trans.* **2009**, 4081–4084.

[48] R. Grün, *Acta Crystallogr. Sect. B* **1979**, *35*, 800–804.

[49] F. Stadler, W. Schnick, *Z. Anorg. Allg. Chem.* **2006**, *632*, 949–954.

[50] The term dreier (3er) ring was coined by Liebau and is derived from the German word "drei", which means three; however, a dreier ring is not a three-membered ring, but a six-membered ring comprising three tetrahedral centers (Si) and three electronegative atoms (N). Similar terms exist for rings comprising four, five, and six tetrahedral centers (and the corresponding number of electronegative atoms), namely vierer (4er), fünfer (5er), and sechser (6er) rings, respectively. (F. Liebau, *Structural Chemistry of Silicates*, Springer, Berlin, **1985**.).

[51] C. Braun, H. Ehrenberg, T. D. Boyko, A. Moewes, W.Schnick, unpublished results.

[52] T. L. Barry, *J. Electrochem. Soc.* **1968**, *115*, 1181–1184.

[53] P. Schmidt, A. Tuecks, J. Meyer, H. Bechtel, D. Wiechert, R. Mueller-Mach, G. Mueller, W. Schnick, Philips Research Europe Aachen (Germany); Proceedings of SPIE—The International Society for Optical Engineering **2007**, 6669 (Seventh International Conference on Solid State Lighting **2007**), 66690P/1–9.

[54] F. Tran, P. Blaha, *Phys. Rev. Lett.* **2009**, *102*, 226401.

[55] E. Z. Kurmaev, R.G Wilks, A. Moewes, L.D Finkelstein, S. Shamin, J. N. Kunes, *Phys. Rev. B* **2008**, *77*, 165127–165131.

[56] Y. N. Xu, W. Y. Ching, *Phys. Rev. B* **1995**, *51*, 17379–17389.

[57] N. Kijima, Y. Shimomura, T. Kurushima, H. Watanabe, S. Shimooka, M. Mikami, K. Uheda, *J. Light Visual Environ.* **2008**, *32*, 202–205.

[58] K. Uheda, N. Hirosaki, H. Yamamoto, *Phys. Status Solidi A* **2006**, *203*, 2712–2717.

[59] R.-J. Xie, N. Hirosaki, T. Suehiro, F.-F. Xu, M. Mitomo, *Chem. Mater.* **2006**, *18*, 5578–5583.

[60] D. C. Rubie, *Phase Transitions* **1999**, *68*, 431–451.

[61] XPREP, Version 6.12, Siemens Analytical X-ray Instruments Inc., Madison, **1996**.

[62] J. F. Berar, P. Lelann, *J. Appl. Crystallogr.* **1991**, *24*, 1–5.

[63] D. L. Decker, *J. Appl. Phys.* **1971**, *42*, 3239–3244.

[64] J. J. Jia, T. A. Callcott, J. Yurkas, A. W. Ellis, F. J. Himpsel, M. G. Samant, J. Stöhr, D. L. Ederer, J. A. Carlisle, E. A. Hudson, L. J. Terminello, D. K. Shuh, R. C. C. Perera, *Rev. Sci. Instrum.* **1995**, *66*, 1394–1397.

[65] T. Regier, J. Krochak, T. K. Sham, Y. F. Hu, J. Thompson, R. I. R. Blyth, *Nucl. Instr. Methods Phys. Res. A* **2007**, *582*, 93–95.

[66] WIEN2k An Augmented Plane Wave+Local Orbitals Program for Calculating Crystal Properties, P. Blaha, K. Schwarz, G. K. H. Madsen, D. Kvasnicka, J. Luitz, Vienna University of Technology (Austria), Revised Edition, **2008**.

[67] K. Schwarz, P. Blaha, G. Madsen, *Comput. Phys. Commun.* **2002**, *147*, 71–76.

[68] K. Schwarz, P. Blaha, *Comput. Mater. Sci.* **2003**, *28*, 259–273.

[69] J. Perdew, K. Burke, M. Ernzerhof, *Phys. Rev. Lett.* **1996**, *77*, 3865–3868.

[70] M. O. Krause, J. H. Oliver, *J. Phys. Chem. Ref. Data* **1979**, *8*, 329–338.

[71] D. A. Goodings, R. Harris, *J. Phys. Pt. Sol. Stat. Phys. C* **1969**, *2*, 1808–1816.

[72] H. A. Höppe, Dissertation, Universität München (Germany), **2003**.

Received: March 15, 2010
Published online: July 28, 2010

THE JOURNAL OF PHYSICAL CHEMISTRY C

Article

pubs.acs.org/JPCC

Electronic Band Gap Reduction in Manganese Carbodiimide: MnNCN

Teak D. Boyko,[†] Robert J. Green,[†] Richard Dronskowski,[‡] and Alexander Moewes*,[†]

[†]Department of Physics and Engineering Physics, University of Saskatchewan, 116 Science Place, Saskatoon, Saskatchewan, S7N 5E2, Canada

[‡]Institute of Inorganic Chemistry, RWTH Aachen University, Landoltweg 1, D-52056 Aachen, Germany

Supporting Information

ABSTRACT: The newly synthesized manganese carbodiimide is antiferromagnetic, green in color, and optically transparent. The electronic properties of MnNCN are relatively unstudied; determining the electronic band gap and understanding the effects of the $O^{2-} \rightarrow NCN^{2-}$ substitution is extremely important to use this material for practical applications. We present high-resolution measurements of the local density of electronic states of MnNCN and compare them to spectra simulated using detailed density functional theory calculations. We further show that MnNCN has a larger degree of covalent bonding than MnO and has a reduced indirect electronic band gap of 3.40 ± 0.20 eV of the charge-transfer type. However, the mechanism for this band gap reduction is not clear and requires further study. In conclusion, MnNCN is a wide band gap, antiferromagnetic semiconductor suitable for applications that currently use MnO but require a smaller electronic band gap.

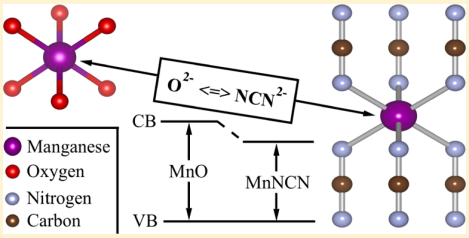

INTRODUCTION

Manganese oxide (MnO) is an antiferromagnetic semiconductor whose electronic[1−3] and magnetic properties[2,4−6] have been thoroughly studied. While applications using MnO do not typically exploit its electronic properties, recently, it has been shown that MnO may be a candidate material for photovoltaic applications if one can mitigate the electron or hole transport issues.[7] Furthermore, the magnetic properties of MnO nanoparticles allow for possible spintronic applications.[5] The recent report of the successful synthesis of manganese carbodiimide (MnNCN),[8] also an antiferromagnetic semiconductor,[9] followed by the discovery of a new MnO structure[3] continues to motivate the study of the electronic properties of Mn^{2+} compounds.

The structure of MnNCN is similar to MnO in that the Mn atoms (and the anions) are both octahedrally coordinated but differ from MnO in that the substitution of $O^{2-} \rightarrow NCN^{2-}$ rearranges the structure to have a rhombohedral distortion from the rock-salt structure of MnO. However, it is well-known that MnO undergoes a rhombohedral distortion during an antiferromagnetic transition[10] at low temperatures. As such, studying the electronic properties of MnNCN is useful not only to understand the behavior of MnNCN but also to elucidate the effect the rhombohedral distortion has on the electronic structure of MnO by comparing the electronic structure of MnO with MnNCN at room temperature.

The magnetic properties of MnNCN and MnO are very similar, as both are antiferromagnetic semiconductors. Nonetheless, the Néel temperature of MnO (118(2) K[11]) is quite a bit higher than MnNCN (28 K[8]). The magnetic arrangement in MnNCN is also very similar to MnO,[9] but the Mn−Mn interaction distance is much larger than in MnO. MnNCN shows strong magnetic coupling, but with a lower Néel temperature suggesting that MnNCN may be useful for applications that use MnO for its magnetic properties. On the other hand, the electronic properties of MnNCN remain relatively unstudied, apart from a published UV absorption spectrum including semiempirical many-body calculations,[12] which show that the Mn−N bonds are slightly more covalent with a reduced π interaction. With no detailed electronic structure (band gap or density of states) calculations or measurements, understanding the electronic properties and determining the electronic band gap of MnNCN is extremely important and may allow for an increase in the performance of devices already using MnO that require a different electronic band gap. While typically the electronic band gap can be probed with UV absorption, the spectrum is full of d−d transitions,[12] making the band gap absorption peak choice ambiguous, and all that is known is that MnNCN should be a wide band gap semiconductor since it is optically transparent.

In this work, we determine the electronic band gap by probing the valence band (VB) and conduction band (CB) independently, therefore determining the band gap indirectly. Furthermore, we show that the electronic structure of the Mn atoms in MnNCN is similar to those in MnO, apart from the increase in covalency, confirming the results of an earlier study.[12]

EXPERIMENTAL DETAILS

The experimental measurements in this study are used to probe the electronic structure. These include X-ray emission spec-

Received: January 3, 2013
Revised: April 5, 2013
Published: May 29, 2013

troscopy (XES), X-ray absorption near edge structure (XANES), and resonant inelastic X-ray scattering (RIXS) measurements. The XES and XANES techniques probe the occupied and unoccupied local partial density of states (LPDOS), respectively. The measurements are restricted to dipole transitions; for example, here were present the C/N Kα XES and C/N 1s XANES measurements, which use the C/N 1s electron to probe the LPDOS restricted to p-states. Further, the Mn Lα,β XES and Mn 2p XANES measurements presented probe the occupied and unoccupied Mn s/d-states, respectively. Contrarily, the RIXS measurements probe d−d transition levels and other multielectronic transitions available in the Mn atoms which provide a detailed analysis of the electronic properties of the Mn occupied states.

These described measurements were performed on powder, polycrystalline samples of MnNCN and MnO. The XES and RIXS measurements presented were performed on Beamline 8.0.1 at the Advanced Light Source (Berkeley, CA, USA),[13] while all of the XANES measurements were performed on the SGM beamline at the Canadian Light Source (Saskatoon, SK, CA).[14] Further details of these measurements are found in the Supporting Information.

The crystal structure of MnNCN has been well characterized previously.[8] Table 1 lists the crystal structure used here, which

Table 1. Crystal Structure Details Used for All DFT Calculations[a]

$R\bar{3}m$ (No. 166), a = 3.3583 Å, c = 28.6940 Å				
atom	Wyckoff Site	x/a	y/b	z/c
Mn↑	3a	0	0	0
Mn↓	3b	0	0	1/2
C	6c	0	0	1/4
$N_{Mn\uparrow}$	6c	0	0	0.29275
$N_{Mn\downarrow}$	6c	0	0	0.20725

[a]Both the fractional coordinates and lattice parameters are specified in a hexagonal coordinate system. The overall electron spin of the Mn atoms is designated by either up (↑) or down (↓), while the N atoms are designated by spin of the Mn atoms participating in the N−Mn bond.

is created using the previously measured structure combined with the measured magnetic structure.[9] The magnetic structure used here is a simplified version of that measured in ref 9, but density functional theory (DFT) calculations show that there will be a negligible difference in the calculated electronic structure of the simplified magnetic structure when compared to the electronic structure of the true magnetic structure. These results are detailed in the Supporting Information. This simplified magnetic structure is sufficient for the scope of the current study and is used as the structure for all DFT calculations.

Electronic structure calculations of transition metal oxides, including MnO, have exposed the shortcomings of conventional DFT calculations. This problem arises from correlation of the Mn d-states, whose accuracy is improved by including these correlation effects using a Hubbard potential.[15] The DFT calculations presented here use the WIEN2k (ver.11.1)[16] software package, which uses a combination of spherical harmonics and augmented planes in a Kohn−Sham relativistic full electron scheme. The calculations presented here do not use the conventional generalized gradient approximation (GGA) functional,[17] but a GGA+U (including the Coulomb repulsion) functional. We use a U_{eff} (the +U_{eff} used the SiC method[18] for the double counting correction) to minimize the number of calculations variables, with $U_{eff} = U - J$ and $J = 0$. This allows us to choose one value which reproduces the experimental results, eliminating any guessing of the value of U_{eff}. All the calculations presented here use a U_{eff} = 9.5 eV; see Supporting Information for more details. Our chosen U_{eff} is comparable to a previously published value for MnO,[19] only 0.5 eV lower.

The DFT calculations are used to simulate the XES and XANES measurements as well as the DOS. While both the simulated XES and calculated DOS use the crystal structure prescribed in Table 1, the simulated XANES spectra require a much larger structure, or supercell, to simulate the effect of the core hole that is present during the XANES measurements, and the calculation details are found in the Supporting Information. We broaden the calculated spectra according to experimental conditions to compare the calculated spectra with the measured spectra; namely, we implement experimental resolution and the inherent lifetime broadening observed in the measurements.[20] The broadening applied here uses Gaussian and Lorentzian line profiles for the instrumental and lifetime broadening, respectively. Since no analysis is made based on this broadening and it is only used to show possible agreement between the calculated and measurement spectra, the exact fwhm values used are of little importance.

The simulated RIXS spectra use the Single Impurity Anderson Model (SIAM) with full multiplet effects. This is similar to models successfully used previously to study RIXS transitions in metal oxides.[21−24] The method used to choose the model variables necessary for these calculations is detailed in the Supporting Information. Once the model variables are determined, the electronic band gaps for MnO and MnNCN are determined using the Zaanen−Sawatzky−Allen approach for charge transfer insulators.[25] This provides a complementary method of obtaining electronic band gaps compared to using either the XES and XANES spectra or DFT methods.

The electronic band gap of any material can be determined using a combination of XES and XANES measurements. The electronic band gap is taken as the separation between the XES spectrum and XANES spectrum, when they are displayed on a common energy scale. We use the second derivatives of the spectra to determine the band edges, which has been shown to unambiguously determine the band edge of a broadened experimental spectrum for a variety of materials.[20,26] There are many methods to determine the band edges in spectral data, but this method provides a reliable and objective way to determine the band edge.[27] We then need to add both the calculated core hole shift and nonequivalent site shifts to the initial value. These effects decrease the measured band gap value and are included by adding them to the measured band gap value. We use the results of the DFT calculations to estimate the value of these shifts similar to previous studies.[26] These corrections make this technique a reliable method to estimate the band gap of materials when there are no other viable methods available.

RESULTS AND DISCUSSION

The electronic structure of the Mn atoms is affected very little by the substitution of $O^{2-} \rightarrow NCN^{2-}$ in MnNCN. However, there are a few subtle differences in both the unoccupied and occupied Mn d-states that are worth noting. We begin with the unoccupied Mn d-states, which are probed using Mn 2p

dx.doi.org/10.1021/jp4000768 | J. Phys. Chem. C 2013, 117, 12754−12761

XANES measurements. The upper panel of Figure 1 shows the Mn 2p XANES, measured in total electron yield (TEY) mode,

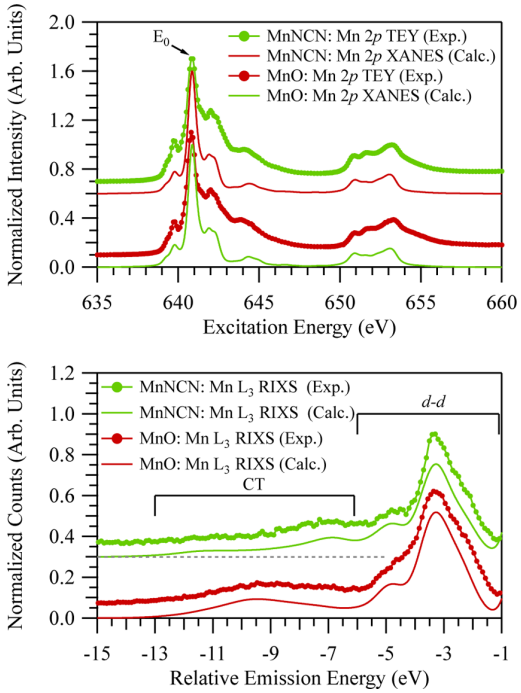

Figure 1. Experimental and calculated Mn 2p XANES (measured in TEY mode) of MnNCN and MnO. The arrow indicates the excitation energy used for the Mn L_3 RIXS measurement. The approximate energy regions for d−d and charge transfer (CT) excitations are indicated. The L_3 elastic line (not shown for clarity) is set to zero energy and corresponds to the location indicated by E_0.

of both MnNCN and MnO. As expected, both Mn 2p XANES spectra exhibit the characteristic shape of Mn^{2+} in an approximately octahedral local crystal field.[1] Since the XANES spectra are a sensitive probe of the local crystal field of the Mn ions,[1] this emphasizes the fact that the $(NCN)^{2-}$ ligands are indeed very similar to the corresponding O^{2-} ligands found in the monoxide. Where the spectra differ the most is in the regions above the L_3 and L_2 edges, at ≈644 eV and ≈654 eV, respectively. These regions are sensitive to charge transfer effects, which are analyzed further using the Mn L_3 RIXS measurements. While the Mn 2p XANES spectra are mainly sensitive to the oxidation state and crystal field symmetry, RIXS spectra can provide more detailed information on the electronic structure properties. The lower panel of Figure 1 shows the RIXS spectra measured with an excitation energy at the Mn L_3 edge maximum (indicated by an arrow in the upper panel of Figure 1), again for both MnNCN and MnO. The spectra are plotted on a relative energy scale with the excitation energy subtracted (energy loss). As expected for a correlated transition metal system, the RIXS spectra can be separated into slightly overlapping regions: the region at lower energy loss which is dominated by d−d excitations (where the final state contains an energetically higher arrangement of the 3d electrons compared to the ground state) and a region at higher energy loss containing charge transfer excitations (where the final state includes the transfer of an electron from the ligand valence band to a Mn 3d orbital). Interestingly, the d−d excitations are quite similar for the two materials (apart from slight differences due to different energy resolutions of the measurements), whereas the charge transfer (CT) excitations are significantly different. While the CT excitations of MnO are somewhat localized to a single peak separated from the d−d excitation region, the CT excitations of MnNCN are more spread out and exhibit more overlap with the d−d excitation region. The increased overlap of the CT and d−d excitations in MnNCN compared to MnO is an indication of a reduced effective charge transfer energy and is quantified with SIAM calculations.

Here, the SIAM was employed to simulate the Mn 2p XANES and Mn L_3 RIXS spectra to extract further information about the electronic structure. Figure 1 shows the calculated and experimental spectra. Good agreement with the experiment is obtained for all spectra, and the variations in the CT excitations between the oxide and carbodiimide are well captured by the theory. It is important to note that the powder nature of the samples leads to surface effects that broaden the TEY spectra somewhat compared to that which would be measured for a thin film or cleaved single crystal.[28] This is due to the surface sensitivity of the TEY method employed to measure the XANES, which probes approximately the top 3−5 nm of the samples.[21] However, it is nonetheless clear that the MnNCN spectra are very similar to that of MnO, for both the measured and calculated spectra. For these calculations, we used ab intio values of the Slater integrals (SI), the hopping integrals (V), and the ionic crystal field splitting (10Dq) similar to those previously calculated for MnO.[28] The difference between the onsite Coulomb interaction (U_{dd}) and the core hole potential acting on 3d electrons, Q, was fixed to the typical value of −1 eV used for transition metal compounds[21] (variations in this value were tested, and −1 eV proved optimal, as expected). The experimental ligand valence bandwidths (W) and shapes obtained from the Kα XES of the anions were used in the model and were thus fixed. Finally, the only free calculation variable used to fit the spectra was the charge transfer energy, Δ, which was expected to vary between the oxide and the carbodiimide due to differences in ligand electronegativity. Table 2 shows the final calculation variable

Table 2. Values of the Parameters Used for the SIAM Calculations of RIXS Spectra[a]

#	[b]SI	[c]V_{e_g} (eV)	[c]$V_{t_{2g}}$ (eV)	[d]$U-Q$ (eV)	[e]Δ (eV)	[f]W (eV)
(1)	75/85	1.70	0.95	−1.0	3.82	8.0
(2)	75/85	1.70	0.95	−1.0	4.32	6.0

[a]The Slater integrals of (1) MnNCN and (2) MnO are given as percentages of Hartree−Fock single ion values used for the initial and core-hole configurations, respectively. The following parameters are integral for the RIXS calculations presented here. [b]Slater integrals. [c]Hopping integrals. [d]Coulomb interaction and core hole potential. [e]Charge transfer energy. [f]Ligand valence bandwidth. Further, a 10Dq value of 0.65 eV is used for both MnO and MnNCN.

values. The charge transfer energies are given as the difference between the lowest $3d^5$ multiplet and the lowest $3d^6\underline{L}$ multiplet in the initial state before the inclusion of hybridization ($\underline{L}$ denotes a hole in the ligand band). Note that this is not the same as the difference between the configuration averaged energies, which is often given,[21−24] but it is more meaningful in this case where variations in ligand band shapes and widths are

dx.doi.org/10.1021/jp4000768 | J. Phys. Chem. C 2013, 117, 12754−12761

considered. For correlated 3d transition metal compounds, it is well-known that large Coulomb repulsion energies and charge transfer energies can lead to insulating gaps of either the Mott–Hubbard or charge transfer type, depending on the relative energy values involved.[25] In this approach, the SIAM can provide information about the nature of the electronic band gaps for MnNCN and MnO and their relative magnitudes. With the values for the variables used in SIAM calculations determined as described above, the electronic band gaps calculated using the standard approach[25] are 3.2 and 3.8 eV for MnNCN and MnO, respectively. These are in close agreement with values obtained from other methods (shown for MnNCN in this work and found previously for MnO[29]).

Turning now to the electronic structure of the carbodiimide groups in the MnNCN lattice, we examine the bonding and determine the electronic band gap using the p-states of the N and C atoms. While the measurements of the electronic structure of the Mn atoms are very elucidating to the effect of replacing $O^{2-} \rightarrow NCN^{2-}$ and estimating the charge-transfer band gap, the measurements of the C and N atoms are a better probe of the PDOS with minimal multielectronic effects. As such, these measurements are simulated well using conventional DFT methods. Figures 2 and 3 show both the measured and calculated C/N Kα XES and C/N 1s XANES spectra, which probe the occupied and unoccupied C/N p-states,

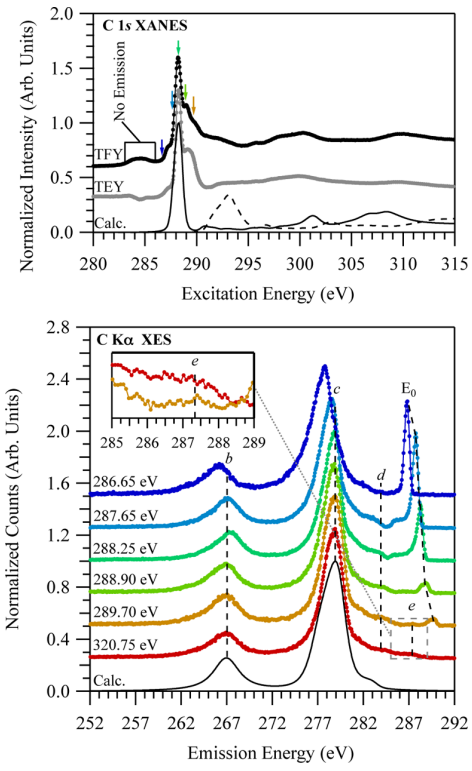

Figure 2. Measured C 1s XANES and C Kα XES spectra are compared to the corresponding calculated spectra. The features of interest are labeled with italicized letters and a vertical dashed line. The excitation peak is labeled with E_0 when visible. The corresponding excitation energy of the resonant C Kα XES spectra is displayed to the left of the spectrum. The arrows above the C 1s XANES indicate the locations of the resonant C Kα XES excitations. The inset panel shows a close-up of feature e', specified by the gray dashed box.

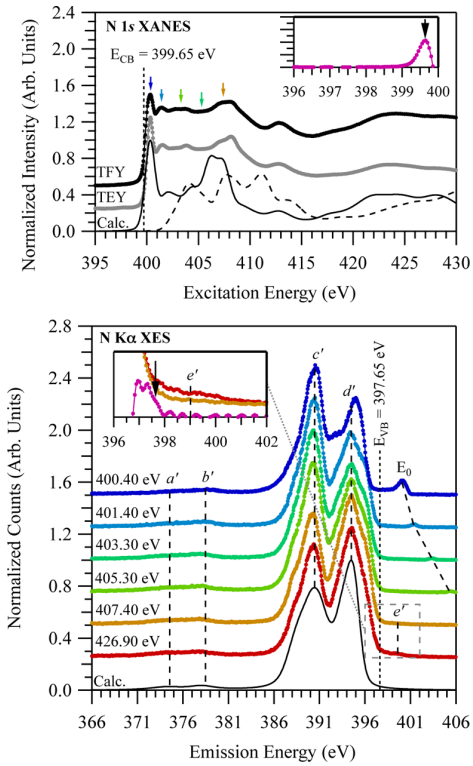

Figure 3. Measured N 1s XANES and N Kα XES spectra are compared to the corresponding calculated spectra. The features of interest are labeled with italicized letters and a vertical dashed line. The excitation peak is labeled with E_0 when visible. The labels with $'$ attached correspond to the labels in Figure 2 and indicate bonding. The corresponding excitation energy of the resonant N Kα XES spectra is displayed to the left of the spectrum. The arrows above the N 1s XANES indicate the locations of the resonant N Kα XES excitations. The inset panel shows a close-up of feature e', specified by the gray dashed box as well as the second derivative of the measured spectra. The spectra were smoothed with a binomial expansion smoothing algorithm before taking the second derivative, and the VB and CB locations are further indicated with an arrow in the inset panel and vertical dashed line in the main panel.

respectively. One observes that, for the most part, all the calculated spectra agree with the measured spectra. The minor disagreement of the XANES spectra observed in the regions 404–408 eV and 289–295 eV can be attributed to the computational limitations imposed when trying to isolate the core hole. The crystal structure of MnNCN is quite complex. Modeling XANES in a sufficiently large supercell to isolate the core hole simulating the experimental conditions is not feasible in a reasonable period, and likely the effect of the core hole is exaggerated somewhat. It is, however, clear that the calculations do represent the electronic structure of MnNCN based on the agreement of the XES and the features in the XANES outside this region of disagreement. Further, the origin of features e' and e in Figures 2 and 3, both not represented in the calculation, is somewhat unknown but likely due to a contamination of other carbonitrides or hydrolyzed MnNCN. When the excitation energy is tuned to a maximum in the XANES spectra, these features disappear due to the preferential excitation of the N 1s and C 1s electrons belonging to MnNCN. The inelastic features present directly lower in energy from the elastic peak E_0 are not directly related to the electronic

dx.doi.org/10.1021/jp4000768 | J. Phys. Chem. C 2013, 117, 12754–12761

structure of the material. These low energy shoulders are quite common for C Kα measurements, and little conclusions can be drawn from their appearance; as such, they should be disregarded from the present discussion.

All the measured occupied p states can be broken down into four regions: (a/a') the lower semicore (SC) states, (b/b') the upper SC states, (c/c') the lower VB, and (d/d') the upper VB. Figures 2 and 3 are appropriately labeled in this way with $'$ corresponding to same bands in N p-states as the C p-states. From this we observe that the lower SC states are composed of only N p-states, while the upper SC states have both N p-states and C p-states indicating possible bonding. Much like the SC states, the VB is split into an upper and lower portion. The lower VB contains both a significant amount of N p-states and C p-states suggesting even more C−N bonding. Conversely, the upper VB is composed of solely N p-states, with little C p-states. So far, the contribution of Mn d-states in the VB has not been discussed, but the measurement of the occupied Mn d-states spectrum compared to the simulated occupied Mn d-states spectrum and its successful reproduction suggests that the calculated DOS for the Mn d-states are sufficient to discuss the composition of the VB (see Supporting Information). While comparing the relative position and intensity of the features in the C/N p-state measurements does elucidate the location of the C/N p-states in the VB and SC states, detailed PDOS calculations can provide much more information. The conclusions drawn from the analysis of the electronic structure calculations are supported by the fact that the simulated spectra agree with the measured spectra.

The PDOS of MnNCN allow a more detailed analysis of the electronic structure measurements and suggest the lower VB is composed of mainly Mn d-states. Figure 4 shows the PDOS of MnNCN elucidating the correct distribution of states present in the overall electronic structure of MnNCN. One sees that N p-states are present in the lower SC states, but there is also a significant amount of N s-states. The same can also be said for the upper SC states, and in addition there are C p-states. Also, the lower SC states contain a significant amount of C s-states. Turning now to the VB we see that the lower VB is made up of mostly Mn d-states with a small amount of N p-states and C p-states. The upper VB is made up of equal amounts of Mn d-states and N p-states with virtually no C p-states. The electronic structure suggests that the C atoms in MnNCN have no direct interaction with the Mn atoms, and the interaction is mediated through the N atoms. This is apparent in the PDOS, namely, the splitting of the SC states into two groups and the splitting of the VB into two groups. This idea of the interaction between the C atoms and Mn atoms (or the interaction between Mn^{2+} and NCN^{2-}) mediated by the N atoms may have important implications leading to a change in the electronic band gap. Since examining the PDOS in energy space does not clearly define bonding, the electron density in real space of the specific band regions helps define what type of bonding is occurring in each band region.

The electron density plots show the charge overlap of specific electron band energy regions and confirm the idea of a two-component system, at least concerning the electronic structure. Figure 5 shows the electron density map (in 2-D) of MnNCN and is extracted by integrating the total charge within the four regions: upper VB, lower VB, upper SC, and lower SC bands. Careful examination of the spatial distribution, namely, the overlap with neighboring atoms and the general shape, elucidates the nature of the bonding in the respective bands.

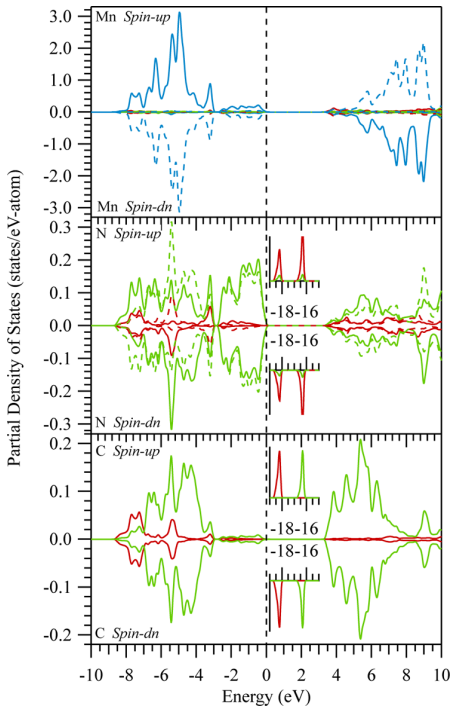

Figure 4. Partial density of states (PDOS) for MnNCN. The s-states, p-states, and d-states are displayed in red, green, and blue, respectively. The first nonequivalent site is displayed as solid and the second as dashed. The inset panels for the N and C PDOS show the semicore states bound by ≈17 eV. The dashed line indicates the top of the occupied state and is set to zero energy (0 eV). The PDOS are broadened using a 0.1 eV Gaussian to aid in visualization.

There are four observations that are readily apparent when continuing the discussion pertaining to the PDOS and bonding. First, the upper VB has very weak covalent bonding and originates mostly from nonbonding N p-states and Mn d-states. Second, the lower VB shows extreme covalent bonding between the N−C and weak covalent Mn−N bonding. Interestingly, the electrons around the Mn atoms in the lower VB seem to be very delocalized. Third, the highest energy semicore band is clearly C p-states hybridized with N s-states. Forth, the lowest energy SC band is composed of N s-states hybridized with C s-states. In conclusion, we have very strong covalent C−N bonding in the lower VB, with somewhat weaker Mn−N bonding in the lower and upper VB. The significant amount of nonbonding N p-states is reminiscent of a group IV nitride system. Furthermore, the two groups of SC states also suggest the upper SC states are C p−N s bonding, but the lower SC states are split due to different bonding occurring, both N−Mn and N−C. Interestingly, the RIXS calculations suggest that the electronic structures of the Mn atoms are similar in both MnNCN and MnO, but MnNCN should have a reduced band gap that could be due to the increase in covalent bonding or possibly the interaction between the carbodiimide anions and the Mn cations.

Lastly, we determine the electronic band gap using measurements of the occupied and unoccupied N p-states. Since the calculated PDOS show that there are little to no C p-states in the upper VB, it makes sense to use the nonresonant N Kα XES spectrum to determine the valence band edge. Conversely, both the C 1s XANES and N 1s XANES can be

dx.doi.org/10.1021/jp4000768 | J. Phys. Chem. C 2013, 117, 12754−12761

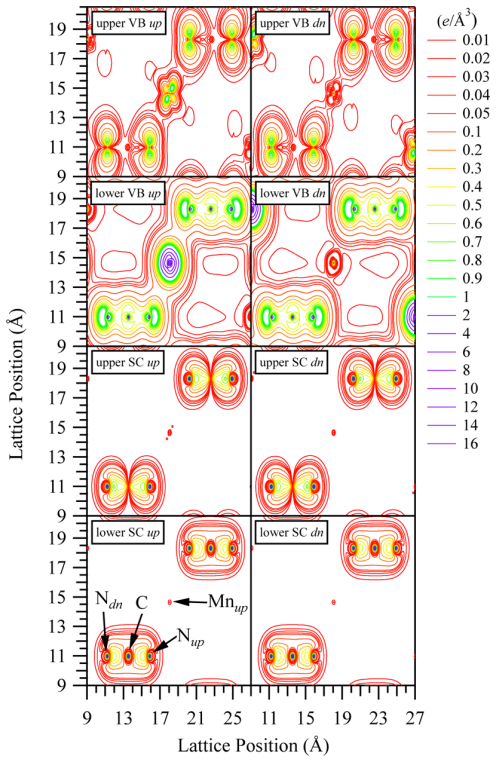

Figure 5. Electron density plot of a plane cutting the crystal with axes in 1,1,1, and 2,−1,−1. The scale is about the crystal axes origin, and the plane cuts through the plane made by the N−Mn−N bonds. We assume that cutting any of the planes though the Mn octahedron will produce the same electron density since the bonding is symmetric. The center of the atoms for all panels is labeled in the bottom left panel.

used to determine the CB edge (with core hole effect), but since we are using the nonresonant N Kα XES spectrum, we must use the N 1s XANES spectrum. Figure 3 shows the second derivative of the spectra and indicates the positions chosen for the VB and CB edges. The position chosen for the VB edge must be done very carefully, and selecting the shoulder instead of the peak is important for this material. The band structure in the supporting material shows that the top of the VB has a very small amount of the states near the Fermi level, ≈0.3 eV higher in energy than the majority of the VB. This small amount of states is why the shoulder is selected. Note that these states are not apparent in the PDOS presented here because they have been broadened for visual clarity.

From this analysis of the band edges we obtain the band gap value, 2.00 ± 0.20 eV, but we must add the calculated core hole shift—1.40 eV—to arrive at the final value of 3.40 ± 0.20 eV. The errors attached to the electronic band gap values are derived from estimating the likely error in the method due to systematic errors and not fundamental errors that could arise from incorrect core hole shift values or material contamination of the experimental measurements, as these errors can not be estimated. The total error in the electronic band gap values is the sum of the uncertainty in calibrating the spectra (0.10 eV for each measurement) and the uncertainty due to the experimental precision of the data (0.05 eV for each measurement) giving a combined error of 0.20 eV as the likely possible error.

The electronic band gap value agrees with the value obtained with SIAM RIXS calculations within experimental error. We also have two electronic band gap values obtained from the DFT calculations, one from the GGA+U_{eff} calculation and another from a special calculation using a relatively new functional, MBJLDA.[30] These values are 2.89 and 3.36 eV for MBJLDA and GGA+U_{eff}, respectively. The latter value agrees with the measured value using XES/XANES measurements, but the former value is slightly too small. This is not surprising and supports the measured band gap value since we expect this value to be underestimated for Mn^{2+} compounds.[30] Additionally, the type of band gap transition, either direct or indirect, can be determined from the band structure and is found to be indirect for MnNCN based on the DFT calculations presented here. Experimentally, this is confirmed with the C Kα and N Kα measurements. In both the C Kα XES and N Kα XES spectra, we observe a shift to lower energy when the excitation energy is tuned near the conduction band edge. This shift indicates an indirect band gap[31] and agrees with the DFT calculations. Additionally, the shape of the states near the edge changes (feature d'). This is inline with the indirect band gap nature of the material. We expect the shape of the edge to change as we begin to probe momentum conserved transitions, and the XES spectra are no longer averaged over all crystal momenta. One should note that the positions of features b−d do change slightly throughout the resonant excitation, but this is not surprising considering the indirect band gap this material exhibits. Finally, MnNCN has an indirect band gap of 3.40 ± 0.20 eV of the charge transfer type, and the value agrees with both calculated electronic band gap values using DFT+U_{eff} (3.36 eV) and SIAM (3.2 eV).

CONCLUSION

In this study we show that MnNCN has electronic properties similar to the corresponding binary oxide but with a decreased electronic band gap and increased covalent bonding. The measured electronic band gap is determined to be 3.40 ± 0.20 eV using a combination of XES and XANES spectra. Moreover, the calculated electronic band gaps of MnNCN are 3.36 and 3.20 eV using DFT+U_{eff} and SIAM calculations, respectively, in good agreement with the measured band gap. The electronic band gap of MnNCN is reduced compared to MnO, but the mechanism responsible for this reduction is not clear and could possibly stem from either the increased covalency or the interaction with the NCN^{2-} groups. For example, with the latter, if the inherent electronic band gap of NCN^{2-} is ≈3 eV and Mn^{2+} is ≈4 eV, then the interaction forces the band gap to be reduced to some median value due to the covalent bonding. The mechanism of the band gap reduction may become clear if one studies FeNCN, CoNCN, and NiNCN to see if the electronic band gap is reduced in all cases compared to their respective oxides.

ASSOCIATED CONTENT

Supporting Information

The supporting information includes the experimental and theoretical details required to reproduce the results presented above. This information includes calibration for the experimental spectra and input values for the theoretical calculations. Further, the Supporting Information shows the comparison of the simulated (at different U_{eff} values) and measured X-ray emission spectra as well as the comparison of the total density of states of the full magnetic structure and simplified magnetic

dx.doi.org/10.1021/jp4000768 | J. Phys. Chem. C 2013, 117, 12754−12761

structure. The contents of the Supporting Information itself do not provide any scientific impact but only justify the theoretical choices used in this study. This material is available free of charge via the Internet at http://pubs.acs.org.

AUTHOR INFORMATION

Corresponding Author

*E-mail: alex.moewes@usask.ca.

Notes

The authors declare no competing financial interest.

ACKNOWLEDGMENTS

The Natural Sciences and Engineering Research Council of Canada (NSERC) and the Canada Research Chair Program supported this work. We gratefully acknowledge the assistance from the staff of the Advanced Light Source at Lawrence Berkeley National Laboratory and the Canadian Light Source. Research described in this paper was performed at the Canadian Light Source, which is supported by the Natural Sciences and Engineering Research Council of Canada, the National Research Council Canada, the Canadian Institutes of Health Research, the Province of Saskatchewan, Western Economic Diversification Canada, and the University of Saskatchewan. The Advanced Light Source is supported by the Director, Office of Science, Office of Basic Energy Sciences, of the U.S. Department of Energy under Contract No. DE-AC02-05CH11231. This research has been enabled by the use of computing resources provided by WestGrid and Compute/Calcul Canada. We would also like to thank Dr. Xiaohui Liu (RWTH Aachen) for having synthesized pure MnNCN samples and Deutsche Forschungsgemeinschaft (DFG) for financial support.

REFERENCES

(1) Cramer, S.; et al. Ligand Field Strengths and Oxidation States from Manganese L-Edge Spectroscopy. *J. Am. Chem. Soc.* **1991**, *113*, 7937−7940.

(2) Nayak, S.; Jena, P. Equilibrium Geometry, Stability, and Magnetic Properties of Small MnO Clusters. *J. Am. Chem. Soc.* **1999**, *121*, 644−652.

(3) Nam, K. M.; Kim, Y.-I.; Jo, Y.; Lee, S. M.; Kim, B. G.; Choi, R.; Choi, S.-I.; Song, H.; Park, J. T. New Crystal Structure: Synthesis and Characterization of Hexagonal Wurtzite MnO. *J. Am. Chem. Soc.* **2012**, *134*, 8392−8395.

(4) Lee, G.; Huh, S.; Jeong, J.; Choi, B.; Kim, S.; Ri, H. Anomalous Magnetic Properties of MnO Nanoclusters. *J. Am. Chem. Soc.* **2002**, *124*, 12094−12095.

(5) Lopez-Ortega, A.; et al. Size-Dependent Passivation Shell and Magnetic Properties in Antiferromagnetic/Ferrimagnetic Core/Shell MnO Nanoparticles. *J. Am. Chem. Soc.* **2010**, *132*, 9398−9407.

(6) Salazar-Alvarez, G.; Lidbaum, H.; Lopez-Ortega, A.; Estrader, M.; Leifer, K.; Sort, J.; Surinach, S.; Dolors Baro, M.; Nogues, J. Two-, Three-, and Four-Component Magnetic Multilayer Onion Nanoparticles Based on Iron Oxides and Manganese Oxides. *J. Am. Chem. Soc.* **2011**, *133*, 16738−16741.

(7) Peng, H.; Lany, S. Semiconducting Transition-Metal Oxides Based on d^5 Cations: Theory for MnO and Fe_2O_3. *Phys. Rev. B* **2012**, *85*, 201202.

(8) Liu, X.; Krott, M.; Müller, P.; Hu, C.; Lueken, H.; Dronskowski, R. Synthesis, Crystal Structure, and Properties of MnNCN, the First Carbodiimide of a Magnetic Transition Metal. *Inorg. Chem.* **2005**, *44*, 3001−3003.

(9) Krott, M.; Houben, A.; Müeller, P.; Schweika, W.; Dronskowski, R. Determination of the Magnetic Structure of Manganese Carbodiimide with Diffraction Experiments using Polarized Neutrons. *Phys. Rev. B* **2009**, *80*, 024117.

(10) Roth, W. L. Magnetic Structures of MnO, FeO, CoO, and NiO. *Phys. Rev.* **1958**, *110*, 1333−1341.

(11) Shaked, H.; Faber, J.; Hitterman, R. L. Low-Temperature Magnetic-Structure of MnO: A High-Resolution Neutron-Diffraction Study. *Phys. Rev. B* **1988**, *38*, 11901−11903.

(12) Liu, X.; Dronskowski, R.; Glaum, R.; Tchougréeff, A. L. Experimental and Quantum-Chemical Investigations of the UV/Vis Absorption Spectrum of Manganese Carbodiimide, MnNCN. *Z. Anorg. Allg. Chem.* **2010**, *636*, 343−348.

(13) Jia, J. J.; et al. First Experimental Results from IBM/TENN/TULANE/LLNL/LBL Undulator Beamline at the Advanced Light-Source. *Rev. Sci. Instrum.* **1995**, *66*, 1394−1397.

(14) Regier, T.; Krochak, J.; Sham, T. K.; Hu, Y. F.; Thompson, J.; Blyth, R. I. R. Performance and Capabilities of the Canadian Dragon: The SGM Beamline at the Canadian Light Source. *Nucl. Instrum. Methods Phys. Res., Sect. A* **2007**, *582*, 93−95.

(15) Franchini, C.; Podloucky, R.; Paier, J.; Marsman, M.; Kresse, G. Ground-State Properties of Multivalent Manganese Oxides: Density Functional and Hybrid Density Functional Calculations. *Phys. Rev. B* **2007**, *75*, 195128.

(16) Schwarz, K.; Blaha, P.; Madsen, G. K. H. Electronic Structure Calculations of Solids using the WIEN2k Package for Material Sciences. *Comput. Phys. Commun.* **2002**, *147*, 71−76.

(17) Perdew, J. P.; Burke, K.; Ernzerhof, M. Generalized Gradient Approximation Made Simple. *Phys. Rev. Lett.* **1996**, *77*, 3865−3868.

(18) Anisimov, V. I.; Solovyev, I. V.; Korotin, M. A.; Czyzyk, M. T.; Sawatzky, G. A. Denisty-Functional Theory and NiO Photoemission Spectra. *Phys. Rev. B* **1993**, *48*, 16929−16934.

(19) Anisimov, V. I.; Zaanen, J.; Andersen, O. K. Band Theory and Mott Insulators: Hubbard U Instead of Stoner I. *Phys. Rev. B* **1991**, *44*, 943−954.

(20) Braun, C.; Seibald, M.; Boerger, S. L.; Oeckler, O.; Boyko, T. D.; Moewes, A.; Miehe, G.; Tuecks, A.; Schnick, W. Material Properties and Structural Characterization of $M_3Si_6O_{12}N_2$:Eu^{2+} (M = Ba, Sr)-A Comprehensive Study on a Promising Green Phosphor for pc-LEDs. *Chem.−Eur. J.* **2010**, *16*, 9646−9657.

(21) De Groot, F.; Kotani, A. *Core Level Spectroscopy of Solids*; Taylor & Francis CRC Press: Boca Raton, FL, 2008.

(22) Ghiringhelli, G.; Matsubara, M.; Dallera, C.; Fracassi, F.; Gusmeroli, R.; Piazzalunga, A.; Tagliaferri, A.; Brookes, N.; Kotani, A.; Braicovich, L. NiO as a Test Case for High Resolution Resonant Inelastic Soft X-ray Scattering. *J. Phys.: Condens. Matter* **2005**, *17*, 5397−5412.

(23) Ghiringhelli, G.; Matsubara, M.; Dallera, C.; Fracassi, F.; Tagliaferri, A.; Brookes, N.; Kotani, A.; Braicovich, L. Resonant Inelastic X-ray Scattering of MnO: $L_{2,3}$ Edge Measurements and Assessment of their Interpretation. *Phys. Rev. B* **2006**, *73*, 035111.

(24) Chiuzbaian, S. G.; et al. Combining M- and L-edge Resonant Inelastic X-ray Scattering for Studies of 3d Transition Metal Compounds. *Phys. Rev. B* **2008**, *78*, 245102.

(25) Zaanen, J.; Sawatzky, G. A.; Allen, J. W. Band Gaps and Electronic Structure of Transition-Metal Compounds. *Phys. Rev. Lett.* **1985**, *55*, 418−421.

(26) Boyko, T. D.; Bailey, E.; Moewes, A.; McMillan, P. F. Class of Tunable Wide Band Gap Semiconductors: γ-$(Ge_xSi_{1-x})_3N_4$. *Phys. Rev. B* **2010**, *81*, 155207.

(27) Kurmaev, E. Z.; Wilks, R. G.; Moewes, A.; Finkelstein, L. D.; Shamin, S. N.; Kuneš, J. Oxygen X-ray Emission and Absorption Spectra as a Probe of the Electronic Structure of Strongly Correlated Oxides. *Phys. Rev. B* **2008**, *77*, 165127.

(28) Haverkort, M. W.; Zwierzycki, M.; Andersen, O. K. Multiplet Ligand-Field Theory Using Wannier Orbitals. *Phys. Rev. B* **2012**, *85*, 165113.

(29) van Elp, J.; Potze, R. H.; Eskes, H.; Berger, R.; Sawatzky, G. A. Electronic Structure of MnO. *Phys. Rev. B* **1991**, *44*, 1530−1537.

(30) Tran, F.; Blaha, P. Accurate Band Gaps of Semiconductors and Insulators with a Semilocal Exchange-Correlation Potential. *Phys. Rev. Lett.* **2009**, *102*, 226401.
(31) Eisebitt, S.; Eberhardt, W. Band Structure Information and Resonant Inelastic Soft X-ray Scattering in Broad Band Solids. *J. Electron Spectrosc. Relat. Phenom.* **2000**, *110*, 335−358.

dx.doi.org/10.1021/jp4000768 | *J. Phys. Chem. C* 2013, 117, 12754−12761

Supporting Information

Teak D. Boyko,[†] Robert J. Green,[†] Richard Dronskowski,[‡] and Alexander Moewes[*,†]

Department of Physics and Engineering Physics, University of Saskatchewan, 116 Science Place, Saskatoon, Saskatchewan, S7N 5E2, Canada, and Institute of Inorganic Chemistry, RWTH Aachen University, Landoltweg 1, D-52056 Aachen, Germany

E-mail: alex.moewes@usask.ca

The XES and RIXS measurements utilized the permanently affixed SXF end-station, which has an effective resolving power of $E/\Delta E \approx 800$ for the Mn L_3 RIXS, $E/\Delta E \approx 350$ for C Kα XES and $E/\Delta E \approx 560$ for N Kα XES. This end-station employs a Rowland circle grating spectrometer with a scattering angle of 90° to the incoming beam. Linearly polarized light is oriented within the scattering plane. The XANES measurements were measured in both Total Electron Yield (TEY) and Total Fluorescence Yield (TFY) modes, with the TFY detector being a Micro-channel Plate (MCP). These measurements also employed linearly polarized light and have a monochromator resolving power of $E/\Delta E \approx 2000$ for the C 1s and N 1s XANES measurements, while the resolving power for the Mn 2p XANES measurements is $E/\Delta E \approx 3000$. In both experiments the measurements were carried out at room-temperature and the samples were all mounted on freshly scraped indium foil to avoid oxygen and carbon contamination. Furthermore, the sample preparation was carried out in a glove bag/box under argon atmosphere as to avoid hydrolysis of MnNCN. Since relative calibration of the XES and XANES spectra, measured at different times on different beamlines, is extremely important, we use well-characterized reference compounds for energy calibration. Highly Orientated Pyrolytic Graphite (HOPG) was use to calibrate the C Kα XES and C 1s XANES spectra. The peak locations for the C Kα XES spectrum of HOPG are set to 276.75 eV and 281.30 eV, while the peak location for C 1s XANES spectrum is set to 285.40 eV. Note that for the C 1s XANES the TEY spectrum for HOPG must be used and the angle of the incident photons must be 60° from the surface normal. The calibration of the N Kα XES and N 1s XANES spectra utilized a powder sample of hexagonal boron nitride (h-BN). The peak locations are set to 392.75 eV and 394.60 eV for the XES measurement and 402.10 eV for the XANES measurement. Again in the case of the XANES calibration, the TEY spectrum of h-BN is used, but with no dependence on angle. Lastly, MnO was used to calibrate both the Mn L_3 RIXS, the Mn Lα, β XES and Mn 2p XANES measurements. The peak locations for the two peaks present in the Mn Lα, β XES spectrum are set to 638.25eV and 649.00 eV, while location of the first peak in Mn 2p XANES spectrum (measured in TEY mode) is set to 640.85 eV. These relative calibration values are important to be able to plot the XES

[*]To whom correspondence should be addressed

[†]Department of Physics and Engineering Physics, University of Saskatchewan, 116 Science Place, Saskatoon, Saskatchewan, S7N 5E2, Canada

[‡]Institute of Inorganic Chemistry, RWTH Aachen University, Landoltweg 1, D-52056 Aachen, Germany

and XANES on a common energy scale in order to determine the electronic band gap.

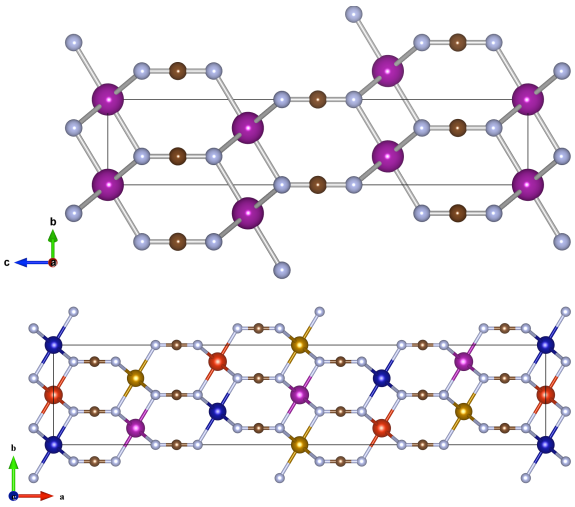

Figure S1: The crystal structure of nonmagnetic MnNCN is very simple (top) requiring only 3 nonequivalent crystals sites within the $R\bar{3}m$ (No. 166) spacegroup, but to define the proper magnetic structure (bottom) the symmetry must be broken and the number of nonequivalent sites increases to 26 within the $P2/m$ (No. 10) space group. In the nonmagnetic structure the Mn atoms are purple, C atoms brown and N atoms grey, but in the magnetic structure the Mn atoms are assigned different colors to represent those with the parallel spins. The ferromagnetic planes are in the $a-b$ and $b-c$ plane directions for the simple and full magnetic structures, respectively.

The XANES calculations used a $3 \times 3 \times 1$ supercell to adequately isolate the necessary included core hole. The DFT calculations required the selection of the muffin-tin radius of atoms n (RMT_n), energy cutoff of the core electrons (E_{cut}) and momentum k-point grid. The calculations here used the following values: RMT_{Mn} = 1.19Å RMT_N = 0.61Å RMT_C = 0.61Å E_{cut} = -6.0 Ryd, $\mathrm{R}_{k_{max}}$ = 6.0, and E_{max} = 4.5 Ryd. The k-point grids used were $10 \times 10 \times 10$ and $6 \times 6 \times 2$ for the XES and XANES calculations, respectively. The XANES calculations implemented the core hole effect by re-

Table S1: The crystal structure.

(1)	$R\bar{3}m$	(No. 166)		
Site	Wyck.	x/a	y/b	z/a
Mn	$3a$	0	0	0
C	$3b$	0	0	1/2
N	$6c$	0	0	0.58550

(2)	$P2/m$	(No. 10)		
Site	Wyck.	x/a	y/b	z/c
Mn_1	$1a$	0	0	0
Mn_2	$1e$	0	1/2	1/2
Mn_3	$1c$	1/2	0	0
Mn_4	$1h$	1/2	1/2	1/2
Mn_5	$2m$	2/3	2/3	0
Mn_6	$2n$	2/3	1/6	1/2
Mn_7	$2n$	1/6	1/6	1/2
Mn_8	$2m$	1/6	2/3	0
C_1	$2m$	1/4	0	0
C_2	$2n$	1/4	1/2	1/2
C_3	$2n$	11/12	1/6	1/2
C_4	$2n$	5/12	1/6	1/2
C_5	$2m$	11/12	2/3	0
C_6	$2m$	5/12	2/3	0
N_1	$2m$	0.29275	0	0
N_2	$2n$	0.29275	1/2	1/2
N_3	$2n$	0.95942	1/6	1/2
N_4	$2n$	0.37392	1/6	1/2
N_5	$2m$	0.95942	2/3	0
N_6	$2m$	0.37392	2/3	0
N_7	$2m$	0.20725	0	0
N_8	$2n$	0.20725	1/2	1/2
N_9	$2n$	0.87392	1/6	1/2
N_{10}	$2n$	0.45942	1/6	1/2
N_{11}	$2m$	0.87392	2/3	0
N_{12}	$2m$	0.45942	2/3	0

The structures of the nonmagnetic crystal **(1)** and the anti-ferromagnetic crystal **(2)**. The lattice constants are a = 3.3583Å, c = 14.347Å and a = 3.3583Å, c = 28.694Å for the nonmagnetic and anti-ferromagnetic crystals, respectively. Both the fractional coordinates (x/a, y/b, z/c) and lattice constants (a, b, c) are specified in a hexagonal coordinate system.

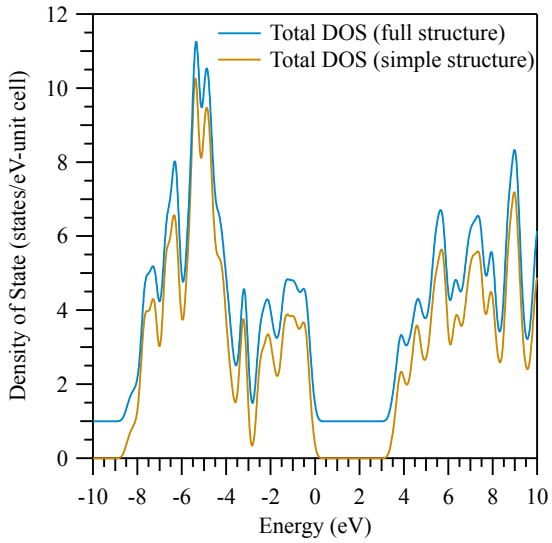

Figure S2: The total DOS pertaining to the simplified structure used in the DFT calculations compared to those of the full magnetic structure. The DOS are broadened using a 0.1 eV Gaussian and vertically offset to aid in visualization.

moving a full core electron and adding a uniform background charge of e. The XES and XANES calculations used a self-consistent field cycle with energy (ec), charge (cc) and force convergence (fc) of 0.0001 Ryd, 0.001 e and 1 mRyd/au, respectively. The XANES calculations did not use force convergence since the additional core hole introduces nonphysical forces in the system.

The SIAM calculations begin with atomic Hartree-Fock simulations of a single transition metal ion.[1] Crystal field effects are then added and hybridization with the ligand band is included by configuration interaction mixing. The code used is a modified version of that created from the efforts of Cowan, Butler, Thole, and Ogasawara.[1–3] The present calculations use the explicit shapes of the ligand band PDOS, using the approximate shape from anion XES measurements. While the XES provides the 2p-projected anion PDOS, it is still an approximation of the pure 2p band as it includes effects from hybridization with the cations. Nonethe-

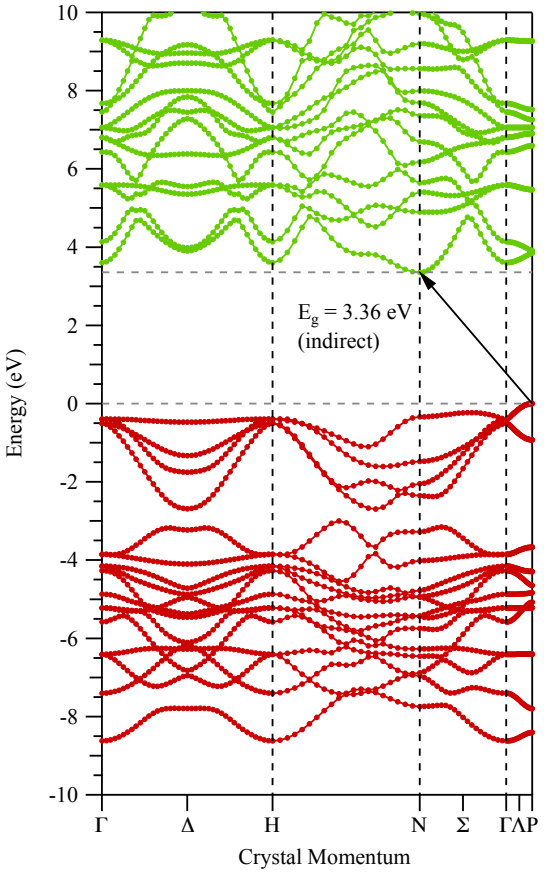

Figure S3: The calculated band structure for MnNCN as a *bcc* lattice for the Brillouin zone points. The occupied states are plotted in red, while the unoccupied states are plotted in green. The arrow indicates the smallest band gap transition and special lattice points are indicated with dashed vertical lines. The CB and VB edges are indicated with horizontal dashed lines.

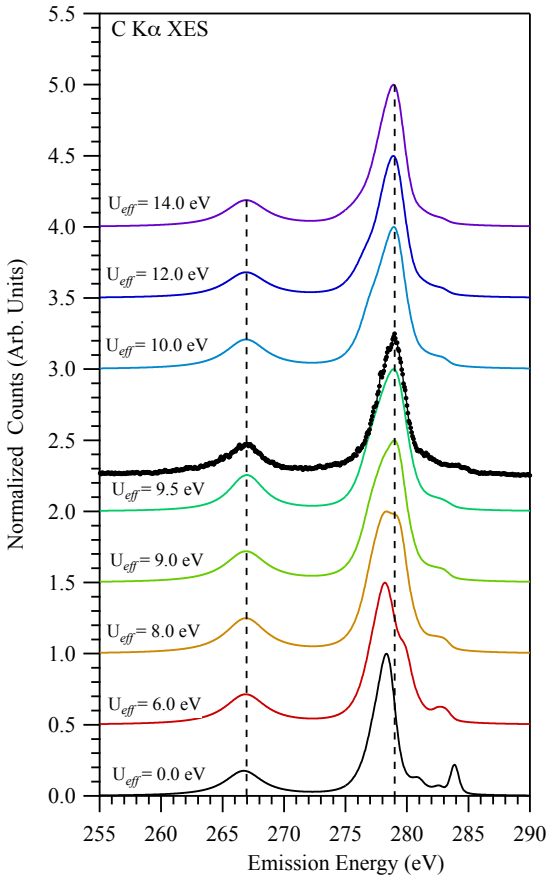

Figure S4: The experimental C Kα XES spectrum (scatter) is compared to calculated C Kα XES spectra (solid lines) with varying U_{eff} values. The vertical dashed lines indicate peaks that should be aligned, with the corresponding U_{eff} values displayed to the left of the calculated spectrum.

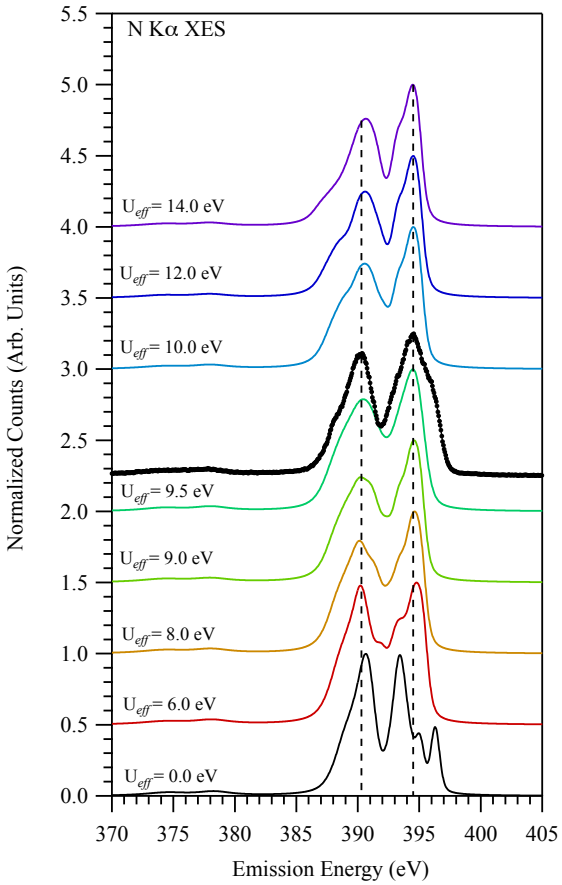

Figure S5: The experimental N Kα XES spectrum (scatter) is compared to calculated N Kα XES spectra (solid lines) with varying U_{eff} values. The vertical dashed lines indicate peaks that should be aligned, with the corresponding U_{eff} values displayed to the left of the calculated spectrum.

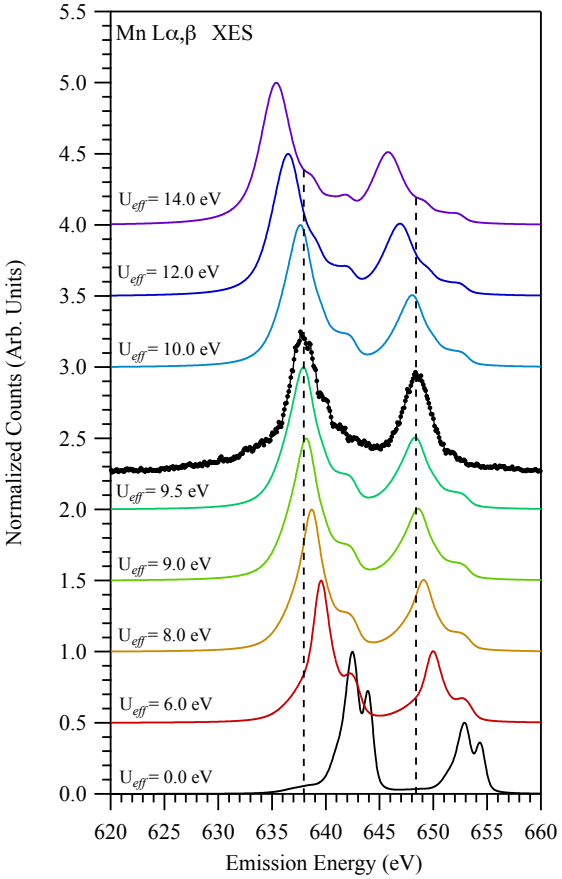

Figure S6: The experimental Mn Lα, β XES spectrum (scatter) is compared to calculated Mn Lα, β XES spectra (solid lines) with varying U_{eff} values. The vertical dashed lines indicate peaks that should be aligned, with the corresponding U_{eff} values displayed to the left of the calculated spectrum.

less, this approach proves to be more accurate than using a typical rectangular or elliptical DOS and works well for the RIXS simulations. The SIAM is a sophisticated model Hamiltonian approach and consequently employs several free variables which are typically adjusted to match experimental results.[4] However, recent progress has been made in obtaining many of the variables through *ab initio* means.[5] In particular, the values of the Slater Coulomb and exchange integrals (SI), hopping integrals (V_{e_g} and $V_{t_{2g}}$), and crystal field splitting ($10Dq$) can be computed directly from first principles and we used values very close to those previously calculated for MnO.[5] Effectively, the only variable which was freely adjusted to fit the experimental data was the charge transfer energy, Δ.

Table S1 lists both the nonmagnetic structural parameters[6] and magnetic structural parameters,[7] which are visualized in Fig. S1. The full magnetic structure is much more complex, but necessary to arrive at the proper spin of the Mn atoms. However, in this study we have found that the magnetic structure can be simplified to alternating aligned ferromagnetic planes. Fig. S2 shows the DOS from both the simplified magnetic structure and the full magnetic structure. The DOS are for all purposes identical, showing that we do not need such a complicated magnetic structure to simulate the band structure for MnNCN. However, in no way does this invalidate the measured magnetic structure.

DFT calculations using a Hubbard potential to simulate electron correlation require a non-*ab initio* variable. There are several options for choosing this variable and the possible choices are: (1) use previously published values, (2) choose a value that provides the desired band gap or (3) choose the value so that the simulated spectra match the measured spectra. The latter choice is used here, see Figs. S4 - S6. Furthermore, we use a $U_{eff} = U - J$ with $J = 0$. This reduces the number of variables to one. Since it is unlikely the calculated spectra will reproduce the measured spectra exactly, we jus-

tify our choice of U_{eff} considering the physics of the material. Varying U_{eff} of the calculated spectra affect the symmetry of the lower VB peak in both the C p-states and N p-states. From this, we chose our U_{eff} to be 9.5 eV, which provides the most symmetric lower VB in both the N p-states and C p-states. However, apparently a larger U_{eff} also accomplishes this goal, but as result the Mn d-states would be pushed out of the VB effectively removing the interaction, which is nonphysical. Consequently, the calculated Mn d-states also agree quite well with the measured spectrum confirming the necessary use of the coulomb repulsion.

References

(1) Cowan, R. *The Theory of Atomic Structure and Spectra*; University of California Press, 1981.

(2) Butler, P. *Point Group Symmetry Applications*; Plenum Press, 1981.

(3) Ogasawara, H.; Kotani, A.; Potze, R.; Sawatzky, G.; Thole, B. Praseodymium $3d$-Core and $4d$-Core Photoemission Spectra of Pr_2O_3. *Phys. Rev. B* **1991**, *44*, 5465–5469.

(4) De Groot, F.; Kotani, A. *Core Level Spectroscopy of Solids*; Taylor & Francis CRC Press, 2008.

(5) Haverkort, M. W.; Zwierzycki, M.; Andersen, O. K. Multiplet Ligand-Field Theory using Wannier Orbitals. *Phys. Rev. B* **2012**, *85*, 165113.

(6) Liu, X.; Krott, M.; Müller, P.; Hu, C.; Lueken, H.; Dronskowski, R. Synthesis, Crystal Structure, and Properties of Mn-NCN, the First Carbodiimide of a Magnetic Transition Metal. *Inorg. Chem.* **2005**, *44*, 3001–3003.

(7) Krott, M.; Houben, A.; Müeller, P.; Schweika, W.; Dronskowski, R. Determination of the Magnetic Structure of Manganese Carbodiimide with Diffraction Experiments using Polarized Neutrons. *Phys. Rev. B* **2009**, *80*, 024117.

Class of tunable wide band gap semiconductors γ-$(Ge_xSi_{1-x})_3N_4$

T. D. Boyko,[1,*] E. Bailey,[2] A. Moewes,[1] and P. F. McMillan[2]
[1]*Department of Physics and Engineering Physics, University of Saskatchewan, 116 Science Place, Saskatoon, Saskatchewan, Canada S7N 5E2*
[2]*Department of Chemistry, University College London, 20 Gordon Street, London WC1H 0AJ, United Kingdom*
(Received 18 January 2010; revised manuscript received 29 March 2010; published 16 April 2010)

The solid solutions of γ-Si_3N_4 and γ-Ge_3N_4, γ-$(Ge_xSi_{1-x})_3N_4$ with $x=0.000$, 0.178, 0.347, 0.524, 0.875, and 1.000, are studied. The band gap values of the solid solutions measured with soft x-ray spectroscopy have a range of $3.50-5.00\pm0.20$ eV. The hardness values of these solid solutions estimated using an empirical relationship have a range of 22.2–36.0 GPa. We use the generalized gradient approximation of Perdew-Ernzerhof-Burke (GGA-PDE) within density functional theory and obtained a calculated band gap value range of 2.20–3.56 eV. The simulated N absorption and emission spectra agree very well with our measurements and the compositional trend among the calculated band gap values corresponds well with the measured values. The agreement between experimental and theoretical spectra indicates that Ge prefers the site with tetrahedral bonding symmetry. The band gap and hardness estimates have two approximately linear regimes, when $0 \leq x \leq 1/3$ and $1/3 \leq x \leq 1$. The band gap decreases as Ge replaces Si on octahedral sites and this suggests that the type of cation in the octahedral sites is mainly responsible for decreasing the band gap in these spinel nitrides. Our results indicate that solid solutions of γ-$(Ge_xSi_{1-x})_3N_4$ provide a class of semiconductors with a tunable wide band gap suitable for UV laser or LED applications.

DOI: 10.1103/PhysRevB.81.155207 PACS number(s): 71.20.Nr, 78.70.Dm, 78.70.En, 71.15.Mb

I. INTRODUCTION

Silicon nitride is a ceramic semiconductor that is widely used in industry. The industrial applications of this material include gas turbine engines, diesel engines and industrial heat exchangers.[1] Silicon nitrides have many desirable mechanical and chemical properties such as high strength at high temperature, good thermal stress resistance and extreme resistance to surface oxidation. Ceramics dissociate rather than melt at high temperatures (greater than 1400 °C)[1] and typically have low thermal expansion coefficients giving them an advantage over conventional metallic alloys. Silicon nitride ceramics also have a lower mass density (40% less than conventional alloys) reducing component weight and moments of inertia.[1] These collective properties allow an increase in operating temperature, reducing the necessary cooling. This in turn increases the efficiency of devices that employ these materials. Beta silicon nitride (β-Si_3N_4) is a low-pressure hexagonal phase nitride ceramic. Gamma silicon nitride (γ-Si_3N_4) and gamma germanium nitride (γ-Ge_3N_4) are newly synthesized high-pressure spinel phase nitride ceramics.[2,3] The Si or Ge cations in these spinel materials adopt octahedral coordination presenting a unique structure that has never been seen before in binary nitride ceramics. γ-Si_3N_4 has a reduced band gap (3.6 eV) (Ref. 4) and an increased hardness (36 GPa) (Ref. 5) in comparison to β-Si_3N_4 making the hardness of γ-Si_3N_4 comparable to stishovite.[2] The increased hardness improves the quality of mechanical coatings for high temperature cutting tools[6] and the reduced band gap allows these materials to be used for optoelectronic applications including UV LEDs and lasers.[6] Studies have been carried out examining the band gap and hardness of γ-Si_3N_4 and γ-Ge_3N_4, but further characterization is necessary to allow these materials to become as widely used as their hexagonal predecessors.

The band gap is arguably one of the more important parameters when characterizing a semiconductor. The calculated band gaps of the spinel phases nitrides are reduced by as much as 33% for γ-Si_3N_4 and 10% for γ-Ge_3N_4 in comparison with their hexagonal phases nitrides (see Table I). The calculated band gap of the ternary spinel phase nitride (γ-$GeSi_2N_4$) is increased significantly (50%) from the pure germanium nitride spinel but is decreased only slightly (4%) from the pure silicon nitride spinel. The range of the theoretical band gap values is 2–4 eV and calculations suggest that the band gap of the solid solutions of these materials may be tuned in a linear fashion[2,7,8] by systematically varying the mole fraction of Ge in the final product. The band gap is also predicted to be direct in γ-Si_3N_4, γ-$GeSi_2N_4$ and γ-Ge_3N_4 allowing the possibility for optical applications in the UV regime (see Table I), such as photocatalysts used to split water.[9] The spinel nitride solid solutions are therefore excellent candidates for a new class of wide band gap semiconductors with tunable direct band gaps.

Spinel nitride ceramics not only have a small direct band gap in the UV regime, but also offer large hardness values that are highly desirable for mechanical applications. The density and hardness of the binary spinel nitrides are significantly increased in comparison to their hexagonal phase. The mass density of γ-Si_3N_4 and γ-Ge_3N_4 is increased by 23% and 20%, respectively. The increase in density is followed by an increase in the calculated (measured) bulk modulus of 11% (14%) and 30% (35%) for γ-Si_3N_4 and γ-Ge_3N_4, respectively. The calculated hardness of γ-Si_3N_4 is increased by 50% over β-Si_3N_4, while the calculated hardness of γ-Ge_3N_4 is approximately the same as β-Si_3N_4. The hardness of the ternary spinel (γ-$GeSi_2N_4$) is increased significantly from the pure germanium spinel but is only decreased slightly from pure silicon nitride. Gilman[10] proposes that there is a linear correlation between the bond modulus (in terms of molecular volume V_m and the band gap E_g) and

TABLE I. The most recently determined bulk modulus (B_0), shear modulus (G_0), Vicker's hardness (H_v), and band gap (E_g) values are displayed. The experimentally determined values are labeled with an asterisk (*), while all other values were calculated using the local density approximation (LDA). The values that have not yet been determined are indicated with a dash (—). The shear modulus labeled with *a* was determined to the be lower limit and is most likely a larger value, while the hardness indicated by *b* has a range which depended on the oxygen content. Furthermore, the type of band gap transition is labeled with (*d*) and (*i*) indicating direct or indirect, respectively.

Material	ρ (g/cm^3)	B_0 (GPa)	G_0 (GPa)	H_v (GPa)	E_g (eV)
β-Si_3N_4	3.20[a]	274[b]	112[c]	20[c]	5.18^{i} [d]
		270*[e]	116*[f]	30*[g]	4.8* [h]
β-Ge_3N_4	5.28[i]	185[j]			2.45^{i} [j]
		185*[k]			
γ-Si_3N_4	3.93[a]	305[l]	258[m]	30[m]	3.45^{d} [n]
		308*[l]	148*^{a}[o]	30–43*^{b}[o]	3.6* [h]
γ-$GeSi_2N_4$	4.79[n]	283[m]	231[m]	28[m]	3.3^{d} [m]
γ-Ge_3N_4	6.36[i]	242[m]	176[m]	18[m]	2.2^{d} [n]
		296*[p]			

[a]Reference 2.
[b]Reference 11.
[c]Reference 12.
[d]Reference 13.
[e]Reference 14.
[f]Reference 15.
[g]Reference 16.
[h]Reference 4.
[i]Reference 3.
[j]Reference 8.
[k]Reference 17.
[l]Reference 18.
[m]Reference 7.
[n]Reference 19.
[o]Reference 5.
[p]Reference 20.

hardness (H_v). The relationship ($H_v[\mathrm{GPa}]=C\frac{E_g}{V_m}$) indicates there is a strong correlation between hardness, structure and the band gap. Therefore, it may be possible to tailor the hardness of these materials to suit an application by tuning the band gap appropriately. The solid solutions of spinel-phase silicon nitride and germanium nitride present excellent candidates for a new class of materials with a tunable band gap and hardness. The large range of the band gap and hardness of these materials requires that reliable experimental measurements of the binary nitrides, ternary nitrides and their solid solutions be conducted to determine band gap and hardness tunability.

γ-Si_3N_4 and γ-Ge_3N_4 have the same crystal structure as all spinel structured group IV binary nitrides. The space group is *Fd*-3*m*, where cations (Ge or Si) occupy the 8*a* (tetrahedral) and 16*d* (octahedral) Wyckoff sites, while anions (N) occupy the 32*e* (tetrahedral) Wyckoff site.[21] The cations of spinel nitrides (Ge or Si) occupy both tetrahedral and octahedral coordination and have an occupancy ratio of 1:2 in the binary spinel nitride materials. Theoretical[7] and experimental[21] results both suggest Ge atoms prefer to occupy tetrahedral sites, while Si atoms prefer to occupy octahedral sites. This means that the available Ge atoms form tetrahedral bonds with N atoms before any octahedral bonds are formed and vice versa for Si atoms. In the solid solutions [γ-$(Ge_xSi_{1-x})_3N_4$]. Ge atoms occupy only tetrahedral sites while Si atoms occupy both tetrahedral and octahedral sites when $x<1/3$. When $x>1/3$, Ge atoms occupy both octahedral and tetrahedral sites, while Si atoms occupy only octahedral sites. The special case when $x=1/3$ produces the stable intermediate phase γ-$GeSi_2N_4$, where all Ge atoms occupy tetrahedral sites and all Si atoms occupy octahedral sites.[7] The three stable spinel nitride phases (γ-$GeSi_2N_4$, γ-Si_3N_4, and γ-Ge_3N_4) along with their intermediate solid solutions phases have varied bonding and structural configurations that may provide useful tunable electronic and mechanical properties.

Here we calculate the electronic structure of the solid solution phases (γ-$(Si,Ge)_3N_4$) including end members (γ-$GeSi_2N_4$ and γ-Ge_3N_4) and compare the results with X-ray emission and absorption measurements on laboratory-synthesized samples. The empirical relationship between the band gap and hardness proposed by Gilman[10] is also used to estimate the hardness of the intermediate solid solutions. The combination of these measurements and calculations is used to predict the hardness and band gap of the solid solutions for the first time.

II. EXPERIMENTAL DETAILS

Soft x-ray spectroscopy (SXS) utilizing synchrotron radiation from modern third generation sources is a powerful tool for probing the electronic structure of materials. The two complementary techniques employed here are x-ray absorption near edge spectroscopy (XANES), and x-ray emission spectroscopy (XES). In general, XANES and XES measure-

ments probe the unoccupied and occupied density of states (DOS), respectively, but there are limitations that can be advantageous to the experimentalist. Photons have angular momentum $\ell=1$. In the soft x-ray regime, photons are described accurately by the electric dipole approximation, so electronic transitions powered by the absorption of soft x-ray photons are restricted to dipole transitions ($\Delta\ell=\pm 1$). The binding energies of the electrons are characteristic for each element and the probability of exciting a core electron is very large when the energy of the incident photon is tuned to the binding energy of the electron. The measurements presented here are the N Kα XES and N 1*s* XANES spectra. During these measurements the N *p*-states are probed by exciting the N 1*s* core electrons into the conduction band (XANES) or by measuring the refilling of the N 1*s* core hole by valence electrons (XES). In summary XANES and XES measurements probe the local partial density of states or LPDOS in an element specific fashion.

During a XANES measurement an x-ray photon is absorbed and the energy is used to promote a core electron into a previously unoccupied conduction band state. This is followed by another electron transition during which a valence electron decays to fill the previously created core hole. A photon can be emitted and counted as a function of excitation energy with the intensity proportional to the unoccupied DOS. The XANES spectra are measured with a non energy-dispersive channeltron fluorescence detector. This method of detection is known as total fluorescence yield (TFY). During an XES measurement a core hole is excited out of the sample (photoionzed) and the system is left in an excited state. This proceeds with a valence band electron refilling the core hole and the energy can be released in the form of a fluorescence photon. The XES spectra are measured with a high-resolution wavelength dispersive grating spectrometer. The rate at which photons are emitted at a given energy is proportional to the occupied DOS.

The materials studied here are solid solutions established between the end members γ-Si_3N_4 and γ-Ge_3N_4. Samples of γ-Si_3N_4 and γ-$(Si,Ge)_3N_4$ solid solutions were synthesized in a resistively heated multianvil press using COMPRES 8/3 MgO assemblies with a $LaCrO_3$ furnace at 1500 °C and $P=23$ GPa for 18–35 min. The pure γ-Ge_3N_4 end member was prepared at 12 GPa and 1200 °C for 2 h using a COMPRES 14/8 MgO assembly with a graphite furnace. All samples were fully characterized using x-ray diffraction, Raman spectroscopy and electron microprobe analysis in a previous study.[21] Further details of the synthesis and analysis procedures are described therein. The stoichiometry of the samples studied is γ-$(Ge_xSi_{1-x})_3N_4$ with $x=0.000$, 0.178, 0.347, 0.524, 0.875, and 1.000. The SGM beamline[22] (Canadian Light Source, Canada) and Beamline 8.0.1[23] (Advanced Light Source, USA) were utilized to collect N 1*s* XANES and N Kα XES data, respectively. The solid solution samples formed small polycrystalline pieces (<1 mm) embedded in epoxy. These were pressed onto carbon tape and placed 30 deg off normal with respect to the incident beam. Powdered samples of the pure end members, γ-Si_3N_4 and γ-Ge_3N_4, were likewise pressed onto carbon tape. The N 1*s* XANES (measured in TFY mode) and Kα XES were calibrated against the reference spectra of *h*-BN. The XES and XANES peaks for *h*-BN nearest the band gap are taken to be 394.4 and 402.1 eV.

III. THEORETICAL DETAILS

The experimental spectra are always subject to inherent experimental and lifetime broadening, there are three different mechanisms of broadening that are unavoidable. First, the core hole of the systems exists for a very short time, which creates an uncertainty in the energy of the photon emitted when the hole is refilled. The lifetime of the core hole is constant for XANES measurements and can be simulated using a Lorentzian broadening function[24] with a constant full width at half maximum (FWHM). The lifetime of the final state of the system is very short also and adds additional broadening to the spectrum for similar reasons. The lifetime of the final state depends largely upon the conduction band state to which the core electron has transitioned. Electrons in higher conduction band states may decay very quickly to lower states within the same band before the core hole is refilled, introducing uncertainty into the final state energy. This creates a variable broadening in the spectrum and is simulated using a Lorentz function[25] with a variable FWHM. Lastly, the spectrum is broadened by the finite spectral resolution of the instruments (the monochromator in XANES and the fluorescence spectrometer for XES measurements). This broadening is simulated using a Gaussian function with a variable FWHM determined by the nominal beamline resolution. In conclusion, all three broadening factors contribute in the same order of magnitude and have to be taken into account for successful simulation of measured XES and XANES spectra.

In solid crystalline materials XES and XANES probe the valence band (VB) and the conduction band (CB) states, respectively. The direct band gap is defined as the minimum energy separation between the VB and CB for the crystal. The energy separation between the XES and XANES spectra is then used to determine the band gap. There are three important considerations when using SXS to determine the band gap. The first consideration is the core hole effect.[26] XES and XANES transitions are considered one-step processes and are subject to the final state rule, which specifies that the final state electron configuration in each process is the most important.[27] In a strict one-electron picture, the final state of a XANES measurement contains a localized core hole and a delocalized electron residing in the conduction band. The final state of an XES measurement contains no core hole, but a delocalized hole resides in the valence band. The effect of the core hole only needs to be taken into account in XANES measurements. The core hole affects the measured spectra by distorting the CB such that the unoccupied LPDOS have large resonance features near the Fermi level.[28] The core hole also can shift the CB states in energy and this effectively reduces the measured band gap.

Second, one needs to consider nonequivalent sites that may have different core level binding energies. The binding energy of the core electrons is determined by the bonding characteristics and differs for nonequivalent crystal lattice sites. The XES and XANES spectra are measured relative to

the core electron's binding energy and measuring a material with two or more nonequivalent sites will produces a spectrum that is a sum of the individual site spectra shifted with respect to the binding energy of each site. The splitting of the spectral contributions effectively decreases the measured band gap since spectra from nonequivalent sites with a larger binding energy are shifted to higher energy in both the XANES and XES spectra. These values are unique for each material and must be determined individually.

Third, the broadening effects must be considered, and as such the VB and CB locations in the presence of experimental broadening are difficult to determine. The second derivative of the spectra is utilized to unambiguously determine these edges.[29] To summarize, the core hole shift and nonequivalent site splitting provide numerical values that must be added to the nominal band gap determined from the second derivatives of the experimental spectra. These three considerations are necessary to provide accurate and reliable band gap estimations.

The *ab initio* density functional theory (DFT) calculations employ the commercially available WIEN2k software.[30] This code uses the Kohn-Sham methodology with spherical wave functions to model core orbitals, and linearized augmented plane waves (LAPW) for semicore and valence or conduction band states.[31] The exchange interaction uses the generalized gradient approximation (GGA) of Perdew-Burke-Ernzerhof.[32] We note that this approximation is known to significantly underestimate the band gap (50%–100%), but can provide good agreement with the shape of the valence and conduction bands and in turn the measured soft x-ray spectra. The effects from this core hole are modeled in the current work by including a single core hole at the atom of interest inside a $1\times1\times2$ supercell. The energy cutoff for the plane wave basis was −6.0 Ryd. A 1000 k-point and 100 k-point mesh for the unit cell and the supercell are used, respectively. The core hole shift was determined by comparing the calculated conduction energy location, including the core hole, to the conduction band energy location calculated without the core hole. The nonequivalent site splitting was determined from the core level energy eigenvalues for the N 1s orbital.

The x-ray diffraction (XRD) patterns indicate that atoms in the solid solution structures all exhibit the same fcc symmetry as the end members. This indicates that the substitution of Ge for Si or vice versa occurred uniformly retaining their fcc symmetry. The Fd-3m spacegroup is reduced to F resulting in two tetrahedral sites and four octahedral sites for a total of six cation sites. The stoichiometry of the actual materials does not result in structures that allow for tractable DFT simulations because the concentrations are not fractions with base six (0.178 as opposed to 0.167) and would result in partial atom substitutions in the unit cell. The calculations were performed using the closest stoichiometry to the real solutions that produced ideal structures, but the stoichiometry used did not deviate more than 7% from the actual values. The lattice parameters and internal N bond parameters were chosen by interpolating the data from previous results.[21] The space group symmetry has been reduced to fcc, but other lattice choices are available to increase the symmetry in the calculation without changing the structure. The structures for γ-$(Ge_xSi_{1-x})_3N_4$ (x=0.000, 0.167, 0.333, and 1.000) retain their cubic lattices, while γ-$(Ge_xSi_{1-x})_3N_4$ (x=0.500 and 0.833) form rhombohedral lattice structures. The only assumptions used are: (1) the cations and anion sites retain fcc symmetry and (2) the tetrahedral sites are first filled with Ge atoms.

IV. RESULTS AND DISCUSSION

A. Soft x-ray spectra

The N Kα XES and N 1s XANES spectra are used to compare the different stoichiometries because the solid solutions and the end members all contain nitrogen in tetrahedral coordination. There is also a large number of N p-states in the CB and VB, making this an appropriate route to examine the electronic structure. The calculated spectra reproduce all the features seen in the experimental spectra (see Fig. 1). The small disagreement observed for N 1s XANES spectra is attributed to the difference between the ideal and experimental stoichiometry of the solid solutions. The three solid solution samples with stoichiometries that were the closest to the experiment samples (i.e., x=0.000, 0.347, and 1.000) exhibit the best agreement between the calculated and measured spectra. Overall, the modeling of the XES and XANES spectra with DFT calculations and the assumptions used for the structural models are appropriate for these materials.

The N Kα XES and N 1s XANES spectra of all samples have a similar appearance due to common local bonding environments (tetrahedral bonds with Si or Ge) and all exhibit intensive features near the Fermi level (see Fig. 1). The XES spectra consist of one strong feature c at ≈393–394 eV followed by two less intense features a and b positioned at 392–393 eV and 386–387 eV. The strong feature c in the XES spectra is due to a large amount of N p states at the top of the VB. The N p states in the VB have a large degree of hybridization with Si or Ge s, p, and d states and the effect of the Ge and Si neighboring atoms is seen in the N Kα XES spectra. The key difference between the XES spectra is manifested in the relative intensity of features a and b in comparison to c. The relative intensity of feature c in comparison to features a and b is greatly increased as the Si content is increased. This indicates that the nonbonding N p states that are situated at the top of the VB are prominent in γ-Si_3N_4 and less so in γ-Ge_3N_4.

The N p CB states display slight differences for the sample series (see Fig. 1). The effect of the core hole is apparent when comparing the ground state N p-states DOS to the corresponding XANES spectrum. The sharpness (width) of the spectral features in the XANES spectra depends on the number of nonequivalent sites within the lattice. The structures with more nonequivalent sites have broader spectral features because of the difference of the N 1s binding energy between the nonequivalent sites. The simulated XANES spectra all utilize a full core hole potential and agree remarkably well with the measured XANES spectra. This demonstrates that the inclusion of the core hole in XANES spectra is essential for correctly reproducing the experimental spectra. The level of agreement also confirms that

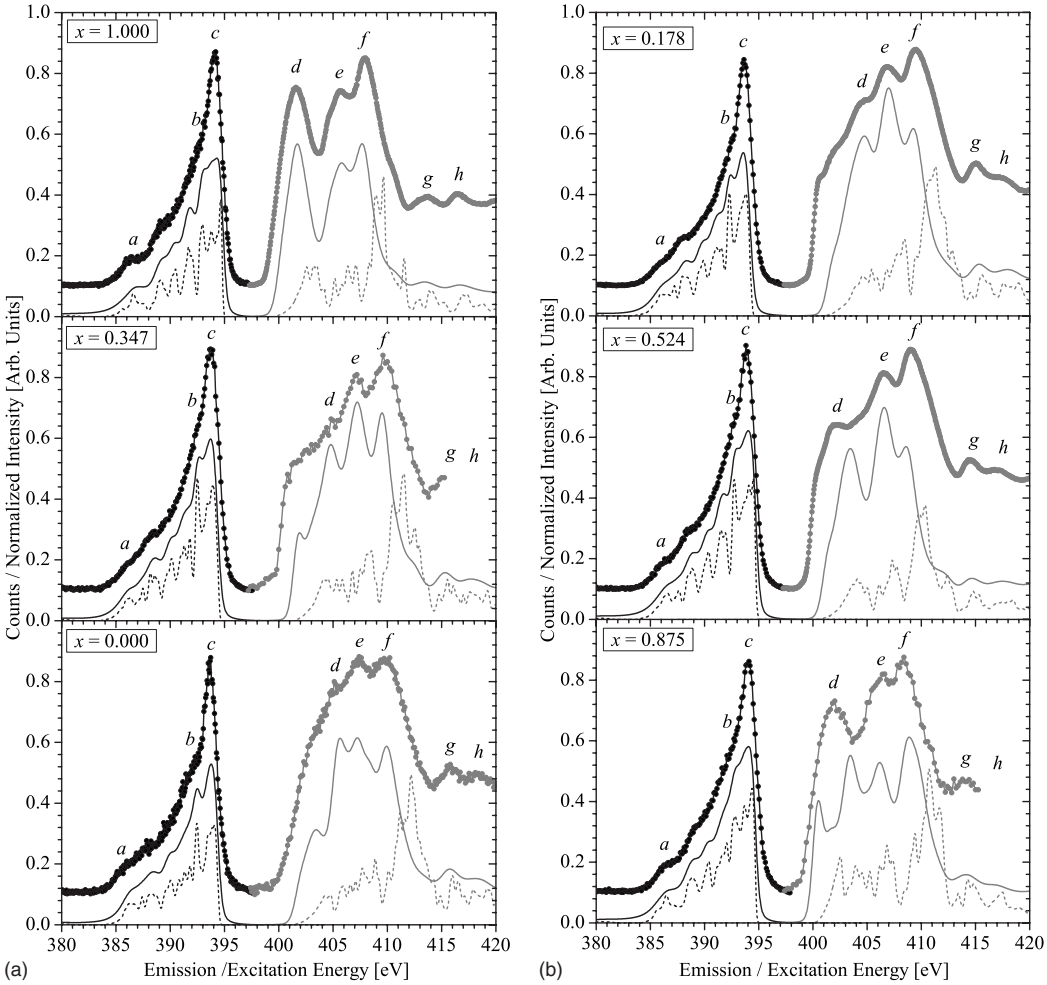

FIG. 1. The N Kα XES (in black) and N 1s XANES (in gray) measured spectra of γ-$(Ge_xSi_{1-x})_3N_4$ are plotted as scatter, while the corresponding calculated spectra are plotted as solid lines. The ground state N p DOS are shown as dashed lines and the comparison between the DOS and the calculated XANES spectra demonstrates the effect of the core hole. The DOS and simulated spectra have been shifted arbitrarily as a whole (with respect to the CB and VB) to achieve optimal peak alignment. The features discussed in the text are labeled with lower case italic lettering.

the DFT calculations successfully determine the shape of the ground state DOS.

The XANES spectra all consist of a similar three-peak structure near the Fermi level followed by a two-peak structure above 413 eV. The two features g and h at 414–415 eV and 418–419 eV are not affected by the core hole and are part of what could be considered the unperturbed N p CB states. The three low energy features d, e and f are influenced by the presence of the core hole. The sharpest features d and e near the Fermi level show the largest distortion, while feature f at approximately 408–410 eV feature is only shifted slightly due to the core hole. Feature f's energy position decreases with an increase in Ge content, except for x=0.178 and 0.347 for which the band gap was predicted to remain the same or increase (see Table II). The XES energy of feature c (see Fig. 1) varies with Ge concentration as well. The general increase of the energy of c in these spectra is due the increase in binding energy of the nitrogen to cation bonds because N-Ge_4 bonds have a larger N 1s binding energy than N-Si_4 bonds. The position of the XES and XANES spectral features suggests that the band gap depends strongly on the stoichiometry.

B. Determining band gap and hardness

The band gaps of the γ-$(Ge,Si)_3N_4$ compounds were determined from the SXS spectra. The effect of the core hole must be taken into account all cases, the highly covalent bonds in these materials show little or no core hole shifting (see Table II). The corrected experimental values are determined by applying the corrections outlined in the experimental section (see Table II). The error attributed to the band gap is determined by two factors: the precision of the experimental spectra (this is reflected in the precision of the second derivative) and the uncertainty of calibration. The value of these errors combined is $\approx$0.20 eV and it is important to

TABLE II. The final corrected band gaps (E_g^{exp}) of the solid solutions are compared to the calculated values (E_g^{calc}) using GGA. The experimental band gap values and structural parameters are used to determine a experimental hardness estimate (H_v^{exp}), these are compared to previous hardness values determined from calculations (H_v^{calc}). Furthermore, the calculated band gaps are determined to be direct (*d*) or indirect (*i*). *x* refers to the experimental (x^{exp}) and simulation x^{calc} mole fraction of Ge. The approximate core hole shift (E_{ch}) is used to correct the measured band gap values to account for the presence of the core hole.

x^{calc} (%Ge)	E_g^{calc} (eV)	H_v^{calc} (GPa)	x^{exp} (%Ge)	E_{ch} (eV)	E_g^{exp} (±0.20 eV)	H_v^{exp} (GPa)
0.000	3.44[d]	30[a]	0.000	0.00	4.85	36.0 ± 9.9
0.167	3.44[d]		0.178	0.00	4.80	35.0 ± 9.7
0.333	3.56[d]	28[a]	0.347	0.15	5.00	35.6 ± 9.8
0.500	2.84[i]		0.524	0.10	4.25	25.2 ± 9.0
0.833	2.22[d]		0.875	0.05	3.65	23.6 ± 8.6
1.000	2.20[d]	18[a]	1.000	0.05	3.50	22.2 ± 8.5

[a]Reference 7.

note that because we use the second derivative to determine the VB and CB edge, the experimental broadening does not provide a significant source of error.

The hardness of covalently bonded materials has been shown to follow the empirical relationship proposed by Gilman[10] that connects hardness with the band gap and structure. This is applied to the solid solutions here and gives an estimate of the hardness tunability. The structures determined from XRD measurements[17] along with the current band gap values are used to calculate the bond modulus ($B_m = E_g / V_m$). The unknown constant ($C = 439.0 \pm 90.7$ Å^3/eV) is fit so the hardness of γ-Si_3N_4 is the experimentally measured value of 36 ± 5 GPa (Ref. 5) (see Fig. 2). The hardness values of the intermediate solid solutions are determined with the fit constant and the experimental band gaps. The error associated with the hardness is due to the uncertainty in the band gap and the proportionality constant. The structure determined from XRD did not contain a significant error. The hardness is then plotted as a function of Ge concentration showing an interesting correlation to the band gap (see Fig. 2).

These errors associated with the measured band gap values are small in comparison to the band gap value (less than 5%) and the only significant source of error is the energy calibration. The difference between the calculated and measured band gaps on average is 1.4 eV, well within the range of acceptable underestimation (50%–100%) of the band gap widely seen with the use of GGA and LDA functionals. The band gap of γ-Si_3N_4 was previously shown to be 4.3 eV[33] and 3.6 eV.[4] The value of 4.3 eV was determined with a similar method (XES and XANES) and 3.6 eV was determined using a plasmon frequency technique. The 4.3 eV band gap differs significantly for the following reasons: the Si $L_{2,3}$ are used and the spin-orbit splitting, core hole effect, and nonequivalent site splitting were not taken into account. Therefore it is not surprising that the value is much smaller than the value we have determined, since these effects will decrease the measured band gap. While there have been other band gap estimations for γ-Si_3N_4, none have rigorously included the factors accounted for here to obtain a reliable band gap value.

The measured and calculated band gap values of the spinel nitride solid solutions exhibit a similar compositional trend. The overall compositional trend of the band gap values for the solid solutions is nonlinear. However, the band gap shows a linear variation with Ge content in the range of $x = 0.333 - 1.00$ with a band gap range of 5.0–3.5 eV providing a large tunable range in the UV regime. When the relative Ge

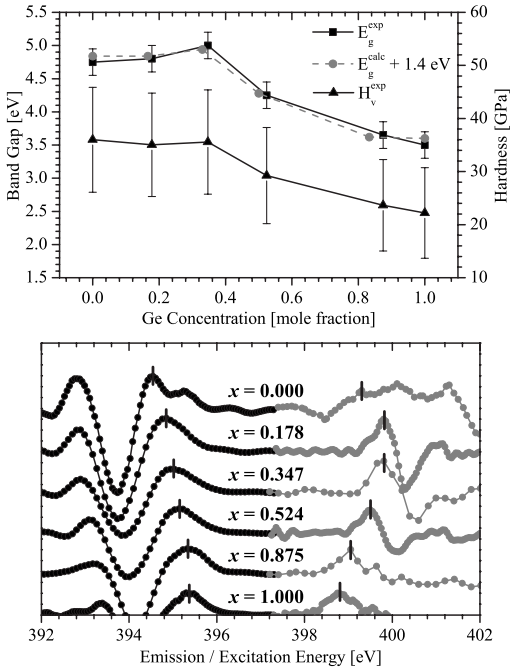

FIG. 2. The bottom panel shows the second derivative of the measured N Kα XES (black) and N 1*s* XANES (gray) spectra displayed in Fig. 1. The second derivative of each spectrum is calculated after the high frequency noise has been filtered out using a fast Fourier transform. The highest occupied states in the VB and the lowest unoccupied states in the CB are each labeled with a vertical line. The calculated and measured band gap values with experimental errors are displayed in the top panel. The calculated band gap values are offset vertically by the average difference between itself and the experimental values, which provides an easy comparison. The top panel also shows the determined hardness values and there is a similar trend to that of the band gap values.

concentration is smaller than 1/3 ($x \leq 1/3$), the tetrahedral sites are first filled with Ge, which increases the band gap. Conversely, when the relative Ge concentration becomes large than 1/3 ($x \geq 1/3$), the octahedral sites are then filled with Ge which decreases the band gap. This suggests that addition of the octahedral sites is possibly responsible for the decrease in the band gap in comparison to the hexagonal phases. The hardness exhibits a similar trend to the band gap values. The hardness decreases as the Ge content increases, however when relative Ge concentration is less than 1/3 ($x \leq 1/3$), the hardness only decreases slightly. The general decrease of hardness occurs because the structure becomes more open decreasing the bond strengths, but the corresponding increase in the band gap with and increase in Ge content ($x \leq 1/3$) mutes the effect. Once the octahedral site begin to fill with Ge the band gap begins to decrease with increasing Ge content, and the hardness decreases dramatically. The band gap for γ-$(Ge_xSi_{1-x})_3N_4$ has a range of 3.5–5.0 eV, while its hardness has a range of 22.2–36.0 GPa.

V. CONCLUSION

The bonding of the cation and anion sites is similar throughout the nitride spinel solid solution series. The bonding in these materials is primarily covalent and the positions of the XANES peaks are largely affected by the core hole. The energy positions of high energy XANES spectral features have a similar trend as the band gap, while the positions of the XES peaks vary in accordance with the N 1*s* binding energy. The measured band gaps of γ-$(Ge_xSi_{1-x})_3N_4$ solid solutions using SXS have a range of $3.50-5.00 \pm 0.20$ eV and the calculated band gaps using DFT calculations (GGA) have a range of 2.20–3.54 eV. The compositional trend of the band gap values agrees within experimental error if the 1.4 eV underestimation of the band gap is neglected. The trend of the hardness values is very similar to the corresponding band gap value trend and the maintained hardness for $x=1/3$ is attributed to the increase of the band gap. The band gap has a linear tunable range when $x=0$ to 1/3 and has a maintained hardness of $\approx$36 GPa. There is a larger linear band gap range when $x=1/3$ to 1, in which the hardness is significantly decreased. The solid solutions of γ-$(Ge_xSi_{1-x})_3N_4$ provide a class of wide band gap semiconductors with two tunable band gap and hardness regimes.

ACKNOWLEDGMENTS

We gratefully acknowledge the Natural Sciences and Engineering Research Council of Canada (NSERC) and the Canada Research Chair program for their support in this research. We also thank the Advanced Light Source and Canadian Light Source along with their staff for helping us to conduct this research. P.F.M. and E.B. acknowledge support from the U.K. EPSRC via Portfolio Award No. EP/D504782. P.F.M. is an EPSRC Senior Research Fellow (EP/D07357X).

*teak.boyko@usask.ca

[1] R. N. Katz, Science **208**, 841 (1980).
[2] A. Zerr, G. Miehe, G. Serghiou, M. Schwarz, E. Kroke, R. Riedel, H. Fuess, P. Kroll, and R. Boehler, Nature (London) **400**, 340 (1999).
[3] G. Serghiou, G. Miehe, O. Tschauner, A. Zerr, and R. Boehler, J. Chem. Phys. **111**, 4659 (1999).
[4] R. G. Egdell, V. E. Henrich, R. Bowdler, and T. Sekine, J. Appl. Phys. **94**, 6611 (2003).
[5] A. Zerr, M. Kempf, M. Schwarz, E. Kroke, M. Göken, and R. Riedel, J. Am. Ceram. Soc. **85**, 86 (2002).
[6] S.-D. Mo, L. Ouyang, W. Y. Ching, I. Tanaka, Y. Koyama, and R. Riedel, Phys. Rev. Lett. **83**, 5046 (1999).
[7] J. Dong, J. Deslippe, O. F. Sankey, E. Soignard, and P. F. McMillan, Phys. Rev. B **67**, 094104 (2003).
[8] J. Dong, O. F. Sankey, S. K. Deb, G. Wolf, and P. F. McMillan, Phys. Rev. B **61**, 11979 (2000).
[9] K. Maeda, N. Saito, D. Lu, Y. Inoue, and K. Domen, J. Phys. Chem. C **111**, 4749 (2007).
[10] J. J. Gilman, J. Phys. D: Appl. Phys. **41**, 074020 (2008).
[11] W. Y. Ching, L. Ouyang, and J. D. Gale, Phys. Rev. B **61**, 8696 (2000).
[12] S. Ogata, N. Hirosaki, C. Kocer, and Y. Shibutani, Acta Mater. **52**, 233 (2004).
[13] Y. H. Duan, K. M. Zhang, and X. D. Xie, Phys. Status Solidi B **200**, 499 (1997).
[14] Y. M. Li, M. B. Kruger, J. H. Nguyen, W. A. Caldwell, and R. Jeanloz, Solid State Commun. **103**, 107 (1997).
[15] J. C. Hay, E. Y. Sun, G. M. Pharr, P. F. Becher, and K. B. Alexander, J. Am. Ceram. Soc. **81**, 2661 (1998).
[16] R. A. Andrievski, Int. J. Refract. Met. Hard. Mater. **19**, 447 (2001).
[17] E. Soignard, P. F. McMillan, C. Hejny, and K. Leinenweber, J. Solid State Chem. **177**, 299 (2004).
[18] E. Soignard, M. Somayazulu, J. J. Dong, O. F. Sankey, and P. F. McMillan, J. Phys.: Condens. Matter, **13**, 557 (2001).
[19] W. Y. Ching, S.-D. Mo, I. Tanaka, and M. Yoshiya, Phys. Rev. B **63**, 064102 (2001).
[20] K. Leinenweber, M. O'Keeffe, M. Somayazulu, H. Hubert, P. F. McMillan, and G. H. Wolf, Chem.-Eur. J. **5**, 3076 (1999).
[21] E. Soignard, P. F. McMillan, and K. Leinenweber, Chem. Mater. **16**, 5344 (2004).
[22] T. Regier, J. Krochak, T. K. Sham, Y. F. Hu, J. Thompson, and R. I. R. Blyth, Nucl. Instrum. Methods Phys. Res. A **582**, 93 (2007).
[23] J. J. Jia, T. A. Callcott, J. Yurkas, A. W. Ellis, F. J. Himpsel, M. G. Samant, J. Stöhr, D. L. Ederer, J. A. Carlisle, E. A. Hudson, L. J. Terminello, D. K. Shuh, and R. C. C. Perera, Rev. Sci. Instrum. **66**, 1394 (1995).
[24] M. O. Krause and J. H. Oliver, J. Phys. Chem. Ref. Data **8**, 329 (1979).
[25] D. A. Goodings and R. Harris, J. Phys. Pt. C: Sol. Stat. Phys. **2**, 1808 (1969).
[26] T. Mizoguchi, I. Tanaka, S.-P. Gao, and C. J. Pickard, J. Phys,:

Condens. Matter **21**, 104204 (2009).
[27] U. von Barth and G. Grossmann, Phys. Rev. B **25**, 5150 (1982).
[28] W. Y. Ching and P. Rulis, J. Phys.: Condens. Matter **21**, 104202 (2009).
[29] E. Z. Kurmaev, R. G. Wilks, A. Moewes, L. D. Finkelstein, S. N. Shamin, and J. Kuneš, Phys. Rev. B **77**, 165127 (2008).
[30] M. Schwarz, G. Miehe, A. Zerr, E. Kroke, B. Poe, H. Fuess, and R. Riedel, Adv. Mater. **12**, 883 (2000).
[31] K. Schwarz, P. Blaha, and G. K. H. Madsen, Comp. Phys. Comm. **147**, 71 (2002).
[32] J. P. Perdew, K. Burke, and M. Ernzerhof, Phys. Rev. Lett. **77**, 3865 (1996).
[33] S. Leitch, A. Moewes, L. Ouyang, W. Y. Ching, and T. Sekine, J. Phys.: Condens. Matter **16**, 6469 (2004).

Electronic Structure of Spinel-Type Nitride Compounds Si_3N_4, Ge_3N_4, and Sn_3N_4 with Tunable Band Gaps: Application to Light Emitting Diodes

T. D. Boyko,[1] A. Hunt,[1] A. Zerr,[2] and A. Moewes[1,*]

[1]*Department of Physics and Engineering Physics, University of Saskatchewan, 116 Science Place, Saskatoon, Saskatchewan S7N 5E2, Canada*

[2]*LSPM-CNRS, Université Paris-Nord, 99 avenue J. B. Clement, 93430 Villetaneuse, France*

(Received 9 June 2013; published 30 August 2013)

In this Letter using experimental and theoretical methods, we show that the solid solutions of group 14 nitrides having spinel structure (γ-M_3N_4 where M = Si, Ge, Sn) exhibit mainly direct electronic band gaps with values that span the entire visible wavelength region, making these hard and thermally stable materials suitable for optoelectronic devices and, in particular, lighting applications. Using the simulated band structure, we also calculate the exciton binding energy. The combination of large exciton binding energies and the tunable electronic band gaps in the visible range makes these binary spinel nitrides and their solid solutions a new class of multifunctional materials with optoelectronic properties that can be engineered to suit the desired application.

DOI: 10.1103/PhysRevLett.111.097402 PACS numbers: 78.70.En, 71.15.Mb, 71.35.−y, 78.70.Dm

Conventional lighting devices (incandescent and fluorescent) consume a large amount of energy and modern technologies such as light emitting diodes (LEDs) and phosphor converting-LEDs (pcLEDs) are used to decrease the global energy demand with regard to lighting. The most recent significant progress in this field was achieved by the development of blue and white LEDs [1]. While the efficiency, operational lifetime and robustness of LEDs exceed that of conventional light devices, the heat released in the diode junction needs to be efficiently managed and demands the use of materials that have high thermal stability. Many LEDs are based on binary or ternary compounds of groups 13 and 15 elements such as GaN, InN, GaAs, GaP, etc. [2], but these compounds have several disadvantages. They are relatively expensive since group 13 elements are rare, some are toxic (e.g., GaAs), and almost all are relatively inefficient due to their small exciton binding energies (E_b) [3,4]. They are also not stable against hydrolysis and oxidation in air, especially at elevated temperatures, and require a passivation layer reducing their overall efficiency.

Zinc oxide (ZnO) and hexagonal boron nitride (h-BN) are some alternative LED materials now under consideration. ZnO has a band gap (E_g) of ≈ 3.3 eV and a large exciton binding energy of $E_b = 60$ meV [5], but it degrades under humid atmosphere, and it is classified as dangerous for the environment. On the other hand, h-BN has a large band gap of $E_g \approx 6.0$ eV [6], but the efficiency is extremely sensitive to deformations, which induce considerable quenching of the exciton emission [7]. A new class of tunable materials is needed to continue the development of more efficient and robust lighting devices.

In this Letter, we investigate the electronic structure of the novel high-pressure nitrides of group 14 elements having a cubic spinel structure (γ-M_3N_4, where M = Si, Ge, Sn) [8–10]. These materials have a unique combination of mechanical, chemical, and electronic properties that make them highly advantageous [11–16] as alternative materials for the fabrication of LEDs when compared with (Ga,In)(As,N), ZnO, or h-BN. Specifically, these three spinel nitrides have direct electronic band gaps and will exhibit efficient conversion of electric power to light when used in LED devices, not accounting for the exciton binding energy which remains to be determined. Contrary to conventional LED materials (GaN, GaAs, etc.), γ-Si_3N_4 and γ-Ge_3N_4 remain stable in air when heated to temperatures of 1400 °C [17] and 700 °C [18], respectively, while γ-Sn_3N_4 remains stable in vacuum to at least 300 °C [10] as well as air to at least 200 °C [19], and thus, these materials do not require any passivation layer.

Initially, group 14 spinel nitrides were synthesized at high temperatures (800–1800 K) and pressures (12–23 GPa) in diamond anvil cells [8], multianvil cells [20,21], or through shock compression [22]. However, there has already been some success in depositing γ-Sn_3N_4 as a thin film, which is evident from the x-ray diffraction pattern [19,23]. Since γ-Sn_3N_4 is synthesized at ambient conditions and deposited as films, we expect that the entire γ-M_3N_4 materials class can be deposited as thin films similar to the related high-pressure c-Zr_3N_4, which shows excellent adhesion to a variety of substrates including silicon, glass, or cemented carbides [24]. With direct electronic band gaps as well as high thermal and oxidation stability, spinel nitrides are suitable for a variety of applications.

The work presented here has two overarching goals. Our first goal is to both measure and calculate the electronic band gaps as well as calculate the exciton binding energies of the three binary spinel nitrides, γ-Si_3N_4, γ-Ge_3N_4, and γ-Sn_3N_4. The expertise gleaned will allow us to realize our second goal: using density functional theory (DFT), we predict the electronic band gap of the solid solutions

γ-(Sn, Ge)$_3$N$_4$. As we shall show, the spinel-structured nitrides form a class of multifunctional compounds with easily tunable band gap values in the visible and near IR range, which is highly desirable in optoelectronics and lighting applications.

The N p states of binary spinel nitrides were chosen here to study the electronic structure of binary spinel nitrides for two reasons. First, our calculations show that the N p states are hybridized throughout the entire conduction band (CB) and valence band (VB), including the very top of the VB and the bottom of the CB. Thus, the N p states provide an accurate measure of the band gap with minimal multielectronic effects. Second, these compounds contain small amounts of oxygen substituting for nitrogen at the anion positions throughout the bulk of the material because the synthesis techniques used to make the materials studied here do not allow one to completely exclude oxygen diffusion in the reaction volume [10,20,25]. As such, the cation measurements would have a significant oxygen contribution and the N p states provide a probe of the electronic structure without any oxygen distortion.

The x-ray emission spectroscopy (XES) and x-ray absorption near edge structure (XANES) measurements were taken using synchrotron radiation at Beamline 8.0.1 (Advanced Light Source) [26] and Spherical Grating Monochromator beamline (Canadian Light Source) [27], respectively. The samples of γ-Si_3N_4 and γ-Ge_3N_4 were synthesized using a multianvil press, while γ-Sn_3N_4 was synthesized at ambient conditions. The synthesis and structural details of all three materials have been previously published [10,20,21]. The γ-Si_3N_4, γ-Ge_3N_4, and γ-Sn_3N_4 samples investigated in this work were a single polycrystalline piece, a polycrystalline powder, and another polycrystalline powder (10 vol. % of SnO_2 and 5 vol. % of SnO), respectively. Prior to the XES and XANES measurements, the γ-Si_3N_4 sample surface was dry polished on a diamond abrasive foil in a glove bag filled with nitrogen gas. The γ-Ge_3N_4 and γ-Sn_3N_4 samples, being both polycrystalline powders, were pressed into freshly scraped indium foil. These materials were affixed to the sample holder and oriented at 30° with respect to the incoming x-ray beam. Figure 1 shows the measured N $K\alpha$ XES and N 1s XANES spectra, which were calibrated using the same procedure described in Ref. [28].

The electronic band gap is the energy separation between the VB and CB states, which can be probed using XES and XANES measurements, respectively. The method used here to determine the band edges for the XES and XANES spectra is the second derivative method [28–30]. This technique has the advantage over conventional band gap determination methods in that it is much less sensitive to impurities and material defects due to the local nature of the measurements. However, it is not enough to simply measure the band gap; the final state of a XANES measurement has a core hole, which can distort the unoccupied density of states severely.

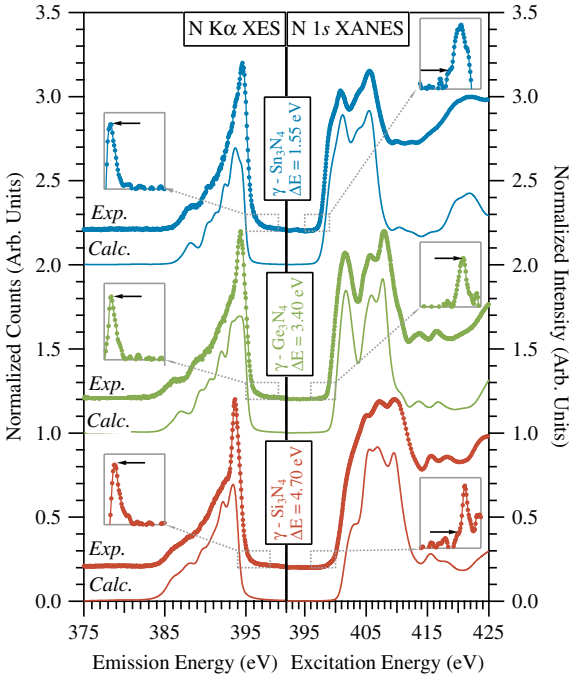

FIG. 1 (color online). The measured and calculated N $K\alpha$ XES and N 1s XANES spectra of γ-M_3N_4 (M = Si, Ge, Sn) are displayed. The second derivatives of the experimental spectra are displayed in the grey panel insets, with the regions displayed enclosed by the connected dashed box. The measured energy separation (excluding the core hole shift) between the measured band edges (ΔE) is labeled.

To quantify the core hole effect, we have performed both ground state and excited state DFT calculations, the latter with a core hole included. The relative difference in CB onsets between the ground and excited states allows one to arrive at a core hole shift (CH).

The XES and XANES spectra were simulated using the commercially available WIEN2K software package (ver. 11.1), an *ab initio* full potential DFT code [31]. These calculations used the generalized gradient approximation (GGA) functional of Perdew-Burke-Ernzerhof [32]. The XANES calculations used a $1 \times 2 \times 2$ supercell in order to adequately isolate the included core hole. The calculations here utilized the following parameters: $E_{cut} = -8.7$ Ryd, $Rk_{max} = 7.0$, and $E_{max} = 4.5$ Ryd. The k-point grids used were $10 \times 10 \times 10$ and $10 \times 5 \times 5$ for the XES and XANES calculations, respectively. The XANES calculations implemented the core hole effect by removing a full core electron and adding a uniform background charge of e. The XES and XANES calculations utilized a self-consistent field cycle with energy and charge convergence of 0.0001 Ryd and 0.001 e, respectively. Our DFT calculations reveal CH values of 0.1, 0.1, and 0.0 eV for γ-Si_3N_4, γ-Ge_3N_4, and γ-Sn_3N_4, respectively. Adding these CH corrections to the experimental band gaps results in true ground state band gap values of 4.8 ± 0.2,

3.5 ± 0.2, and 1.6 ± 0.2 eV for γ-Si_3N_4, γ-Ge_3N_4, and γ-Sn_3N_4, respectively.

The simulated XANES spectra (see Fig. 1) reproduce not only the general shape of the experimental spectra but also every spectral feature for all the examined binary spinel nitrides. This agreement suggests that the values of the CH shifts extracted from the DFT calculations are correct since the core hole must be included in order to simulate the measured N 1*s* XANES spectra. Further, the agreement between the simulated and measured spectra clearly shows that the materials are not contaminated with other N-containing materials. The values for γ-Si_3N_4 and γ-Ge_3N_4 have been determined previously through similar methods [28] and agree with the values presented here within experimental error, but the values presented here are a result of much higher quality XES and XANES measurements and improved DFT calculations. In the case of γ-Sn_3N_4, our work is, to our knowledge, the first experimental measurement of its electronic structure and band gap. Although, calculations of the XANES spectra of γ-Sn_3N_4 were previously published [14], our calculations here have better agreement with measurements.

The typical GGA exchange functional (used to calculate the simulated spectra), in most cases, strongly underestimates the electronic band gap. One can see that, compared to the previously predicted band gap values [13,14] where GGA exchange functionals were used, the measured electronic band gaps are $\approx 30\%$ to 60% larger. However, one can predict the electronic band gaps with significantly improved accuracy when the modified Becke-Johnson potential (MBJLDA), implemented within WIEN2K [33], is used instead of the GGA functional. The MBJLDA functional, in the case of *sp* semiconductors does not change the band curvature and only increases the separation between the VB and CB. Since using the MBJLDA functional for core hole calculations is nonphysical, we only use this functional to obtain the correct electronic band gap values. We obtain, through these calculations using a more dense *k*-point grid of $20 \times 20 \times 20$, electronic band gap values of 4.97, 3.59, and 1.61 eV for γ-Si_3N_4, γ-Ge_3N_4, and γ-Sn_3N_4, respectively.

While the binary spinel nitrides presented here are interesting, one can satisfy the needs of a larger range of applications by increasing the variability of the electronic and mechanical properties using solid solutions. Spinel ternary compounds or solid solutions are made by mixing two parent compounds to form ternary spinel nitrides with random occupations of the cation sites. Changing the composition of these materials allows one to engineer the electronic and mechanical properties. Previously, solid solutions of γ-Si_3N_4 and γ-Ge_3N_4 [γ-$(Ge_xSi_{1-x})_3N_4$] have been synthesized and their structure characterized [21]. These solid solutions form in a very symmetric way with the cations retaining their *fcc* arrangement significantly simplifying the crystal structure. The electronic properties of these materials have also been measured and the electronic band gap was found to vary nearly linearly from 3.50 to 4.85 eV [28].

Our simulations of the electronic structures of the binary spinel nitrides are highly accurate, as shown by the agreement between experimental and theoretical electronic structure and band gap. From this, we apply the same method to confirm the electron band gap trend measured for γ-$(Ge_xSi_{1-x})_3N_4$ [28]. We then extend these predictions to include solid solutions of γ-Ge_3N_4 and γ-Sn_3N_4 [γ-$(Sn_{1-x}Ge_x)_3N_4$]. The structures of the solid solutions are modeled using a few simple assumptions. These are that the solid solutions, γ-$(Sn_{1-x}Ge_x)_3N_4$, form in a similar way to γ-$(Ge_xSi_{1-x})_3N_4$ [21]. In particular, we assumed that: (1) the larger cation fills the tetrahedral site before the octahedral site, (2) the lattice constants vary linearly with composition, and (3) the anion bonding parameter varies linearly from the optimized ternary compounds with the filling of tetrahedral sites and octahedral sites. Here, the optimized anion bonding parameters are 0.261 57 and 0.264 13 for γ-$GeSi_2N_4$ and γ-$SnGe_2N_4$, respectively.

Figure 2 shows the theoretical values of the band gaps for the solid solutions, which cover the entire energy range from 1.61 to 4.97 eV. Most the electronic band gaps are predicted to be direct, but a few have slightly smaller indirect electronic band gaps, which are indicated in Fig. 2. It is important to note that the real structure of these materials may be slightly different, since solid solutions, γ-$(Sn_{1-x}Ge_x)_3N_4$, have yet to be synthesized, possibly changing the type of band gap transition with minimum energy. Since our simulation of the end-member compound band gap values using the MBJLDA potential was successful, the calculated band gaps of the solid solutions should be close to their actual values. The previous band gap measurements of γ-$(Ge_xSi_{1-x})_3N_4$ agree with the

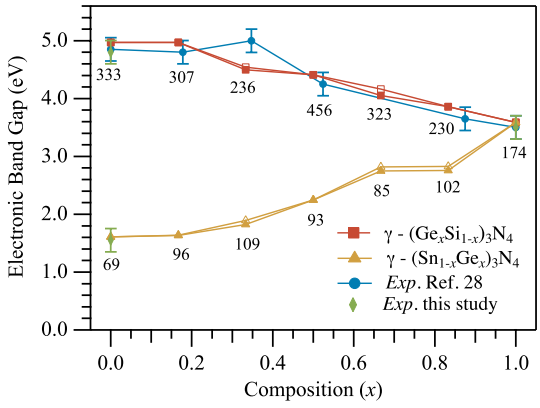

FIG. 2 (color online). The final calculated and measured values for the band gap discussed in this Letter. The direct electronic band gap values are displayed with corresponding open symbols, if the minimum energy transition is indirect. The previous values from Ref. [28] are displayed for comparison. Further, the calculated exciton binding energies, in meV units, are labeled below their respective data points.

calculations presented here within experimental (except for one instance, γ-$GeSi_2N_4$), but has much better agreements than previous calculations [34]. These calculations and measurements showcase the band gap engineering capability of these materials making them appealing for optoelectronic and lighting applications.

According to our results, group 14 spinel nitrides have band gaps spanning the visible wavelength range. However, for a material to be an efficient light emitter, it must not only have a direct electronic band gap, but must also have a large exciton binding energy. If an exciton has a large binding energy, the probability is much greater that it will radiatively decay before the hole and electron can dissociate into free charge carriers. We use the formalism put forth by Ref. [35] to determine the binding energy of a hydrogenic-type exciton quasiparticle. The effective masses and dielectric constants are determined from the band structure of the ground state MBJLDA calculations. Figure 2 shows the exciton binding energy next to the symbols indicating the electronic band gap. While the exciton binding energy is decreased significantly in the γ-$(Sn_{1-x}Ge_x)_3N_4$ solid solutions compared to γ-Si_3N_4, it is still quite large when compared to GaAs ($E_b = 4.20 \pm 0.30$ meV) [36], which has a similar electronic band gap.

We show in this Letter that the solid solutions of spinel-structured group 14 nitrides have tunable electronic band gaps that span the entire visible wavelength region and extend to the near UV and IR. The electronic band gap values for the parent compounds, γ-Si_3N_4, γ-Ge_3N_4, and γ-Sn_3N_4, measured here are 4.8 ± 0.2, 3.5 ± 0.2, and 1.6 ± 0.2 eV, respectively. The calculated exciton binding energy values of γ-Si_3N_4, γ-Ge_3N_4, and γ-Sn_3N_4 are 333, 174, and 69 meV, respectively. The tunability of the electronic band gap and the large exciton binding energies of the spinel-structured group 14 nitride solid solutions suggest that these materials are suitable for optoelectronic applications that require large chemical, thermal, and mechanical stability.

We would like to thank NSERC Canada and the Canadian Research Chair program for their support. XANES measurements were performed at the Canadian Light Source, which is supported by NSERC Canada, NRC Canada, the CIHR, the Province of Saskatchewan, WD Canada, and the University of Saskatchewan. XES measurements used the Advanced Light Source, which is supported by the Office of Basic Energy Sciences of the U.S. DOE under Contract No. DE-AC02-05CH11231. This research has also been enabled by the use of computing resources provided by WestGrid and Compute/Calcul Canada. We also thank H. Jacobs for providing the γ-Sn_3N_4 sample.

*alex.moewes@usask.ca

[1] F. A. Ponce and D. P. Bour, Nature (London) **386**, 351 (1997).
[2] H. Morkoc, S. Strite, G. B. Gao, M. E. Lin, B. Sverdlov, and M. Burns, J. Appl. Phys. **76**, 1363 (1994).
[3] Y.-L. Chang, Y. Song, Z. Wang, M. G. Helander, J. Qiu, L. Chai, Z. Liu, G. D. Scholes, and Z. Lu, Adv. Funct. Mater. **23**, 705 (2013).
[4] B.-G. Kim, C.-G. Zhen, E. J. Jeong, J. Kieffer, and J. Kim, Adv. Funct. Mater. **22**, 1606 (2012).
[5] D. C. Reynolds, D. C. Look, and B. Jogai, Solid State Commun. **99**, 873 (1996).
[6] Y. Kubota, K. Watanabe, O. Tsuda, and T. Taniguchi, Science **317**, 932 (2007).
[7] K. Watanabe, T. Taniguchi, T. Kuroda, and H. Kanda, Appl. Phys. Lett. **89**, 141902 (2006).
[8] A. Zerr, G. Miehe, G. Serghiou, M. Schwarz, E. Kroke, R. Riedel, H. Fueß, P. Kroll, and R. Boehler, Nature (London) **400**, 340 (1999).
[9] G. Serghiou, G. Miehe, O. Tschauner, A. Zerr, and R. Boehler, J. Chem. Phys. **111**, 4659 (1999).
[10] N. Scotti, W. Kockelmann, J. Senker, S. Traßel, and H. Jacobs, Z. Anorg. Allg. Chem. **625**, 1435 (1999).
[11] A. Zerr, R. Riedel, T. Sekine, J. E. Lowther, W.-Y. Ching, and I. Tanaka, Adv. Mater. **18**, 2933 (2006).
[12] S.-D. Mo, L. Ouyang, W. Y. Ching, I. Tanaka, Y. Koyama, and R. Riedel, Phys. Rev. Lett. **83**, 5046 (1999).
[13] W. Y. Ching, S. D. Mo, and L. Ouyang, Phys. Rev. B **63**, 245110 (2001).
[14] W. Y. Ching and P. Rulis, Phys. Rev. B **73**, 045202 (2006).
[15] J. Dong, O. F. Sankey, S. K. Deb, G. Wolf, and P. F. McMillan, Phys. Rev. B **61**, 11979 (2000).
[16] Y. C. Ding, H. P. Zhou, M. Xu, Y. B. Shen, Q. Y. Chen, W.-J. Zhu, and H. L. He, Int. J. Mod. Phys. B **22**, 2157 (2008).
[17] J. Z. Jiang, F. Kragh, D. J. Frost, K. Stahl, and H. Lindelov, J. Phys. Condens. Matter **13**, L515 (2001).
[18] H. L. He, T. Sekine, T. Kobayashi, and K. Kimoto, J. Appl. Phys. **90**, 4403 (2001).
[19] N. Takahashi, K. Terada, and T. Nakamura, J. Mater. Chem. **10**, 2835 (2000).
[20] M. Schwarz, G. Miehe, A. Zerr, E. Kroke, B. T. Poe, H. Fuess, and R. Riedel, Adv. Mater. **12**, 883 (2000).
[21] E. Soignard, P. F. McMillan, and K. Leinenweber, Chem. Mater. **16**, 5344 (2004).
[22] T. Sekine, H. L. He, T. Kobayashi, M. Zhang, and F. F. Xu, Appl. Phys. Lett. **76**, 3706 (2000).
[23] T. Maruyama and T. Morishita, J. Appl. Phys. **77**, 6641 (1995).
[24] M. Chhowalla and H. E. Unalan, Nat. Mater. **4**, 317 (2005).
[25] M. Shemkunas, G. Wolf, K. Leinenweber, and W. Petuskey, J. Am. Ceram. Soc. **85**, 101 (2002).
[26] J. J. Jia, T. A. Callcott, J. Yurkas, A. W. Ellis, F. J. Himpsel, M. G. Samant, J. Stöhr, D. L. Ederer, J. A. Carlisle, E. A. Hudson, L. J. Terminello, D. K. Shuh, and R. C. C. Perera, Rev. Sci. Instrum. **66**, 1394 (1995).
[27] T. Regier, J. Krochak, T. K. Sham, Y. F. Hu, J. Thompson, and R. I. R. Blyth, Nucl. Instrum. Methods Phys. Res., Sect. A **582**, 93 (2007).
[28] T. D. Boyko, E. Bailey, A. Moewes, and P. F. McMillan, Phys. Rev. B **81**, 155207 (2010).
[29] E. Z. Kurmaev, R. G. Wilks, A. Moewes, L. D. Finkelstein, S. N. Shamin, and J. Kuneš, Phys. Rev. B **77**, 165127 (2008).
[30] C. Braun, M. Seibald, S. L. Boerger, O. Oeckler, T. D. Boyko, A. Moewes, G. Miehe, A. Tuecks, and W. Schnick, Chem. Eur. J. **16**, 9646 (2010).

[31] K. Schwarz, P. Blaha, and G. K. H. Madsen, Comput. Phys. Commun. **147**, 71 (2002).
[32] J. P. Perdew, K. Burke, and M. Ernzerhof, Phys. Rev. Lett. **77**, 3865 (1996).
[33] F. Tran and P. Blaha, Phys. Rev. Lett. **102**, 226401 (2009).
[34] J. N. Hart, N. L. Allan, and F. Claeyssens, Phys. Rev. B **84**, 245209 (2011).
[35] N. W. Ashcroft and N. D. Merimin, *Solid State Physics* (Brooks Cole, Belmont, MA, 1976).
[36] S. B. Nam, D. C. Reynolds, C. W. Litton, R. J. Almassy, T. C. Collins, and C. M. Wolfe, Phys. Rev. B **13**, 761 (1976).

Chapter 3

Crystal Structure

3.1 Conventional Techniques

The crystal structure of materials determines many of the intrinsic electronic and mechanical properties. The most widely used technique to measure the crystal structure of materials is X-ray diffraction (XRD). This technique relies on Bragg diffraction of X-rays off of the electron clouds provided by the atoms frozen in place in the crystal. The reliance of the X-ray scattering amplitude on the total electronic charge Z of an atom is one of the drawbacks of XRD. The short-comings include insensitivity to elements with similar scattering factors and low scattering amplitudes for light elements. In short, XRD can not distinguish between elements with a similar atomic number $\Delta Z \pm 1$ and elements with a small atomic number $Z < 18$. The same is true for other X-ray scattering techniques (EXAFS, etc.), but an alternative is to use neutrons to scatter off of the nuclei. Since in neutron diffraction (ND) the scattering amplitude no longer depends on Z, light elements are equally likely to have large scattering amplitudes. Although ND is seemingly the solution to the short-comings of XRD, it also has disadvantages that have prevented it from becoming the staple structural measurement technique. The available sources for neutrons are either spallation sources or nuclear reactors, both producing a relatively low neutron flux compared to modern synchrotron facilities. The neutron beam size in ND is very large compare to X-rays, which are used to carry out XRD of micron sized single crystals. The characteristics of the available neutron beams requires that the material be very large quantity, high purity and of high structural quality. Any of these attributes are not commonly associated with novel ultra-hard materials. An alternative method that does not depend on the total electron charge or require pristine materials would be advantageous for studying the structure of novel materials.

3.2 Electronic Structure

The measured and calculated electronic structure described in Sec. 2.2 does not only depend on the total electronic charge, but also the charge density of the atoms in the crystal. Furthermore, DFT suggests that every unique crystal structure produces a unique charge density. The only problem that arises with using core-level spectroscopy is that the measured spectra need be modelled sufficiently well to distinguish between different structural models and the lifetime broadening may obscure the differences between the electronic structural models. This consideration not only stresses the need to carry out the highest quality electronic structure measurements, but also the methods used to simulate XES and XANES measurements need to be treated properly. The discussion regarding saturation effects and proper treatment of the lifetime broadening in XES and XANES spectra aimed to do just that, develop a method to determine the crystal structure of materials using the measured and calculated XES and XANES spectra. Determining the crystal structure of materials through electronic structure measurements is actually quite simple: (1) Based on the current knowledge of the structure through complementary techniques such as XRD create several possible crystal structures and (2) simulate the XES and XANES measurements using the techniques described Sec. 2.2. The measured electronic structure in this way provides a unique alternative method to determine the crystal structure.

3.3 Publications

The three publications described below, two published and one prepared for publication, are examples of using this technique described above to determine the crystal structure of materials where no other methods were feasible. The respective authors completed all of the writing pertaining to the specified contributed work of authors listed.

Ca_3N_2 and Mg_3N_2: Unpredicted High-Pressure Behavior of Binary Nitrides

Authors: *C Braun, S L Börger, T D Boyko, G Miehe, H Ehrenberg, P Höhn, A Moewes, and W Schnick*

Summary and Author Contributions:

In this study [53], the synthesis details, crystal structure and electronic structure of the novel calcium nitride Ca_3N_2 were studied. In this paper, the collaborators – C Braun, Saskia L Börger, G Miehe, H Ehrenberg, P Höhn, and W Schnick – carried out the synthesis and structural characterization of Ca_3N_2. Additionally, the high-pressure behaviour of Mg_3N_2 was studied, but otherwise was omitted from further study. The electronic structure was studied using XES and XANES measurements as well as DFT calculations that were all carried out by T D Boyko under the supervision of A Moewes. The interest in this material, contrary to the previous publications discussed, was only with regard to possible vacancies in the crystal structure. Although XRD measurements have easily determined the crystal structure, the aforementioned problems prevented conclusive determination of whether nitrogen vacancies were present. In order to ascertain whether N vacancies indeed do occur we have measured the XES and XANES spectra. These measurements presented extreme difficulty as this material is extremely air sensitive and will decompose from Ca_3N_2 to CaO in less than fifteen minutes when left in atmosphere. Through careful XES and XANES measurements in order to avoid exposure to oxygen, the electronic structure was used to confirm the existence of vacancies. The extent of the N vacancies determined by introducing N vacancies into the crystal structure and comparing both the simulated spectra resulting from the structures with no vacancies as well N vacancies to the measured spectra. The addition of N vacancies resulted in a simulated electronic structure that agreed better with the measured electronic structure. The testing of a few different structural models showed that the N vacancies were distributed uniformly as opposed to clustering. This publication was the first instance of the author using electronic structure to examine crystal structure indirectly, which laid the ground work to approach more difficult problems regarding the fine details of the crystal structure that is important for studying hardness.

Anion Ordering in Spinel-type Gallium Oxonitride

Authors: *T D Boyko, C E Zvoriste, I Kinski, R Riedel, S Hering, H Huppertz, and A Moewes*

Summary and Author Contributions:

In this study [54], the electronic structure of the spinel structured gallium oxonitide (Ga_3O_3N) is studied to determine the anion ordering and the electronic band gap. The material studied was provided by our collaborators, C E Zvoriste, I Kinski, R Riedel, S Hering, H Huppertz. The electronic structure measurements including XES and XANES spectra as well DFT calculations were carried out by T D Boyko under the supervision of A Moewes. Measuring the electronic band gap of materials using XES and XANES measurements requires the crystal structure to be known since DFT calculations are required to apply corrections to the measured value. However, the crystal structure needs to be known exactly and it is common that the anion ordering (the location of different anions, oxygen and nitrogen) is unknown for oxonitrides. Stemming from the inability of XRD to distinguish similar Z elements as described in section 3.1, only the general crystal structure for Ga_3O_3N was known [55]. In order to determine the crystal structure fully, we assumed the anions will be uniformly distributed and a few structural models were created and tested. Comparing the simulated XES and XANES spectra that resulted from the model structures to the measured XES and XANE spectra tested the structural models. The results show that the most symmetric crystal structure, described using the R-3m space group (No. 166) is most appropriate, which also validated the previous assumption since less uniform structures will be more disordered and no benefit would arise from considering more complicated structural models. From this, the electronic band gap was measured to be 2.95 ± 0.30 eV, and the calculated band gap using the MBJLDA functional of 2.79 eV agreed with the measured value. This study was a large step forward in developing and using the measured electronic structure combined with DFT calculations to determine the crystal structure of materials where XRD or ND are not feasible. This is very important regarding the study of ultra-hard oxonitrides where one would like to know both the detailed crystal structure and electronic band gap.

The Crystal Structure and Electronic Band Gap of β-sialons

Authors: *T D Boyko, T Gross, H Fuess, M Schwarz, and A Moewes*

Summary and Author Contributions:

In this study [56], the electronic structure and crystal structure of β-sialons is examined through XRD measurements, XES and XANES measurements and DFT calculations. The collaborators – T Gross, H Fuess, M Schwarz – provided the materials studied as well as conducted the XRD measurements that determined the crystal structure that was used for the DFT calculations. The DFT calculations, XES and XANES measurements were performed by T D Boyko under the supervision of A Moewes. The crystal structure and electronic band gap of these materials, although studied for several decades, are not well known. As in the previous manuscript, the crystal structure needs to be ascertained before the electronic band gap. The problem for these materials, with regard to determining the crystal structure is also similar to Ref. 54 in that the specific distribution of Si, Al, O, and N atoms is not well known. In the order to determine both the cation and anion ordering, we test two prominent structural models, both exactly the same structure in principle, but the arrangement of cations Si and Al, and anions O and N are different. These two structural models were proposed in previous publications [57–59]. This is the first time these complex structure models were used to simulate electronic measurements in order to determine the crystal structure, contrary to previous studies which were limited to superstructures of 28 atoms [60]. The complexity of the structural models tested pushed what was considered feasible for DFT calculations on the current computer hardware that was available and the duration these simulations approached nearly one year. However, the results were very promising and there was a clear structural preference when the simulated XES and XANES spectra were compared with the corresponding measured spectra. Not only was the agreement between the simulated and measured electronic structure good, but the changes in the electronic structure with change in composition were correctly predicted. Next, the electronic band gap was determined, and contrary to previous results it varied linearly with composition similar to the other properties of β-sialons. The measured electronic band gap values for β-$Si_{6-z}Al_zO_zN_{8-z}$

with $z = 0.0$, 2.0 and 4.0 are 7.2 eV, 6.2 eV and 5.0 eV (all ± 0.2 eV), respectively. However, the calculated electronic band gap values using MBJLDA are much smaller at 5.88 eV, 3.45 eV and 2.39 eV for β-$Si_{6-z}Al_zO_zN_{8-z}$ with $z = 0.0$, 2.0 and 4.0, respectively. This underestimation may be due to both small differences in the crystal structure used throughout the calculations and the typical underestimation of electronic band gap using DFT calculations. The correct determination of the crystal structure was necessary for measuring the electronic band gap since both the non-equivalent site splitting the core hole shifting affected the measured band gap significantly. The innovations achieved throughout this study further developed the technique of using electronic structure to determine crystal structure.

JACS
JOURNAL OF THE AMERICAN CHEMICAL SOCIETY

ARTICLE

pubs.acs.org/JACS

Ca_3N_2 and Mg_3N_2: Unpredicted High-Pressure Behavior of Binary Nitrides

Cordula Braun,[†] Saskia L. Börger,[†] Teak D. Boyko,[‡] Gerhard Miehe,[§] Helmut Ehrenberg,[§,⊥] Peter Höhn,[¶] Alexander Moewes,[‡] and Wolfgang Schnick[†,*]

[†]Ludwig-Maximilians-Universität München, Department Chemie, Butenandtstrasse 5-13, D-81377 München, Germany

[‡]Department of Physics and Engineering Physics, University of Saskatchewan, 116 Science Place, Saskatoon, Saskatchewan, S7N 5E2 Canada

[§]Institut für Materialwissenschaft, Technische Universität Darmstadt, Petersenstr. 23, D-64287 Darmstadt, Germany

[⊥]Karlsruhe Institute of Technology (KIT), Institute for Applied Materials (IAM), Hermann-von-Helmholtz-Platz 1, D-76344 Eggenstein-Leopoldshafen, Germany

[¶]Max-Planck-Institut für Chemische Physik fester Stoffe, Nöthnitzer Str. 40, D-01187 Dresden, Germany

ABSTRACT: High-pressure synthesis allows both fundamental and materials science research to gain unprecedented insight into the inner nature of materials properties at extreme environment conditions. Here, we report on the high-pressure synthesis and characterization of γ-Ca_3N_2 and the high-pressure behavior of Mg_3N_2. Investigation of M_3N_2 (M = Ca, Mg) at high-pressure has been quite challenging due to the high reactivity of these compounds. Ex situ experiments have been performed using a multianvil press at pressures from 8 to 18 GPa (1000−1200 °C). Additional in situ experiments from 0 to 6 GPa (at RT) at the multianvil press MAX 80 (HASYLAB, Beamline F.2.1, Hamburg) have been carried out. The new cubic high-pressure phase γ-Ca_3N_2 with anti-Th_3P_4 defect structure exhibits a significant increase in coordination numbers compared to α-Ca_3N_2. Contrary, Mg_3N_2 shows decomposition starting at surprisingly low pressures, thereby acting as a precursor for Mg nanoparticle formation with bcc structure. Soft X-ray spectroscopy in conjunction with first principles DFT calculations have been used to explore the electronic structure and show that γ-Ca_3N_2 is a semiconductor with inherent nitrogen vacancies.

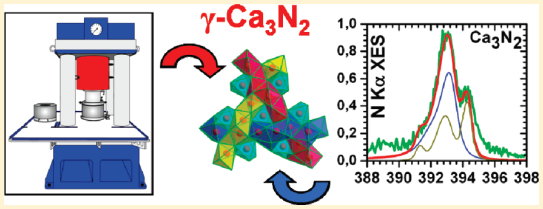

INTRODUCTION

High-pressure synthesis is the method of choice to access the still vast realm of superhard materials and promising new phases, being widely used and highly sought after for various applications. The first compelling high-pressure synthesis of diamond in 1953[1] initiated the quest for novel synthetic superhard materials.[2] Subsequent synthesis of c-BN[3] is widely regarded as the milestone of artificial superhard material synthesis and has stimulated the growing interest in this field of research. Nowadays, there is a notable interest in high-pressure research targeting novel extreme condition phases of elements[4,5] or compounds featuring new and exciting properties (e.g., high-temperature superconductivity).[6−8]

The behavior of binary nitrides under extreme conditions has been an important research field triggered by the discovery of γ-Si_3N_4.[9] Such nitridic spinels exhibit a remarkable increase in coordination numbers (CN), resulting in significantly increased hardness and materials properties suitable for industrial applications. High-pressure phases of chemically and thermally stable nitrides have recently been investigated thoroughly owing to their various applications and exciting properties. Nitrides M_3N_4 (M = Hf, Zr)[10] were found to have Th_3P_4 structure with high CN ($M^{[8]}$) and advanced properties (e.g., high hardness).[10] The (anti-)Th_3P_4 structure, which has been found for the new high-pressure phase as well, exhibits a broad range of characteristics[11,12] and provides promising candidates for superconducting behavior.[13,14] The experimental results[10] have been confirmed by DFT calculations[15] and illustrate the potential still dormant in the multifaceted family of nitride materials. The high-pressure (HP)-behavior of binary nitrides is diverse and less predictable than expected, even α-C_3N_4, a carbon(IV)nitride with complete sp^3 hybridization of the C atoms, is still elusive[16] and only theoretically predicted, whereas a novel binary tantalum nitride[17] with U_2S_3 structure has become recently accessible by high-pressure synthesis.

α-Ca_3N_2 (antibixbyite-type) has various industrial applications, which include precursors for host lattices of rare-earth doped phosphors in LEDs,[18] catalysts for the crystallization of c-BN[19,20] or as gas-generating agent in airbags.[21] Furthermore, the Ca_3N_2−CaNH-system has been studied as a promising candidate for hydrogen storage.[22] The yellow high temperature (HT) phase of Ca_3N_2,[23] previously thought to be γ-Ca_3N_2, has recently been identified as calcium dinitride cyanamide $Ca_4[CN_2]N_2$[24] and a potential high-pressure/high-temperature (HP/HT) phase[25] has not been explored further.

Received: July 21, 2010
Published: March 09, 2011

Recently described β-Ca_3N_2[26] (anti-Al_2O_3-structure) as well as various applications of α-Ca_3N_2 (e.g., as starting material for the synthesis of binary alkaline earth nitrides) underline the interest in this compound. Novel high-pressure modifications of Ca_3N_2 are not only interesting from a scientific point of view but also relevant based on their potential hydrogen storage capabilities for example in the system Ca_3N_2−CaNH,[22] which may lead to further applications.

Theoretical calculations have been reported by Römer et al.,[27,28] which predict the existence of several hitherto unknown HP-phases of Ca_3N_2 and Mg_3N_2. The selected models base on the HP-behavior of corundum. Concerning the high-pressure behavior of M_3N_2 (M = Ca, Mg), there are experimental and theoretical investigations of Hao et al.,[29,30] of which the theoretical results are in agreement with the ones of Römer et al.[27,28] However, the proposed high-pressure phases are not supported by the experimental XRD patterns displayed in refs 29 and 30. The appearance of two new weak reflections is most probable due to reactions of M_3N_2 (M = Ca, Mg) with the used but inappropriate pressure medium silicone oil.

These comprehensive studies have led to intensive investigations of the HP-behavior of the binary nitrides M_3N_2 (M = Ca, Mg).

EXPERIMENTAL SECTION

Synthesis. For the investigations of the high-pressure behavior of Ca_3N_2 and Mg_3N_2 the starting materials α- and β-Ca_3N_2 and α-Mg_3N_2 (99.5%, Aldrich Chemical Co., Milwaukee) were used. The quality of α-/β-Ca_3N_2 and α-Mg_3N_2 was ascertained by powder X-ray diffraction and elemental analysis; no impurities (esp. C, H, O) were detected. For a detailed description of the synthesis of α- and β-Ca_3N_2 see ref 26.

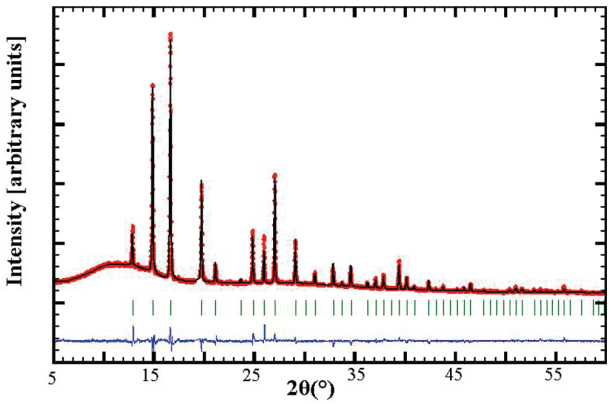

Figure 1. γ-Ca_3N_2: Observed (circles) and calculated (line) X-ray powder diffraction pattern together with their difference curve after Rietveld refinement (λ = 0.709026 Å).

High-Pressure Synthesis of γ-Ca_3N_2 and bcc−Mg. The high-pressure syntheses of γ-Ca_3N_2 and bcc−Mg were carried out using the multianvil technique[31−33] with a hydraulic press. All sample preparation had to be done in argon atmosphere and to prevent the sample from oxidation during the experiment it was additionally surrounded by an inert and protecting metal foil. Ex situ experiments with the multianvil press have been conducted at the following pressures and temperatures: 8, 12 GPa at ∼1000 °C and 14, 16, 18 GPa at ∼1200 °C. Cr_2O_3-doped MgO octahedra (Ceramic Substrates & Components Ltd., Isle of Wight) with edge lengths of 14 and 10 mm were used for pressures up to 12 and 18 GPa, respectively.

Exemplarily only one pressure and temperature program will be described in the following. Eight truncated tungsten carbide cubes separated by pyrophyllite gaskets served as anvils for the compression of the octahedra. The truncation edge length for the 14/8 assembly was 8 mm. Powder of ambient-pressure M_3N_2 (M = Ca, Mg) was loaded into a cylindrical capsule of hexagonal boron nitride (Henze, Kempten) with a capacity of 9 mm^3 (14/8 assembly) and sealed with a BN cap. The capsule was centered within two nested graphite tubes, which acted as an electrical resistance furnace. The remaining volume at both ends of the sample capsule was filled out with two cylindrical pieces of magnesium oxide. The arrangement was placed into a zirconium dioxide tube and then transferred into a pierced MgO octahedron. The electrical contact of the graphite tubes was arranged by two plates of molybdenum. For the 8 GPa experiment the assembly was compressed at room temperature within 2.5 h and then heated up to 1000 °C within 12 min. Under these conditions, the sample was treated for 12 min and cooled down to 600 °C within 30 min. After that the sample was quenched to room temperature, followed by a decompression of 7.5 h. Using high-pressure synthesis, γ-Ca_3N_2 and Mg_3N_2 (including bcc−Mg) were obtained as red and yellow-grayish substances, respectively. The temperature was calculated from the electrical power applied to the furnace, which was determined on the basis of calibration curves from measurements with a thermocouple, which is directly connected to an Eurotherm 2404 temperature controller (Limburg a. d. Lahn, Germany). Therefore, some uncertainties in the specific synthesis temperatures result but are within a sufficiently narrow temperature range not to affect the observed phase formation. For temperatures up to 1500 °C Pt−$Pt_{87}Rh_{13}$ was used as a thermocouple, above 1500 °C W_3Re_{97}−$W_{25}Re_{75}$ (SPPL−010, SP13RH−010, W3W25−010, Newport Omega, Deckenpfronn, Germany). For the pressure calibration as a function of hydraulic oil pressure, the commonly used phase transitions in Bi (the I−II at 2.55 GPa, II−III at 3.15 GPa and III−V transition at 7.70 GPa) and the semiconductor to metal transitions

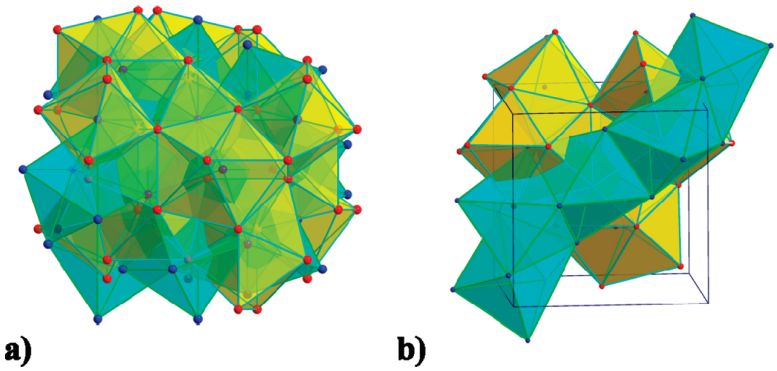

Figure 2. **a**) and **b**) corner, edge and face sharing octahedra (turquoise) and dodecahedra (yellow) forming the anti-Th_3P_4 structure type.

Table 1. Crystallographic Data of γ-Ca_3N_2 Derived from Rietveld Refinement

formula	γ-Ca_3N_2
formula mass/g mol^{-1}	148.26
crystal system	cubic
space group	$I\bar{4}3d$ (no. 220)
cell parameters/Å	a = 7.7212(3)
cell volume/Å^3	460.32(3)
formula units/cell	5 1/3
diffractometer	STOE STADI P
radiation/Å	Mo−Kα_1 (λ = 0.70926 Å)
monochromator	Ge (111)
temperature/K	293
data range (2θ), step width	$5° \le 2\theta \le 60°$, 0.01°
structure refinement	Rietveld refinement, *Fullprof*[36]
background treatment	15 fixed background points
profile function	pseudo-Voigt (no. 7)
R_{Bragg}	7.89
GOF	2.1
reduced χ^2	4.55

in ZnTe (15.5 GPa) and GaAs (18.3 GPa) have been performed. A detailed description of temperature and pressure calibration can be found in refs 31 and 34 and the references therein.

In situ High-Pressure Measurements. In situ high-pressure measurements for Ca_3N_2 and Mg_3N_2 (0 to 6 GPa at RT) were performed with the multianvil high-pressure apparatus MAX80 (NRD Tsukuba, Japan), which is located at the Hamburger Synchrotronstrahlungslabor (HASYLAB, Beamline F.2.1) for in situ high-pressure and high-temperature X-ray diffraction investigations. Energy-dispersive diffraction patterns are recorded using white X-rays from the storage ring DORIS III. The pressure was measured by using the high-pressure equation of state for admixed NaCl by Decker.[35] The beamline is equipped with a Ge solid-state detector, situated at the press frame and tracking the adjustment of the whole apparatus in relation to the X-ray beam. The multianvil apparatus is equipped with six tungsten carbide anvils, which are driven by a 2.500 N uniaxial hydraulic ram. The top and bottom anvil are driven directly, the lateral anvils by two load frames and four reaction bolsters. The maximum pressure for the 8 mm cube setup is approximately 9 GPa with temperatures up to 1600 °C, which are produced by an internal graphite heater. The high-pressure cell consists of a cube made of boron epoxy resin and the gaskets between the anvils are formed from the boron epoxy cube's material during the runs. The high-pressure cell (BN) is filled with the ground sample, the graphite heater, the pressure standard (NaCl) and the thermocouple, which is insulated by boron nitride. All sample preparation was done in argon atmosphere and the sample was protected by an additional metal foil. Rings made from heated pyrophyllite provide electrical insulation and act as a quasi-hydrostatic pressure transmitting medium. Copper rings contact the heater at the top and bottom anvils.

Powder X-ray Diffraction. The obtained crystallites were too small for single-crystal X-ray diffraction analysis, so the structure refinements of γ-Ca_3N_2 and bcc−Mg were based on ex situ X-ray powder diffraction data. X-ray diffraction experiments on the products of the high-pressure reactions of Ca_3N_2 and Mg_3N_2 were performed on a STOE STADI P powder diffractometer in Debye−Scherrer geometry with Ge(111)-monochromatized Mo-Kα_1 radiation (λ = 0.709026 Å). The samples were enclosed in glass capillaries with 0.5 mm diameter. A Rietveld refinement was carried out using the program package *Fullprof*.[36]

Details of the X-ray data collection, structural refinements, final equivalent atomic coordinates and isotropic displacement parameters are listed in Tables 1−7. Further details of the crystal structure investigations can be obtained from the Fachinformationszentrum Karlsruhe, 76344 Eggenstein-Leopoldshafen, Germany (fax: (+49)7247−808−666, e-mail: crysdata@fiz-karlsruhe.de) on quoting the depository numbers CSD-421950 and CSD-421951.

EDX Measurements. The samples were also analyzed by energy-dispersive X-ray micro analysis where only the elements Ca and Mg as well as N were detected in the γ-Ca_3N_2 and Mg_3N_2 phases, respectively. A carbon coated sample was examined with a scanning electron microscope (SEM) JSM-6500F (Joel, Japan, maximum acceleration voltage 30 kV). Qualitative and semiquantitative elemental analyses were carried out using an energy dispersive spectrometer (Model 7418, Oxford Instruments, United Kingdom).

Soft X-ray Spectroscopy and DFT Calculations. The X-ray emission spectroscopy (XES) measurements was performed at the Advanced Light Source (Berkley, CA, USA) on beamline 8.0.1,[37] whereas X-ray absorption spectroscopy (XAS) measurements (measured in total fluorescence yield mode) took place at the Canadian Light Source (Saskatoon) on the SGM beamline.[38] The samples were prepared by pressing small fragments of calcium nitride into freshly scraped indium foil under argon atmosphere (the samples were never exposed to an oxygen or nitrogen environment). The N Kα XES and N 1s XAS were calibrated in energy using *h*-BN with the peaks near were the band gap located at 394.4 and 402.1 eV, respectively. The calculations were performed using the *WIEN2k* density functional theory (DFT) software[39] utilizing the generalized gradient approximation of Perdew−Burke−Ernzerhof (GGA−PBE).[40] A (9, 9, 3) k-point mesh integration with −6.0 Ryd plane wave cutoff was used. The RMT spheres for both the nitrogen and calcium atoms were 2.26 Bohr with an RK_{max} of 7.0. The XAS spectra were simulated with a full core hole potential correction. For further details on simulating XAS and XES with *WIEN2k*, see ref 41.

RESULTS AND DISCUSSION

In this work, we have investigated the HP/HT-behavior of the binary nitrides Ca_3N_2 and Mg_3N_2 employing the multianvil technique. The new dark red high-pressure phase γ-Ca_3N_2 was ex situ obtained by applying pressures between 8 and 18 GPa and temperatures below 1200 °C starting from ambient pressure α-Ca_3N_2, as well as β-Ca_3N_2.[26] In situ investigations at the synchrotron showed the phase transformation already at much lower pressures (0.8 GPa). HP/HT-investigations of Mg_3N_2 were carried out in a multianvil press at pressures from 8 to 18 GPa (1000−1200 °C) and in situ from 0 to 6 GPa (at RT), starting from ambient pressure α-Mg_3N_2. All handling had to be done in argon atmosphere as Ca_3N_2 and Mg_3N_2 are extremely air sensitive. Furthermore, the high-pressure experiments and the ex situ investigations also required special oxygen and moisture free conditions.

Structural Analysis of γ-Ca_3N_2. The powder pattern of γ-Ca_3N_2 (Figure 1) matched a cubic body-centered lattice with lattice parameter a = 7.7212(3) Å. All observed systematic extinctions correspond only to one space group, namely $I\bar{4}3d$ (no. 220). The crystal structure of the nitrides M_3N_4 (M = Zr, Hf),[10] crystallizing in the same space group, provided the starting model for the structure solution. Table 1 shows crystallographic data and details of the Rietveld refinement of γ-Ca_3N_2 and Table 2 displays the occupied Wyckoff sites, refined atomic coordinates and isotropic displacement parameters. Estimated standard deviations are calculated in agreement with ref 42.

Structure Description of γ-Ca_3N_2. The new high-pressure phase γ-Ca_3N_2 is the first binary nitride derived from the multifaceted anti-Th_3P_4 structure type family which exhibits a broad

Table 2. Occupied Wyckoff Sites, Refined Atomic Coordinates and Isotropic Displacement Parameters B_{iso} (in Å^2) of γ-Ca_3N_2 (Standard Deviation in Parentheses)

atom	Wyck.	*x*	*y*	*z*	s.o.f.	B_{iso}
Ca	16*c*	0.04762(7)	0.04762(7)	0.04762(7)	1	1.86(3)
N	12*a*	3/8	0	1/4	0.88[a]	2.61(2)

[a] calculated value from composition; refined occupancy for N: 0.93(3).

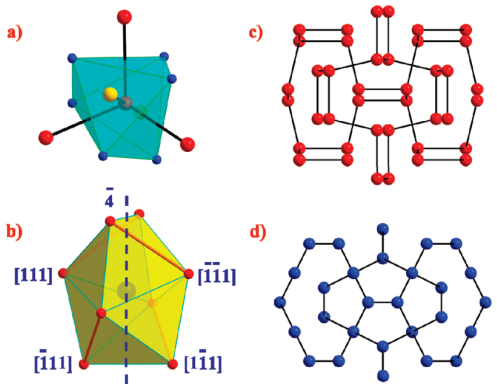

Figure 3. **a**) Ca^{2+}-octahedron with five next Ca-atoms (distances: Ca (red)−Ca (red) = 3.21 Å, Ca (red)−Ca (yellow) = 3.34 Å), **b**) N^{3-}-dodecahedron (yellow) with the $\bar{4}$ and the four different ⟨111⟩ directions in a rod packing, the 3-fold axes (orange) run along the edges of the dodecahedron, **c**) Ca^{2+}-lattice forming a 10,3-net, **d**) N^{3-}-lattice, (Ca (red) N (blue)).

spectrum of compositions (e.g., A_3B_4 with *A* = La, Ce, Pr, Nd, Tb, Dy, Ho, *B* = Ge, Sb, Bi[43] or Rb_4O_6[44] and Pu_2C_3).[45] γ-Ca_3N_2 ($[Ca^{2+}]_4([N^{3-}]_{2.67}[\square]_{0.33})$) constitutes a disordered defect variant of the anti-Th_3P_4 type (Figure 2). Vacancy and charge ordering phenomena of this structure type have been discussed in detail elsewhere.[46] The significant increase in CN from α-Ca_3N_2 to γ-Ca_3N_2, facilitated by high-pressure synthesis, is in accordance with the pressure-coordination rule.[47] α-Ca_3N_2 has CN = 4 for Ca^{2+}, forming tetrahedra with N^{3-} ligands. The Ca^{2+}-ions in γ-Ca_3N_2 are topologically 6-fold coordinated (part a of Figure 3), and the effective number of neighbors is 5.33 due to the defect structure. Face sharing of the octahedra is realized by the five next Ca-atoms. For N^{3-} the CN increases from 6 in α-Ca_3N_2 to 8 in γ-Ca_3N_2, building distorted dodecahedra. The distances within the polyhedra can be divided into two groups: one with short distances and one with long ones (Table 3). The Ca^{2+}-octahedra as well as the N^{3-}-dodecahedra (Figure 2) are condensed through common faces and are additionally interlinked through corners and edges. Subsequently, octahedral and dodecahedral polyhedra form columns running along the body diagonals ⟨111⟩ of the cubic unit cell.

O'Keeffe et al.[48] proposed a new approach to further characterize the complex crystal structure of the (anti-)Th_3P_4 structure type family. The authors introduced rod packings (Figure 4) or columns as a unifying principle to simplify the characterization of intricate crystal structures. They used a bcc rod packing scheme, as depicted in part a of Figure 4, to describe the Th_3P_4 structure with the nearest neighbors of a given atom along the ⟨111⟩ directions, and all of the atoms of the structure are located on rods along these directions.

Bärnighausen et al.[11] however described the Th_3P_4 structure by analyzing the enantiomeric 10,3-networks with cubic symmetry

Table 3. Selected Bond Lengths (in Angstroms) and Angles (in Degrees) of γ-Ca_3N_2, (Standard Deviations in Parentheses)

atom	distance
Ca−N (3*x*)	2.4027(5)
Ca−N (3*x*)	2.9944(5)
N−Ca (4*x*)	2.4027(5)
N−Ca (4*x*)	2.9944(5)
Ca−Ca (3*x*)	3.2106(8)
Ca−Ca (2*x*)	3.3434(8)
Ca−Ca (2 + 4*x*)	3.5014(8)
N−N	3.6113(1)
atom	**angle**
N−Ca−N (3*x*) short dist.	97.442(18)
N−Ca−N (3*x*) long dist.	74.170(15)
Ca−N−Ca (2*x*) short dist.	93.55(3)
Ca−N−Ca (2*x*) short dist.	151.20(4)
Ca−N−Ca (2*x*) long dist.	64.84(2)
Ca−N−Ca (2*x*) long dist.	135.45(3)

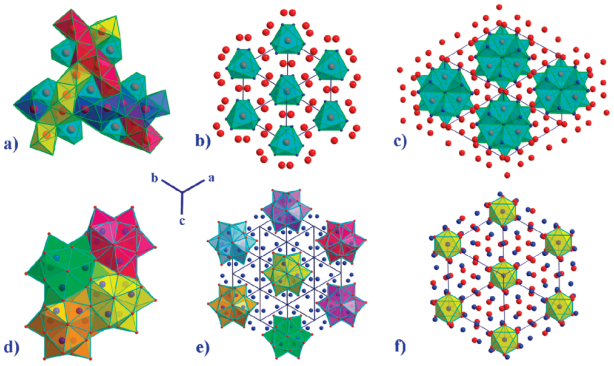

Figure 4. γ-Ca_3N_2: **a**) bcc rod packing of Ca^{2+}-octahedra (yellow, turquoise, pink and green) parallel to different ⟨111⟩, **b**) pattern of rods of Ca^{2+}-octahedra running along ⟨111⟩, **d**) and **e**) rods of N^{3-}-dodecahedra viewed along ⟨111⟩, α-Ca_3N_2: rods of c) Ca^{2+}-tetrahedra and f) N^{3-}-octahedra running along ⟨111⟩, (Ca (red) N (blue)).

formed by the anion lattice (e.g., Sm_3S_4)[11] opposed to the rod packings description used by O'Keeffe and co-workers.[48] The 10,3-networks form two chiral networks whose structure depends upon their respective angles (part c of Figure 3).

Comparison of α-, *β*-, and γ-Ca_3N_2. In α-Ca_3N_2 as well as in γ-Ca_3N_2, both Ca^{2+}- and N^{3-}-ions form rods along ⟨111⟩. The rod packing concept is a powerful tool for the comparison of α-Ca_3N_2 with the HP-phase. The directions ⟨111⟩ in α-Ca_3N_2 are only partially occupied by Ca^{2+}-ions, contrary to γ-Ca_3N_2. The connectivity of the polyhedra only through corners and edges in α-Ca_3N_2 leads to a layered pattern with vacancies due to the missing connection through common faces. The lack of these vacancies in γ-Ca_3N_2 generates an increased density compared to α-Ca_3N_2.

The density increases significantly from α-Ca_3N_2 (2.60 gcm^{-3}) to *β*-Ca_3N_2 (2.69 gcm^{-3}) and to γ-Ca_3N_2 (2.85 gcm^{-3}), resulting in a difference of 9.6% (Table 4). The γ-Ca_3N_2 phase has a notably higher density (2.85 gcm^{-3}) compared to the

Table 4. Comparison of α-, *β*-, and *γ*-Ca_3N_2

Ca_3N_2	S.G.	cell [Å]	Wyck./ Ca	ρ [g cm^{-3}]	V [Å^3]	V/atom [Å^3]
α	$Ia\bar{3}$(no.206)	a = 11.47	48e	2.60	1502	18.87
β	$R\bar{3}c$ (no.167)	a = 6.19	18e	2.69	550	18.43
		c = 16.62				
γ	$I\bar{4}3d$ (no.220)	a = 7.72	16c	2.85	460	17.25

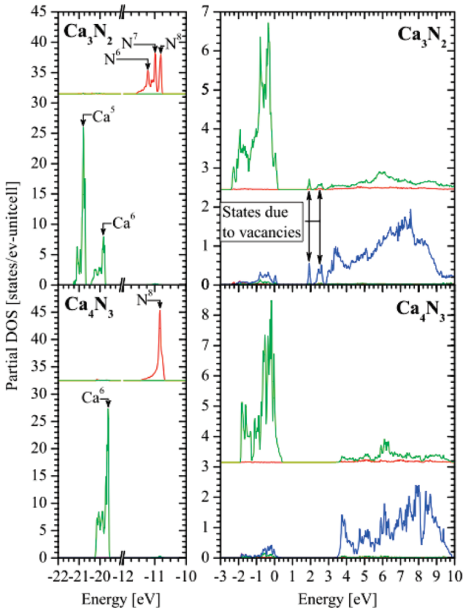

Figure 5. Calculated partial density of states (pDOS) for the nitrogen sites are displayed in the top portion of each panel, calcium in the lower portion. The s-states (red), p-states (green), and d-states (blue) are color-coded. The pDOS are offset vertically by an arbitrary value for display purposes; the relative pDOS value remains accurate. The introduction of nitrogen vacancies splits the tightly bound states (N s and Ca p) and creates localized states in the band gap. These tightly bound states are labeled N[x] and Ca[y] (where x and y refer to the number of N nearest neighbors).

calculated value of 2.79 g·cm^{-3} by Römer et al.[27] for the theoretically predicted *γ*-phase (anti-Rh_2O_3—II structure) expected to form between 5 and 10 GPa. According to the principle of Le Chatelier this precludes the existence of the above calculated phase as our experiments established the in situ formation of cubic *γ*-Ca_3N_2 beginning at 0.8 GPa.

The structure types of the three hitherto identified Ca_3N_2 modifications show no direct group—subgroup symmetry relations. The phase transitions from the metastable *β*-Ca_3N_2 with anticorundum structure to α-Ca_3N_2 as well as *γ*-Ca_3N_2 are reconstructive. α-Ca_3N_2 and *γ*-Ca_3N_2 can be described by the rod-packing concept employing different types of rods, but this model cannot be applied to the *β*-phase because its structure is distinctly characterized by layers. *β*-Ca_3N_2 is probably a low-temperature phase, which is metastable at room temperature and based on its observation at 5 K has a higher density compared to the α-phase (there is a *β* to α transition at 810 K).[26] Therefore, the formation of *γ*-Ca_3N_2 from α-Ca_3N_2 might proceed via an intermediate formation of *β*-Ca_3N_2.

Soft X-ray Spectroscopy and DFT Calculations of *γ*-Ca_3N_2. Soft X-ray spectroscopy in conjunction with first principles DFT calculations can elucidate the chemical bonding and electronic behavior of *γ*-Ca_3N_2 and gain additional insight into its structure. Two different superstructure models — one with and one without nitrogen vacancies — are compared. The partial densities of states (pDOS) calculated using DFT are shown in Figure 5, where the vacancy model (referred to hereafter as Ca_3N_2), is compared to the nonvacancy model (referred to hereafter as Ca_4N_3). If we assume that all atoms would prefer to exist in their formal oxidation states, Ca^{2+} and N^{3-}, then the molecular formula should be Ca_3N_2 requiring that 1.333 ($1 + {}^1/_3$) N atoms must be removed from the unit cell. This is achieved with a $1 \times 1 \times 3$ supercell in which four nitrogen atoms are removed. The vacancies are uniformly distributed in such a way that there is no bond ordering and thus results a space group symmetry that is now *P*1 (all crystallographic sites are nonequivalent, Figure 6).

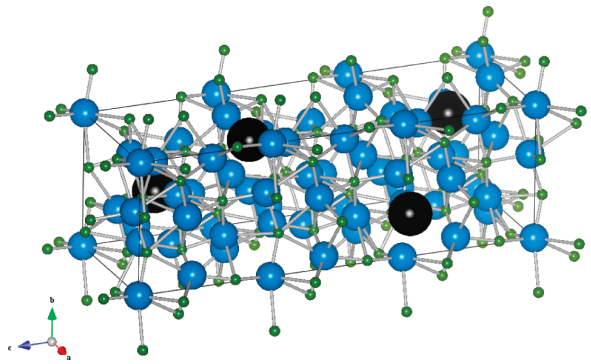

Figure 6. Super cell used to calculate the DOS of Ca_3N_2. The calcium, nitrogen, and vacancies are displayed in blue, green, and black, respectively.

The DOS for both models (Figure 5) suggests that bonding in this material is strongly ionic in the sense that most of the Ca valence electrons have been transferred to the N atoms. The evidence for this is manifested in that the valence band (which is energetically localized and about 2 eV wide) is predominately comprised of occupied N *p*-states. The conduction band, however, consists predominately of unoccupied Ca *d*-states. The valence and conduction band contribution of the Ca- and N-states respectively are negligible. Such ionic bonding character further supports the vacancy model because N vacancies are necessary for all atoms to exist in their formal oxidation states. The effect of the N vacancies is readily seen in the pDOS in both the low-energy conduction band states and the sub-valence band (sub-band) states. The tightly bonded sub-bands (Ca 3p and N 2s) are split into the contributions of the Ca and N nonequivalent sites and occur due to the creation of nonequivalent sites in Ca_3N_2. There are eight Ca atoms surrounding all three N sites, however the next coordination shell including the missing N atoms (vacancies) perturbs the electronic structure creating multiple localized states (Figure 7). This is further illustrated by the Ca *p*-band splitting between the Ca atoms with and without an N atom missing from their octahedron. In the conduction band, the nitrogen vacancies create interband states, which play a key role in distinguishing the model that best simulates the experimental measurements because this seems to be the only observable difference in the electronic states.

The pDOS of this material suggests that it possesses some very interesting electronic properties. In particular for Ca_4N_3, there is a substantial amount of valence electron states that are unfilled

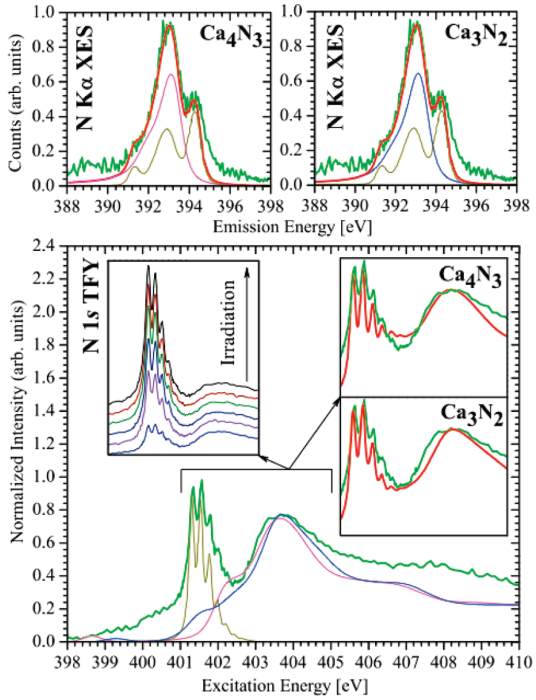

Figure 7. Experimental X-ray emission spectra (XES) and X-ray absorption spectra (measured in total fluorescence mode — TFY). The experimental spectra are shown in green, the simulated spectra (appropriately broadened with a pseudo-Voigt function) are shown in blue (Ca_3N_2) and magenta (Ca_4N_3). The reference N_2 spectra from refs 49 (XES) and 50 (TFY) shown in brown are added to the calculated spectra, which takes into account the N_2 gas in the material. In successive scans the amount of trapped N_2 increases. The comparison of the added spectra (red) with the measured spectra (green) favors the inclusion of N vacancies.

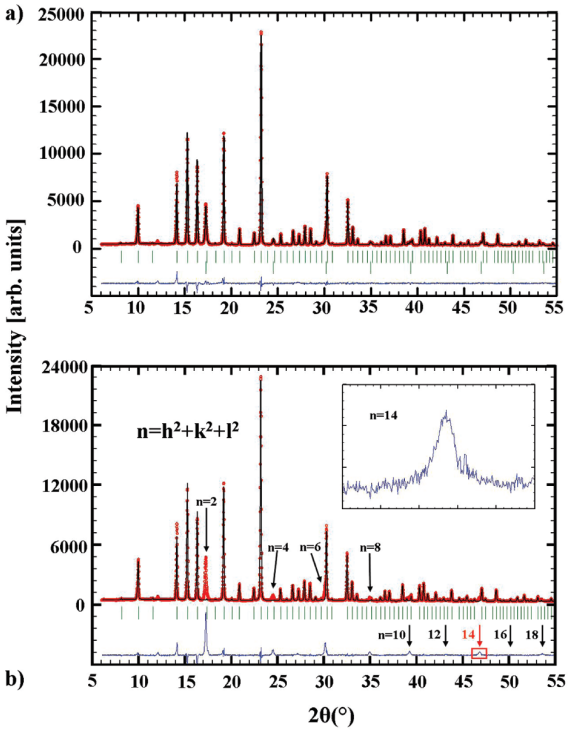

Figure 8. a) Observed (circles) and calculated (line) X-ray powder diffraction pattern together with their difference curve after Rietveld refinement (λ = 0.709026 Å). The upper row of reflection marks corresponds to Mg_3N_2 and the lower one to HP—Mg (10% w/w), b) X-ray powder diffraction pattern of only Mg_3N_2. The reflections in the difference plot correspond to HP—Mg.

suggesting that this material exhibits semimetal properties. These unfilled valence states are diminished when the structure includes N vacancies; the unfilled states in Ca_4N_3 and Ca_3N_2 are 0.768*e* and 0.519*e*, respectively. These materials have a calculated direct band gap of 2.59 and 1.64 eV for Ca_4N_3 and Ca_3N_2, respectively. Strictly speaking this is not the energy separation between occupied and unoccupied states but a forbidden energy gap within the unoccupied states. The band gap of Ca_3N_2 shrinks due the decrease in periodic symmetry of the Ca and N sites within the lattice creating interband states at the bottom of the conduction band. Therefore, the N vacancies increase the semiconductor nature of calcium nitride. Calcium nitride has a tendency to hydrolyze readily, therefore only the nitrogen spectral measurements are presented since the calcium measurements are distorted due to inherent CaO surface contamination. These experimental measurements compared to those simulated using DFT calculations of Ca_4N_3 and Ca_3N_2 are shown in Figure 7. The measurements themselves create interstitial N_2 (gas) within the material as a result of X-ray irradiation. Taking successive XAS scans and noting that the N_2 portion of spectra increases in intensity with progressive exposure to radiation is a verification of this. There is clear evidence that an N_2 gas contribution exists in both the XES and XAS spectra (Figure 7), therefore calculated N_2 spectra[49,50] have been added to the simulated calcium nitride spectra to account for this contribution and provide a more meaningful comparison between measured and simulated spectra. The N Kα XES spectra do not allow us to determine whether N vacancies are present due to the large lifetime broadening the spectra exhibit — both models agree equally well with the experimental measurements. The N 1s XAS spectra show a larger sensitivity to N vacancies; the vacancies reduce the band gap and produce states further away from the large feature at ~404 eV (previously mentioned in the DOS). In the region from 401 to 404 eV, the experimental spectrum is best reproduced by the Ca_3N_2 simulation, confirming that there are N vacancies present in the material. The feature at 398.8 and 399.2 eV (Figure 7) for Ca_4N_3 and Ca_3N_2 respectively is diminished for Ca_3N_2. Because this feature is not present in the measured spectrum this would suggest that vacancies must be present (the presence of the core hole reduces the intensity of this feature from that seen in the DOS). Whereas both simulated spectra of Ca_4N_3 and Ca_3N_2 have a quite satisfactory fit, the Ca_3N_2 model fits significantly better.

High-Pressure Behavior of Mg_3N_2. *Structural Analysis of bcc—Mg.* Concerning the high-pressure behavior of Mg_3N_2, ex situ multianvil experiments at 9 GPa showed no changes in the powder diffraction pattern of α-Mg_3N_2, apart from further crystallization. However at 12 GPa new reflections appeared in the powder pattern (part a of Figure 8). The newly formed phase remains metastable after quenching for several hours at room temperature and ambient pressure. At first, the structure determination for the new phase was attempted corresponding to the structure solution of γ-Ca_3N_2. The refined structure did not match with the measured pattern, which

precluded a HP−Mg_3N_2 phase with anti-Th_3P_4 structure. Furthermore, the structure did not belong to any of the predicted phases for Mg_3N_2 calculated by Römer, Hao, and co-workers.[28,29] The new reflections could be indexed based on a body-centered cubic (bcc) unit cell with a = 3.3381(2) Å and V = 37.19 Å^3. Without additional extinction rules and based on reasonable interatomic distances within the small unit cell volume, the structure of bcc metals with $Im\bar{3}m$ (no. 229) space group symmetry (Table 5) and only atoms on the 2a-site (0, 0, 0) is proposed (Table 6). Estimated standard deviations are calculated in agreement with ref 42.

For illustration of the contribution from the bcc−Mg phase to the powder diffraction pattern, a simulated pattern of only α-Mg_3N_2 was compared with the measured pattern. The difference plot marks the peaks of bcc−Mg very clearly (part b of Figure 8). Note that an alternative indexing, based on a primitive cubic (pc) structure with $a_{pc} = a_{bcc}/\sqrt{2}$ is not possible. The reflection with $n_{bcc} = h^2 + k^2 + l^2 = 14$ is observed and cannot be explained by the alternative pc structure, because $n_{pc} = 7$ is not possible. Such diffraction patterns have been observed under in situ conditions as well, where only Mg can form such a bcc−metal structure. Rietveld refinement[36] confirmed the formation of about 10% (w/w) bcc−Mg with a volume-weighted averaged crystallite diameter between 30 and 35 nm.

High-Pressure Behavior of Mg. In high-pressure studies Olijnyk et al.[52] observed the formation of bcc−Mg from hcp−Mg at 58 GPa and the transition back to the hcp phase during pressure release at 44 GPa. The bcc modification found by Olijnyk et al.[52] at 58 GPa (and measured at that pressure) has a compressed lattice parameter (a = 2.9539 Å) and a considerably decreased volume (V = 25.77 Å^3) compared to our values, which

Table 5. Crystallographic Data of HP−Mg Derived from Rietveld Refinement

formula	Mg
formula mass/g mol^{-1}	24.30
crystal system	cubic
space group	$Im\bar{3}m$ (no. 229)
cell parameters/Å	a = 3.3381(2)
cell volume/Å^3	37.1963(9)
formula units/cell	2
diffractometer	STOE STADI P
radiation/Å	Mo−Kα_1 (λ = 0.70926 Å)
monochromator	Ge 111 (curved)
temperature/K	293
data range (2θ), step width	$5° \le 2\theta \le 56°$, 0.01°
structure refinement	Rietveld refinement, *Fullprof*[36]
background treatment	17 fixed background points
profile function	pseudo-Voigt (no. 7)
R_{Bragg}	2.84
GOF	1.7
reduced χ^2	3.05

Table 6. Occupied Wyckoff Sites, Refined Atomic Coordinates, and Isotropic Displacement Parameters B_{iso} (in Å^2) of Mg (hcp)[51] and HP−Mg (bcc), (Standard Deviation in Parentheses)

	atom	Wyck.	x	y	z	s.o.f.	B_{iso}
Mg (hcp)	Mg	2c	1/3	2/3	1/4	1	0.49(5)
HP−Mg (bcc)	Mg	2a	0	0	0	1	0.44(14)

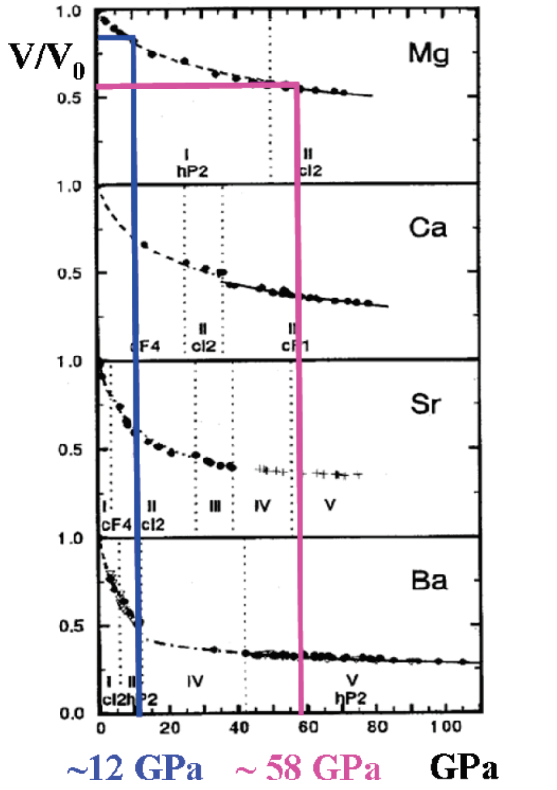

Figure 9. Equation of State of Mg:[51−53] V/V_0-data of HP−Mg (V/V_0 = 0.80) at 12 and 58 GPa[53] (V/V_0= 0.55).

Table 7. Comparison of Mg (hcp) and HP−Mg (bcc),

	Mg (hcp)	HP−Mg (bcc)	
crystal system	hexagonal[51]	cubic	cubic[52,53]
space group	$P6_3/mmc$ (no. 194)	$Im\bar{3}m$ (no. 229)	$Im\bar{3}m$ (no. 229)
cell parameters/Å	a = 3.20	a = 3.33	a = 2.95 (at 586Pa)
	c = 5.21		
cell volume/Å^3	46.48	37.19	25.75
formula units/cell	2	2	
density/ρ	1.73	2.17	3.14
formation pressure	ambient pressure	2 (in situ)/ 12 (ex situ) GPa	58−48 (in situ) GPa
distance Mg−Mg/Å	3.19 (12x)	2.89 (8x)	2.55 (8x)

dx.doi.org/10.1021/ja106459e |*J. Am. Chem. Soc.* 2011, 133, 4307–4315

is due to the extremely high pressure. A rough estimate of the bulk modulus B using these[52] and our data coincide perfectly with the EOS measurements of Mg up to 70 GPa made by Winzenick et al.[53] (Figure 9) in a reasonable order of magnitude (mean $B \approx$ 160 GPa).

These HP-phase transitions are well-known for metals (e.g., Cs,[54] Yb,[55,56] Y).[57] Note that the required pressure for the formation of HP-phases can significantly be reduced for nanosized particles, even down to ambient conditions.[58] The pressure-induced elimination of nitrogen from Mg_3N_2 causes the formation of nanosized[58] Mg-particles because of diffusion-limited crystallite growth. Mg_3N_2 is therefore a suitable precursor for the preparation of a metastable high-pressure bcc−Mg phase at very moderate pressures (e.g., ex situ 12 GPa and in situ 2 GPa) working via precipitation of nanosized Mg metal during decomposition. For a comparison of Mg (hcp) and HP−Mg (bcc), see Table 7. The formation of the high-pressure bcc phase instead of the hcp phase of Mg can be explained with surface curvature effects[58] of the nanoparticles as well as *d*-electron effects resulting from the lowering and partial filling of the initially unoccupied 3d-band with sufficiently high pressure.[59] The tendency of Mg_3N_2 to decompose under extreme conditions might constitute a fine precursor for industrial applications, but at the same time renders any predicted high-pressure phase of Mg_3N_2 improbable.

CONCLUSIONS

In this work, we investigated the high-pressure behavior of the alkaline earth binary nitrides Ca_3N_2 and Mg_3N_2. These two compounds present an entirely different behavior, which might be due to the fact that calcium is much larger and therefore much more compressible than magnesium. With the larger Ca the high-pressure structure seems to be stabilized, whereas no phase transformation takes place for Mg_3N_2 but the smaller magnesium is only forced out of the structure.

Ca_3N_2 forms the very dense high-pressure phase γ-Ca_3N_2 at 9 GPa, with a new defect structure type for binary nitrides. The intricate anti-Th_3P_4 structure type exhibits high CN (for $Ca^{[6]}$ (topologically) and $N^{[8]}$) and has already shown interesting materials properties in numerous compounds. The ab initio DFT calculations suggest that ($[Ca^{2+}]_4([N^{3-}]_{2.67}[\square]_{0.33}$) may even have semimetal properties, but to a lower degree compared with a hypothetical Ca_4N_3, which was also taken into consideration. The calcium nitrogen bonding is highly ionic and shows a large amount of charge transfer suggesting that the N and Ca exist in their formal oxidation states. The simulated γ-Ca_3N_2 spectra (for a vacancy model) reproduce the measured calcium nitride spectra best. To conclude, the high-pressure calcium nitride structure has a propensity to form N vacancies. In contrast to the high-pressure behavior of Ca_3N_2, Mg_3N_2 shows decomposition behavior starting already at moderate pressures (at room temperature). The advancing bcc modification of elemental Mg nanoparticles is metastably quenchable and might be a promising precursor for the customized design of new compounds with promising properties and new applications.

AUTHOR INFORMATION

Corresponding Author
wolfgang.schnick@uni-muenchen.de

ACKNOWLEDGMENT

The authors gratefully acknowledge financial support from the Fonds der Chemischen Industrie and the Deutsche Forschungsgemeinschaft (priority program SPP 1236, project SCHN 377/13) Germany. We further would like to thank the Natural Sciences and Engineering Research Council of Canada (NSERC) and the Canada Research Chair Program. Tom Z. Regier from the Canadian Light Source (CLS) is acknowledged for his help in setting up the measurements at CLS.

REFERENCES

(1) Bundy, F. P.; Hall, H. T.; Strong, H. M.; Wentorf, R. H. *Nature* **1955**, *176*, 51.
(2) McMillan, P. F. *Nat. Mater.* **2002**, *1*, 19.
(3) Wentorf, R. H. *J. Chem. Phys.* **1957**, *26*, 956.
(4) Oganov, A. R.; Chen, J.; Gatti, C.; Ma, Y.; Ma, Y.; Glass, C. W.; Liu, Z.; Yu, T.; Kurakevych, O. O.; Solozhenko, V. L. *Nature* **2009**, *457*, 863.
(5) Zarechnaya, E. Yu.; et al. *Phys. Rev. Lett.* **2009**, *102*, 185501–1.
(6) Amaya, K.; Shimizu, K.; Eremets, M. I. *Int. J. Mod. Phys. B* **1999**, *13*, 3623.
(7) Eremets, M. I.; Gregoryanz, E. A.; Struzhkin, V. V.; Mao, H.-K.; Hemley, R. J.; Mulders, N.; Zimmerman, N. M. *Phys. Rev. Lett.* **2000**, *83*, 2797.
(8) Eremets, M. I.; Struzhkin, V. V.; Mao, H.-K.; Hemley, R. J. *Science* **2001**, *293*, 272.
(9) Zerr, A.; Miehe, G.; Serghiou, G.; Schwarz, M.; Kroke, E.; Riedel, R.; Fuess, H.; Kroll, P.; Boehler, R. *Nature* **1999**, *400*, 340.
(10) Zerr, A.; Miehe, G.; Riedel, R. *Nat. Mater.* **2003**, *2*, 185.
(11) Heim, H.; Bärnighausen, H. *Acta Crystallogr., Sect. B* **1978**, *34*, 2084.
(12) Flahaut, J.; Guitard, M.; Patrie, M.; Pardo, M.; Golbai, S.; Domange, L. *Acta Crystallogr.* **1965**, *19*, 14.
(13) Wang, X.; Loa, I.; Syassen, K.; Kremer, R.; Simon, A.; Hanfland, M.; Ahn, K. *Phys. Rev. B* **2005**, *72*, 064520–1.
(14) Westerhold, K.; Timmer, F.; Bach *Phys. Rev. B* **1985**, *32*, 2985.
(15) Kroll, P. *Phys. Rev. Lett.* **2003**, *90*, 125501–1.
(16) Horvath-Bordon, E.; Riedel, R.; Zerr, A.; McMillan, P. F.; Auffermann, G.; Prots, Y.; Bronger, R.; Kniep, R.; Kroll, P. *Chem. Soc. Rev.* **2006**, *35*, 987.
(17) Zerr, A.; Miehe, G.; Li, J.; Dzivenko, D. A.; Bulatov, V. K.; Höfer, H.; Bolfan-Casanova, N.; Fialin, M.; Brey, G.; Watanabe, T.; Yoshimura, M. *Adv. Funct. Mater.* **2009**, *19*, 2282.
(18) Hirosaki, N.; Uheda, K.; Yamamoto, H. PCT WO/2005/052087 A1.
(19) Solozhenko, V. L.; Turkevich, V. Z.; Will, G. *J. Am. Ceram. Soc.* **1996**, *79*, 2798.
(20) Bocquillon, G.; Loriers-Susse, C.; Loriers, J. *J. Mater. Sci.* **1993**, *28*, 3547.
(21) Akihiko, T.; Kaoru, M.; Kenjirok, I.; Ryo, M.; Moriyoshi, K.; Makoto, I.; Akihiko, K.; Eishi, S.; K.Takeshi, Eiichiro, Y.; , EP 0952131 A1.
(22) Xiong, Z.; Chen, P.; Wu, G.; Lin, J.; Tan, K. L. *J. Mater. Chem.* **2003**, *13*, 1676.
(23) Laurent, Y.; David, J.; Lang, J. *C. R. Acad. Sci. Paris* **1964**, *259*, 1132.
(24) Reckeweg, O.; DiSalvo, F. *Z. Anorg. Allg. Chem.* **2001**, *627*, 371.
(25) Bradley, R.; Munro, D.; Whitfield, M. *J. Inorg. Nucl. Chem.* **1966**, *28*, 1803.
(26) Höhn, P.; Hoffmann, S.; Hunger, J.; Leoni, S.; Nitsche, F.; Schnelle, W.; Kniep, R. *Chem.—Eur. J.* **2009**, *15*, 3419.
(27) Römer, S. R.; Schnick, W.; Kroll, P. *J. Phys. Chem. C* **2009**, *113*, 2943.
(28) Römer, S. R.; Dörfler, T.; Kroll, P.; Schnick, W. *Phys. Status Solidi B* **2009**, *246*, 1604.

(29) Hao, J.; Li, Y.; Zhou, Q.; Liu, D.; Li, M.; Li, F.; Lei, W.; Chen, X.; Ma, Y.; Cui, Q.; Zou, G.; Liu, J.; Li, X. *Inorg. Chem.* **2009**, *48*, 9737.
(30) Hao, J.; Li, Y. W.; Wang, J. S.; Ma, C. L.; Huang, L. Y.; Liu, R.; Cui, Q. L.; Zou, G. T.; Liu, J.; Li, X. D. *J. Phys. Chem. C* **2010**, *114*, 16750.
(31) Huppertz, H. *Z. Kristallogr.* **2004**, *219*, 330.
(32) Walker, D.; Carpenter, M. A.; Hitch, C. M. *Am. Mineral.* **1990**, *75*, 1020.
(33) Walker, D. *Am. Mineral.* **1991**, *76*, 1092.
(34) Rubie, D. C. *Phase Trans.* **1999**, *68*, 431.
(35) Decker, D. L. *J. Appl. Phys.* **1971**, *42*, 3239.
(36) Rodriguez-Carvajal, J. *Fullprof.2k* — version 4.40, 2008.
(37) Jia, J. J.; Callcott, T. A.; Yurkas, J.; Ellis, A. W.; Himpsel, F. J.; Samant, M. G.; Stöhr, J.; Ederer, D. L.; Carlisle, J. A.; Hudson, E. A.; Terminello, L. J.; Shuh, D. K.; Perera, R. C. C. *Rev. Sci. Instrum.* **1995**, *66*, 1394.
(38) Regier, T.; Krochak, J.; Sham, T. K.; Hu, Y. F.; Thompson, J.; Blyth, R. I. R. *Nucl. Instrum. Methods Phys. Res., Sect. A* **2007**, *582*, 93.
(39) Schwarz, K.; Blaha, P.; Madsen, G. K. H. *Comput. Phys. Commun.* **2002**, *147*, 71.
(40) Perdew, J. P.; Burke, K.; Ernzerhof, M. *Phys. Rev. Lett.* **1996**, *77*, 3865.
(41) Boyko, T. D.; Bailey, E.; McMillan, P. F.; Moewes, A. *Phys. Rev. B* **2010**, *81*, 155207.
(42) Berar, J. F.; Lelann, P. *J. Appl. Crystallogr.* **1991**, *24*, 1.
(43) Honke, D.; Parthé, E. *Acta Crystallogr.* **1966**, *21*, 435.
(44) Jansen, M.; Korber, N. *Z. Anorg. Allg. Chem.* **1991**, *598/599*, 163.
(45) Zachariasen, W. *Acta Crystallogr.* **1952**, *5*, 17.
(46) Carter, F. *J. Solid State Chem.* **1972**, *5*, 300.
(47) Neuhaus, A. *Chimia* **1964**, *18*, 93.
(48) O'Keeffe, M.; Andersson, S. *Acta Crystallogr., Sect. A* **1977**, *33*, 914.
(49) Glans, P.; Skytt, P.; Gunnelin, K.; Guo, J.-H.; Nordgren, J. *J. Electron Spectrosc. Relat. Phenom.* **1996**, *82*, 193.
(50) Rubensson, J.-E.; Neeb, M.; Biermann, M.; Xu, Z.; Eberhardt, W. *J. Chem. Phys.* **1993**, *99*, 1633.
(51) Straumanis, M. E. *J. Appl. Phys.* **1949**, *20*, 726.
(52) Olijnyk, H.; Holzapfel, W. B. *Phys. Rev. B* **1985**, *31*, 4682.
(53) Winzenick, M.; Holzapfel, W. B. In *High Pressure Science and Technology, Proceedings of the Joint XV AIRAPT and XXXIII EHPRG International Conference on High Pressure Science and Technology*; Trzeciakowski, W. A., Ed.; 384; World Scientific Publ. Co.: Singapore, 1996.
(54) Takemura, K.; Syassen, K. *Phys. Rev. B* **1985**, *32*, 2213.
(55) Takemura, K.; Syassen, K. *J. Phys. F: Met. Phys.* **1985**, *15*, 543.
(56) Kayser, F. X. *Phys. Status Solidi A* **1971**, *8*, 233.
(57) Vohra, Y. K.; Olijnik, H.; Grosshans, W.; Holzapfel, W. B. *Phys. Rev. Lett.* **1981**, *47*, 1065.
(58) Guo, B.; Harvey, A. S.; Neil, J.; Kennedy, I. M.; Navrotsky, A.; Risbud, S. H. *J. Am. Ceram. Soc.* **2007**, *90*, 3683.
(59) Moriarty, J. A.; McMahan, A. K. *Phys. Rev. Lett.* **1982**, *48*, 809.

Anion ordering in spinel-type gallium oxonitride

Teak D. Boyko,[1,*] Carmen E. Zvoriste,[2] Isabel Kinski,[3] Ralf Riedel,[2] Stefanie Hering,[4]
Hubert Huppertz,[4] and Alexander Moewes[1]

[1]*Department of Physics and Engineering Physics, University of Saskatchewan, Saskatoon, Saskatchewan, Canada S7N 5E2*
[2]*Fachbereich Material- und Geowissenschaften, Technische Universität Darmstadt, D-64287 Darmstadt, Germany*
[3]*Fraunhofer Institute for Ceramic Technologies and Systems, D-01277 Dresden, Germany*
[4]*Department Chemie, Ludwig-Maximilians-Universität München, D-81377 München, Germany*

(Received 16 June 2011; revised manuscript received 1 August 2011; published 19 August 2011)

The specific locations of the anions—nitrogen and oxygen—in the crystallographic sites are not known in the spinel-type gallium oxonitride. We report here on an indirect method for determining the specific location of the light elements N and O in a defect spinel-structured gallium oxonitride, $Ga_{2.79}O_{3.05}N_{0.76}$. The locations of elements that are adjacent in the periodic table ($\Delta Z = \pm 1$) are indistinguishable with conventional x-ray diffraction techniques. However, by examining the local electronic structure we show that the anions are spatially ordered such that $R\bar{3}m$ (no. 166) is the most appropriate defect-free space group. Finally, we determined the electronic band gap of $Ga_{2.79}O_{3.05}N_{0.76}$ experimentally to be 2.95 ± 0.30, agreeing with our calculated value of 2.79 eV (direct) for Ga_3O_3N using a local density approximation functional including a semilocal potential modified from that of Becke and Johnson (the MBJLDA functional).

DOI: 10.1103/PhysRevB.84.085203 PACS number(s): 61.50.−f, 71.20.Mq, 78.70.En, 61.05.cj

I. INTRODUCTION

Over the last decade, spinel-structured nitrides have been an active area of research spurred by the synthesis of the first spinel-structured nitride, silicon nitride (γ-Si_3N_4).[1] Almost simultaneously, spinel-structured germanium nitride[2] (γ-Ge_3N_4) was synthesized using similar methods. These nitride phases are synthesized in a high-pressure (15 GPa) and high-temperature (2000 K) environment from their low-pressure trigonal or hexagonal phase (α-Si_3N_4 or β-Si_3N_4) via shock synthesis experiments[3] or diamond anvil cell[4] and multianvil cell[5] experiments. Several studies have been carried out regarding ternary nitrides and oxonitrides[6–15] in an effort to tailor the highly desirable mechanical and electronic properties associated with spinel nitrides to suit specific applications.

Gallium oxonitride (Ga_3O_3N) with spinel structure was first predicted by Lowther *et al.*[16] and has since been synthesized recently by several groups.[12,14,17] The large amount of interest in this material is due to the widespread use of w-GaN and β-Ga_2O_3. Furthermore, Ga_3O_3N is thought to have robust mechanical and chemical properties similar to the binary phases in the Ga-O-N system, and a predicted direct electronic band gap.[10–12]

The electronic band gap of a functional material is arguably one of the most important properties. Numerous theoretical studies have focused on the electronic properties and electronic band gaps of compounds with spinel structure.[6,7,18] Spinel-structured nitrides, in comparison to their respective low-pressure phases, exhibit reduced band gap values allowing these materials to be used in applications that require the device to absorb visible light.[6,19] With the knowledge that these cubic crystals with large coordination numbers have reduced electronic band gaps, research has expanded further into spinel-type oxonitrides in an effort to engineer the band gap value by varying the N:O ratio. Previously, theoretical studies show that gallium oxonitride with ideal structure (Ga_3O_3N) might have a band gap comparable to that of w-GaN or slightly larger,[10,12] allowing potentially useful electronic applications. Direct band gap values calculated using the local density approximation (LDA) and generalized gradient approximation (GGA) are 1.72 and 1.37 eV, respectively.[13] However, it is well known that LDA and GGA calculations underestimate the band gap[20] and the actual band gap value of Ga_3O_3N may be as large as 4 eV.[10] To date, we know of no reports of a measured band gap value for cubic gallium oxonitride.

There are two recent reports on the synthesis of a defect structure gallium oxonitride.[12,14] These studies show that in gallium oxonitride the octahedral site in the spinel structure is not fully occupied and has inherent octahedral gallium vacancies. The two studies report gallium oxonitride with similar stoichiometry, $Ga_{2.79}\square_{0.21}O_{3.05}N_{0.76}\square_{0.19}$ (Ref. 14) and $Ga_{2.81}O_{3.24}N_{0.64}$ (Ref. 12), where □ indicates cationic and anionic vacancies. The occupation of the cation sites, 2.79/3.00 (Ref. 14) and 2.81/3.00 (Ref. 12), was determined through x-ray diffraction (XRD) measurements. However, in order to determine the anion occupations, the ratio of N to O was determined with electron microprobe or electron energy loss spectroscopy measurements and used as a fitting parameter. The complete structural picture (including differentiating between the positions of N and O) of spinel-type gallium oxonitride is not well known. The current experimental results show that the $Ga_{2.79}O_{3.05}N_{0.76}$ system crystallizes in the spinel-type structure ($Fd\bar{3}m$, no. 227) with tetrahedrally and octahedrally coordinated gallium cations, while the anions are tetrahedrally coordinated. The site occupation of the cations (Ga Wyckoff sites 8*a* and 16*d*) is well known, but the positions of the different anions (N and O) are not distinguishable with XRD and are generalized to a single Wyckoff site, 32*e*.[14,21] Determination of a complete structural picture of $Ga_{2.79}O_{3.05}N_{0.76}$ is invaluable for understanding its electronic and mechanical properties. A better understanding of the crystal structure will also facilitate more efficient synthesis methods to produce purer phases with tailored mechanical and electronic properties.

Several theoretical works exist in which the anion ordering in Ga_3O_3N is discussed.[10,12] In one of these studies,[12] it was

assumed that N and O retain their F arrangements, resulting in three distinct ideal (i.e., defect-free with an N:O ratio of 1:3) crystallographic groups: $Imm2$ (no. 44), $Ima2$ (no. 46), and $R\bar{3}m$ (no. 166). Density functional theory (DFT) calculations based on these structures considering equilibrium energy yielded the $R\bar{3}m$ space group as the likely candidate structure; placing the nitrogen atoms in positions such that they are as far away from other nitrogen atoms as possible minimizes the calculated total energy.[10] An experimental confirmation has not yet been reported however. This motivates the use of x-ray absorption spectroscopy (XAS) measurements, which is a useful tool to examine the local electronic structure. For example, XAS has been employed to determine the local crystal structure of β-SiAlON compounds.[22] While this technique does not directly probe the crystal structure, it analyzes the local electronic structure and as such provides a way to indirectly determine the local bonding environment. This technique and the results presented here determine a possible local structure and the band gap of spinel-type gallium oxonitride.

II. METHODS

The spinel-type gallium oxonitride sample was synthesized using a multianvil device based on a Walker-type module and a 1000-ton press (Voggenreiter, Mainleus, Germany). A mixture of w-GaN (99.9%, Alfa Aesar, Karlsruhe, Germany) and β-Ga_2O_3 (99.9%, Sigma Aldrich, Munich, Germany), with the molar ratio of w-GaN:β-Ga_2O_3 = 6:4, was filled into a hexagonal boron nitride capsule (Henze BNP GmbH, HeBoSint S10, Kempten, Germany) and then placed in an 18/11 assembly, which was compressed by eight tungsten carbide cubes (TSM-10 Ceratizit, Reutte, Austria). The peak pressure and temperature values were 5 GPa and 1250 °C. The sample required 15 min to heat and was allowed to cool to 800 °C for a duration of 25 min after the peak temperature was achieved. The sample was then quenched once the temperature reached 800 °C. Final products were separated from the surrounding crucible and XRD was used for the phase analyses of each sample. The data were collected with a Stoe Stadi P diffractometer using monochromatized Cu $K\alpha$ (λ = 1.540 51 Å) radiation. The β-Ga_2O_3 in the starting mixtures reacted totally to form the spinel gallium oxonitride, and a Rietveld refinement of the powder diffraction pattern showed the presence of the spinel gallium oxonitride (>95%) next to remaining w-GaN.

The local electronic structure around the anions was probed with a combination of x-ray emission spectroscopy (XES) and x-ray absorption near-edge spectroscopy (XANES) measurements. XES and XANES were used to probe both the valence band (VB) and conduction band (CB) in $Ga_{2.79}O_{3.05}N_{0.76}$. The unoccupied and occupied states that were probed with N 1s and O 1s excitations were limited to N and O p states due to the dipole selection rule ($\Delta l = \pm 1$); thereby XES and XANES probe the local partial occupied and unoccupied density of states (LPDOS), respectively.

The XES measurements were performed on beamline 8.0.1 at the Advanced Light Source (Berkeley, CA, USA),[23] and were recorded with the grating spectrometer permanently affixed to the beamline. The sample was set to an incidence angle of 30° (between the normal surface vector and incident beam). The XANES measurements were performed on the SGM beamline at the Canadian Light Source (Saskatoon, SK, Canada).[24] The XANES measurements were recorded in total fluorescence yield mode with a high-voltage channel plate detector with the sample surface perpendicular to the incident beam. The XANES measurements were normalized during the experiment using the photocurrent from a highly transparent gold mesh to monitor changes in the incident photon flux. XES and XANES spectra were energy calibrated using the reference compounds h-BN and bismuth germanate, and the energy locations of the spectra used were the same as those in Ref. 25.

The sample synthesis and structural characterization proceeded similarly to those described in Ref. 14, and as such the structural parameters described therein were used to create the structural models presented here. The structural models (see Table I), nos. 1–3, were created using the lattice parameters and fractional coordinates found in Ref. 14. In the refinement of the spinel-type structured gallium oxonitride within the space group $Fd\bar{3}m$, all of the anions and vacancies are placed on the Wyckoff position 32e possessing an F symmetry, and thus an ordering of the anions would lead to a reduction of the symmetry. Three different space groups were identified in which an ordering of the anions could be described. It is important to note that these structures only differ by the

TABLE I. The structural details of all crystal structures used in this study are listed. Please note that the fractional coordinates for structure 3 are given in rhombohedral coordinates and the lattice parameters are given using hexagonal lattice vectors. All structures were created from the structural details of Ref. 14.

Atom	Wyckoff	Fractional x	Fractional y	Fractional z
		Structure 1[a]		
Ga1	4a	1/2	0	3/4
Ga2	4b	3/4	3/8	3/4
Ga3	4b	1/4	1/4	0
N	4b	1/4	0.0069	0.5138
O1	4b	1/4	0.4931	0.4862
O2	8c	0.4862	0.2569	1/4
		Structure 2[b]		
Ga1	2a	0	0	0
Ga2	2b	0	1/2	1/4
Ga3	4c	3/4	0	3/8
Ga4	4d	0	1/4	5/8
N	4c	0.2638	0	0.1319
O1	4c	0.7638	0	0.6181
O2	4d	0	0.7638	0.3819
O3	4d	0	0.7362	0.8681
		Structure 3[c]		
Ga1	1a	0	0	0
Ga2	2c	0.3750	0.3750	0.3750
Ga3	3d	1/2	0	0
N	2c	0.2431	0.2431	0.2431
O	6h	0.2431	0.2431	0.7707

[a]Structure 1 $Ima2$ (no. 46): a,c = 5.8534 Å, b = 8.2780 Å.
[b]Structure 2 $Imm2$ (no. 44): a,b = 5.8534 Å, c = 8.2780 Å.
[c]Structure 3 $R\bar{3}m$ (no. 166): a,b = 5.8534 Å, c = 14.3379 Å.

placement of the N and O atoms in the anion sites. If the N and O were indistinguishable, the space group would revert back to $Fd\bar{3}m$. The N:O ratio was a 2:6 occupation of the eight available anionic sites in the F lattice. In contrast, the structure determination of a single crystal (Ref. 14) showed vacancy rates of 7% (cation) and 5% (anion), but these were not included in the model structures used herein as they would not contribute significantly to the experimental measurements due to the limited available resolution, and therefore would not affect any comparison to the experimental data (but would increase the complexity of the calculations significantly).

The software package WIEN2K was used for all DFT calculations.[26] The exchange correlation functionals used were the generalized gradient approximation of Perdew-Burke-Ernzerhof[27] (PDE) and a LDA functional including a semilocal potential modified from that of Becke and Johnson (the MB-JLDA functional).[20] A $12 \times 12 \times 12$ k-point mesh was employed for a unit cell with plane wave energy cutoff of -6.0 Ry and an $R_{k\,\max}$ of 7.0. The sphere sizes used to enclose the core electron wave functions were 2.000, 1.5600, and 1.5600 bohrs for Ga, N, and O, respectively. A $1 \times 2 \times 1$ supercell incorporating a full core hole was used to simulate the XANES, and the k-point mesh was reduced to $8 \times 4 \times 8$. Four important aspects need to be taken into account when comparing XES and XANES measurements directly to theoretical LPDOS calculations. These are final-state considerations, lifetime broadening, instrumental broadening, and nonequivalent-site contributions. Further details pertaining to simulating XANES and XES with this method are described elsewhere.[15,25]

The band gap or energy gap of a material is the difference in energy between the highest occupied DOS (or the top of the VB probed by XES) and the lowest unoccupied DOS (or the bottom of the CB probed by XANES). The band gap can therefore be determined by combining XES and XANES measurements on a common energy scale. There are three important experimental effects that need to be accounted for when using XES and XANES to determine the band gap. Core hole effects can shift the CB states to lower energies, effectively decreasing the measured band gap. Nonequivalent sites will have different core level binding energies, resulting in splitting of the spectral contributions and effectively decreasing the measured band gap. The VB and CB are affected by experimental broadening and the VB and CB locations are determined using the second derivative of the corresponding spectrum.[28] Corrections for these three effects help provide more reliable and accurate band gap estimates.

III. RESULTS AND DISCUSSION

A. Anion ordering

The anion ordering in spinel-type gallium oxonitride is a pertinent question. Ascertaining the exact nature of the bonding allows for further study of the electronic and mechanical properties. As mentioned previously, each unique crystal structure produces a unique electronic structure. While we cannot directly measure the local anion ordering (the location of the N and O atoms), we can probe the electronic structure and indirectly determine the specific location of the anion atoms.

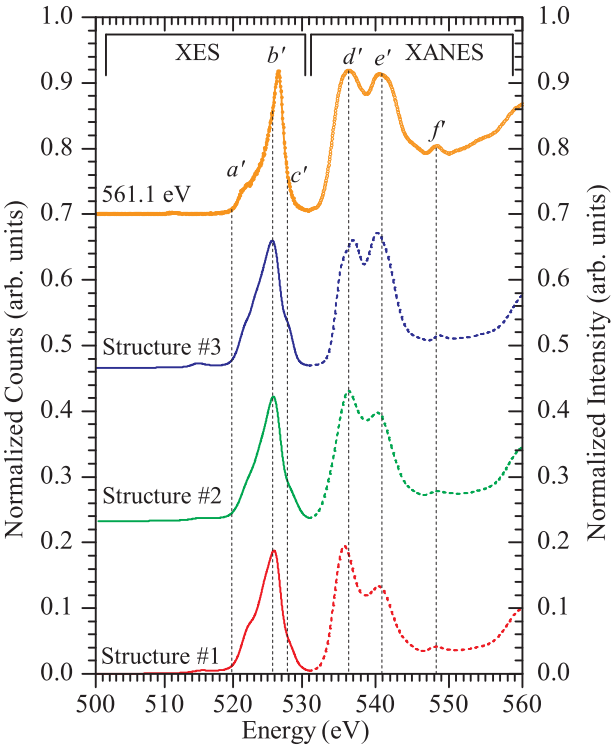

FIG. 1. (Color online) The measured (points) and simulated (solid and dashed lines) O $K\alpha$ XES and O 1s XANES spectra probe the occupied and unoccupied O p states, respectively. A comparison of the simulated and measured data determines which structural model best reproduces the experiment. Vertical dashed lines indicate spectral features and are used to guide the eye to the comparable features of the simulated and measured spectra. The annotation to the left of the spectrum indicates the corresponding structural model outlined in Table I or the excitation energy of the measured O $K\alpha$ XES spectra.

Figure 1 shows a comparison of the measured and simulated O 1s XANES spectra, which suggest that structure 3 exhibits the most correct anion ordering. The unoccupied O p states have three features labeled d', e', and f', but only two features, d' and e', change among the different structures. The measured unoccupied O p states suggest that the relative intensity of these features, d' and e', should be approximately the same. The origin of these features may be elucidated with the partial density of states (PDOS). Figure 2 shows the PDOSs for structures 1, 2, and 3; they are used to look at the detailed electronic structure information since simulation of the XES and XANES spectra requires significant broadening, resulting in a loss of detail. Here, the PDOSs clearly show that feature d' can be attributed to Ga s–O p hybridization, while feature e' can be attributed to Ga p–O p hybridization. Examining Fig. 1, we see that of the structures 1–3, no. 3 has the largest amount of Ga p–O p hybridization and best reproduces the measured unoccupied O p states.

Figure 1 also shows a comparison of the measured and simulated O $K\alpha$ XES spectra, which also suggest that structure 3 has the most appropriate anion ordering. The simulated occupied O p states have a similar shape between the different structures. There is, however, one key distinguishing feature,

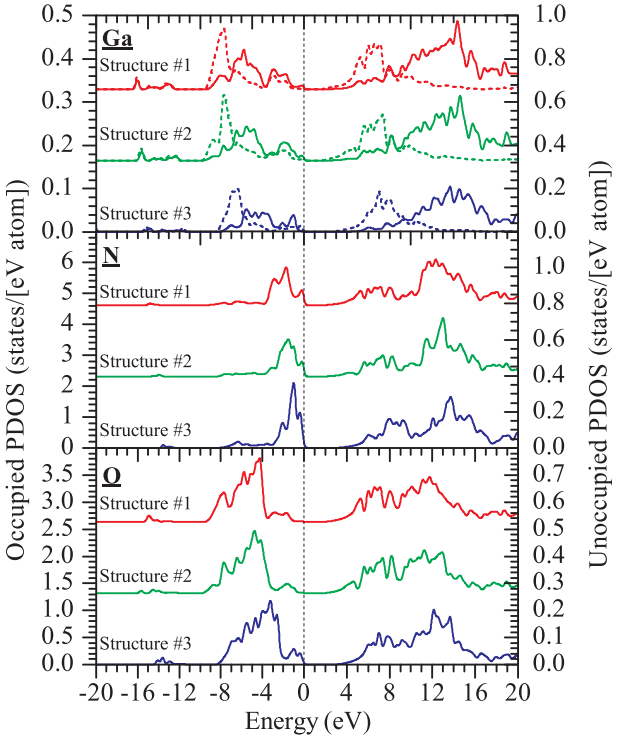

FIG. 2. (Color online) The partial densities of states of Ga_3O_3N including Ga *s* states (dashed) and Ga, N, and O *p* states (solid) for structures 1, 2, and 3 (displayed in red, blue, and green, respectively). The PDOS has been broadened to allow for easy comparisons. The top of the valence band is set to 0.0 eV and is indicated with a vertical dashed line. The colors of the PDOSs correspond to specific structural models as in Figs. 1 and 3.

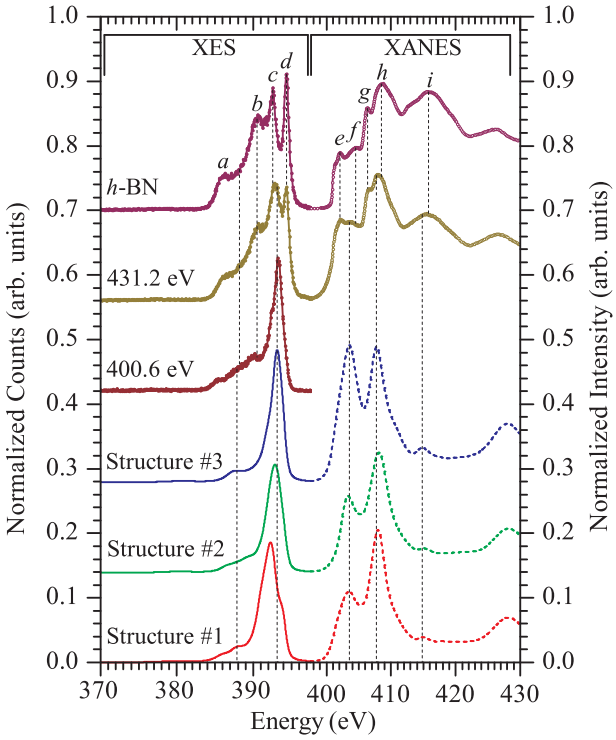

FIG. 3. (Color online) The measured (points) and simulated (solid and dashed lines) N *Kα* XES and N 1*s* XANES spectra probe the occupied and unoccupied N *p* states, respectively. A comparison of the simulated and measured data determines which structural model best reproduces the experiment. Vertical dashed lines indicate spectral features and are used to guide the eye to the comparable features of the simulated and measured spectra. The annotation to the left of the spectrum indicates the corresponding structural model outlined in Table I or the excitation energy of the measured N *Kα* XES spectra.

which is the prevalence of occupied O *p* states near the Fermi level (feature *c*′). The origin of this effect is explained by examining the calculated unbroadened PDOS. The occupied O *p* states near the Fermi level change significantly between structural models. The difference in *c*′ between the different structures is that in structures 1 and 2, the occupied O *p* states are withdrawn from the Fermi level and do not contribute at the top of the VB. This is in contrast to structure 3 in which the occupied O *p* states do contribute at the top of the VB. Now in the measured O *Kα* XES spectra, the O *p* states contribute greatly to the top of the VB, best corresponding to the occupied O *p* states of structure 3, which is the only model where the occupied O *p* states are at the top of the VB. This small but definite difference suggests that structure 3 is the appropriate structure since the measurements suggest that O *p* states do contribute to the top of the VB. This suggests the structure 3 is the most appropriate model for the $Ga_{2.79}O_{3.05}N_{0.76}$ compound studied here.

Figure 3 shows a comparison of the measured and simulated N 1*s* XANES spectra, which further elucidates the appropriate anion ordering, but these measurements are contaminated with remaining *h*-BN that was used as the crucible material during the synthesis of $Ga_{2.79}O_{3.05}N_{0.76}$. We therefore need to take into account the effect the *h*-BN impurity will have on the measured N *p* states making it not readily apparent which structural model best reproduces the measured N *p* states. The measured unoccupied N *p* states of $Ga_{2.79}O_{3.05}N_{0.76}$ bear a striking resemblance to the *h*-BN unoccupied N *p* states, but with a few subtle differences. These differences are that the relative intensity ratio of the features *f* and *h* is smaller for *h*-BN and that the unoccupied N *p* states of $Ga_{2.79}O_{3.05}N_{0.76}$ extend lower in energy, indicating a smaller band gap than in *h*-BN, which we expect from theoretical calculations presented here. With a difference in the intensity of features *f* and *h* in mind, we would expect that for our simulated unoccupied N *p* states the relative intensity ratio of *f*:*h* would be larger than the measured value in $Ga_{2.79}O_{3.05}N_{0.76}$, since the addition of an *h*-BN spectrum will reduce the relative intensity.

This ratio again can be correlated with the electronic structure, and Fig. 2 shows the PDOS for the unoccupied N *p* states. These figures show that feature *f* is a result of N *p*–Ga *s* hybridization and feature *h* is due to N *p*–Ga *p* hybridization. The unoccupied N *p* states in structure 3 have the largest relative intensity ratio of these features, suggesting that it is the appropriate structural model for $Ga_{2.79}O_{3.05}N_{0.76}$. While the reduced band gap of $Ga_{2.79}O_{3.05}N_{0.76}$ is not useful for the comparison of the unoccupied N *p* states it does prove fruitful in the comparison of the occupied N *p* states.

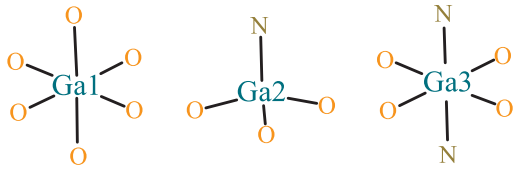

FIG. 4. (Color online) The bonding polyhedra of structure 3 are Ga-O_6 (left), Ga-O_3N (center), and Ga-O_4N_2 (right). These highly symmetric polyhedra represent the local bonding environment that is responsible for the bond hybridization.

Figure 3 also shows a comparison of the measured and simulated N $K\alpha$ XES spectra, which confirm that the anion ordering in structure 3 best reproduces the measured occupied N p states. The band gap difference of $Ga_{2.79}O_{3.05}N_{0.76}$ in comparison to h-BN allows us to tune the XES spectrum excitation energy to the lowest value possible in order to avoid photons being absorbed by h-BN. Thus, we predominantly probe the occupied N p states of the $Ga_{2.79}O_{3.05}N_{0.76}$ present in the sample as opposed to both h-BN and $Ga_{2.79}O_{3.05}N_{0.76}$. The corresponding XES spectrum is labeled as 400.6 eV in Fig. 3. The measured occupied N p states change drastically and look almost identical to those calculated for structure 3, confirming our previous conclusion drawn from the comparison of the measured and simulated unoccupied N p states: that the appropriate structure is no. 3.

So far, structure 3 is determined to provide the most correct model of the anion ordering out of the three structures tested. This is largely based on the nature of the bond hybridization that is seen in the experimental measurements. The cause of this large degree of hybridization of the Ga-O and Ga-N bonds may be the highly symmetric nature of the bonding polyhedra; see Fig. 4. As discussed earlier, the nitrogen atoms substitute such that they increase their separation as much as possible; however, the increased stability may be due to the symmetry of the polyhedra that occur. This is not uncommon for spinel structure compounds; for example, in the solid solutions γ-$(Si,Ge)_3N_4$ Ge occupies the tetrahedral sites because that allows the most symmetric N-(Ge,Si) tetrahedra to exist.[8,9] With the notion that the anions would prefer to be distributed as symmetrically as possible in bonding polyhedra, it seems unlikely that a random distribution of anions would achieve better results.

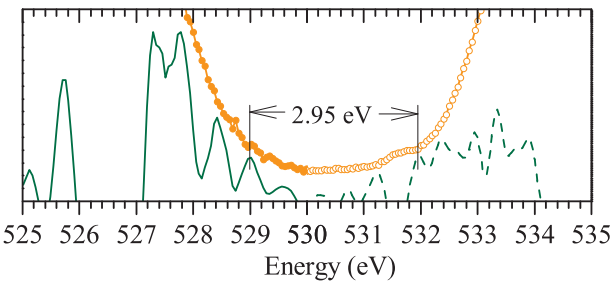

FIG. 5. (Color online) The second derivatives (solid and dashed) of the measured (points) nonresonant O $K\alpha$ XES and O 1s XANES spectra determine the top of the VB and bottom of the CB. The first peak above the background noise level is used to determine the VB and CB edges.

TABLE II. The calculated band gap values using the PDE (E_g^{PDE}) and MBJLDA (E_g^{MBJLDA}) functionals are compared to the experimentally determined value (E_g^{expt}). The type of band gap transition that can occur is indicated in parentheses. The calculated band gap values using the same method for w-GaN and β-Ga_2O_3 illustrate the reliability of the calculated values.

Material	E_g^{PBE} (eV)	E_g^{MBJLDA} (eV)	E_g^{expt} (eV)
$Ga_{2.79}O_{3.05}N_{0.76}$	1.14 (direct)	2.79 (direct)	2.95 ± 0.30
w-GaN	1.94	3.23	3.4 ± 0.1
β-Ga_2O_3	2.50	4.96	4.8 ± 0.1

B. Electronic band gap

Now that we have determined the most probable model for the anion ordering to be structure 3, we turn our attention to the electronic band gap of $Ga_{2.79}O_{3.05}N_{0.76}$. The measured oxygen data are not affected by h-BN impurities and are used to evaluate the electronic band gap.

The band gap is determined by combining the measured occupied and unoccupied O p states on the same energy scale as in Fig. 1. Figure 5 displays the second derivative of the measured occupied and unoccupied O p states and is used to determine the location of the VB and CB edges. There is no significant core hole shift (0.0 ± 0.1 eV) as determined from our DFT calculations by comparing the calculations with and without a core hole. This places the measured band gap of $Ga_{2.79}O_{3.05}N_{0.76}$ at 2.95 ± 0.30 eV with no corrections necessary since there is only one oxygen site in structure 3. The error associated with this band gap value is evaluated by including three considerations: the error in the experimental precision in energy (± 0.20 eV), the error in the relative calibration (± 0.20 eV), and the error in the core hole shift (± 0.1 eV).

The electronic band gap values were also implicitly calculated from the DFT results. Table II lists the band gap values calculated with both the PBE and MBJLDA functionals. It is well known that conventional GGA (PBE) calculations underestimate the band gap, but including a semilocal screening potential provides significantly more accurate values.[20] The calculated band gap values for structure 3 are used as the theoretical values for $Ga_{2.79}O_{3.05}N_{0.76}$. The reliability of MBJLDA band gap calculations of similar compounds, w-GaN and β-Ga_2O_3, suggests that the value should be within 0.2 eV, which is what we see when we compare the calculated and measured values.

IV. CONCLUSIONS

Here we tested three structural models for Ga_3O_3N in which there is a significant level of anion ordering, in contrast to XRD measurements, which generalize the anions to a single site. We confirm that of the three possible structure types tested, the appropriate structural model is that which adopts the $R\bar{3}m$ space group. This structure provides the appropriate hybridization of Ga s and p with N and O p states. The high level of hybridization stems from the increased symmetry of the Ga-O_6 and Ga-O_4N_2 octahedra and Ga-O_3N tetrahedra. The measured band gap of $Ga_{2.79}O_{3.05}N_{0.76}$ is 2.95 ± 0.30 eV using the O $K\alpha$ XES and O 1s XANES spectra and agrees

with the calculated value of 2.79 eV. We used a combination of DFT calculations along with XES and XANES measurements to experimentally determine both the band gap and anion ordering in spinel-type gallium oxonitride. This technique is not limited to this material but may be applied to any material where the locations of the elements, differing by $\Delta Z \pm 1$, are not easily determined with XRD.

ACKNOWLEDGMENTS

We gratefully acknowledge the Natural Sciences and Engineering Research Council of Canada (NSERC) and the Canada Research Chair program for their support in this research. Research described in this paper was performed at the Canadian Light Source, which is supported by the Natural Sciences and Engineering Research Council of Canada, the National Research Council Canada, the Canadian Institutes of Health Research, the Province of Saskatchewan, Western Economic Diversification Canada, and the University of Saskatchewan. The Advanced Light Source is supported by the Director, Office of Science, Office of Basic Energy Sciences, of the US Department of Energy under Contract No. DE-AC02-05CH11231. The Deutsche Forschungsgemeinschaft financially supported this work (Contracts No. KI 838/3-1 and No. HU 966/5-1). R.R. is grateful to the Fonds der Chemischen Industrie for financial support.

*teak.boyko@usask.ca

[1] A. Zerr, G. Miehe, G. Serghiou, M. Schwarz, E. Kroke, R. Riedel, H. Fuess, P. Kroll, and R. Boehler, Nature (London) **400**, 340 (1999).
[2] G. Serghiou, G. Miehe, O. Tschauner, A. Zerr, and R. Boehler, J. Chem. Phys. **111**, 4659 (1999).
[3] T. Sekine, H. L. He, T. Kobayashi, M. Zhang, and F. F. Xu, Appl. Phys. Lett. **76**, 3706 (2000).
[4] K. Leinenweber, M. O'Keeffe, M. Somayazulu, H. Hubert, P. F. McMillan, and G. H. Wolf, Chem. Eur. J. **5**, 3076 (1999).
[5] M. Schwarz, G. Miehe, A. Zerr, E. Kroke, B. Poe, H. Fuess, and R. Riedel, Adv. Mater. **12**, 883 (2000).
[6] W. Y. Ching, S.-D. Mo, I. Tanaka, and M. Yoshiya, Phys. Rev. B **63**, 064102 (2001).
[7] W. Y. Ching, S. D. Mo, and L. Ouyang, Phys. Rev. B **63**, 245110 (2001).
[8] J. Dong, J. Deslippe, O. F. Sankey, E. Soignard, and P. F. McMillan, Phys. Rev. B **67**, 094104 (2003).
[9] E. Soignard, P. F. McMillan, and K. Leinenweber, Chem. Mater. **16**, 5344 (2004).
[10] P. Kroll, R. Dronskowski, and M. Martin, J. Mater. Chem. **15**, 3296 (2005).
[11] P. Kroll, Phys. Rev. B **72**, 144407 (2005).
[12] E. Soignard, D. Machon, P. F. McMillan, J. J. Dong, B. Xu, and K. Leinenweber, Chem. Mater. **17**, 5465 (2005).
[13] O. U. Okeke and J. E. Lowther, Phys. Rev. B **77**, 094129 (2008).
[14] H. Huppertz, S. A. Hering, C. E. Zvoriste, S. Lauterbach, O. Oeckler, R. Riedel, and I. Kinski, Chem. Mater. **21**, 2101 (2009).
[15] T. D. Boyko, E. Bailey, A. Moewes, and P. F. McMillan, Phys. Rev. B **81**, 155207 (2010).
[16] J. E. Lowther, T. Wagner, I. Kinski, and R. Riedel, J. Alloys. Compd. **376**, 1 (2004).
[17] I. Kinski, G. Miehe, G. Heymann, R. Theissmann, R. Riedel, and H. Huppertz, Z. Naturforsch. B **60**, 831 (2005).
[18] W. Y. Ching and P. Rulis, Phys. Rev. B **73**, 045202 (2006).
[19] Y. N. Xu and W. Y. Ching, Phys. Rev. B **51**, 17379 (1995).
[20] F. Tran and P. Blaha, Phys. Rev. Lett. **102**, 226401 (2009).
[21] E. Soignard, P. F. McMillan, C. Hejny, and K. Leinenweber, J. Solid State Chem. **177**, 299 (2004).
[22] K. Tatsumi, T. Mizoguchi, S. Yoshioka, T. Yamamoto, T. Suga, T. Sekine, and I. Tanaka, Phys. Rev. B **71**, 033202 (2005).
[23] J. J. Jia, T. A. Callcott, J. Yurkas, A. W. Ellis, F. J. Himpsel, M. G. Samant, J. Stöhr, D. L. Ederer, J. A. Carlisle, E. A. Hudson, L. J. Terminello, D. K. Shuh, and R. C. C. Perera, Rev. Sci. Instrum. **66**, 1394 (1995).
[24] T. Regier, J. Krochak, T. K. Sham, Y. F. Hu, J. Thompson, and R. I. R. Blyth, Nucl. Instrum. Methods Phys. Res., Sect. A **582**, 93 (2007).
[25] C. Braun, M. Seibald, S. L. Boerger, O. Oeckler, T. D. Boyko, A. Moewes, G. Miehe, A. Tuecks, and W. Schnick, Chem. Eur. J. **16**, 9646 (2010).
[26] K. Schwarz, P. Blaha, and G. K. H. Madsen, Comput. Phys. Commun. **147**, 71 (2002).
[27] J. P. Perdew, K. Burke, and M. Ernzerhof, Phys. Rev. Lett. **77**, 3865 (1996).
[28] E. Z. Kurmaev, R. G. Wilks, A. Moewes, L. D. Finkelstein, S. N. Shamin, and J. Kuneš, Phys. Rev. B **77**, 165127 (2008).

The Local Crystal Structure and Electronic Band Gap of β-sialons

T. D. Boyko,[1,*] T. Gross,[2] M. Schwarz,[3] H. Fuess,[4] and A. Moewes[1]

[1] *Department of Physics and Engineering Physics, University of Saskatchewan, 116 Science Place, S7N5E2, Saskatoon*

[2] *Eduard-Zintl-Institute for Inorganic and Physical Chemistry, Technische Universität Darmstadt, Petersenstraße 20, 64287 Darmstadt, Germany*

[3] *Institute for Inorganic Chemistry, Technische Universität-Bergakademie Freiberg, 09596 Freiberg, Germany*

[4] *Institute for Materials Science, Technische Universität Darmstadt, 64287, Darmstadt, Germany*

(Dated: October 9, 2013)

Solid solutions of silicon nitride (Si_3N_4) with aluminum oxide (Al_2O_3) that form β-sialons (β-$Si_{6-z}Al_zO_zN_{8-z}$) provide a host of materials with both, useful electronic and mechanical properties. These electronic properties are relatively unknown and here we provide measurements and calculations of the electronic band gap using a combination of X-ray emission spectroscopy, X-ray absorption spectroscopy and density functional theory, respectively. The measured electronic band gaps of β-$Si_{6-z}Al_zO_zN_{8-z}$ with $z = 0.0$, 2.0 and 4.0 are determined to be 7.2 eV, 6.2 eV and 5.0 eV (all $\pm$0.2 eV), respectively. The measured band gap values, however, are only agree fairly well with the calculated values of 5.88 eV, 3.45 eV and 2.39 eV for β-$Si_{6-z}Al_zO_zN_{8-z}$ with $z = 0.0$, 2.0 and 4.0, respectively. The smaller calculated band gap values are attributed to the shortcomings of DFT, which often underestimates the electronic band gap. In contrast to previous observations, the band gap energy shows a linear dependence on composition. The electronic structure measurements also reveal a single bonding environment for both the Si and Al atoms. This supports the specific structural arrangements proposed originally by Okatov. Furthermore, β-sialons are wide-band gap semiconductors with the band gap reduction arising from the O p-states moving toward the Fermi level. This band gap reduction also provides the ability for direct band gap transitions, which is very important for practical applications.

PACS numbers: 71.20.Nr,61.66Dk,61.10Ht,78.40Pg, 78.70.En

I. INTRODUCTION

The formation of solid solutions between silicon nitride (Si_3N_4) and aluminum oxide (Al_2O_3) was discovered simultaneously by Jack and Wilson[1] as well as Oyama and Kamigoto[2]. These compounds are named sialons, an acronym dubbed for the constituent elements, Si - Al - O - N, and since the sialons are derived from Si_3N_4, they are also systematically named after their isostructural relatives: α-sialons (α-Si_3N_4), β-sialons (β-Si_3N_4) and most recently γ-sialons (γ-Si_3N_4)[3]. These materials exhibit outstanding high temperature performance (i.e. good mechanical properties, thermochemical corrosion resistance and excellent thermal shock resistance) giving rise to multiple engineering applications[4]. Similar to the end member β-Si_3N_4, β-sialons can be applied as either porous materials in separation membranes at high temperatures for hot gas filtration applications or as densely-sintered ceramics for use in high-speed cutting inserts and coatings for gas turbines. More recently, the focus of applications has changed from a strict mechanical perspective (i.e. thermomechanical and thermochemical properties) to more functionalized ones. For example, the introduction of Eu atoms into the β-sialon lattice has led to efficient phosphors for white light emitting diodes (LEDs)[5,6]. The crystal structure of β-sialon has hexagonal symmetry (P 6_3/m; No. 176) and is analogous to β-Si_3N_4. The β-sialon system is typically described as β-$Si_{6-z}Al_zO_zN_{8-z}$ (i.e. two formula units in the hexagonal cell) with Al and O atoms substituting Si and N atoms, respectively[7]. The range of stable compositions for β-sialons is known to be $0.0 \leq z \leq 4.2$[8,9]. The crystal structure of β-Si_3N_4, contrary to β-sialons, is very simple with only three nonequivalent sites. The crystal structure of β-sialon is measured quite easily with X-ray diffraction (XRD), however, distinguishing between the Al and Si or O and N atoms is nearly impossible as their X-ray scattering factors are too similar. The obvious alternative is to use neutron diffraction, but neutron diffraction experiments require a very large amount of pure material, which is still quite difficult to obtain, and so far has shown limited success[10]. Instead, the crystal structure can be derived from the electronic structure, which is very sensitive to the bond ordering and hence the local and long range ordering[11,12]. This technique is much more sensitive to the local and long range ordering in the crystal and provides a method to test complete structural models, rather than being limited to ascertaining the local bonding environment. Various forms of Al - O arrangements and structural ordering have been proposed. Several spectroscopic methods have to some extent elucidated the local crystal structure: nuclear magnetic resonance (NMR)[13–16], extended X-ray absorption fine structure[17], core level X-ray photoemission spectroscopy[18], and X-ray absorption near edge structure (XANES)[12]. The measurements consistently reveal a predominance of Al - O and Si - N bonds. These experimental results have been confirmed with *ab initio* density functions theory (DFT) calculations[19–21]. From the reported measurements and calculations two

structural models have emerged. One proposed by Okatov *et al.*[21] using the extended Hückel theory approximation and the second structure based on NMR measurements by Dupree *et al.*[14,15]. These models can be summarized as follows (1) In the Okatov model the O atoms are only connected to Al forming hexagonal rings. These are stacked along c, so that some of the channels typical for the β-Si_3N_4 structure essentially become Al - O tubes. This structure is simulated using a $3 \times 3 \times 1$ supercell of the original unit cell for β-Si_3N_4. (2) In the Dupree model the Al and O atoms are clustered in slabs, that are extending (infinitely) within the a-b plane and are inserted at certain distances along c of the β-Si_3N_4 parent structure. This created a somewhat heterogeneous structure with interface layers. Fig. 1 shows the crystal structure of the Okatov and Dupree models with $z = 2.0$ and $z = 4.0$. While previously, the structure of β-sialons has been studied through a comparison of measurements with the simulated electronic structure and generalized local bonding environments[12], no reports of comparing a specific crystal structure or space group to experimental measurements are available. One unique

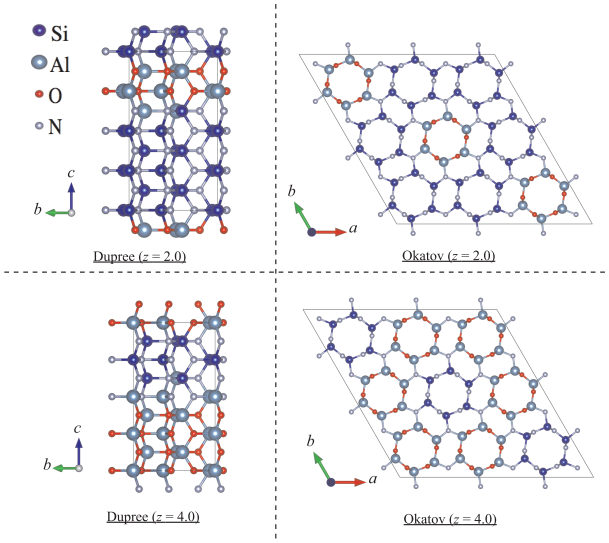

FIG. 1. (Color Online) The crystal structure models for β-sialons $z = 2.0$ (top) and $z = 4.0$ (bottom) with the ordering proposed by Dupree *et al.*[15] (left) and Okatov *et al.*[21] (right). The Dupree structure is viewed from the b-c place and the Okatov structure from the a-b place to showcase the layering and the hexagonal rings, respectively.

feature of β-sialons is the ability to adjust the physical properties by changing the composition. The tunability of β-sialons continues to motivate research into new and less expensive synthesis techniques[22–25]. While many of the physical properties of the β-sialons, such as lattice parameters and elastic constants, thermal conductivity, hardness, intrinsic fracture toughness, and friction coefficients exhibit a linear dependence on the composition[26], the dependence of the electronic structure with composition is non-linear[5,27]. Previous theoretical calculations have shown that there is a vast reduction in the band gap from ≈ 4.2 eV at $z = 0.0$ to ≈ 1.3 eV at $z = 4.0$[5,27]. Furthermore, the lowest energy models exhibit impurity-like states near the band edges for $z < 2.0$, with a direct electronic band gap for all β-sialons with $z > 0.0$. Even though there have been a few studies determining the electronic band gap through theoretical means, there are no experimental reports of the electronic band gap for β-sialons. The correlation between the electronic band gap and the degree or type of Si - N vs. Al - O substitution in β-sialons is important for further potential applications into (opto)electronic devices. In this study, we (1) compare the calculations of the two structural models, Dupree and Okatov, comparing the simulated spectra from the Okatov model to the experimental measurements of β-sialons with $z = 0.0$, 2.0 and 4.0 and (2) determine the electronic band gap using a combination of the electronic structure measurements and density functional theory calculations.

II. EXPERIMENTAL DETAILS

Two different β-sialons studied were hot-pressed platelets with nominal compositions $z = 2.0$ and 4.0. The preparation was identical for all stoichiometries. The preparation of β-sialon with $z = 2.0$ shall be given exemplarily: Considering the residual oxygen contents within the nitrides, a powder mixture of 66.61 wt.% Si_3N_4 (SN-E-10, Ube Industry, Japan, 1.32 wt.% O), 11.40 wt.% AlN (Type F, Tokuyama Soda Co., CA, 0.9 wt.% O), and 21.99 wt.% Al_2O_3 (AKP 50, Sumitomo Chemical America, NY) was prepared to give the nominal composition Si_2AlON_3 or β-sialon with $z = 2.0$. The powder was attrition-milled in isopropyl alcohol for 2 hrs. with high purity Si_3N_4 milling media in a teflon-coated jar. The slurry was dried in a polyethylene beaker under a halogen lamp while being stirred. Finally, charges of the powders were hot pressed in a graphite furnace (1775°C / 2 hrs./ 30 MPa N_2). The phase purity of the two β-sialons was verified by X-ray powder diffraction and the materials were further investigated with scanning electron microscopy in combination with energy-dispersive X-ray spectroscopy. The N and O content was determined using the established dependence of the lattice parameters on z[9], combustion elemental analysis and electron probe microanalysis for the β-sialons. The grain sizes as determined by SEM were $\approx$ 1-3 μm for compositions with a low Al–O content and up to 100 μm for the more highly substituted sialons. The β-Si_3N_4 or β-sialon with $z = 0.0$ was prepared by ultra-hotisostatic pressing of an admixture of β-Si_3N_4 powder (Bayer) and 20 wt.% silicon nitride imide (Si_2N_2NH) without any further sintering aid at 13 GPa and 1773 K for 90 mins. The method and assembly were identical to the one used in Ref. 28. The resulting compact material consisted of pure beta β-Si_3N_4 with close to 100% phase density and grain sizes between

0.2 and 3 μm. The oxygen content was below the detection limit of the energy-dispersive X-ray spectrometer attached to the scanning electron microscope. XRD was carried out using two different Stadi-P diffractometers (STOE) in transmission geometry with curved Ge-(111) monochromators. One is equipped with a molybdenum tube (Mo-Kα = 0.709262 Å) and a linear position sensitive detector (PSD) with an aperture of 6° and the other is equipped with a copper tube (Cu-Kα = 1.540562 Å) and a curved PSD with an aperture of 40°. The patterns were collected in an angular range of 5-55° (2θ) with a step width of 0.02° for Mo-Kα and 10-86° (2θ) with a step width of 0.03° for Cu-Kα, respectively. Full pattern analysis was performed using the Rietveld method with the FullProf Suite software package[29]. Fig. 2 shows the XRD patterns and refinements with the lattice constants and fractional coordinates of the β-sialons given in Table I. The SGM beamline[30] (Canadian Light Source, Canada)

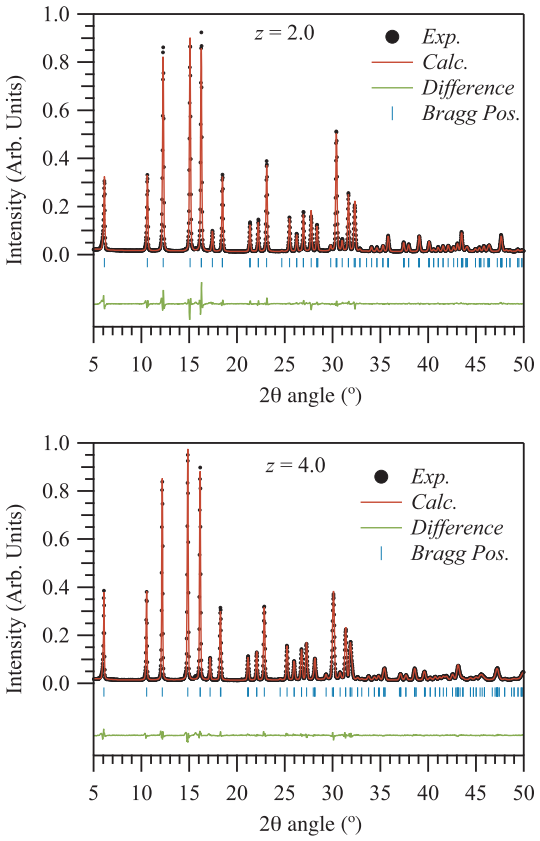

FIG. 2. X-ray diffractogram of β-sialons $z = 2.0$ (top) and $z = 4.0$ (bottom). The plot includes the measured data points (red dots), fit pattern (black line), expected Bragg positions (blue markers), and difference plot (green line).

was used to collect the O 1s, N 1s, Al 1s, and Si 1s XANES spectra. The PGM beamline[31] (Canadian Light Source, Canada) was used to collect the Si 2p XANES spectra, while Beamline 8.0.1[32] (Advanced Light Source, USA) was used to collect the Si $L_{2,3}$, O Kα and N Kα X-ray emission spectra (XES). These samples were pressed onto carbon tape and placed 30 deg off normal with respect to the incident beam with all measurements performed at room temperature. The O 1s, N 1s and Al 1s XANES were measured in both total fluorescence yield (TFY) using a micro channel plate detector and partial fluorescence yield (PFY) modes using a silicon drift detector. The Si 1s XANES was measured in TFY and PFY modes along with inverse partial fluorescence yield (IPFY) mode monitoring the Al Kα emission using a silicon drift detector. The Si 2p XANES was measured only in TFY mode. All of the XES spectra, which include N Kα, O Kα and Si $L_{2,3}$ XES, were measured using the soft X-ray fluorescence spectrometer permanently affixed to Beamline 8.0.1. The calibration of the N Kα XES and N 1s XANES spectra used a powder sample of hexagonal boron nitride (h-BN). The peak locations are 392.75 eV and 394.60 eV for the XES measurement and 402.10 eV for the XANES measurement. In the case of the XANES calibration, the TEY spectrum of h-BN is used. For the O Kα XES and O 1s XANES spectra a powder sample of bismuth germanium oxide (BGO) was used. The peak locations are 517.90 eV and 526.00 eV for the XES measurement and 532.70 eV for the XANES measurement. Again, in the case of the XANES calibration, the TEY spectrum of BGO is used. The Si $L_{2,3}$ XES and Si 2p XANES are calibrated using amorphous silicon dioxide (a-SiO_2). The peak locations are 88.85 eV and 94.75 eV for the XES measurement and 108.10 eV for the XANES measurement. Contrarily, in the case of the XANES calibration, the TFY spectrum of a-SiO_2 is used. For the remaining measurements, the Al 1s and Si 1s XANES, the spectra were not calibrated since no analysis is made based on the energy scale of the spectra. The electronic band gap of any material can be determined using a combination of XES and XANES measurements. The electronic band gap is taken as the separation between the XES spectrum and XANES spectrum, when they are displayed on the same energy scale. We use the second derivatives of the spectra to determine the band edge, which has been shown to unambiguously determine the band edge of a broadened experimental spectrum for a variety of materials[33,34]. We then need to add both the calculated core hole shift and nonequivalent site shifts to the initial value as these effects decrease the measured band gap value. We use the results of our DFT calculations to estimate the value of these shifts similar to previous studies[33]. These corrections make this technique a reliable method to determine the electronic band gap of materials, in particular when there are no other viable methods available.

III. THEORETICAL DETAILS

The *ab initio* DFT calculations employ the commercially available WIEN2k software (ver. 12.1). This code uses the Kohn-Sham methodology with spherical wave functions to model core orbitals, and linearized augmented plane waves for semi-core, valence and conduction band states[35]. The exchange interaction used the Generalized Gradient Approximation (GGA) of Perdew-Burke-Ernzerhof[36] and local density approximation with the added modified Becke-Johnson potential (MBJLDA)[37]. The energy cut-off for the plane wave basis was -6.0 Ryd. For the ground state calculation of β-sialon with $z = 0.0$ a k-point mesh of $8 \times 8 \times 19$ was used. While, $4 \times 4 \times 28$ and $8 \times 8 \times 6$ k-point meshes were used for other the ground state calculations using the Okatov and Dupree structures, respectively. The core hole effects are modeled by including a single core hole at the atom of interest inside a $3 \times 2 \times 2$ supercell of the unit cell of β-Si_3N_4. For these calculations, a $4 \times 4 \times 14$ k-point mesh was used. The core hole shift was determined by comparing the calculated conduction band energy location, including the core hole, to the conduction band location calculated without the core hole. The non-equivalent site splitting was determined from the core level energy eigenvalues. Both structural models use a triclinic symmetry. Whereas the Dupree model is based on 56 nonequivalent sites ($P1$, No. 1) Okatov uses 63 nonequivalent sites (P-1, No. 2). Completing proper simulations of the total measured XES and XANES spectra would require as many calculations as there are nonequivalent sites. However, many nonequivalent crystal sites have equivalent electronic structure depending on the sensitivity to long range ordering. Unfortunately, all of the atoms have a unique local electronic structure for the Dupree model. For the Okatov model, groups of nonequivalent crystal sites with equivalent local electronic structure exist. The number of XANES calculations, here 63, is thus reduced to only 7 calculations. The sites are classified by their local bonding structure, but in some cases this is extended to the second coordination shell.

IV. RESULTS AND DISCUSSION

The equilibrium energy calculated using DFT (provided the calculation parameters are similar) could be used as a measure of the relative stability of materials. Table I lists the energy of the three β-sialon compositions studied within the two models considered. The total energy of the unit cell will decrease as we substitute Al for Si and O for N since the energy difference between Si and Al is larger than O and N. But, there is also a definite decrease in equilibrium energy for the Okatov structure over the Dupree structure. This is a clear indication that the Okatov structure is more favorable with regard to the equilibrium energy. This result is not very surprising considering that the Okatov structure is a theoretically optimized structure, however, below we compare the resulting calculated electronic structure to measurements to confirm the validity of this structure. Additionally, one implicitly calculates the total inter-atomic forces during a DFT calculation. Similar to the total equilibrium energy, the total atomic forces for the Okatov structure are effectively zero in contrast to the Dupree structure. Similar to the Okatov structure, the total inter-atomic forces for β-sialon $z = 0.0$ are also zero. Considering both the equilibrium energy and the inter-atomic forces, the Okatov structure is the most appropriate structure to describe β-sialons. On the basis of the arguments given above only the calculations based on the Okatov model are used for the comparison with the experimental results. Using the electronic structure measurements of the N p-states is a useful route to compare the differences in the electronic structure of all the β-sialon compositions. Figs. 4 - 5 shows the measured and calculated N p-states probed using N Kα XES and N 1s XANES. The calculated N Kα XES and N 1s XANES, compared to the measurements reproduce most of the spectral features. Specifically, the calculated N 1s XANES spectra agree very well with the measured corresponding spectra. The calculated spectra have sharper features than the measured spectra, but this is due to saturation of the fluorescence signal during the XANES measurement, which is prevalent in non-dilute materials. More importantly, the calculated spectra predict the behavior exhibited through resonant N Kα XES measurements and also the changes in the N p-states of β-sialons going from $z = 0.0$ to 4.0. First, tuning the excitation of the N Kα XES of β-sialon $z = 0.0$ to a maximum in the N_{2c} N 1s XANES (402.1 eV), there is a significant reduction in the relative intensity of feature a (Fig. 4). This reduction is expected considering the calculated N Kα XES spectrum corresponding to the N_{2c} site. Similar differences among the nonequivalent sites continues for the other the β-sialons (Figs. 5 and 6) in that the relative intensity of feature a is also reduced. But in these cases this is due to preferentially exciting the nitrogen that is bonded to aluminum rather than a specific site point symmetry. Second, the localization of feature b in Figs. 4 - 5 observed in the measured non-resonant N Kα XES spectra is reproduced in the corresponding calculated spectra. Third, the relative intensity of features a and c, which decreases with increasing z, is reproduced in the calculated N Kα XES spectra. The agreement between the measured and calculated electronic structure, namely the N p-states, suggests that the Okatov model correctly predicts the electronic structure differences between the different compositions. Now that we have ascertained the most appropriate crystal structure, we turn to determining the electronic band gap. With the available measurements there are several types of electronics states that can be used to determine the band gap, these include: N p-states, O p-states and Si s/d-states. Fig. 3 shows both the electronic band structure and the partial density of states (PDOS) for all three β-sialons. Table I

TABLE I. The structural parameters of β-$Si_{6-z}Al_zO_zN_{8-z}$ with z = 0.0, 2.0 and 4.0 are specified within the spacegroup $P6_3m$. Density functional theory calculations including total energy, inter-atomic forces, core hole and nonequivalent site shift (ΔE_{shift}) and electronic band gap using GGA (E_g^{GGA}) and MBJLDA (E_g^{MBJ}) functionals are shown. The measured electronic band gap (E_g^*) is determined from the N Kα XES and N 1s XANES measurements and includes the added correction ΔE_{shift}.

Materials	Lattice (Å)	cation 6h	anion 6h	Model	Energy (Ryd)	Forces (mRyd/bohr)	E_g^{GGA} (eV)	E_g^{MBJ} (eV)	ΔE_{shift} (eV)	E_g^* (±0.2 eV)
$z = 0.0$	$a = 7.5962(9)$	$x/a = 0.17685$	$x/a = 0.31928$		-4357.53	0.000	4.32	5.88	2.2	7.2
	$c = 2.9083(4)$	$y/a = 0.76944$	$y/a = 0.01348$							
$z = 2.0$	$a = 7.65915(10)$	$x/a = 0.17126$	$x/a = 0.33378$	Okatov	-4250.93	0.000	1.83	3.45	1.7	6.2
	$c = 2.95644(4)$	$y/a = 0.7672$	$y/a = 0.03144$	Dupree	-4250.89	1.904	2.19	3.54		
$z = 4.0$	$a = 7.71365(7)$	$x/a = 0.16737$	$x/a = 0.33465$	Okatov	-4144.19	0.000	0.76	2.39	1.2	5.0
	$c = 3.00789(3)$	$y/a = 0.76382$	$y/a = 0.02869$	Dupree	-4144.09	1.424	0.00	0.05		

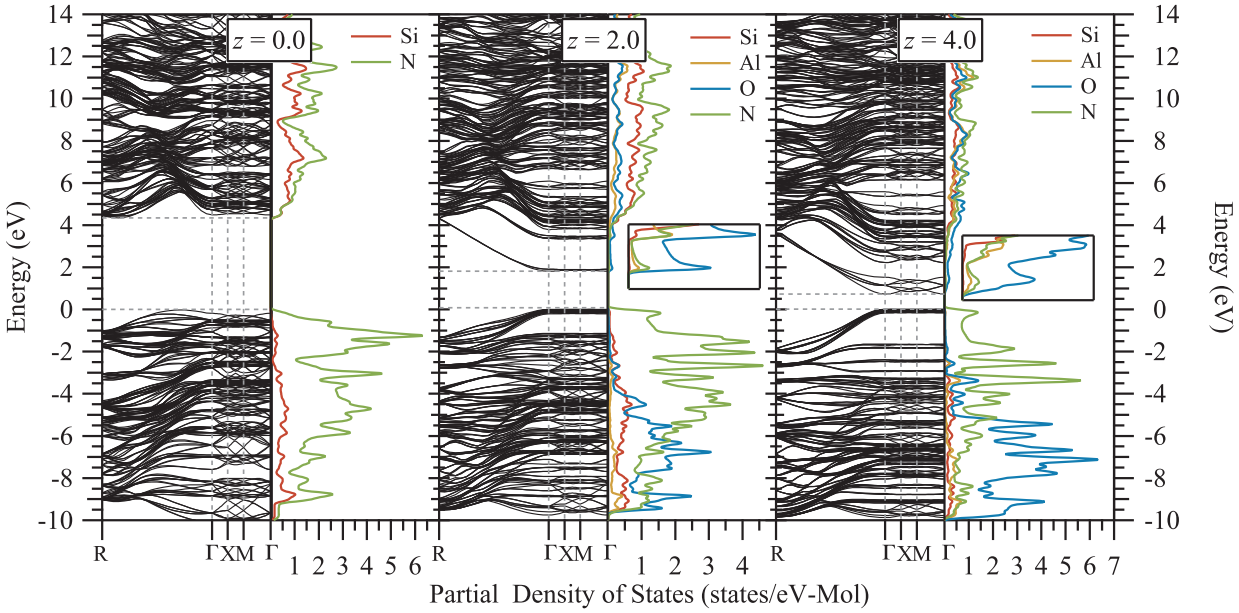

FIG. 3. (Color Online) The calculated electron band structure and partial densities of states of β-sialon $z = 0.0$ (left), $z = 2.0$ (middle) and $z = 4.0$ (right). The band structure is plotted for a cubic Brillouin zone. The inset panels are enlargements of the unoccupied partial density of states of the lower conduction band. The valence band and conduction band edges are indicated with horizontal dashed lines.

also displays the calculated electronic band gap for these materials. A clear reduction in electronic band gap arises with the addition of Al and O atoms. The band gap reductions seemingly arise from the lower conduction bands (CBs) moving away from the main CB. The lower CBs are primary composed of oxygen electronic states, with the next largest contribution being nitrogen electronic states. This is similar to the study of Ching *et al.*[20] in which they describe impurity like states being added to the CB. There is the slight difference here in that there is no discontinuity in the total DOS. Interestingly, the top of the valence band (VB) is primarily nitrogen electronic states with basically no other contribution. Measuring the nitrogen electronic states is the most viable method to determine the electronic band gap due to the nitrogen playing such a major role in the VB as well as a minor role in the bottom of the CB. Furthermore, there are no oxygen, silicon or aluminum electronic states at the top of the VB making the use of these electronic structure measurements to determine the electronic band gap not possible. The electronic band gap is determined using N Kα XES and N 1s XANES measurements for all the materials studied here. Figs. 4 - 5 show both the measured and simulated N Kα XES and N 1s XANES, which are plotted on a common energy scale to determine the electronic band gap. The simulated and observed nitro-

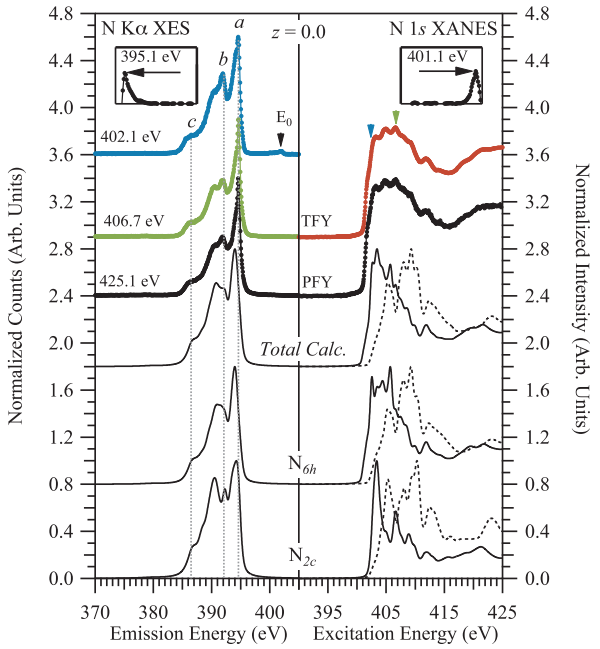

FIG. 4. (Color Online) The measured N Kα XES and N 1s XANES (connected dots) of β-sialon $z = 0.0$ are compared to the simulated spectra (lines). The excitation energy of the resonant XES spectra is displayed to the left above the spectrum and indicated with an arrow above the XANES spectrum. Elastic scattering features have been labeled with E_0. The inset panels above the corresponding measured spectra show the second derivative with the top of the valence band and bottom of the conduction band indicated by an arrow and labeled directly above. The symmetry of the nonequivalent crystal site is labeled directly above the corresponding spectra. Lastly, the XANES spectra, from the ground state calculation (dashed lines), show the effect of the core hole when compared to the XANES spectra with an included core hole (solid lines).

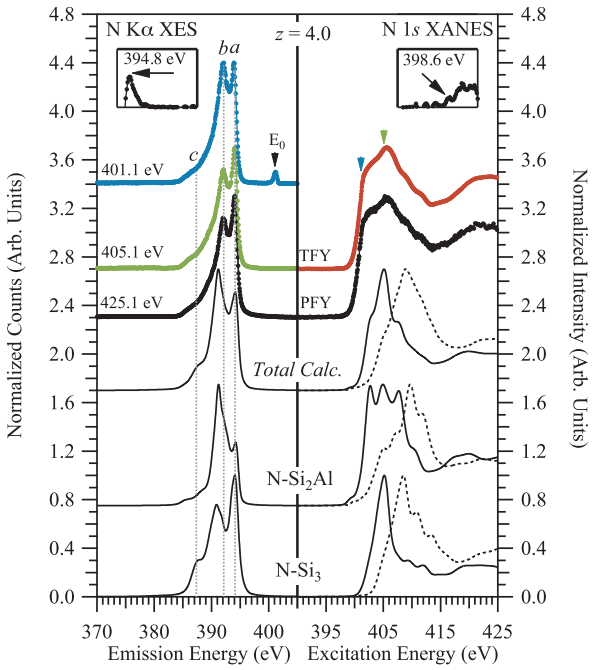

FIG. 5. (Color Online) The measured N Kα XES and N 1s XANES (connected dots) of β-sialon $z = 4.0$ are compared to the simulated spectra (lines) similar to Fig. 4.

gen electronic structure agree well and thus confirm the adopted structural model. The agreement furthermore supports the obtained values of the core hole shifts and the nonequivalent site shifts. Table I lists the adjusted measured electronic band gap values, which take into account the core hole shifts and non-equivalent site shifts. The measured electronic band gap values are 7.2 ± 0.2 eV, 6.2 ± 0.2 and 5.0 ± 0.2 for β-sialon $z = 0.0$, 2.0 and 4.0, respectively. These values are slightly larger than the calculated values, but not entirely unexpected since DFT, even using the MBJLDA functional will sometimes greatly underestimate the electronic band gap. Of course, one has to realize that the structure used for the DFT calculations will also greatly affect the calculated electronic band gap. While the Okatov model is a good base for β-sialons a larger superstructure with defects could still improve the agreement. It is worth mentioning that an even lower band gap energy (almost conductive behavior) is obtained by the Dupree model from the current DFT calculations, see Table I. Despite the fact that the difference between calculation and experiment exceeds the experimental error, the trend of both as a function of composition is similar. Especially the experimental values are linear in contrast to previous results[5,27]. The large band gap values may prove useful for doped pc-LED applications[34]. So far, we have analyzed only the measurements of the N p-states. However, much more can be learned through studying the electronic structure of the other atoms present. These include measurements of the O p-states (O Kα XES and O 1s XANES), the Si s/d-states (Si $L_{2,3}$ XES and Si 2p XANES), the Si p-states (Si 1s XANES), and finally the Al p-states (Al 1s XANES). Since it is clear that the Okatov model performs far better than the Dupree model, considering the calculated energy and inter-atomic forces as well as the behavior of the electronic structure with different compositions, only the calculated spectra using the Okatov model are presented. While not explicitly mentioned, measurements of the N p-states have a distinct advantage over the other measurements as N is unlikely to form impurity phases. For example, it is well known that silicon nitride forms a silicon dioxide passivation layer on the surface meaning that there is likely both, silicon dioxide (SiO_2)and Al_2O_3 on the surface of the β-sialons, which could affect the measured electronic structure in some cases. The measured O p-states have fairly good agreement with the

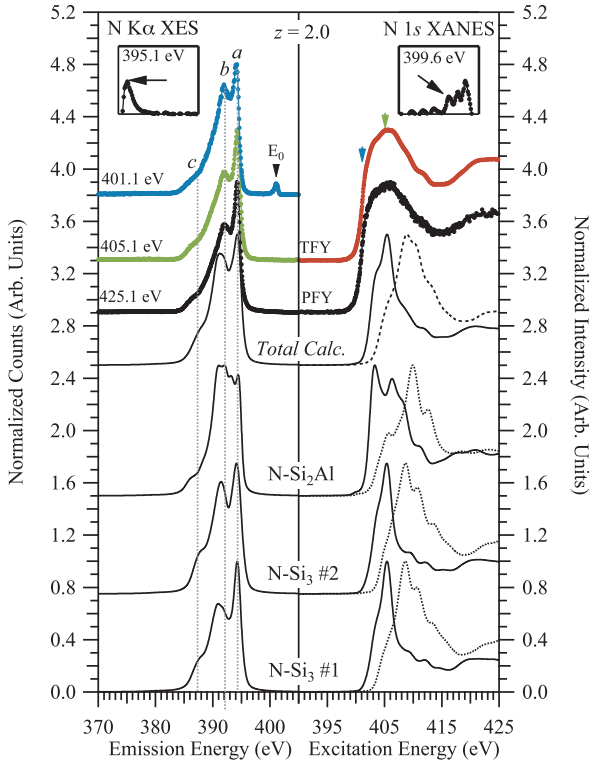

FIG. 6. (Color Online) The measured N Kα XES and N 1s XANES (connected dots) of β-sialon $z = 2.0$ are compared to the simulated spectra (lines) similar to Fig. 4.

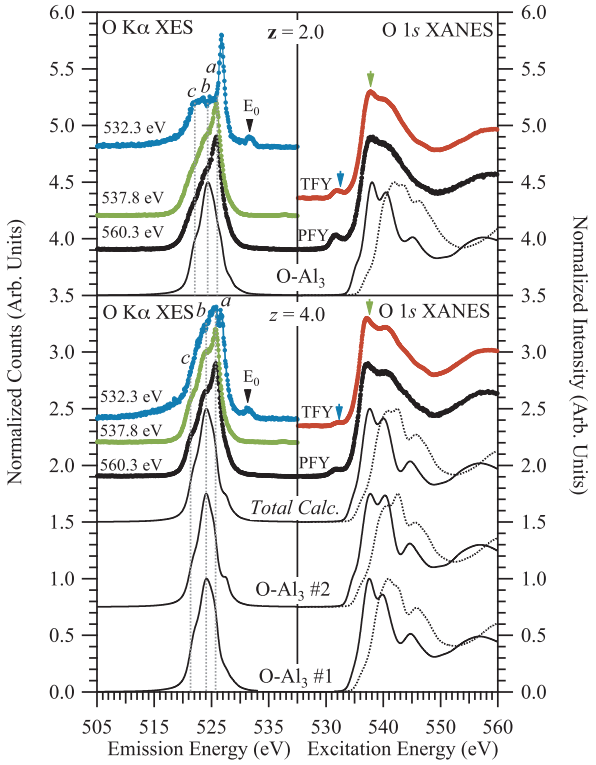

FIG. 7. (Color Online) The measured O Kα XES and O 1s XANES (connected dots) of β-sialon $z = 2.0$ and $z = 4.0$ are compared to the simulated spectra (lines) similar to Fig. 4.

calculated electronic structure. Fig. 7 shows the comparison of the measured and calculated O Kα XES and O 1s XANES spectra for both β-sialon compositions $z = 2.0$ and 4.0. Turning first to the O 1s XANES spectra, the agreement is quite good. However, as previously mentioned there may be contaminant silicon dioxide and the O 1s XANES spectra of β-sialons are remarkably similar to that of SiO_2[34]. That aside, there is also a small feature, reduced for $z = 4.0$, that is not reproduced by the calculated spectra. This pre-edge feature at ≈ 532.2 eV is due to scattering, which is not modeled in one electron DFT calculations and thus not reproduced in the current calculations. This scattering is evident in the β-sialon $z = 2.0$ resonant O Kα XES spectrum (with excitation 532.3 eV) where both elastic and inelastic scattering features are present. In the O Kα XES spectra, there is fairly good agreement between the measured and calculated spectra. However, some silicon dioxide is present as feature a is much too large and its position appears similar to previous silicon dioxide measurements[34]. Otherwise the VB width and positions of features b and c are correctly reproduced by the calculated spectra. Therefore, the O p-states, are for the most part, successfully reproduced using the Okatov model. The measured Si s/d-states show significant contributions from SiO_2 due to the short penetration depth of the low energy X-rays used to measure the spectra. Fig. 8 shows the comparison of the measured and calculated Si $L_{2,3}$ XES and Si 2p XANES spectra. The calculated spectra of β-sialon $z = 0.0$ agree very well with the corresponding measurements. However, the agreement between calculated and measured Si 2p XANES deteriorates as the oxygen content increases, which is likely due to the increase in silicon dioxide content. The silicon dioxide content is obvious from the characteristic features[38] present in the Si 2p XANES of the β-sialons. However, since silicon dioxide is a very large band gap insulator, we can tune the excitation energy for the Si $L_{2,3}$ XES spectra below the absorption of silicon dioxide in order to excite only the β-sialon Si s/d-states. This produces a significant reduction in features a and b making the measured spectra better resemble the calculated spectra. The expected behavior of the near edge XANES is reproduced by the calculated spectra in that the onset is broadened so that the Si electronic states increase in energy relative to the lower CB. Overall, the measured Si electronic structure is well reproduced by the calculations. The unoccupied Si and Al p-states are much less sensitive to the composition of the β-sialons than the measurements presented so far. Fig. 9 shows the comparison of the measured and calculated Al

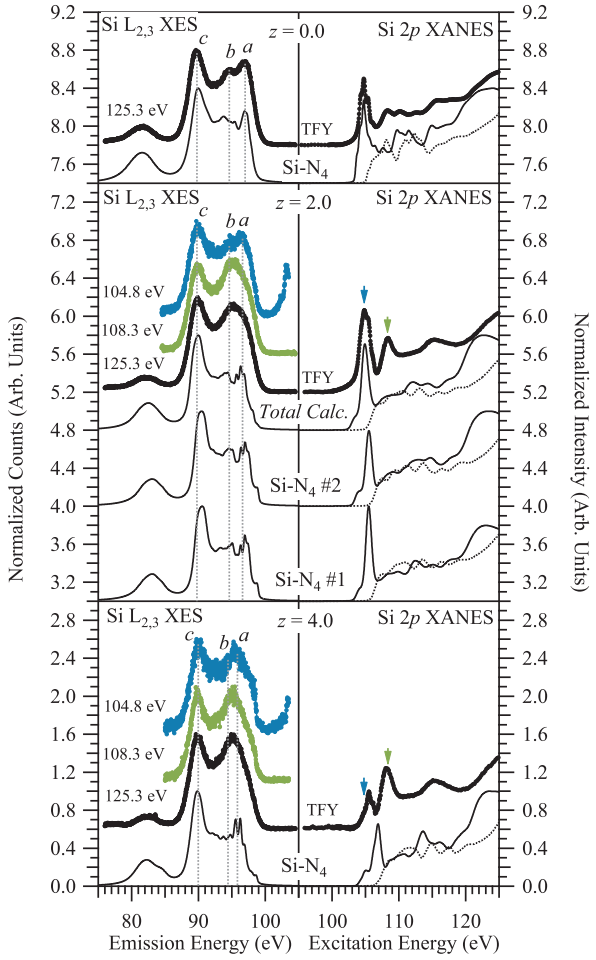

FIG. 8. (Color Online) The measured Si $L_{2,3}$ XES and Si $2p$ XANES (connected dots) of β-sialon $z = 0.0$, 2.0 and 4.0 are compared to the simulated spectra (lines) similar to Fig. 4.

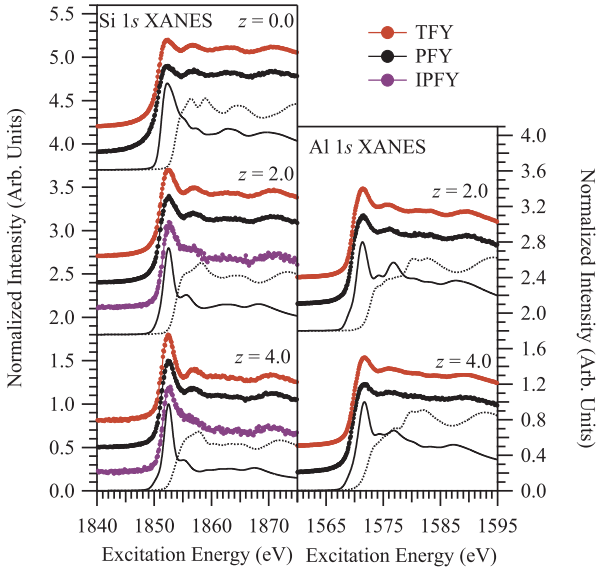

FIG. 9. (Color Online) The measured Al $1s$ XANES and Si $1s$ XANES (connected dots) of β-sialon $z = 0.0$, 2.0 and 4.0 are compared to the simulated spectra (lines). The nonequivalent crystal sites are added together.

$1s$ and Si $1s$ XANES spectra. Only a small difference was observed for the previously measured Al $1s$ XANES spectra[12] supports again the reliability of the Okatov model. In this model the Al and Si local bonding environments are identical for all compositions. The significant differences in the intensity of the lower energy feature for all Si and Al $1s$ XANES spectra can be attributed to saturation where the intensity decreases as the concentration of the element, either Si or Al, increases. This is even more evident with the Si $1s$ IPFY measurements, which utilize the Al Kα emission without any saturation. IPFY has the distinct advantage over PFY in that it is free of saturation[39]. The intensity of the lower energy feature in the IPFY is nearly identical, as expected from the comparison to the calculated spectra. Turning to the Al $1s$ XANES a similar effect is observed. The spectra are similar for all compositions if saturation is excluded. This cannot be experimentally verified since Al $1s$ IPFY measurements are not feasible. The similarities of both the Al and Si $1s$ XANES spectra suggest that the local bonding environment does not change for Si and Al consistent with the Okatov model whose calculated spectra successfully reproduce the measured spectra.

V. CONCLUSIONS

We measured the electronic band gap using XES and XANES measurements combined with DFT calculations. The electronic band gaps of β-$Si_{6-z}Al_zO_zN_{8-z}$ with $z = 0.0$, 2.0 and 4.0 are determined to be 7.2 eV, 6.2 eV and 5.0 eV (all with 0.2 eV experimental error), respectively. These values are all larger than the calculated band gap values of 5.88 eV, 3.45 eV and 2.39 eV for β-$Si_{6-z}Al_zO_zN_{8-z}$ with $z = 0.0$, 2.0 and 4.0, respectively, but this is expected due to the underestimation of the electronic band gap associated with DFT calculations. Furthermore, the experimental band gap measurements show a linear dependence on composition, which is contrary to calculations. The calculated band structure shows that the band gap reduction arises from the O p-states moving toward the Fermi level and the electronic band gap is now direct. Additionally, the large electronic band gap is prerequisite for using β-sialons in pc-LED devices[34]. Lastly, the electronic structure measurements show that there is a single bonding environment for the Si and Al atoms suggesting that β-sialons do crystallize in specific structural arrangements. In this case the Okatov structure reproduces most of the exper-

imental measurements and it is a good structural model for β-sialons.

ACKNOWLEDGMENTS

The Natural Sciences and Engineering Research Council of Canada and the Canada Research Chair Program supported this work. We gratefully acknowledge the assistance from the staff of the Advanced Light Source at Lawrence Berkeley National Laboratory and the Canadian Light Source. Research described in this paper was performed at the Canadian Light Source, which is supported by the Natural Sciences and Engineering Research Council of Canada, the National Research Council Canada, the Canadian Institutes of Health Research, the Province of Saskatchewan, Western Economic Diversification Canada, and the University of Saskatchewan. The Advanced Light Source is supported by the Director, Office of Science, Office of Basic Energy Sciences, and the U.S. Department of Energy under Contract No. DE-AC02-05CH11231. This research has been enabled by the use of computing resources provided by WestGrid and Compute/Calcul Canada. T. Gross gratefully acknowledges the financial support of this work by the Deutsche Forschungsgemeinschaft (Project Nos. KR 1739/8-1 and FU 125/39). The authors gratefully acknowledge the syntheses by M. Zenotchkine from Prof. Chen's group (University of Pennsylvania, Dept. of Materials Science and Engineering).

---

* teak.boyko@usask.ca

[1] K. H. Jack and W. I. Wilson, Nature-Phys. Sci. **238**, 28 (1972).
[2] Y. Oyama and O. Kamigait, Japan J Appl. Phys. **10**, 1637 (1971).
[3] T. Sekine, H. He, T. Kobayashi, M. Tansho, and K. Kimoto, Chem. Phys. Lett. **344**, 395 (2001).
[4] K. Liddell and D. Thompson, in *SiAlONs*, Key. Engin. Mater., Vol. 237, edited by K. Komeya, M. Mitomo, and Y. Cheng (2003) pp. 1–9.
[5] N. Hirosaki, C. Kocer, S. Ogata, and K. Tatsumi, Phys. Rev. B **71**, 104105 (2005).
[6] N. Kimura, K. Sakuma, S. Hirafune, K. Asano, N. Hirosaki, and R.-J. Xie, Appl. Phys. Lett. **90**, 051109 (2007).
[7] T. Ekstrom and M. Nygren, J. Am. Ceram. Soc. **75**, 259 (1992).
[8] L. J. Gauckler, H. L. Lukas, and G. Petzow, J. Am. Ceram. Soc. **58**, 346 (1975).
[9] T. Ekstrom, P. O. Kall, M. Nygren, and P. O. Olsson, J. Mater. Sci. **24**, 1853 (1989).
[10] F. K. Vandijen, R. Metselaar, and R. B. Helmholdt, J. Mater. Sci. Lett. **6**, 1101 (1987).
[11] T. D. Boyko, C. E. Zvoriste, I. Kinski, R. Riedel, S. Hering, H. Huppertz, and A. Moewes, Phys. Rev. B **84**, 085203 (2011).
[12] K. Tatsumi, T. Mizoguchi, S. Yoshioka, T. Yamamoto, T. Suga, T. Sekine, and I. Tanaka, Phys. Rev. B **71**, 033202 (2005).
[13] N. D. Butler, R. Dupree, and M. H. Lewis, J. Mater. Sci. Lett. **3**, 469 (1984).
[14] R. Dupree, M. H. Lewis, G. Lengward, and D. S. Williams, J. Mater. Sci. Lett. **4**, 393 (1985).
[15] R. Dupree, M. H. Lewis, and M. E. Smith, J. Appl. Crystallogr. **21**, 109 (1988).
[16] M. E. Smith, J. Phys. Chem. **96**, 1444 (1992).
[17] J. Sjoberg, T. Ericsson, and O. Lindqvist, J. Mater. Sci. **27**, 5911 (1992).
[18] T. Hagio, A. Takase, and S. Umebayashi, J. Mater. Sci. Lett. **11**, 878 (1992).
[19] K. Tatsumi, I. Tanaka, H. Adachi, and M. Yoshiya, Phys. Rev. B **66**, 165210 (2002).
[20] W. Y. Ching, M. Z. Huang, and S. D. Mo, J. Am. Ceram. Soc. **83**, 780 (2000).
[21] S. V. Okatov and A. L. Ivanovskii, Int. J. Inorg. Mater. **3**, 923 (2001).
[22] X. Xu, T. Nishimura, N. Hirosaki, R. Xie, Y. Yamamoto, and H. Tanaka, Nanotechnology **16**, 1569 (2005).
[23] K. J. D. MacKenzie and D. Van Barneveld, J. Eur. Ceram. Soc. **26**, 209 (2006).
[24] M. D. Alcala, J. M. Criado, F. J. Gotor, and C. Real, J. Mater. Sci. **41**, 1933 (2006).
[25] F. J. Li, T. Wakihara, J. Tatami, K. Komeya, and T. Meguro, J. Eur. Ceram. Soc. **27**, 2535 (2007).
[26] L. Benco, J. Hafner, Z. Lences, and P. Sajgalik, J. Am. Ceram. Soc. **86**, 1162 (2003).
[27] W. Y. Ching, S.-D. Mo, L. Z. Ouyang, P. Rulis, I. Tanaka, and M. Yoshiya, J. Am. Ceram. Soc. **85**, 75 (2002).
[28] M. Schwarz, G. Miehe, A. Zerr, E. Kroke, B. T. Poe, H. Fuess, and R. Riedel, Adv. Mater. **12**, 883 (2000).
[29] T. Roisnel and J. Rodriguez-Carvajal, in *EPDIC 7: European Powder Diffraction, Pts. 1 and 2*, Mater. Sci. Forum, Vol. 378-3, edited by R. Delhez and E. J. Mittemeijer (2001) pp. 118–123.
[30] T. Regier, J. Krochak, T. K. Sham, Y. F. Hu, J. Thompson, and R. I. R. Blyth, Nucl. Instrum. Methods Phys. Res. Sect. A **582**, 93 (2007).
[31] Y. F. Hu, L. Zuin, G. Wright, R. Igarashi, M. McKibben, T. Wilson, S. Y. Chen, T. Johnson, D. Maxwell, B. W. Yates, T. K. Sham, and R. Reininger, Rev. Sci. Instrum. **78**, 083109 (2007).
[32] J. J. Jia, T. A. Callcott, J. Yurkas, A. W. Ellis, F. J. Himpsel, M. G. Samant, J. Stöhr, D. L. Ederer, J. A. Carlisle, E. A. Hudson, L. J. Terminello, D. K. Shuh, and R. C. C. Perera, Rev. Sci. Instrum. **66**, 1394 (1995).
[33] T. D. Boyko, E. Bailey, A. Moewes, and P. F. McMillan, Phys. Rev. B **81**, 155207 (2010).
[34] C. Braun, M. Seibald, S. L. Böerger, O. Oeckler, T. D. Boyko, A. Moewes, G. Miehe, A. Tüecks, and W. Schnick, Chem. Eur. J. **16**, 9646 (2010).
[35] K. Schwarz, P. Blaha, and G. K. H. Madsen, Comput. Phys. Commun. **147**, 71 (2002).
[36] J. P. Perdew, K. Burke, and M. Ernzerhof, Phys. Rev. Lett. **77**, 3865 (1996).
[37] F. Tran and P. Blaha, Phys. Rev. Lett. **102**, 226401 (2009).
[38] J. A. McLeod, E. Z. Kurmaev, P. V. Sushko, T. D. Boyko, I. A. Levitsky, and A. Moewes, Chem. -Eur. J. **18**, 2912

(2012).

[39] A. J. Achkar, T. Z. Regier, H. Wadati, Y. J. Kim, H. Zhang, and D. G. Hawthorn, Phys. Rev. B **83**, 081106 (2011).

Chapter 4

Predicting the Structure of Materials

4.1 Hardness Predictions and Structure

Predicting the hardness of materials is very important as it will allow for the improvement of current technological and mechanical devices. However, the electronic band gap is seemingly intertwined with the mechanical hardness [16] and could be exploited to evaluate hypothetical materials. The success of calculating the hardness of materials [15] and electronic band gap [38] with an *ab intio* approach suggests these methods could be combined with Eq. 1.15. This would allow one to evaluate the likelihood of a specific material to exist. This provides a very powerful tool to study the not only the hardness, but the existence of hypothetical ultra-hard materials. In summary, given the well-defined linear relation between mechanical hardness and the intrinsic electronic band gap, a material must exhibit the correct mechanical and electronic properties in order to exist.

4.2 Publication

The following publication is an innovative look on determining whether a hypothetical material is likely to exist. The materials studied are restricted semiconductors with covalent bonding, and also relies on the accurate calculations of the electronic structure and electronic band gap using DFT. The following paper was written solely by T D Boyko under the supervision of A Moewes.

Predicting the Existence of Spinel Nitrides

Authors: *T D Boyko and A Moewes*

Summary and Author Contributions:

In this study [61], the hardness of all group 14 spinel nitrides, γ-C_3N_4, γ-Si_3N_4, γ-Ge_3N_4, γ-Sn_3N_4, γ-Pb_3N_4, and their ternary compounds are calculated. This is achieved solely through the calculation of the electronic structure using DFT calculations performed by T D Boyko under the supervision of A Moewes. This study aims not only to the calculate the intrinsic hardness of the group 14 spinel-type nitrides, but also use the calculated electronic band gap and hardness to evaluate the likelihood of whether further group 14 spinel-type nitrides may be synthesized. The only experimentally realized binary spinel nitrides areγ-Si_3N_4, γ-Ge_3N_4 and γ-Sn_3N_4, while the others remain only hypothetical. Much research has been carried out regarding the hardness of γ-C_3N_4 with little notion as to whether this material would ever exist. We use the bond modulus equation proposed by Gilman [16] to compare both the calculated hardness and calculated electronic band gap. The electronic band gap is calculated using DFT calculations with the MBJLDA functional, while the hardness is calculated using the approach of Ref. [15]. The spinel nitrides that have been synthesized exhibit the predicted linear relationship between hardness and bond modulus as do some of the hypothetical compounds. However, the coveted γ-C_3N_4 strongly diverges from the linear relationship suggesting its existence will remain hypothetical. In order to validate this model, we apply the same method to the pure group 14 compounds C through Sn with diamond structure, which also show a near perfect linear correspondence between hardness and bond modulus. This publication highlights the strong correlation between hardness and the electronic structure showing that by using calculations for the electronic band gap, not only can the hardness of materials be predicted, but even their likelihood of being synthesized. This results here further motivate the development of techniques used to measured the intrinsic electronic band gap regarding research into ultra-hard materials.

Predicting the Existence of Spinel Nitrides

T. D. Boyko and A. Moewes*
Department of Physics and Engineering Physics, University of Saskatchewan, 116 Science Place, Saskatoon, Saskatchewan, S7N 5E2 (Canada)
(Dated: October 9, 2013)

The hypothetical spinel carbon nitride (γ-C_3N_4) has received a large amount of attention due to its predicted hardness being comparable to diamond. The group 14 spinel binary nitrides that have been synthesized are limited so far to γ-Si_3N_4, γ-Ge_3N_4 and γ-Sn_3N_4. However, there still remains significant interest in γ-C_3N_4 in the hope that it will eventually be synthesized, but there are no successful reports making the study of γ-C_3N_4 strictly theoretical. The hardness and electronic band gap are calculated using *ab initio* density functional theory. Through an empirical relationship that correlates hardness, crystal structure and the electronic band gap we show that γ-C_3N_4 and the solid solutions γ-$(C,Si)_3N_4$ will never be synthesized. This relationship also shows that in the case of the solid solutions γ-$(Si,Ge)_3N_4$ and γ-$(Ge,Sn)_3N_4$ the tetrahedral site is filled first by the larger cation, Ge and Sn. Furthermore, a new method to calculate the hardness using the nitrogen bonding tetrahedron provides more unambiguous results and the trend of the hardness is in better agreement with experimental measurements.

PACS numbers: 62.20.Qp 71.15.Mb 71.20.-b

Ultra-hard materials, which are materials with a hardness larger than 40 GPa, are widely used in industry today for cutting blade coatings, industrial abrasives and component coatings providing a wear resistant surface. Diamond, although the hardest known material, has the disadvantage that the carbon reacts with iron when used as an abrasive. This has since been replaced in most cases with the second hardest material, cubic boron nitride (*c*-BN) [1]. Increasing the number of available ultra-hard materials, other than diamond and *c*-BN, could significantly improve the efficiency of industrial machining/polishing and the longevity of mechanical components, particularly if a material harder than diamond was discovered. Spinel structured binary group 14 nitrides have been studied, since the discovery of spinel silicon nitride (γ-Si_3N_4) [2], for their large hardness [3] and their desirable electronic properties [4]. While the hardness of γ-Si_3N_4 is less than that of diamond [5, 6], its hardness is much larger than the hexagonal phase (β-Si_3N_4) [5] and reported measurements are as large as 43 GPa [7], which place it firmly in the ultra-hard materials class. However, there is still significant interest in the still not synthesized spinel carbon nitride (γ-C_3N_4), which has a predicted hardness possibly exceeding that of *c*-BN [8]. Measuring the hardness of these spinel nitrides has proven to be difficult due to the quality of available materials for testing and as a result there is a large range of values for the few measurements that have been reported. Microhardness and nanohardness measurements place the hardness value of γ-Si_3N_4 somewhere between 31 to 43 GPa [6, 7, 9, 10] depending on the oxygen content. In addition, these values are also highly dependent on the indentation load and indentation method. For the other spinel nitrides, γ-Ge_3N_4 and γ-Sn_3N_4, the values have much less variation with hardness values ranging from 28 to 31 GPa and 11 to 13 GPa [9], respectively. However, this is due to the small number of reported measurements and makes these values seemingly reliable. The aim to predict new ultra-hard materials combined with the ambiguity of hardness measurements drives the need to develop methods that calculate the intrinsic hardness. There are a few theoretical methods that have been developed in order to calculate the intrinsic hardness; these range from empirical [11**?** , 12] to semi-*ab initio* [3, 13, 14] or in one case strictly *ab initio* [15]. While these methods are quite successful in determining the hardness of diamond and other materials with well-established hardness values, there is a large variation in the reported values for spinel nitrides. The reported calculated hardness of γ-Si_3N_4 and γ-Ge_3N_4 ranges from 27 to 34 GPa [3, 14–16] and 19 to 25 GPa [3, 15], respectively. The range of predicted hardness values for γ-C_3N_4 is larger still at 56 to 71 GPa [3, 8, 15]. Conversely, the hardness of γ-Sn_3N_4 remains unstudied theoretically. It is clear that there must be some cause for this discrepancy in the calculated hardness values for spinel nitrides, which is reexamined here and compared to recent experimental values. Calculated hardness is expressed as the bond strength per unit volume. Therefore, determining the effective bonding volume is very important and greatly affects the calculated hardness values. The bonding volume for many simple materials (diamond, *c*-BN, etc.) is determined easily; there is only one bonding polyhedron and one simply divides the unit cell volume by the number of polyhedrons. The spinel structure is much more complicated than the structure of diamond and determining the effective volumes of the polyhedrons can be somewhat ambiguous. Until now, the hardness of spinel nitrides was calculated using the polyhedrons of the cations (tetrahedral and octahedral) with the effective volume determined separately [3, 8, 14–16]. Here, we calculate the effective bonding volume using the tetrahe-

dron of the anion, which is determined by dividing the total unit cell volume by the number of nitrogen bonding tetrahedrons. This is contrary to previous methods and makes the calculation of the effective bonding volume more straightforward. The hardness calculations use the method proposed in Ref. 15, but they are modified to treat the mixed coordination of spinel structure properly as discussed above. Previously, this hardness calculation method was shown to be quite successful for simple binary materials with only one bonding coordination and was generalized to multiple bonding coordinations, but was later shown to be incorrect [17]. We tailor the hardness equations for spinel structure, γ-AD_2N_4 with A and D having tetrahedral and octahedral coordination, respectively. Eq. 1 is used to calculate the hardness H from the bond strengths of the tetrahedral bonds S_{AN} and the octahedral bonds S_{DN}. The effective bonding volume is calculated using the lattice constant c. The scaling constants η and σ are required to fit the hardness values for well-studied materials, similar to Ref. [15]. Eq. 2 determines bond strength from the bond lengths d_{AN} and d_{DN} and the average electron densities e_i using density functional theory (DFT) to calculate the radius of a sphere R_i required to enclose the total valence charge Z_i of the cations and nitrogen atoms $i = A, D, N$. Additionally, the effective difference in the bonding potentials, Eq. 3, is also changed to reflect the correct arithmetic and geometric averages. As one can see, the only input for determining hardness in this way is the crystal structure.

$$H = \frac{32\eta}{c^3}(S_{AN}S_{DN}^3)^{\frac{1}{4}}e^{-\sigma f_e}, \quad \eta = 1550, \quad \sigma = 4 \quad (1)$$

$$S_{AN} = \frac{\sqrt{e_A e_N}}{4d_{AN}}, \quad S_{DN} = \frac{\sqrt{e_D e_N}}{6d_{DN}}, \quad e_i = Z_i/R_i \quad (2)$$

$$f_e = 1 - \left(\frac{7\sqrt[7]{e_A e_D^2 e_N^4}}{(e_A + 2e_D + 4e_N}\right)^2, \quad i = A, D, N \quad (3)$$

Conventional DFT calculations are well known to underestimate the band gap with exchange correlation functionals such as the generalized gradient approximations (GGA-PBE)[18] and the local density approximation (LDA). Instead, the band gap and thereby the electron density are calculated more accurately with a modified form of the LDA functional, namely MBJLDA [19]. These calculations were performed using WIEN2k [20] with a $20 \times 20 \times 20$ k-point mesh and energy cutoff of -6.0 Rydberg using the new MBJLDA functional [19]. The charge integration for calculating the hardness was carried out using CRITIC [21] with a $100 \times 50 \times 100$ point mesh for the $r \times \phi \times \theta$ grid, respectively. The spinel structure, although having 56 atoms in the unit cell, can be defined with two parameters: the lattice constant and the anion bond parameter. Table I lists the structure parameters for the synthesized binary spinel nitrides [2, 22, 23]: γ-Si_3N_4, γ-Ge_3N_4 and γ-Sn_3N_4. The structures of γ-C_3N_4 and γ-Pb_3N_4 have been optimized using DFT and the GGA-PBE functional [18] using a $10 \times 10 \times 10$ k-point mesh. The ternary compounds are created by assuming that the lattice constants vary linearly with composition similar to the materials studied in Ref. 22. The anion bonding parameters for the ternary spinel structures were optimized for minimal inter-atomic forces. The ternary compounds, aside from γ-$GeSi_2N_4$ remain only hypothetical and have not been synthesized. In order to study the site preference of the cations, both preferential site occupations are considered. For example, in the case of γ-SiC_2N_4, Si and C occupy the tetrahedral and octahedral sites, respectively. While in the case of γ-CSi_2N_4, C and Si occupy the tetrahedral and octahedral sites, respectively. This way the ternary compounds all have spinel structure and thus are defined using the Fd-$3m$ (No. 227) spacegroup. The calculated hardness values using Eq. 1 agrees with most of the reported hardness measurements within experimental error [6, 9, 26]. However, the calculated hardness values here assume isotropic material indentation meaning that the calculated values, in general, are likely to be smaller than the experimental values. The

TABLE I. The lattice constants c, calculated sphere radii R_i, calculated hardness values H, anion bond parameters u, and band gap values E_g for the spinel nitrides γ-AD_2N_4 are compared to the experimentally measured hardness and band gap values. The available reported measurements are displayed below their respective calculated values.

Material	c (Å)	u	R_A (Å)	R_D (Å)	R_N (Å)	H (GPa)	E_g (eV)
γ-C_3N_4	6.7630	0.25600	1.001	1.018	0.955	76.9	1.57
γ-SiC_2N_4	7.0880	0.24881	1.235	1.039	0.954	58.5	0.69
γ-CSi_2N_4	7.4131	0.26364	1.048	1.269	0.949	42.9	2.32
γ-Si_3N_4	7.7381	0.25968	1.316	1.278	0.942	33.3	4.97
						37^d	4.8^a
						35^e	4.9^b
γ-$GeSi_2N_4$	7.7962	0.26157	1.369	1.295	0.953	31.1	4.50
γ-$SiGe_2N_4$	8.0544	0.25337	1.310	1.374	0.963	26.5	3.27
γ-Ge_3N_4	8.2125	0.2577	1.388	1.379	0.972	24.0	3.59
						28^h	3.5^a
						31^i	3.5^b
γ-$SnGe_2N_4$	8.4873	0.26413	1.542	1.395	0.984	19.9	2.75
γ-$GeSn_2N_4$	8.7621	0.25210	1.422	1.544	0.992	16.3	1.90
γ-Sn_3N_4	9.0370	0.25960	1.589	1.553	1.000	13.8	1.60
						13^j	1.6^a
γ-$PbSn_2N_4$	9.2088	0.26278	1.653	1.565	1.104	13.2	0.30
γ-$SnPb_2N_4$	9.3805	0.25519	1.599	1.639	1.027	11.3	0.00
γ-Pb_3N_4	9.5523	0.25960	1.670	1.636	1.049	10.5	0.00

The experimental errors (hardness method) are: [a]Ref. 24: ±0.2 eV, [b]Ref. 25: ±0.2 eV, [d]Ref. 6: ±7 GPa (Nano), [e]Ref. 26: ±4 GPa (Knoop), [h]Ref. 9: ±5 GPa (Vickers), [i]Ref. 9: ±6 GPa (Nano), [j]Ref. 9: ±5 GPa (Nano).

calculated hardness values are similar to previous calculations [3, 8, 14–16], but are less ambiguous since the bonding volume is calculated using the nitrogen tetrahedrons. As a result, the calculated hardness trend agrees with the reported measurements very well. Moreover, the calculated band gap values using MBJLDA agree with recent measurements and calculations [24]. There has been significant progress in relating the hardness of materials to their band gap using an empirical relationship [12]. Based on the idea of the dislocation activation energy being correlated to the band gap [11], this relationship is valid for a large array of materials [12] and as we shall show it can be used to ascertain if a hypothetical material will exhibit the proper combination of electronic and mechanical properties making its existence possible. While this method cannot directly predict the hardness of materials from the structure, it is a very useful tool for analyzing the hardness of semi-conducting materials and can possibly predict the hardness of hypothetical materials if one knows their band gap value. This theory states, in Eq. 4, that the hardness of semi-conducting materials has a linear dependence on the bond modulus B_m. Eq. 4 is used to calculate the bond modulus from the band gap E_g and molecular volume V_m, with the molecular volume calculated from the lattice constant using Eq. 4. The arbitrary constants, E and G, are specific to a material class, in this case the spinel structure. This means that for each class of materials there will be unique values for E and G. Although this equation has been tested for experimental hardness and band gap values, it should also be valid for theoretical values, and thus using Eq. 4 in this way significantly increasing its predictive ability.

$$H = EB_m + G, \quad B_m = \frac{E_g}{V_m}, \quad V_m = \frac{c^3}{8} \qquad (4)$$

Figure 1 shows the calculated bond modulus plotted against the calculated hardness, which produces a nearly perfect linear relationship when considering only the binary nitrides that have been synthesized. Additionally, the recently synthesized γ-$GeSi_2N_4$ [22] also agrees well with Eq. 4, falling near perfectly on the line created with a linear fit of the binary nitrides. This is contrary to γ-$SiGe_2N_4$, which diverges from Eq. 4 significantly. This shows Eq. 4 could have predicted the preferential site occupation of Ge in the spinel structure [22, 27, 28]. For the solid solutions γ-$(Sn,Ge)_3N_4$ there is also a slight preference for Sn to occupy the tetrahedral site, similar to previous results [22]. More importantly, Eq. 4 also shows that the spinel nitrides containing C or Pb are not likely to exist since the band gap (or bond modulus) will be much too small for their intrinsic hardness. However, since γ-Pb_3N_4 and γ-$SnPb_2N_4$ are not semi-conductors Eq. 4 does not apply and thus no conclusions about their existence can be drawn. In order to confirm the validity of using Eq. 4 to evaluate materials with their calculated hardness and band gap values from DFT calculations,

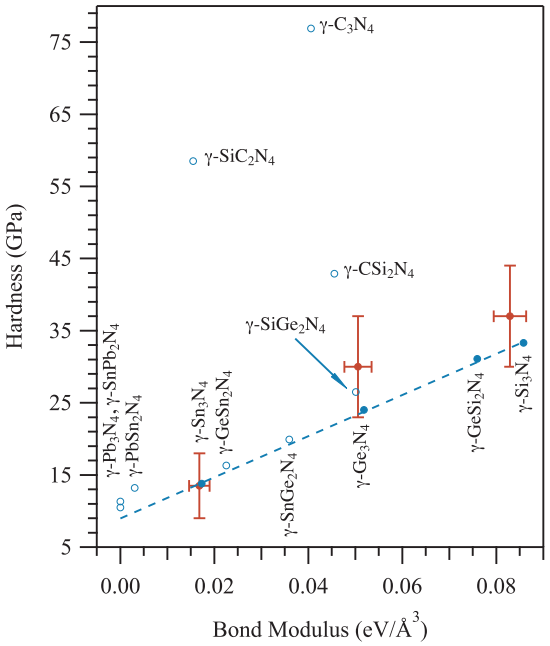

FIG. 1. (Color Online) The calculated (•) and measured (•) hardness H values for all synthesized binary spinel nitrides are compared to their calculated and measured bond modulus B_m. These calculated values are fit with line (– – –) having a linear fit factor of $R^2 = 0.9995$. Furthermore, the calculated hardness (○) of the hypothetical binary spinel nitrides and ternary spinel nitrides using theoretical structures are also compared to their calculated bond modulus B_m. The measured hardness errors illustrate the range of reported values and bond modulus error use the results from Ref. [24], both listed in Table I.

the bond modulus and hardness are computed for the diamond structure (Fd-$3m$) group 14 materials: diamond, silicon, germanium, and tin (α-Sn). The hardness equations, Eq. 1 and Eq. 2 are modified for more simple materials with only one type of bond reducing the necessary equations to include only Eq. 5. The structures used for these calculations were taken from Ref. 29 with the same DFT calculation parameters used for the spinel nitrides.

$$H = \frac{4\eta}{c^3}S, \quad S = \frac{e}{4d}, \quad e = Z/R, \quad \eta = 1550 \qquad (5)$$

Table II shows the calculated hardness and band gap values. The calculated hardness is plotted against the bond modulus using Eq. 4 in Fig. 2, which shows that the calculated bond modulus and hardness of the group 14 compounds have a nearly perfect linear relationship. Furthermore, the comparison the measured hardness and bond modulus values show that a linear relationship is also present for the measured values. The calculated hardness and band gap values have good agreement with

previously measured values [5, 19, 30], however, there are little to no experimental hardness values for α-Sn (Sn in diamond structure is not stable at room temperature). The success of applying Eq. 4 to group 14 elements confirms using the calculated hardness and band gap values with Eq. 4 is valid when applied to materials that are modeled well using density functional theory. In conclusion, a new method to calculate the hardness of spinel nitrides is presented. The trend of calculated hardness values agrees better with current experimental measurements than previous results. Furthermore, a well established linear relationship between the bond modulus and hardness is applied to show that the class of group 14 spinel nitrides is limited to γ-Si_3N_4, γ-Ge_3N_4, γ-Sn_3N_4 and their ternary nitrides with the tetrahedral sites occupied first by the larger cation. This suggests that γ-Si_3N_4 will remain the hardest spinel nitride and that the elusive γ-C_3N_4 will never be synthesized.

TABLE II. The lattice constants c, calculated sphere radii R_i, calculated hardness values H and band gap values E_g for group 14 elements are compared to available measured values H^{exp} and E_g^{exp}.

Material	c (Å)	R (Å)	H (GPa)	H^{exp} (GPa)	E_g (eV)	E_g^{exp} (eV)
Diamond	3.5668	0.976	91.6	96.0	4.94	5.48
Silicon	5.4307	1.455	11.3	11.3	1.17	1.17
Germanium	5.6574	1.510	9.3	8.8	0.86	0.74
Tin	6.4912	1.721	4.7		0.00	

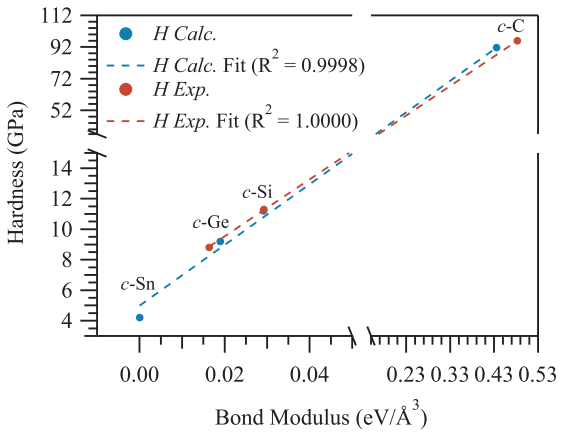

FIG. 2. (Color Online) The calculated (blue) and measured (red) hardness values H for group 14 elements with diamond structure are compared to their calculated and measured bond modulus B_m.

We would like to thank the Natural Science and Engineering Research Council of Canada, and the Canada Research Chair program for funding this research. This research has also been enabled by the use of computing resources provided by WestGrid and Compute/Calcul Canada.

* alex.moewes@usask.ca

[1] J. Haines, J. M. Leger, and G. Bocquillon, Ann. Rev. Mater. Res. **31**, 1 (2001).
[2] A. Zerr, G. Miehe, G. Serghiou, M. Schwarz, E. Kroke, R. Riedel, H. Fueß, P. Kroll, and R. Boehler, Nature (London) **400**, 340 (1999).
[3] F. M. Gao, R. Xu, and K. Liu, Phys. Rev. B **71**, 052103 (2005).
[4] S.-D. Mo, L. Ouyang, W. Y. Ching, I. Tanaka, Y. Koyama, and R. Riedel, Phys. Rev. Lett. **83**, 5046 (1999).
[5] R. A. Andrievski, Int. J. Refract. Met. Hard. Mat. **19**, 447 (2001).
[6] A. Zerr, M. Kempf, M. Schwarz, E. Kroke, M. Göken, and R. Riedel, J. Am. Ceram. Soc. **85**, 86 (2002).
[7] I. Tanaka, F. Oba, T. Sekine, E. Ito, A. Kubo, K. Tatsumi, H. Adachi, and T. Yamamoto, J. Mater. Res. **17**, 731 (2002).
[8] J. L. He, L. C. Guo, X. J. Guo, R. P. Liu, Y. J. Tian, H. T. Wang, and C. X. Gao, Appl. Phys. Lett. **88**, 101906 (2006).
[9] M. Shemkunas, W. Petuskey, A. Chizmeshya, K. Leinenweber, and G. Wolf, J. Mater. Res. **19**, 1392 (2004).
[10] W. Wang, D. He, M. Tang, F. Li, L. Liu, and Y. Bi, Diam. Relat. Mat. **27-28**, 49 (2012).
[11] J. J. Gilman, Science **261**, 1436 (1993).
[12] J. J. Gilman, J. Phys. D-Appl. Phys. **41**, 074020 (2008).
[13] F. M. Gao, J. L. He, E. D. Wu, S. M. Liu, D. L. Yu, D. C. Li, S. Y. Zhang, and Y. J. Tian, Phys. Rev. Lett. **91**, 015502 (2003).
[14] F. M. Gao and L. H. Gao, J. Superhard. Mater. **32**, 148 (2010).
[15] A. Šimůnek and J. Vackář, Phys. Rev. Lett. **96**, 085501 (2006).
[16] J. He, L. Guo, D. Yu, R. Liu, Y. Tian, and H. Wang, Appl. Phys. Lett. **85**, 5571 (2004).
[17] Z. Y. Liu, X. Guo, J. He, D. Yu, and Y. Tian, Phys. Rev. Lett. **98**, 109601 (2007).
[18] J. P. Perdew, K. Burke, and M. Ernzerhof, Phys. Rev. Lett. **77**, 3865 (1996).
[19] F. Tran and P. Blaha, Phys. Rev. Lett. **102**, 226401 (2009).
[20] K. Schwarz, P. Blaha, and G. K. H. Madsen, Comput. Phys. Commun. **147**, 71 (2002).
[21] A. Otero-de-la Roza, M. A. Blanco, A. M. Pendas, and V. Luana, Comput. Phys. Commun. **180**, 157 (2009).
[22] E. Soignard, P. F. McMillan, and K. Leinenweber, Chem. Mater. **16**, 5344 (2004).
[23] N. Scotti, W. Kockelmann, J. Senker, S. Traßel, and H. Jacobs, Z. Anorg. Allg. Chem. **625**, 1435 (1999).
[24] T. D. Boyko, A. Hunt, A. Zerr, and A. Moewes, Phys. Rev. Lett. **111**, 097402 (2013).
[25] T. D. Boyko, E. Bailey, A. Moewes, and P. F. McMillan, Phys. Rev. B **81**, 155207 (2010).
[26] J. Z. Jiang, F. Kragh, D. J. Frost, K. Stahl, and H. Lindelov, J. Phys.: Condens. Matter **13**, L515 (2001).

[27] J. Dong, J. Deslippe, O. F. Sankey, E. Soignard, and P. F. McMillan, Phys. Rev. B **67**, 094104 (2003).
[28] W. Y. Ching, S.-D. Mo, I. Tanaka, and M. Yoshiya, Phys. Rev. B **63**, 064102 (2001).
[29] R. W. G. Wyckoff, *Crystal Structures* (John Wiley & Sons, 1963).
[30] L. M. Qian, M. Li, Z. R. Zhou, H. Yang, and X. Y. Shi, Surf. Coat. Technol. **195**, 264 (2005).

Chapter 5

Conclusions

Ultra-hard materials are exceptionally useful materials that find uses in a wide array of applications. However, the cause of the large hardness in these materials is still being studied in an effort to predict hypothetical materials that could exceed the hardness of the currently known hardest materials. The most obvious route to study hardness would be measurements, however, measuring hardness is problematic. The measured hardness is largely dependent on the extrinsic material properties such as purity, form and synthesis techniques. This precludes measured hardness from being considered a fundamental property, and as such cannot be easily studied for hypothetical or novel materials. Instead, several theoretical models have been developed in order to further study the hardness of materials as a fundamental property.

The intrinsic hardness of materials has been studied in an effort to predict the hardness of hypothetical materials. Contrary to hardness measurements, the intrinsic hardness is a fundamental quantity that is independent of the material's macroscopic properties. The models used to determine the intrinsic hardness depend on two further intrinsic properties, namely the crystal structure and electronic structure. The crystal structure is measured using various diffraction techniques (XRD, ND, EXAFS, etc.), but the electronic structure as a whole is very complicated. Still, the fundamental quantity that persists is the electronic band gap. Presumably if one knows the electronic band gap and the crystal structure then the intrinsic hardness could be determined easily.

The electronic band gap, as an intrinsic quantity, can be difficult to measure. Conventional measurements such as UV-Vis reflection or transmission are plagued with inter-band transitions and exciton effects. The intrinsic band gap, independent of the application, can be measured more reliably with core-level spectroscopy techniques such as XES and XANES. Since with these techniques, the VB and CB are measured independently with little inter-

action between them, the measured band gap will be the intrinsic electronic band gap as opposed to the optical band gap or electric band gap. However, measuring the band gap with core-level spectroscopy requires careful measurements and calculations to correct for the core hole shift in order to arrive at the appropriate electronic band gap value. The results of Refs. 46 and 47 show that using a combination of XES and XANES measurements with DFT calculations provide an alternative means to measure the electronic band gap.

The electronic band gap, being a fundamental intrinsic quantity, is very useful not only for semiconducting applications, but also to study hardness. Since the intrinsic electronic band gap is inherently related to the intrinsic hardness, the electronic band gap can actually be used to predict the hardness of materials. The results of Ref. [50] show that the intrinsic hardness can be predicted for materials provided that one knows the structure and electronic band gap. This suggests that measuring the electronic band gap of novel materials provides a means to further study its intrinsic properties. However, in order to measure the electronic band gap and predict the hardness of materials, the crystal structure must be well known.

The crystal structure, measured with conventional methods has some limitations when it comes to oxonitrides and other novel materials. Conventional XRD measurements are unable to distinguish between light elements with similar atomic numbers and ND measurements require a large amount of material. Instead, we show that the crystal structure can often be inferred using electronic structure measurements, where the structural models are tested by comparing the calculated electronic structure to the measured electronic structure. The crystal structure is used to calculate the core hole shift and the electronic band gap. Therefore, determining the full crystal structure, including anion ordering, is invaluable. The results of Refs. 54 and 56 illustrate how the anion and cation ordering in the crystal structure can be determined using XES and XANES measurements and DFT calculations.

The electronic band gap is usually measured, as the calculated electronic band gap value typically is strongly underestimated by DFT. However, with the recent progress in ECFs the electronic band gap can be calculated more reliably. The results of Ref. 52 shows that the measured intrinsic electronic band gap agrees with previous results. But more importantly, it also shows that the calculation of the electronic band values agree very well with the measured electronic band gap values. Furthermore, the electronic band gap and exciton binding energy

of hypothetical materials are calculated predicting that they would be very useful for optical applications. With the ability to predict both the hardness and electronic band gap using *ab intio* methods the very existence of materials can be ascertained from first principles.

Many of the theories regarding the calculation of the intrinsic hardness rely on the intrinsic electronic band gap in one form or another. Therefore, being able to calculate both the hardness and the electronic band gap allows one to predict the existence of materials. Both of these fundamental quantities, although strongly correlated, are determined independently. The results of Ref. 61 suggest that with using the bond modulus model, put forth by Gilman, hypothetical materials can be analysed to ascertain whether they will exhibit the proper linear relationship between the intrinsic hardness and electronic band gap. These results firmly place the electronic band gap at the forefront of hardness research and determining a material's intrinsic hardness is imperative if one would like to determine the intrinsic hardness of materials.

References

[1] R A Andrievski. Superhard materials based on nanostructured high-melting point compounds: achievements and perspectives. *Int. J. Refract. Met. Hard. Mat.*, 19(4-6):447–452, 2001.

[2] I Tanaka, F Oba, T Sekine, E Ito, A Kubo, K Tatsumi, H Adachi, and T Yamamoto. Hardness of cubic silicon nitride. *J. Mater. Res.*, 17(4):731–733, 2002.

[3] A Y Liu and M L Cohen. Prediction of new low compressibility solids. *Science*, 245(4920):841–842, 1989.

[4] A Zerr, G Miehe, G Serghiou, M Schwarz, E Kroke, R Riedel, H Fueß, P Kroll, and R Boehler. Synthesis of cubic silicon nitride. *Nature (London)*, 400(6742):340–342, 1999.

[5] T Sekine, H L He, T Kobayashi, M Zhang, and F F Xu. Shock-induced transformation of β-Si_3N_4 to a high-pressure cubic-spinel phase. *Appl. Phys. Lett.*, 76(25):3706–3708, 2000.

[6] M Schwarz, G Miehe, A Zerr, E Kroke, B T Poe, H Fuess, and R Riedel. Spinel-Si_3N_4: Multi-anvil press synthesis and structural refinement. *Adv. Mater.*, 12(12):883–887, 2000.

[7] E Soignard, M Somayazulu, J J Dong, O F Sankey, and P F McMillan. High pressure-high temperature synthesis and elasticity of the cubic nitride spinel γ-Si_3N_4. *J. Phys.-Condens. Matter*, 13(4):557–563, 2001.

[8] T Sekine. Shock synthesis of cubic silicon nitride. *J. Am. Ceram. Soc.*, 85(1):113–116, 2002.

[9] G Serghiou, G Miehe, O Tschauner, A Zerr, and R Boehler. Synthesis of a cubic Ge_3N_4 phase at high pressures and temperatures. *J. Chem. Phys.*, 111(10):4659–4662, 1999.

[10] K Leinenweber, M O'Keeffe, M Somayazulu, H Hubert, P F McMillan, and G H Wolf. Synthesis and structure refinement of the spinel, γ-Ge_3N_4. *Chem. -Eur. J.*, 5(10):3076–3078, 1999.

[11] H L He, T Sekine, T Kobayashi, and K Kimoto. Phase transformation of germanium nitride (Ge_3N_4) under shock wave compression. *J. Appl. Phys.*, 90(9):4403–4406, 2001.

[12] E Soignard, P F McMillan, and K Leinenweber. Solid solutions and ternary compound formation among Ge_3N_4-Si_3N_4 nitride spinels synthesized at high pressure and high temperature. *Chem. Mater.*, 16(25):5344–5349, 2004.

[13] N Scotti, W Kockelmann, J Senker, S Traßel, and H Jacobs. Sn_3N_4, a tin(IV) nitride - syntheses and the first crystal structure determination of a binary tin-nitrogen compound. *Z. Anorg. Allg. Chem.*, 625(9):1435–1439, 1999.

[14] F M Gao, J L He, E D Wu, S M Liu, D L Yu, D C Li, S Y Zhang, and Y J Tian. Hardness of covalent crystals. *Phys. Rev. Lett.*, 91(1):015502, 2003.

[15] A Šimůnek and J Vackář. Hardness of covalent and ionic crystals: First-principle calculations. *Phys. Rev. Lett.*, 96(8):085501, 2006.

[16] J J Gilman. Electronic basis of hardness and phase transformations (covalent crystals). *J. Phys. D-Appl. Phys.*, 41(7):074020, 2008.

[17] K Li, X Wang, F Zhang, and D Xue. Electronegativity identification of novel superhard materials. *Phys. Rev. Lett.*, 100(23):235504, 2008.

[18] F M Gao and L H Gao. Microscopic models of hardness. *J. Superhard. Mater.*, 32(3):148–166, 2010.

[19] J S Tse. Intrinsic hardness of crystalline solids. *J. Superhard. Mater.*, 32(3):177–191, 2010.

[20] A R Fee, R Segabache, and E L Tobolski. *Knoop and Vickers Microhardness*, volume 8 of *ASM Handbook*. ASM International, 1985.

[21] F Birch. Finite elastic strain of cubic crystals. *Phys. Rev.*, 71(11):809–824, 1947.

[22] W Voigt. *Lehrbuch der kristallphysik*. Leipzig, B.G. Teubner, Berlin, 1910.

[23] A Reuss. Account of the liquid limit of mixed crystals on the basis of the plasticity condition for single crystal. *Z. angew. Math. Mech.*, 9:49–58, 1929.

[24] R Hill. The elastic behaviour of a crystalline aggregate. *Proc. Phys. Soc. A*, 65(389):349–355, 1952.

[25] J J Gilman. Chemical and physical "hardness". *Mater. Res. Innov.*, 1(2):71–76, 1997.

[26] J J Gilman. Flow of covalent solids at low-temperatures. *J. Appl. Phys.*, 46(12):5110–5113, 1975.

[27] J J Gilman. Relationship between impact yield stress and indentation hardness. *J. Appl. Phys.*, 46(4):1435–1436, 1975.

[28] J J Gilman. Why silicon is hard. *Science*, 261(5127):1436–1439, 1993.

[29] J C Phillips. Ionicity of the chemical bond in crystals. *Rev. Mod. Phys.*, 42(3):317–356, 1970.

[30] L Pauling. *The nature of the chemical bond*. Cornell University Press, Ithaca NY, 3^{rd} edition, 1960.

[31] X Liu, R Dronskowski, R Glaum, and A L Tchougréeff. Experimental and quantum-chemical investigations of the UV/Vis absorption spectrum of manganese carbodiimide, MnNCN. *Z. Anorg. Allg. Chem.*, 636(2):343–348, 2010.

[32] Joachim Stöhr. *NEXAFS Spectroscopy*. Springer, 1992.

[33] A. J. Achkar, T. Z. Regier, H. Wadati, Y. J. Kim, H. Zhang, and D. G. Hawthorn. Bulk sensitive x-ray absorption spectroscopy free of self-absorption effects. *Phys. Rev. B*, 83(8):081106, 2011.

[34] S Cottenier. *Denisty Functional Theory and the family of (L)APW-methods: a step-by-step introduction*. Instituut voor Kern-en Stralingsfysica, K. U. Leuven, Belgium, 2002.

[35] P Hohenberg and W Kohn. Inhomogeneous electron gas. *Phys. Rev. B*, 136(3B):B864–B871, 1964.

[36] W Kohn and L J Sham. Self-consistent equations including exchange and correlation effects. *Phys. Rev.*, 140(4A):1133–1138, 1965.

[37] J P Perdew, K Burke, and M Ernzerhof. Generalized gradient approximation made simple. *Phys. Rev. Lett.*, 77(18):3865–3868, 1996.

[38] F Tran and P Blaha. Accurate band gaps of semiconductors and insulators with a semilocal exchange-correlation potential. *Phys. Rev. Lett.*, 102(22):226401, 2009.

[39] K Schwarz, P Blaha, and G K H Madsen. Electronic structure calculations of solids using the WIEN2k package for material sciences. *Comput. Phys. Commun.*, 147(1-2):71–76, 2002.

[40] L Zhou, T A Callcott, J J Jia, D L Ederer, and R Perera. Sulfur $L_{2,3}$ and zinc $M_{2,3}$ soft-X-ray fluorescence spectra in CdS and ZnS. *Phys. Rev. B*, 55(8):5051–5061, 1997.

[41] J H Seo, C Y Kim, S J Kang, K-H Yoo, C N Whang, A Moewes, and G S Chang. Electronic structure of NPB and BCP molecules probed by x-ray emission spectroscopy. *J. Chem. Phys.*, 126(6):064706, 2007.

[42] E Z Kurmaev, R G Wilks, A Moewes, L D Finkelstein, S N Shamin, and J Kuneš. Oxygen X-ray emission and absorption spectra as a probe of the electronic structure of strongly correlated oxides. *Phys. Rev. B*, 77(16):165127, 2008.

[43] U von Barth and G Grossmann. Dynamical effects in X-ray spectra and the final-state rule. *Phys. Rev. B*, 25(8):5150–5179, 1982.

[44] M O Krause and J H Oliver. Natural widths of atomic K-levels and L-levels, Kα X-ray-lines and several KLL auger lines. *J. Phys. Chem. Ref. Data*, 8(2):329–338, 1979.

[45] D A Goodings and R Harris. Calculations of X-ray emission bands of copper using augmented plane wave bloch finctions. *J. Phys. Pt. C: Sol. Stat. Phys.*, 2(10):1808–1816, 1969.

[46] C Braun, M Seibald, S L Böerger, O Oeckler, T D Boyko, A Moewes, G Miehe, A Tüecks, and W Schnick. Material properties and structural characterization of $M_3Si_6O_{12}N_2$:Eu^{2+} (M = Ba, Sr) - A comprehensive study on a promising green phosphor for pc-LEDs. *Chem. Eur. J.*, 16(31):9646–9657, 2010.

[47] T D Boyko, R J Green, R Dronskowski, and A Moewes. Electronic band gap reduction in manganese carbodiimide: MnNCN. *J. Phys. Chem. C*, 117:12754–12761, 2013.

[48] XH Liu, M Krott, P Müller, CH Hu, H Lueken, and R Dronskowski. Synthesis, crystal structure, and properties of MnNCN, the first carbodiimide of a magnetic transition metal. *Inorg. Chem.*, 44(9):3001–3003, 2005.

[49] J. van Elp, R. H. Potze, H. Eskes, R. Berger, and G. A. Sawatzky. Electronic structure of MnO. *Phys. Rev. B*, 44:1530–1537, 1991.

[50] T D Boyko, E Bailey, A Moewes, and P F McMillan. Class of tunable wide band gap semiconductors γ- $(Ge_xSi_{1-x})_3N_4$. *Phys. Rev. B*, 81(15):155207, 2010.

[51] W Y Ching, S-D Mo, L Z Ouyang, P Rulis, I Tanaka, and M Yoshiya. Theoretical prediction of the structure and properties of cubic spinel nitrides. *J. Am. Ceram. Soc.*, 85(1):75–80, 2002.

[52] T D Boyko, A Hunt, A Zerr, and A Moewes. Electronic structure of spinel-type nitride compounds Si_3N_4, Ge_3N_4, and Sn_3N_4 with tunable band gaps: Application to light emitting diodes. *Phys. Rev. Lett.*, 111(9):097402, 2013.

[53] C Braun, Saskia L Börger, T D Boyko, G Miehe, H Ehrenberg, P Höhn, A Moewes, and W Schnick. Ca_3N_2 and Mg_3N_2: Unpredicted high-pressure behavior of binary nitrides. *J. Am. Chem. Soc.*, 133(12):4307–4315, 2011.

[54] T D Boyko, C E Zvoriste, I Kinski, R Riedel, S Hering, H Huppertz, and A Moewes. Anion ordering in spinel-type gallium oxonitride. *Phys. Rev. B*, 84:085203, 2011.

[55] Hubert Huppertz, Stefanie A. Hering, Carmen E. Zvoriste, Stefan Lauterbach, Oliver Oeckler, Ralf Riedel, and Isabel Kinski. High-pressure synthesis, electron energy-loss spectroscopy investigations, and single crystal structure determination of a spinel-type gallium oxonitride $Ga_{2.79}\triangle_{0.21})(O_{3.05}N\triangle_{0.76}0.19)$. *Chem. Mater.*, 21(10):2101–2107, 2009.

[56] T D Boyko, T Gross, H Fuess, M Schwarz, and Moewes A. The crystal structure and electronic band gap of β-sialons. *Phys. Rev. B*, Prepared for submission.

[57] S V Okatov and A L Ivanovskii. Chemical bonding and atomic ordering effects in β-SiAlON. *Int. J. Inorg. Mater.*, 3(7):923–930, 2001.

[58] R Dupree, M H Lewis, G Lengward, and D S Williams. Coordination of Si atoms in silicon-oxynitrides determined by magic-angle-spinning nmr. *J. Mater. Sci. Lett.*, 4(4):393–395, 1985.

[59] R Dupree, M H Lewis, and M E Smith. Structural characterization of ceramic phases with high-resolution Al-27 NMR. *J. Appl. Crystallogr.*, 21(Part 2):109–116, 1988.

[60] K Tatsumi, T Mizoguchi, S Yoshioka, T Yamamoto, T Suga, T Sekine, and I Tanaka. Distribution of solute atoms in beta- and spinel $Si_{6-z}Al_zO_zN_{8-z}$ by AlK-edge X-ray absorption near-edge structure. *Phys. Rev. B*, 71(3):033202, 2005.

[61] T D Boyko and Moewes A. Predicting the existence of spinel nitrides. *Phys. Rev. Lett.*, Submitted LG14585.

Appendix A

Author Publications

13. T D Boyko, T Gross, H Fuess, M Schwarz, and A Moewes. The crystal structure and electronic band gap of β-sialons. *Phys. Rev. B*, Prepared for submission.

12. T D Boyko and A Moewes. Predicting the existence of spinel nitrides. *Phys. Rev. Lett.*, Submitted LG14585.

11. T D Boyko, A Hunt, A Zerr, and A Moewes. Electronic structure of spinel-type nitride compounds Si_3N_4, Ge_3N_4, and Sn_3N_4 with tunable band gaps: Application to light emitting diodes. *Phys. Rev. Lett.*, 111(9):097402, 2013.

10. T D Boyko, R J Green, R Dronskowski, and A Moewes. Electronic band gap reduction in manganese carbodiimide: MnNCN. *J. Phys. Chem. C*, 117:12754–12761, 2013.

9. A Hunt, D A Dikin, E Z Kurmaev, T D Boyko, P Bazylewski, G S Chang, and A Moewes. Epoxide speciation and functional group distribution in graphene oxide paper-like materials. *Adv. Funct. Mater.*, 22(18):3950–3957, 2012.

8. J A McLeod, A Buling, R J Green, T D Boyko, N A Skorikov, E Z Kurmaev, M Neumann, L D Finkelstein, N Ni, A Thaler, S L Bud'ko, P C Canfield, and A Moewes. Effect of $3d$ doping on the electronic structure of $BaFe_2As_2$. *J. Phys.-Condens. Matter*, 24(21):215501, 2012.

7. J A McLeod, E Z Kurmaev, P V Sushko, T D Boyko, I A Levitsky, and A Moewes. Selective response of mesoporous silicon to adsorbants with nitro groups. *Chem. -Eur. J.*, 18(10):2912–2922, 2012.

6. E J McDermott, E Z Kurmaev, T D Boyko, L D Finkelstein, R J Green, K Maeda, K Domen, and A Moewes. Structural and band gap investigation of GaN:ZnO heterojunction solid solution photocatalyst probed by soft X-ray spectroscopy. *J. Phys. Chem. C*, 116(14):7694–7700, 2012.

5. T D Boyko, C E Zvoriste, I Kinski, R Riedel, S Hering, H Huppertz, and A Moewes. Anion ordering in spinel-type gallium oxonitride. *Phys. Rev. B*, 84:085203, 2011.

4. C Braun, Saskia L Börger, T D Boyko, G Miehe, H Ehrenberg, P Höhn, A Moewes, and W Schnick. Ca_3N_2 and Mg_3N_2: Unpredicted high-pressure behavior of binary nitrides. *J. Am. Chem. Soc.*, 133(12):4307–4315, 2011.

3. C Braun, M Seibald, S L Böerger, O Oeckler, T D Boyko, A Moewes, G Miehe, A Tüecks, and W Schnick. Material properties and structural characterization of $M_3Si_6O_{12}N_2$:Eu^{2+} (M = Ba, Sr) - A comprehensive study on a promising green phosphor for pc-LEDs. *Chem. -Eur. J.*, 16(31):9646–9657, 2010.

2. T D Boyko, E Bailey, A Moewes, and P F McMillan. Class of tunable wide band gap semiconductors γ- $(Ge_xSi_{1-x})_3N_4$. *Phys. Rev. B*, 81(15):155207, 2010.

1. T Boyko, S Kasap, R Johanson, S Kobayashi, T Aoki, and A Moewes. Electronic structure of hydrogenated amorphous $Si_{1-x}N_x$ thin films using soft X-ray emission and absorption measurements. *Phys. Status Solidi A-Appl. Mat.*, 206(5):935–939, 2009.

Appendix B

Copyright Agreements

'I hereby grant to University of Saskatchewan and/or its agents the non-exclusive license to archive and make accessible, under the conditions specified below, my thesis, dissertation, or project report in whole or in part in all forms of media, now or for the duration of my copyright ownership. I retain all other ownership rights to the copyright of the thesis, dissertation or project report. I also reserve the right to use in future works (such as articles or books) all or part of this thesis, dissertation, or project report.

I hereby certify that, if appropriate, I have obtained and attached hereto a written permission statement from the owner(s) of each third party copyrighted matter that is included in my thesis, dissertation, or project report, allowing distribution as specified below. I certify that the version I submitted is the same as that approved by my advisory committee.'

The following are exerts from the FAQ section of all publishing agencies: APS, ACS and Wiley. Additionally, the copyright agreements are attached.

B.1 APS

As the author of an APS-published article, may I include my article or a portion of my article in my thesis or dissertation?

Yes, the author has the right to use the article or a portion of the article in a thesis or dissertation without requesting permission from APS, provided the bibliographic citation and the APS copyright credit line are given on the appropriate pages.

B.2 ACS

I am a student writing my thesis. May I use papers I have authored in ACS journals, or material from them, in my thesis without obtaining explicit permission?

You may reuse all or part of the Submitted, Accepted, or Published versions of your ACS papers in your thesis or dissertation. Such reuse is permitted subject to the ACS' Ethical Guidelines to Publication of Chemical Research and you should secure written confirmation from the respective ACS journal editor(s) to avoid potential conflicts with journal prior publication policies. The ACS copyright credit line should be noted on the appropriate pages and appropriate citation of any Published versions. If the thesis or dissertation to be published is in electronic format, a direct link to the Published Work must be included using the ACS

Articles on Request link.

Although ACS grants students automatic permission to use their ACS articles in theses, it is highly likely that the graduate school requires a statement of written permission. Students should use Rightslink to obtain permission, and provide their graduate school with the written document provided by Rightslink.

B.3 Wiley

What rights do I retain if I sign a Copyright Transfer Agreement (CTA)?

The Contributor or, if applicable, the Contributor's Employer, retains all proprietary rights other than copyright, such as patent rights, in any process, procedure or article of manufacture described in the contribution.

Contributors may re-use unmodified abstracts for any non-commercial purpose. For online use of the abstract, Wiley encourages but does not require linking back to the final published contribution.

Contributors may use the articles in teaching duties and in other works such as theses.

Contributors may re-use figures, tables, data sets, artwork, and selected text up to 250 words from their contributions without seeking permission, provided the following conditions are met:

- Full and accurate credit must be given to the contribution.
- Modifications to the figures, tables and data must be noted. Otherwise, no changes may be made.
- The reuse may not be made for direct commercial purposes, or for financial consideration to the Contributor.
- Re-use rights shall not be interpreted to permit dual publication in violation of journal ethical practices.

November 2012

Terms and conditions associated with the American Physical Society Transfer of Copyright Agreement

Copyright to the [above-listed] unpublished and original article submitted by the [above] author(s), the abstract forming part thereof, and any subsequent errata (collectively, the "Article") is hereby transferred to the American Physical Society (APS) for the full term thereof throughout the world, subject to the Author Rights (as hereinafter defined) and to acceptance of the Article for publication in a journal of APS. This transfer of copyright includes all material to be published as part of the Article (in any medium), including but not limited to tables, figures, graphs, movies, other multimedia files, and all supplemental materials. APS shall have the right to register copyright to the Article in its name as claimant, whether separately or as part of the journal issue or other medium in which the Article is included.

The author(s), and in the case of a Work Made For Hire, as defined in the U.S. Copyright Act, 17 U.S.C. §101, the employer named [below], shall have the following rights (the "Author Rights"):

1. All proprietary rights other than copyright, such as patent rights.
2. The nonexclusive right, after publication by APS, to give permission to third parties to republish print versions of the Article or a translation thereof, or excerpts therefrom, without obtaining permission from APS, provided the APS-prepared version is not used for this purpose, the Article is not republished in another journal, and the third party does not charge a fee. If the APS version is used, or the third party republishes in a publication or product charging a fee for use, permission from APS must be obtained.
3. The right to use all or part of the Article, including the APS-prepared version without revision or modification, on the author(s)' web home page or employer's website and to make copies of all or part of the Article, including the APS-prepared version without revision or modification, for the author(s)' and/or the employer's use for educational or research purposes.
4. The right to post and update the Article on free-access e-print servers as long as files prepared and/or formatted by APS or its vendors are not used for that purpose. Any such posting made or updated after acceptance of the Article for publication shall include a link to the online abstract in the APS journal or to the entry page of the journal. If the author wishes the APS-prepared version to be used for an online posting other than on the author(s)' or employer's website, APS permission is required; if permission is granted, APS will provide the Article as it was published in the journal, and use will be subject to APS terms and conditions.
5. The right to make, and hold copyright in, works derived from the Article, as long as all of the following conditions are met: (a) at least one author of the derived work is an author of the Article; (b) the derived work includes at least ten (10) percent of new material not covered by APS's copyright in the Article; and (c) the derived work includes no more than fifty (50) percent of the text (including equations) of the Article. If these conditions are met, copyright in the derived work rests with the authors of that work, and APS (and its successors and assigns) will make no claim on that copyright. If these conditions are not met, explicit APS permission must be obtained. Nothing in this Section shall prevent APS (and its successors and assigns) from exercising its rights in the Article.
6. If the Article was prepared under a U.S. Government contract, the government shall have the rights under the copyright to the extent required by the contract.

All copies of part or all of the Article made under any of the Author Rights shall include the appropriate bibliographic citation and notice of the APS copyright.

By signing this Agreement, the author(s), and in the case of a Work Made For Hire, the employer, jointly and severally represent and warrant that the Article is original with the author(s) and does not infringe any copyright or violate any other right of any third parties, and that the Article has not been published elsewhere, and is not being considered for publication elsewhere in any form, except as provided herein. If each author's signature does not appear [below], the signing author(s) represent that they sign this Agreement as authorized agents for and on behalf of all authors who have the legal right to transfer copyright and that this Agreement and authorization is made on behalf of the same. The signing author(s) (and, in the case of a Work Made For Hire, the signing employer) also represent and warrant that they have the full power to enter into this Agreement and to make the grants contained herein.

AMERICAN CHEMICAL SOCIETY
JOURNAL PUBLISHING AGREEMENT
Form A: Authors Who Hold Copyright and Works-for-Hire

Control #2011-10-11

Manuscript ID, if Available

Received Date (Office Use Only)

SECTION I: Copyright

1. Submitted Work: The Corresponding Author, with the consent of all co-authors, hereby transfers to the ACS the copyright ownership in the referenced Submitted Work, including all versions in any format now known or hereafter developed. If the manuscript is not accepted by ACS or withdrawn prior to acceptance by ACS, this transfer will be null and void.

2. Supporting Information: The copyright ownership transferred to ACS in any copyrightable* Supporting Information accompanying the Submitted Work is nonexclusive. The Author and the ACS agree that each has unlimited use of Supporting Information. Authors may use or authorize the use of material created by the Author in the Supporting Information associated with the Submitted or Published Work for any purpose and in any format.

*Title 17 of the United States Code defines copyrightable material as "original works of authorship fixed in any tangible medium of expression" (Chapter 1, Section 102). To learn more about copyrightable material see "Frequently Asked Questions about Copyright" on the Publications Division website, at http://pubs.acs.org/page/copyright/learning_module/module.html.

SECTION II: Permitted Uses by Author(s)

1. Reuse/Republication of the Entire Work in Theses or Collections: Authors may reuse all or part of the Submitted, Accepted or Published Work in a thesis or dissertation that the Author writes and is required to submit to satisfy the criteria of degree-granting institutions. Such reuse is permitted subject to the ACS' "Ethical Guidelines to Publication of Chemical Research"

Continued on Page 2

SIGNATURES

Signing this agreement constitutes acceptance by the Author(s) and, in the case of a Work-Made-for-Hire, the company/employer of all contents contained herein, including the attached Appendix A: Author Warranties, Obligations, Definitions, and General Provisions.

Corresponding Author's Name

_____
Signature

Date

Employer/Organization (Work-for-Hire only)

_____
Authorized Signature(s) of Employer/Organization (Work-for-Hire only)

Date U.S. Government Contract #, if available

INSTRUCTIONS FOR FORM A

Form A should be signed **ONLY** by Author(s) who hold Copyright or who have created Works-for-Hire.

This manuscript will be considered with the understanding you have submitted it on an exclusive basis. You will be notified of a decision as soon as possible.

1. Complete all information in the **Manuscript Details** section.
2. Sign and date the form.
3. Submit **ALL PAGES OF THIS FORM** to the Editor's Office or upload it in ACS Paragon Plus.

MANUSCRIPT DETAILS

Name of ACS Publication:

Manuscript Title:

Corresponding Author's Name and Address:

List Names of ALL Author(s):

(http://pubs.acs.org/ethics); the Author should secure written confirmation (via letter or email) from the respective ACS journal editor(s) to avoid potential conflicts with journal prior publication**/embargo policies. Appropriate citation of the Published Work must be made. If the thesis or dissertation to be published is in electronic format, a direct link to the Published Work must also be included using the ACS Articles on Request author-directed link (see http://pubs.acs.org/page/policy/articlesonrequest/index.html).

Authors also may reuse the Submitted, Accepted, or Published work in printed collections that consist solely of the Author's own writings; if such collections are to be posted online or published in an electronic format, please contact ACS at copyright@acs.org to inquire about terms for licensed electronic use.

2. Reuse of Figures, Tables, Artwork, and Text Extracts in Future Works: Authors may reuse figures, tables, artwork, illustrations, text extracts of up to 400 words, and data from the Author's Submitted, Accepted, or Published Work in which the ACS holds copyright for teaching or training purposes, in presentations at conferences and seminars, in subsequent scholarly publications of which they are an Author, and for posting on the Author's personal website, university networks, or primary employer's institutional websites, and conference websites that feature presentations by the Author(s) provided the following conditions are met:

- Appropriate citation to the Published Work is given
- Modifications to the presentation of previously published data in figures and tables are noted and distinguished from any new data not contained in the Published Work, and
- Reuse is not to illustrate news stories unrelated to the Published Work
- Web posting by the Author(s) is for non-commercial purposes.

To reuse figures, tables, artwork, illustrations, and text from ACS Published Works in general, ACS requests that interested parties use the Copyright Clearance Center Rightslink service. For information see http://pubs.acs.org/page/copyright/rightslink.html

General ACS permission information can be found at http://pubs.acs.org/page/copyright/permissions.html.

3. Reuse in Teaching or In-House Training: In order to preserve the integrity of the scientific record, the Author(s) are encouraged to link to the Published Work using the ACS Articles on Request author-directed link as applicable for teaching and in-house training and this use is subject to the conditions identified below (see http://pubs.acs.org/page/policy/articlesonrequest/index.html). Regardless, the Author(s) may reproduce their Submitted, Accepted, or Published Work for instructional use in courses as a stand-alone handout, as part of a packet, or electronically for use by students enrolled in the course the Author is teaching as long as the following conditions are met:

- Proper credit must be given to the Published Work and a link to the Published Work must be included using the ACS Articles on Request author-directed link (see http://pubs.acs.org/page/policy/articlesonrequest/index.html). The following notice should either be posted with or printed on all uses of the Accepted Work described in this clause:
  "This material is excerpted from a work that was [accepted for publication/published] in [JournalTitle], copyright © American Chemical Society after peer review. To access the final edited and published work see [insert ACS Articles on Request author-directed link to Published Work, see http://pubs.acs.org/page/policy/articlesonrequest/index.html]."
- Electronic access must be provided via a password-protected website only to students enrolled in the course (i.e. not the general public). Availability to students should terminate when the course is completed.
- If a fee for distributed materials is charged for the use of Published Work in connection with the instructional use, prior written permission from the ACS must be obtained.

4. Presentation at Conferences: Subject to the ACS' "Ethical Guidelines to Publication of Chemical Research" (http://pubs.acs.org/ethics) and written confirmation (via letter or email) from the appropriate ACS journal editor to resolve potential conflicts with journal prior publication**/embargo policies, Authors may present orally or otherwise display all or part of the Submitted, Accepted, or Published Work in presentations at meetings or conferences. Authors may provide copies of the Submitted and Accepted Work either in print or electronic form to the audience.

**Prior publication policies of ACS journals are posted on the ACS website at http://pubs.acs.org/page/policy/prior/index.html.

Sharing of the Published Work with conference attendees is permitted if it is done either via the ACS Articles on Request author-directed link (see http://pubs.acs.org/page/policy/articlesonrequest/index.html) or in print. Audience recipients should be informed that further distribution or reproduction of any version of the Work is not allowed.

5. Share with Colleagues: Subject to the ACS' "Ethical Guidelines to Publication of Chemical Research" (http://pubs.acs.org/ethics), Authors may send or otherwise transmit electronic files of the Submitted or Accepted Work to interested colleagues prior to, or after, publication. Sharing of the Published Work with colleagues is permitted if it is done via the ACS Articles on Request author-directed link (see http://pubs.acs.org/page/policy/articlesonrequest/index.html). The sharing of any version of the Work with colleagues is only permitted if it is done for non-commercial purposes; that no fee is charged; and that it is not done on a systematic basis, e.g. mass emailings, posting on a listserv, etc. Recipients should be informed that further redistribution of any version of the Work is not allowed.

Authorized users of the ACS Publications website (http://pubs.acs.org/) may also email a link to the Author's article directly to colleagues as well as recommend and share a link to the Author's article with known colleagues through popular social networking services such as CiteULike, Digg, and Newsvine (see http://pubs.acs.org/sda/63224/index.html for more information).

6. Posting Submitted Works on Websites and Repositories: A digital file of the Submitted Work may be made publicly available on websites or repositories (e.g. the Author's personal website, preprint servers, university networks or primary employer's institutional websites, third party institutional or subject-based repositories, and conference websites that feature presentations by the Author(s) based on the Submitted Work) under the following conditions:

- The Author(s) have received written confirmation (via letter or email) from the appropriate ACS journal editor that the posting does not conflict with journal prior publication/embargo policies (see http://pubs.acs.org/page/policy/prior/index.html)
- The posting must be for non-commercial purposes and not violate the ACS' "Ethical Guidelines to Publication of Chemical Research" (see http://pubs.acs.org/ethics).
- If the Submitted Work is accepted for publication in an ACS journal, then the following notice should be included at the time of posting, or the posting amended as appropriate:
  "This document is the unedited Author's version of a Submitted Work that was subsequently accepted for publication in [JournalTitle], copyright © American Chemical Society after peer review. To access the final edited and published work see [insert ACS Articles on Request author-directed link to Published Work, see http://pubs.acs.org/page/policy/articlesonrequest/index.html]."

If any prospective posting of the Submitted Work, whether voluntary or mandated by the Author(s)' funding agency, primary employer, or, in the case of Author(s) employed in academia, university administration, would violate any of the above conditions, the Submitted Work may not be posted. In these cases, Author(s) may either sponsor the immediate public availability of the final Published Work through participation in the fee-based ACS AuthorChoice program (for information about this program see http://pubs.acs.org/page/policy/authorchoice/index.html) or, if applicable, seek a waiver from the relevant institutional policy.

7. Posting Accepted and Published Works on Websites and Repositories: A digital file of the Accepted Work and/or the Published Work may be made publicly available on websites or repositories (e.g. the Author's personal website, preprint servers, university networks or primary employer's institutional websites, third party institutional or subject-based repositories, and conference websites that feature presentations by the Author(s) based on the Accepted and/or the Published Work) under the following conditions:

- It is mandated by the Author(s)' funding agency, primary employer, or, in the case of Author(s) employed in academia, university administration.
- For mandates from non-governmental institutions (e.g. universities, private sector corporations, non-governmental organizations, etc.), the Author(s) have received written confirmation (via letter or email) from the appropriate ACS journal editor that the posting does not conflict with journal prior publication policies (see http://pubs.acs.org/page/policy/prior/index.html).
- If the mandated public availability of the Accepted Manuscript is sooner than 12 months after online publication of the Published Work, a waiver from the relevant institutional policy should be sought. If a waiver cannot be obtained, the Author(s) may sponsor the immediate availability of the final Published Work through participation in the ACS

AuthorChoice program—for information about this program see http://pubs.acs.org/page/policy/authorchoice/index.html.

- If the mandated public availability of the Accepted Manuscript is not sooner than 12 months after online publication of the Published Work, the Accepted Manuscript may be posted to the mandated website or repository. The following notice should be included at the time of posting, or the posting amended as appropriate:
  "This document is the Accepted Manuscript version of a Published Work that appeared in final form in [JournalTitle], copyright © American Chemical Society after peer review and technical editing by the publisher. To access the final edited and published work see [insert ACS Articles on Request author-directed link to Published Work, see http://pubs.acs.org/page/policy/articlesonrequest/index.html]."
- The posting must be for non-commercial purposes and not violate the ACS' "Ethical Guidelines to Publication of Chemical Research" (see http://pubs.acs.org/ethics).
- Regardless of any mandated public availability date of a digital file of the final Published Work, Author(s) may make this file available only via the ACS AuthorChoice Program. For more information, see http://pubs.acs.org/page/policy/authorchoice/index.html.

Author(s) may post links to the Accepted Work on the appropriate ACS journal website if the journal posts such works. Author(s) may post links to the Published Work on the appropriate ACS journal website using the ACS Articles on Request author-directed link (see http://pubs.acs.org/page/policy/articlesonrequest/index.html).

Links to the Accepted or Published Work may be posted on the Author's personal website, university networks or primary employer's institutional websites, and conference websites that feature presentations by the Author(s). Such posting must be for non-commercial purposes.

SECTION III: Retained and Other Rights

1. Retained Rights: The Author(s) retain all proprietary rights, other than copyright, in the Submitted Work. Authors should seek expert legal advice in order to secure patent or other rights they or their employer may hold or wish to claim.

2. Moral Rights: The Author(s) right to attribution and the integrity of their work under the Berne Convention (article 6bis) is not compromised by this agreement.

3. Extension of Rights Granted to Prior Publications: The rights and obligations contained in Section II: Permitted Uses by Author(s), Section III: Retained and Other Rights, and Appendix A, Section I: Author Warranties and Obligations of this agreement are hereby extended to the Author(s)' prior published works in ACS journals.

SECTION IV: Works-for-Hire

If the Submitted Work was written by the Author(s) in the course of the Author(s)' employment as a "Work-Made-for-Hire" as defined under U.S Copyright Law, the Submitted Work is owned by the company/employer which must sign the Journal Publishing Agreement (in addition to the Author(s) signature). In such case, the company/employer hereby assigns to ACS, during the full term of copyright, all copyright in and to the Submitted Work for the full term of copyright throughout the world as specified in Section I, paragraph 1 above.

In the case of a Work-Made-for-Hire, Authors and their employer(s) have the same rights and obligations as contained in Section II: Permitted Uses by Author(s), Section III: Retained and Other Rights, and Appendix A, Section I: Author Warranties and Obligations.

Any restrictions on commercial use in this agreement do not apply to internal company use of all or part of the information in the Submitted, Accepted, or Published Work.

The Author(s)' employers may systematically distribute (but not re-sell) print copies of the Published Work externally for promotional purposes, provided that such promotions do not imply endorsement by ACS. Although printed copies so made shall not be available for individual re-sale, they may be included by the employer as part of an information package included with software or other products the employer offers for sale or license. Posting of the final Published Work by the employer on a public access website may only be undertaken by participation in the ACS AuthorChoice option, including payment of applicable fees.

APPENDIX A: Author Warranties, Obligations, Definitions, and General Provisions

SECTION I: Author Warranties and Obligations

1. ACS Ethical Guidelines: By signing this agreement, Author(s) acknowledge they have read and understand the ACS' "Ethical Guidelines to Publication of Chemical Research" (http://pubs.acs.org/ethics).

2. Author Warranties: By signing this agreement the Corresponding Author and all co-authors (and in the case of a Work-Made-for-Hire, the Author(s)' employer(s)) jointly and severally warrant and represent the following:

- The Submitted Work is original.
- The Submitted Work does not contain any statements or information that is intentionally misleading or inaccurate.
- All Authors have been informed of the full content of the Submitted Work at, or prior to, the time of submission.
- The Submitted Work has not been previously published in any form (except as permitted in Section II: Permitted Uses by Author(s)).
- The Submitted Work is not being considered for publication elsewhere in any form and will not be submitted for such consideration while under review by ACS.
- Nothing in the Submitted Work is obscene, defamatory, libelous, or otherwise unlawful, violates any right of privacy or infringes any intellectual property rights (including without limitation copyright, patent, or trademark) or any other human, personal. or other rights of any kind of any person or entity, and does not contain any material or instructions that might cause harm or injury. Any unusual hazards inherent in the chemicals, equipment, or procedures used in an investigation are clearly identified in the Submitted Work.
- Nothing in the Submitted Work infringes any duty of confidentiality which the Author(s) may owe to another party or violates any contract, express or implied, that the Author(s) may have entered into, and all of the institutions where the work, as reflected in the Submitted Work, was performed have authorized publication.
- Permission has been obtained and included with the Submitted Work for the right to use and authorize use in print and online formats, or of any format that hereafter may be developed for any portions that are owned or controlled by a third party. Payments, as appropriate, have been made for such rights, and proper credit has been given in the Submitted Work to those sources.
- Potential and/or relevant competing financial or other interests that might be affected by publication of the Submitted Work have been disclosed to the appropriate ACS journal editor.

The Author (and, in the case of a Work-Made-for-Hire, the Author(s)' employer(s)) represent and warrant that the undersigned has the full power to enter into this Agreement and to make the grants contained herein.

The Author(s) (and, in the case of a Work-Made-for-Hire, the Author(s)' employer(s)) indemnify the ACS and/or its successors and assigns for any and all claims, costs, and expenses, including attorney's fees, arising out of any breach of this warranty or other representations contained herein.

3. General Author Obligations: If the Submitted Work includes material that was published previously in a non-ACS journal, whether or not the Author(s) participated in the earlier publication, the copyright holder's permission must be obtained to republish such material in print and online with ACS. It is the Author's obligation to obtain any necessary permissions to use prior publication material in any of the ways described in Section II: Permitted Uses by Author(s). No such permission is required if the ACS is the copyright holder.

All uses of the Submitted, Accepted, or Published Work made under any of activities described in Section II: Permitted Uses by Author(s) must include appropriate citation. Appropriate citation should include, but is not limited to, the following information (if available): author, title of article, title of journal, volume number, issue number (if relevant), page range (or first page if this is the only information available), date, and Copyright © [year] American Chemical Society. Copyright notices or the display of unique Digital Object Identifiers (DOIs), ACS or journal logos, bibliographic (e.g. authors, journal, article title, volume, issue, page numbers) or other references to ACS journal titles, Web links, and any other journal-specific "branding" or notices that are included by ACS in the Accepted or Published Work or that are provided by the ACS with instructions that such should accompany its display, should not be removed or tampered with in any way.

SECTION II: Definitions

Accepted Work: The version of the Submitted Work that has been accepted for publication in an ACS journal that includes, but is not limited to, changes resulting from peer review but prior to ACS' copy editing and production.

ACS Articles on Request: A link emailed to Corresponding Authors upon publication of their article in an ACS journal that provides free e-prints of the Published Work. For more information, see: http://pubs.acs.org/page/policy/articlesonrequest/index.html.

ACS AuthorChoice: A fee-based program that allows ACS Authors or their funding agencies to provide immediate, unrestricted online access to the Published Work from the ACS website. Under this program Authors may also post the Published Work on

personal websites and institutional repositories of their choosing. For more information, see http://pubs.acs.org/page/policy/authorchoice/index.html.

Author: An individual who has made significant scientific contributions to the Submitted Work and who shares responsibility and accountability for the results and conclusions contained therein. For further clarification of the criteria for participation in authorship, see ACS' "Ethical Guidelines to Publication of Chemical Research" at http://pubs.acs.org/ethics.

Commercial Use: Use of the Submitted, Accepted, or Published Work for commercial purposes (except as provided for employers in the case of a Work-Made-for-Hire; see Section IV: Works-for-Hire) is prohibited or requires ACS' prior written permission. Examples of prohibited commercial purposes or uses that require prior permission include but are not limited to:

- Copying or downloading of the Submitted, Accepted, or Published Work, or linking to postings of the Submitted, Accepted, or Published Work, for further access, distribution, sale or licensing, for a fee;
- Copying, downloading, or posting by a site or service that incorporates advertising with such content;
- The inclusion or incorporation of the Submitted, Accepted, or Published Work in other works or services (other than as permitted in Section II: Permitted Uses by Author(s)) that are then available for sale or licensing, for a fee;
- Use of the Submitted, Accepted, or Published Work (other than normal quotations with appropriate citation) by a for-profit organization for promotional purposes, whether for a fee or otherwise;
- Systematic distribution to others via email lists or list servers (to parties other than known colleagues), whether for a fee or for free;
- Sale of translated versions of the Submitted, Accepted, or Published Work that have not been authorized by license or other permission from the ACS.

Corresponding Author: The Author who transmits the Submitted Work on behalf of any co-authors and who receives and engages in all subsequent editorial communications regarding the status of the Submitted Work (including its reviews and revisions), and who is responsible for the dissemination of reviewers' comments and other manuscript information to co-authors (as appropriate). The Corresponding Author authorizes all revisions to the Submitted and Accepted Work prior to publication and is the primary point of contact after publication of the Version of Record. In some instances, more than one co-author may be designated as a Corresponding Author.

Published Work: The version of the Submitted Work as accepted for publication in an ACS journal that includes but is not limited to all materials in the Submitted Work and any changes resulting from peer review, editing, and production services by ACS.

Submitted Work: The version of the written manuscript or other article of intellectual property as first submitted to ACS for review and possible publication. The Submitted Work consists of the manuscript text or other contribution including but not limited to the text (including the abstract or other summary material) and all material in any medium to be published as part of the Submitted Work, including but not limited to figures, illustrations, diagrams, tables, movies, other multimedia files, and any accompanying Supporting Information.

Supporting Information: Ancillary information that accompanies the Submitted Work and is intended by the Author to provide relevant background information for evaluation of the Submitted Work during the peer review process, or that is made available as a further aid to interested readers of the Published Work, but is not considered essential for comprehension of the main body of the Submitted, Accepted, or Published Work. Supporting Information may also be material that is deemed by the Editor to be too lengthy or of too specialized and limited interest for inclusion in the main body of the Accepted or Published Work. Examples of Supporting Information include but are not limited to: computer software program code, machine-readable data files or other background datasets, supporting applications and derivations, and complex tables, illustrations, diagrams, and multimedia files (e.g. video, audio, animation, 3D graphics, or high-resolution image files).

SECTION III: General Provisions

ACS shall have the right to use any material in the Submitted, Accepted, or Published Work, including use for marketing, promotional purposes, and on publication covers, provided that the scientific meaning and integrity of the content is not compromised.

When the ACS is approached by third parties for permission to use, reprint, or republish entire articles the undersigned Author's or employer's permission may also be sought at the discretion of ACS.

The American Chemical Society or its agents will store the information the Corresponding Author supplies in connection with the Submitted Work within its electronic records. Information about ACS activities, products, and services may be sent to ACS Authors by mail, telephone, email, or fax. Authors may inform ACS if they do not wish to receive news, promotions, and special offers about our products and services. No personal information will be shared with third parties.

Headings contained in this Agreement are for reference purposes only and shall not be deemed to be an indication of the meaning of the clause to which they relate.

COPYRIGHT TRANSFER AGREEMENT

WILEY-VCH

Date: _____ Contributor name: _____

Contributor address: _____

Manuscript number (if available): _____

Re: Manuscript entitled _____

_____ (the "Contribution")

for publication in _____ (the "Journal")

published by Wiley-VCH Verlag GmbH & Co. KGaA ("Wiley-VCH").

Dear Contributor(s):
Thank you for submitting the Contribution for publication. In order to expedite the editing and publishing process and enable Wiley-VCH to disseminate the Contribution to the fullest extent, we need to have this Copyright Transfer Agreement signed and returned as directed in the Journal's instructions for authors as soon as possible. If the Contribution is not accepted for publication, or if the Contribution is subsequently rejected, this Agreement shall be null and void. **Publication cannot proceed without a signed copy of this Agreement.**

A. RIGHTS GRANTED

1. The Contributor hereby grants to Wiley-VCH for the duration of the statutory term of copyright protection, the full and exclusive rights comprised in the Contribution including but not limited to the right to publish, republish, transmit, sell, distribute, store and process in electronic media of any kind, include in document delivery services and otherwise use the Contribution in whole or in part in electronic and print editions of the Journal and in derivative works throughout the world, in all languages and in all media of expression now known or later developed, and to license or permit others to do so.

2. Reproduction, posting, transmission or other distribution or use of the final Contribution in whole or in part in any medium by the Contributor as permitted by this Agreement requires a citation to the Journal and an appropriate credit to Wiley-VCH as Publisher, suitable in form and content as follows: (Title of Article, Author, Journal Title and Volume/Issue Copyright © [year] copyright owner as specified in the Journal).

3. Please note that Wiley-VCH reserves the right to require changes to the Contribution, including changes to the length of the Contribution, as a condition of acceptance.

4. Please note that Wiley-VCH reserves the right, notwithstanding acceptance, not to publish the Contribution if for any reason such publication would in the reasonable judgement of Wiley-VCH, result in legal liability or violation of journal ethical practices.

B. RETAINED RIGHTS

Notwithstanding the above, the Contributor or, if applicable, the Contributor's Employer, retains all proprietary rights other than copyright, such as patent rights, in any process, procedure or article of manufacture described in the Contribution.

C. PERMITTED USES BY CONTRIBUTOR

1. Submitted Version. Wiley-VCH licenses back the following rights to the Contributor in the version of the Contribution as originally submitted for publication:

a. After publication of the final article, the right to self-archive on the Contributor's personal intranet page or in the Contributor's institution's/employer's institutional intranet repository or archive. The Contributor may not update the submission version or replace it with the published Contribution. The version posted must contain a legend as follows: This is the pre-peer reviewed version of the following article: FULL CITE, which has been published in final form at [Link to final article].

b. The right to transmit, print and share copies with colleagues.

2. Accepted Version. Reuse of the accepted and peer-reviewed (but not final) version of the Contribution shall be by separate agreement with Wiley-VCH. Wiley-VCH has agreements with certain funding agencies governing reuse of this version. The details of those relationships, and other offerings allowing open web use are set forth at the following website: http://www.wiley.com/go/funderstatement. NIH grantees should check the box at the bottom of this document.

3. Final Published Version. Wiley-VCH hereby licenses back to the Contributor the following rights with respect to the final published version of the Contribution:

a. Copies for colleagues. The personal right of the Contributor only to send or transmit individual copies of the final published version to colleagues upon their specific request provided no fee is charged, and further-provided that there is no systematic distribution of the Contribution, e.g. posting on a listserve, website or automated delivery. For those Contributors who wish to send high-quality e-prints, purchase reprints, or who wish to distribute copies more broadly than allowed hereunder (e.g. to groups of colleagues or mailing lists), please contact the publishing office.

b. Re-use in other publications. The right to re-use the final Contribution or parts thereof for any publication authored or edited by the Contributor (excluding journal articles) where such re-used material constitutes less than half of the total material in such publication. In such case, any modifications should be accurately noted.

c. Teaching duties. The right to include the Contribution in teaching or training duties at the Contributor's institution/place of employment including in course packs, e-reserves, presentation at professional conferences, in-house training, or distance learning. The Contribution may not be used in seminars outside of normal teaching obligations (e.g. commercial seminars). Electronic posting of the final published version in connection with teaching/training at the Contributor's institution/place of employment is permitted subject to the implementation of reasonable access control mechanisms, such as user name and password. Posting the final published version on the open Internet is not permitted.

d. Oral presentations. The right to make oral presentations based on the Contribution.

4. Article Abstracts, Figures, Tables, Data Sets, Artwork and Selected Text (up to 250 words).

a. Contributors may re-use unmodified abstracts for any non-commercial purpose. For on-line uses of the abstracts, Wiley-VCH encourages but does not require linking back to the final published versions.

b. Contributors may re-use figures, tables, data sets, artwork, and selected text up to 250 words from their Contributions, provided the following conditions are met:

(i) Full and accurate credit must be given to the Contribution.
(ii) Modifications to the figures, tables and data must be noted. Otherwise, no changes may be made.
(iii) The reuse may not be made for direct commercial purposes, or for financial consideration to the Contributor.
(iv) Nothing herein shall permit dual publication in violation of journal ethical practices.

CTA-VCH

D. CONTRIBUTIONS OWNED BY EMPLOYER

1. If the Contribution was written by the Contributor in the course of the Contributor's employment (as a "work-made-for-hire" in the course of employment), the Contribution is owned by the company/employer which must sign this Agreement (in addition to the Contributor's signature) in the space provided below. In such case, the company/employer hereby grants to Wiley-VCH the full and exclusive rights comprised in the Contribution as specified in paragraph A above throughout the world for the duration of the statutory term of protection.

2. In addition to the rights specified as retained in paragraph B above and the rights granted back to the Contributor pursuant to paragraph C above, Wiley-VCH hereby grants back, without charge, to such company/employer, its subsidiaries and divisions, the right to make copies of and distribute the final published Contribution internally in print format or electronically on the Company's internal network. Copies so used may not be resold or distributed externally. However the company/employer may include information and text from the Contribution as part of an information package included with software or other products offered for sale or license or included in patent applications. Posting of the final published Contribution by the institution on a public access website may only be done with Wiley-VCH's written permission, and payment of any applicable fee(s). Also, upon payment of Wiley-VCH's reprint fee, the institution may distribute print copies of the published Contribution externally.

E. GOVERNMENT CONTRACTS

In the case of a Contribution prepared under U.S. Government contract or grant, the U.S. Government may reproduce, without charge, all or portions of the Contribution and may authorize others to do so, for official U.S. Government purposes only, if the U.S. Government contract or grant so requires. (U.S. Government, U.K. Government, and other government employees: see notes at end.)

F. COPYRIGHT NOTICE

The Contributor and the company/employer agree that any and all copies of the final published version of the Contribution or any part thereof distributed or posted by them in print or electronic format as permitted herein will include the notice of copyright as stipulated in the Journal and a full citation to the Journal as published by Wiley-VCH.

G. CONTRIBUTOR'S REPRESENTATIONS

The Contributor represents that the Contribution is the Contributor's original work, all individuals identified as Contributors actually contributed to the Contribution, and all individuals who contributed are included. If the Contribution was prepared jointly, the Contributor agrees to inform the co-Contributors of the terms of this Agreement and to obtain their signature to this Agreement or their written permission to sign on their behalf. The Contribution is submitted only to this Journal and has not been published before. (If excerpts from copyrighted works owned by third parties are included, the Contributor will obtain written permission from the copyright owners for all uses as set forth in Wiley-VCH's permissions form or in the Journal's Instructions for Contributors, and show credit to the sources in the Contribution.) The Contributor also warrants that the Contribution contains no libelous or unlawful statements, does not infringe upon the rights (including without limitation the copyright, patent or trademark rights) or the privacy of others, or contain material or instructions that might cause harm or injury.

CHECK ONE BOX:

☐ Contributor-owned work

ATTACH ADDITIONAL SIGNATURE PAGES AS NECESSARY

Contributor's signature _____ Date _____

Type or print name and title _____

Co-contributor's signature _____ Date _____

Type or print name and title _____

☐ Company/Institution-owned work (made-for-hire in the course of employment)

Company or Institution (Employer-for-Hire) _____ Date _____

Authorized signature of Employer _____ Date _____

☐ U.S. Government work

Note to U.S. Government Employees
A contribution prepared by a U.S. federal government employee as part of the employee's official duties, or which is an official U.S. Government publication, is called a "U.S. Government work," and is in the public domain in the United States. In such case, the employee may cross out Paragraph A.1 but must sign (in the Contributor's signature line) and return this Agreement. If the Contribution was not prepared as part of the employee's duties or is not an official U.S. Government publication, it is not a U.S. Government work.

☐ U.K. Government work (Crown Copyright)

Note to U.K. Government Employees
The rights in a Contribution prepared by an employee of a U.K. government department, agency or other Crown body as part of his/her official duties, or which is an official government publication, belong to the Crown. U.K. government authors should submit a signed declaration form together with this Agreement. The form can be obtained via http://www.opsi.gov.uk/advice/crown-copyright/copyright-guidance/publication-of-articles-written-by-ministers-and-civil-servants.htm

☐ Other Government work

Note to Non-U.S., Non-U.K. Government Employees
If your status as a government employee legally prevents you from signing this Agreement, please contact the editorial office.

☐ NIH Grantees

Note to NIH Grantees
Pursuant to NIH mandate, Wiley-VCH will post the accepted version of Contributions authored by NIH grant-holders to PubMed Central upon acceptance. This accepted version will be made publicly available 12 months after publication. For further information, see http://www.wiley.com/go/funderstatement.

CTA-VCH